

Structural Integrity 24

Series Editors: José A. F. O. Correia · Abílio M. P. De Jesus

Grzegorz Lesiuk · Szymon Duda ·
Jose A. F. O. Correia ·
Abilio M. P. De Jesus *Editors*

Fatigue and Fracture of Materials and Structures


Contributions from ICMFM XX
and KKMP2021


 Springer

Structural Integrity

Volume 24

Series Editors

José A. F. O. Correia , Faculty of Engineering, University of Porto, Porto, Portugal

Abílio M. P. De Jesus , Faculty of Engineering, University of Porto, Porto, Portugal

Advisory Editors

Majid Reza Ayatollahi, School of Mechanical Engineering, Iran University of Science and Technology, Tehran, Iran

Filippo Berto, Department of Mechanical and Industrial Engineering, Faculty of Engineering, Norwegian University of Science and Technology, Trondheim, Norway

Alfonso Fernández-Canteli, Faculty of Engineering, University of Oviedo, Gijón, Spain

Matthew Hebdon, Virginia State University, Virginia Tech, Blacksburg, VA, USA

Andrei Kotousov, School of Mechanical Engineering, University of Adelaide, Adelaide, SA, Australia

Grzegorz Lesiuk, Faculty of Mechanical Engineering, Wrocław University of Science and Technology, Wrocław, Poland

Yukitaka Murakami, Faculty of Engineering, Kyushu University, Higashiku, Fukuoka, Japan

Hermes Carvalho, Department of Structural Engineering, Federal University of Minas Gerais, Belo Horizonte, Minas Gerais, Brazil

Shun-Peng Zhu, School of Mechatronics Engineering, University of Electronic Science and Technology of China, Chengdu, Sichuan, China

Stéphane Bordas, University of Luxembourg, ESCH-SUR-ALZETTE, Luxembourg

Nicholas Fantuzzi , DICAM Department, University of Bologna, BOLOGNA, Bologna, Italy

Luca Susmel, Civil Engineering, University of Sheffield, Sheffield, UK

Subhrajit Dutta, Department of Civil Engineering, National Institute Of Technology Silchar, Silchar, Assam, India

Pavlo Maruschak, Ternopil IP National Technical University, Ruska, Ukraine

Elena Fedorova, Siberian Federal University, Krasnoyarsk, Russia

The *Structural Integrity* book series is a high level academic and professional series publishing research on all areas of Structural Integrity. It promotes and expedites the dissemination of new research results and tutorial views in the structural integrity field.

The Series publishes research monographs, professional books, handbooks, edited volumes and textbooks with worldwide distribution to engineers, researchers, educators, professionals and libraries.

Topics of interested include but are not limited to:

- Structural integrity
- Structural durability
- Degradation and conservation of materials and structures
- Dynamic and seismic structural analysis
- Fatigue and fracture of materials and structures
- Risk analysis and safety of materials and structural mechanics
- Fracture Mechanics
- Damage mechanics
- Analytical and numerical simulation of materials and structures
- Computational mechanics
- Structural design methodology
- Experimental methods applied to structural integrity
- Multiaxial fatigue and complex loading effects of materials and structures
- Fatigue corrosion analysis
- Scale effects in the fatigue analysis of materials and structures
- Fatigue structural integrity
- Structural integrity in railway and highway systems
- Sustainable structural design
- Structural loads characterization
- Structural health monitoring
- Adhesives connections integrity
- Rock and soil structural integrity.

**** Indexing: The books of this series are submitted to Web of Science, Scopus, Google Scholar and Springerlink ****

This series is managed by team members of the ESIS/TC12 technical committee.

Springer and the Series Editors welcome book ideas from authors. Potential authors who wish to submit a book proposal should contact Dr. Mayra Castro, Senior Editor, Springer (Heidelberg), e-mail: mayra.castro@springer.com

More information about this series at <https://link.springer.com/bookseries/15775>

Grzegorz Lesiuk · Szymon Duda ·
José A. F. O. Correia · Abílio M. P. De Jesus
Editors

Fatigue and Fracture of Materials and Structures


Contributions from ICMFM XX
and KKMP2021


 Springer

Editors

Grzegorz Lesiuk
Faculty of Mechanical Engineering
Wrocław University of Science
and Technology
Wrocław, Poland

Szymon Duda
Faculty of Mechanical Engineering
Wrocław University of Science
and Technology
Wrocław, Poland

José A. F. O. Correia 
Faculty of Engineering
University of Porto
Porto, Portugal

Abílio M. P. De Jesus 
Faculty of Engineering
University of Porto
Porto, Portugal

ISSN 2522-560X

ISSN 2522-5618 (electronic)

Structural Integrity

ISBN 978-3-030-97821-1

ISBN 978-3-030-97822-8 (eBook)

<https://doi.org/10.1007/978-3-030-97822-8>

© The Editor(s) (if applicable) and The Author(s), under exclusive license to Springer Nature Switzerland AG 2022

This work is subject to copyright. All rights are solely and exclusively licensed by the Publisher, whether the whole or part of the material is concerned, specifically the rights of translation, reprinting, reuse of illustrations, recitation, broadcasting, reproduction on microfilms or in any other physical way, and transmission or information storage and retrieval, electronic adaptation, computer software, or by similar or dissimilar methodology now known or hereafter developed.

The use of general descriptive names, registered names, trademarks, service marks, etc. in this publication does not imply, even in the absence of a specific statement, that such names are exempt from the relevant protective laws and regulations and therefore free for general use.

The publisher, the authors and the editors are safe to assume that the advice and information in this book are believed to be true and accurate at the date of publication. Neither the publisher nor the authors or the editors give a warranty, expressed or implied, with respect to the material contained herein or for any errors or omissions that may have been made. The publisher remains neutral with regard to jurisdictional claims in published maps and institutional affiliations.

This Springer imprint is published by the registered company Springer Nature Switzerland AG
The registered company address is: Gewerbestrasse 11, 6330 Cham, Switzerland

Preface

This volume contains forty-two papers presented at the “20th International Colloquium on Mechanical Fatigue of Metals” (ICMFM XX) held in Wroclaw, Poland, September 15–17, 2021, in a virtual mode. The ICMFM XX conference was divided into eight minisymposiums. The symposia are “Fatigue Failure Analysis and Environmentally Assisted Fatigue,” “Fatigue and Fracture of Welded Connections and Complex Structures,” “Probabilistic Fatigue and Fracture Approaches Applied to Materials and Structures,” “Recent Advances on Mixed-Mode Fatigue and Fracture,” “Fatigue and Structural Integrity of Metallic Bridges,” “Structural Integrity and Fatigue Assessment of Additive Manufactured Metals and Biomaterials,” “Structural Integrity And Fatigue Assessment Of Pressurized Metallic Components (Pressure Vessels, Pipes, Hydraulic Components) And Materials,” and “Cyclic Deformation Behaviour and Fatigue of Metastable, High Entropy and Smart Materials.” Each symposium was led by prominent scientists in the field.

This international colloquium was intended to facilitate and encourage the exchange of knowledge and experiences among the different communities involved in both basic and applied researches in this field, the fatigue of metals, looking at the problem of fatigue from a multiscale perspective, and exploring analytical and numerical simulative approaches, without losing the perspectives of the application.

The attendees of ICMFM XX had an opportunity to interact with the most outstanding world scientists and get acquainted with the latest research in fracture mechanics and fatigue of metals. The eight keynote speaker delivered the latest research updates from the scientific world. This event that lasts for three days will provide a great opportunity to exchange thoughts as well as highlight the latest trends in science.

More than a hundred participants attended ICMFM XX. Considering country affiliation, almost 75% of the scientists were from Europe. People from the Czech Republic and Portugal influence this quantity the most. Secondly, due to the great presents of the Chinese Scientist, Asia is represented by 20% of researchers from the entire participants. The last 5% was represented by scientists from north and south America.

We very sincerely thank the authors who have contributed to this volume, the symposium/sessions organizers for their hard work and dedication and the referees who reviewed the quality of the submitted contributions. The tireless effort of the members of the organizing committee as well as of other numerous individuals and people behind the scenes is appreciated.

Wrocław, Poland
Wrocław, Poland
Porto, Portugal
Porto, Portugal
December 2021

Grzegorz Lesiuk
Szymon Duda
José A. F. O. Correia
Abílio M. P. De Jesus

Contents

Part I Numerical Approaches Applied to Fatigue and Fracture Assessment

1 Numerical Simulation of Fatigue Crack Growth in Different Welded Joint Zones	3
Milivoje Jovanović, Simon Sedmak, Aleksandar Sedmak, Zijah Burzić, and Ivica Čamagić	
2 Calculation of the Stress State in Coatings by Analytical and Numerical Methods Considering Thermal Loads	9
Nikolay Dolgov, Leonid Vinogradov, Ilmars Blumbergs, and Rafal Chatys	
3 Numerical Simulation and Constructal Design Applied to Perforated Plate Subjected to Biaxial Buckling	23
Guilherme Ribeiro Baumgardt, Eysler Queiroz De Sousa, Leonardo Willian Barbosa Pinto, Elizaldo Domingues Dos Santos, Thiago Da Silveira, and Liércio André Isoldi	
4 Fatigue Damage Simulation of a Metal Sandwich Panel Under Four-Point Bending Conditions	29
M. K. Faidzi, S. Abdullah, M. F. Abdullah, S. S. K. Singh, A. H. Azman, José A. F. O. Correia, and D. Hui	
5 Analysis of Pulse Load of a Steel Roller in the Numerical Simulation Method	39
Dariusz Pyka, Kayode Olaleye, Adam Kurzawa, Tetiana Roik, Grzegorz Ziolkowski, Mirosław Bocian, and Krzysztof Jamroziak	

Part II Fatigue and Fracture Assessment of Joints and Complex Structures	
6	Fatigue Analysis of Thin-Walled Welded Hollow Section Joints 49 Martin Machač, Jan Papuga, Karel Doubrava, and Jakub Fišer
7	Analytical Solutions of Water Hammer in Metal Pipes. Part I—Brief Theoretical Study 57 Kamil Urbanowicz, Anton Bergant, Michał Stosiak, and Marek Lubecki
8	Analytical Solutions of Water Hammer in Metal Pipes. Part II—Comparative Study 69 Kamil Urbanowicz, Anton Bergant, Michał Stosiak, and Krzysztof Towarnicki
9	Experimental and Theoretical Analysis of Hydraulic Cylinder Loads 85 Marek Lubecki, Michał Stosiak, Michał Banaś, Piotr Stryczek, and Kamil Urbanowicz
10	A New Anti-fatigue Design Method for Welded Structures Based on Stiffness Coordination Strategy and Its Application 93 Chunliang Niu, Suming Xie, and Tao Zhang
11	Characterization of Multiaxial Strain Road Loads in Assessing the Durability of Automotive Coil Spring 101 N. M. Hazmi, S. S. K. Singh, S. Abdullah, L. Abdullah, A. H. Azman, and M. R. M. Rasani
12	Identification of Key Fatigue Welds of Bogie Welded Frame 111 Suming Xie, Zhipeng Xu, Chunliang Niu, Chungue Nie, and Tao Zhang
13	Susceptibility of Steel Sucker Rods Operated in Oil Well to Environmentally Assisted Fatigue 119 Olha Zvirko, Oleksandr Tsyurulnyk, and Nataliya Kret
14	Increasing the Durability of Critical Parts in Heavy-Duty Industrial Machines by Deep Cryogenic Treatment 127 Pavlo Krot, Serhii Bobyr, Ivan Zharkov, Ihor Prykhodko, and Przemysław Borkowski
15	Risk-Based Inspection Strategies of Miter Gates Based on Structural Health Monitoring 135 Thuong Van Dang and Philippe Rigo

16 Fatigue Behavior of Re-tightened Bolted Joints Affected by Vibration-Induced Loosening 141
 Baris Tanrikulu, Ramazan Karakuzu, Sarper Dogan, and Sezgin Yurtdas

17 Friction Resistances in Internal Gear Pump with Modified Sickle Made of Plastic 147
 Krzysztof Towarnicki, Michał Stosiak, Piotr Antoniak, Tadeusz Leśniewski, Kamil Urbanowicz, and Paweł Śliwiński

18 Defect Development in Ultra-Supercritical Steam Turbine Rotors According to British Standards 155
 Mariusz Banaszekiewicz and Janusz Badur

Part III Probabilistic Fatigue and Fracture Approaches Applied to Materials and Structures

19 Fatigue Life Assessment Within the Frequency Domain for Explosive Cladded Joints Under Non-Gaussian Random Loading 169
 Michał Böhm

20 Cluster Analysis in the Choice of Operating Modes in Durability Analysis of Random Time-History Records 177
 Irina Gadolina, Julian Marcell Enzweiler Marques, and Denis Benasciutti

21 Comparison of Different Fatigue Laws for Probabilistic Modeling of Mechanical Fatigue with Censored Data Using Maximum Likelihood Estimation Method 185
 Ivan Rukavina, Faouzi Adjed, Charlotte Chabanas, Samuel Van De Hel, Mohcine Nfaoui, and Alexandre Demenais

22 Evaluating Confidence Interval of Fatigue Damage from One Single Measured Non-stationary Time-History 193
 Julian M. E. Marques and Denis Benasciutti

23 Review of the Models for Determining the Moment of the Initiation of the Fatigue Crack in the Frequency Domain for Random Loads with Non-Gaussian Distribution 201
 Michał Böhm

Part IV Failure Analysis and Recent Advances on Mixed-Mode Fatigue and Fracture

24 On High- and Very High Cycle Fatigue of Metals and Alloys at Axial Loading 211
 E. B. Zavoychinskaya

25	Analysis of Aramid Fabric Damage Mechanisms as a Result of Different Load Speeds	219
	Pawel Zochowski, Dariusz Pyka, Adam Kurzawa, Marcin Bajkowski, Mariusz Magier, Ilmars Blumbergs, Roman Grygoruk, Miroslaw Bocian, and Krzysztof Jamroziak	
26	Experimental Identification of Viscoelastic Properties of Plates Made of Quiet Aluminum	227
	Pasquale Grosso, Alessandro De Felice, and Silvio Sorrentino	
27	Influence of Different Surface- and Heat Treatments; Elevated Temperature, Orientation on the Fatigue Properties of Ti6Al4V Processed by L-PBF for Controlled Powder Properties	235
	Benjamin Meier, Fernando Warchomicka, Reinhard Kaindl, Christoph Sommitsch, and Wolfgang Waldhauser	
28	Fatigue Crack Growth Resistance of Heat-Resistant Steel 15H11MF After Operation in Blades of a Steam Turbine	245
	Halyna Krechkovska, Myroslava Hredil, and Oleksandra Student	
29	Operational Degradation of Fatigue Strength of Structural Steels: Role of Corrosive-Hydrogenating Environments	253
	Hryhoriy Nykyforchyn and Olha Zvirko	
30	Global Statistical Analysis of Old Iron and Steel Properties Based on Old and Recent Literature Review	259
	Stéphane Sire	
31	Forming Stress-Induced Initial Damage in Case Hardening Steel 16MnCrS5 Under Cyclic Axial Loading in LCF Regime	267
	Kerstin Moehring and Frank Walther	
32	Stress Ratio Effect on Fatigue Crack Growth Rate Based on Magnetic Flux Leakage Parameters	275
	Azli Arifin, Shahrum Abdullah, Ahmad Kamal Ariffin, Nordin Jamaludin, and Salvinder Singh Karam Singh	
33	Influence of Heat Treatment Temperature on Fatigue Toughness in Medium-Carbon High-Strength Steels	283
	G. Wheatley, R. Branco, José A. F. O. Correia, R. F. Martins, W. Macek, Z. Marciniak, and M. Szala	
34	Effect of Specimen Thickness on Fatigue Crack Growth Resistance in Paris Region in AISI 304 STEEL	291
	Stanislav Seitl, Pavel Pokorný, Jan Klusák, Szymon Duda, and Grzegorz Lesiuk	

35 Fracture Mechanics Assessment of Notches Subjected to Very High-Cycle Fatigue Loading 299
 Kamila Kozakova and Jan Klusak

36 Fatigue Failure of 51CrV4 Steel Under Rotating Bending and Tensile 307
 V. M. G. Gomes, Abílio M. P. De Jesus, M. Figueiredo, José A. F. O. Correia, and R. Calcada

37 The Role of the Surface in Crack Initiation in Sharp and Bi-material Notches 315
 Jan Klusák and Dalibor Kopp

38 Experimental Study on Failure Mechanisms of Novel Visco-Hyperelastic Material Target Under Ballistic Impact Conditions 323
 Pawel Zochowski, Marcin Cegła, Marcin Bajkowski, Roman Grygoruk, Mariusz Magier, Krzysztof Szczurowski, Jędrzej Maczak, Mirosław Bocian, Roman Gieleta, and Krzysztof Jamroziak

Part V Structural Integrity and Fatigue Assessment of Additive Manufactured Metals and Biomaterials

39 Fatigue Behavior of As-Built L-PBF Inconel 718 and Surface Roughness-Based Modeling 333
 Gianni Nicoletto and Federico Uriati

40 Fatigue Behavior of the Titanium-Tantalum Alloy Obtained by Additive Manufacturing 341
 Teresa Morgado, Catarina Valente, Josu Leunda, Alexandre Velhinho, and Rui Silva

41 Some Observation Concerning Fatigue Response of Additively Manufactured Specimens from Ti-6Al-4V 351
 Martin Nesládek, Martin Matušů, Jan Papuga, Matěj Mžourek, and Michaela Roudnická

42 Cyclic Plasticity and Low-Cycle Fatigue of an AISI 316L Stainless Steel Tested at Room Temperature 359
 Denis Benasciutti, Marco Pelegatti, Alex Lanzutti, Enrico Salvati, Jelena Srnc Novak, and Francesco De Bona

43 Contribution to the Study of the Fatigue of Riveted Joints, Influence of the Material and of the Stress Ratio 367
 Stéphane Sire, Paul Dario Toasa Caiza, Bernard Espion, and Muriel Ragueneau

Part I
**Numerical Approaches Applied to Fatigue
and Fracture Assessment**

Chapter 1

Numerical Simulation of Fatigue Crack Growth in Different Welded Joint Zones



Milivoje Jovanović, Simon Sedmak, Aleksandar Sedmak , Zijah Burzić, and Ivica Čamagić

Abstract This paper involves the numerical analysis of fatigue behaviour of welded joints made of steel SA-387 Gr. 91, with special attention devoted to its regions, which have very different mechanical and fatigue properties. Extensive experimental research, which was performed in order to obtain the coefficients necessary for the analysis of fatigue life of structures and parts made of this steel, was used as the base for the finite element method simulation, performed in ANSYS R19.2. Due to the typical applications of steels from this group, all experiments were performed at elevated temperature of 575 °C, which corresponds to the exploitation conditions for this material. Obtained results have shown noticeable difference in fatigue crack growth resistance of different welded joint regions, as was expected from the experimental results.

Keywords Fatigue crack growth · Welded joints · xFEM · Paris law coefficients

1.1 Introduction

The aim of this research was to numerically simulate fatigue crack growth through different regions of a welded joint regions, including the parent material, the weld metal and the heat-affected zone. To achieve this goal, finite element method [1–5] was used in combination with the experimentally obtained results. Welded joints were made of SA-387 Gr. 91 steel [6], typically used for structures which work at elevated temperatures. Due to this, finite element method simulations were carried

M. Jovanović · I. Čamagić

Faculty of Technical Sciences, University K. Mitrovica, Mitrovica, Serbia

S. Sedmak (✉)

Innovation Center of the Faculty of Mechanical Engineering, Belgrade, Serbia

A. Sedmak

Faculty of Mechanical Engineering, University of Belgrade, Belgrade, Serbia

Z. Burzić

Institute for material testing, Belgrade, Serbia



Fig. 1.1 $C(T)$ specimens for different regions of the welded joint

out under such conditions, with mechanical and fatigue properties (Paris coefficients in this case) taken from experiments that were performed at 575 °C.

The obtained results for each welded joint region were then compared mutually, in terms of number of cycles, in order to determine which welded joint region had the highest resistance to fatigue crack growth, i.e. which one had the longest fatigue life in the presence of an initial crack. This research was inspired by similar work [7, 8], which also involved different types of steels, also focusing on the heterogeneity of welded joint regions [5, 9, 10] in terms of mechanical properties and its effect of fatigue behaviour of welded joints. In this way, the authors of the paper were able to further improve the methodology which was recently developed in Sedmak et al. [7], confirming its application to different types of materials.

1.2 Experimental Results

Experimental determination of C and m parameters from Paris law ($da/dN = C \cdot \Delta K^m$) was performed in a standard way ASTM E647, at elevated temperature of 575 °C, using modified $C(T)$ specimens for all three welded joint zones, Fig. 1.1.

Results are shown as the combination of C and m values which provides the highest fatigue crack growth in each welded joint zone:

- $C = 6.00 \times 10^{-12}$ and $m = 3.22$ for the parent metal (PM).
- $C = 2.59 \times 10^{-11}$ and $m = 3.46$ for the weld metal (WM).
- $C = 2.60 \times 10^{-10}$ and $m = 2.20$ for the heat affected zone (HAZ).

1.3 Numerical Simulation

Numerical simulations of fatigue behaviour of $C(T)$ specimens at elevated temperatures included the following steps:

- Development of models based on the geometry of the modified specimens used in the experiment stage of this research.
- Defining of mechanical and fatigue properties in the manner described in the previous section.
- Defining of boundary conditions and loads which would correspond to the real experimental conditions as closely as possible.
- Introducing a fatigue crack in the location where it had occurred in the real specimens.
- Defining the number of substeps necessary for the fatigue crack to reach the limit length of 5 mm (according to the maximum measuring capacity of the measuring foils used in the experiment).

Since $C(T)$ specimens are typically loaded via the two holes through which they are also supported, a similar approach was used in ANSYS. This version of the software has an option for defining a special boundary condition which prevents most displacements and rotations around the axes other than the one in which the load is acting—and it can be applied to the inner surfaces of the two holes. In this way, there was no need to define separate load and boundary conditions, since both could be introduced using the same option. An additional boundary condition was also applied to the middle section of the specimens curved surface, in order to fix the model itself and prevent it from having unexpected displacements once fatigue crack starts propagating, since at this point the load conditions are no longer necessarily symmetrical.

The loads, defined in the form of two tensile forces acting in the opposite directions, were defined in accordance with the tensile test results, with values taken from tables made based on force–displacement diagrams. For all three cases, force magnitudes were slightly above 7 kN and the loads in the models were defined accordingly. The load step was divided into a number of substeps, since these control the overall crack length. The total amount of substeps necessary for the crack length to reach 5 mm varied, depending on the mechanical properties and loads (the latter not being significant, due to very similar load magnitudes for all models). The needed number of substeps was determined iteratively, until the desired length of ~5 mm was reached. Finite element mesh was generated using TET elements, Fig. 1.4, with finer mesh near the crack tip.

1.3.1 Numerical Results

Results are given in Figs. 1.3, 1.4 and 1.5 in the form of crack length, a , dependence on number of cycles, N , for PM, WM and HAZ, respectively. Obtained results have shown significant differences in terms of the number of cycles to reach $a = 5$ mm, indicating significant differences in welded joint zones. Initial fatigue crack length in all three cases was 0.2 mm, and as was shown in Fig. 1.2, it was placed at the tip of the notch in the $C(T)$ specimen model. These differences in all cases show that

the effect of welded joint heterogeneity on the fatigue behaviour of $C(T)$ specimens in this case was considerable.

As can be seen from the a-N diagrams shown in Figs. 1.5, 1.6, 1.7, the parent material had shown the best fatigue resistance of all three welded joint regions, reaching a total of 1729 cycles, almost three times as much as the heat-affected zone model (657 cycles). Weld metal performed the worst, compared to the other two regions, with a very low number of total cycles, at 65. This suggests that the behaviour of a welded joint made with steel SA-387 Gr. 91 under fatigue load would be significantly affected by the location of the fatigue crack in a real structure. Since the welded joint in this case was overmatched, the crack would typically

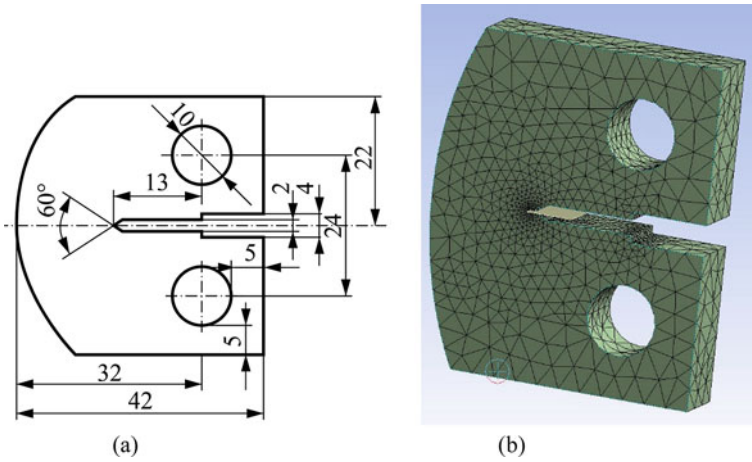


Fig. 1.2 a CT specimen and its b finite element model

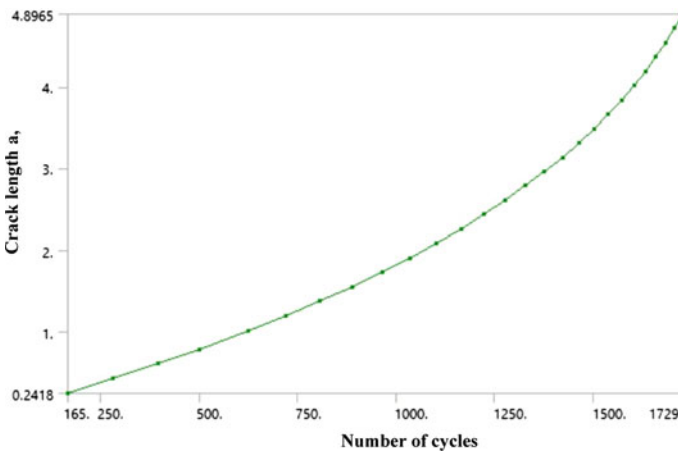


Fig. 1.3 Crack length versus number of cycles diagram for parent metal

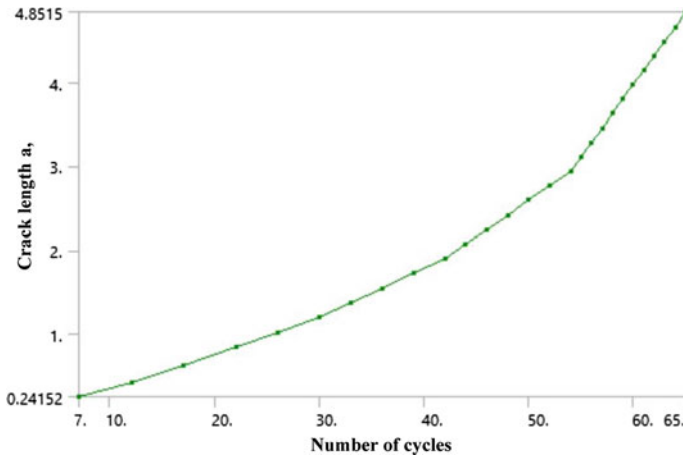


Fig. 1.4 Crack length versus number of cycles diagram for weld metal

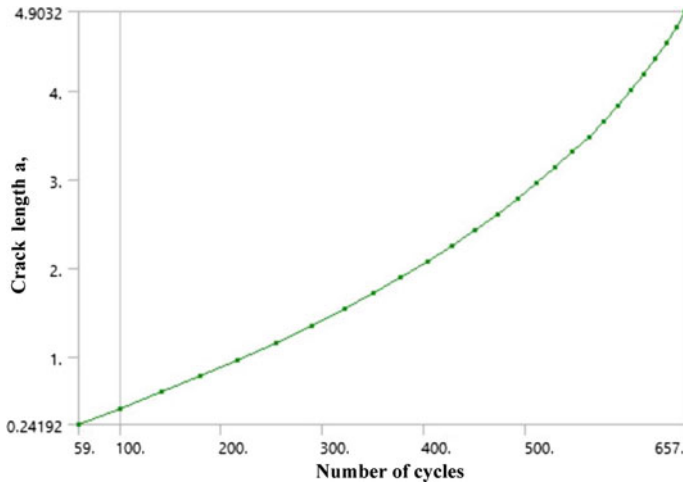


Fig. 1.5 Crack length versus number of cycles diagram for heat affected zone

initiate in the parent material, which would be a favourable scenario, since it has the highest resistance to fatigue crack growth. On the other hand, crack initiating in the weld metal would lead to quick failure due to fatigue, which should be taken into account as it is a possibility in the case of an inadequately defined/performed welding technology. All of this applies to elevated temperatures, which are characterised by noticeable changes in mechanical properties of materials involved, which suggests that similar tests should also be performed at room temperature, in order to determine if the relationship between the mechanical and fatigue properties of all welded joint regions would remain more or less the same.

1.4 Conclusions

The following conclusions were drawn based on the obtained results:

- Simulations shown in this paper can achieve sufficiently good results in very little time, and it is easy to adjust the models to different materials.
- Results for different regions can differ significantly, and this needs to be further related to the microstructural aspect of welded joint heterogeneity.

Acknowledgements This research was supported by the Ministry of Sciences and Technology of Republic of Serbia through the contracts 451-03-9/2021-14/200105 and 451-03-68/2020-14/200105.





References

1. Sedmak A (2018) Computational fracture mechanics: an overview from early efforts to recent achievements. *Fatigue Fract Eng Mater Struct* 41:2438–2474
2. Hemer A, Arandjelović M, Milović Lj, Kljajin M, Lozanović Šajjić J (2020) J. analytical vs. numerical calculation of fatigue life for different welded joint regions, accepted for publishing *Technical Gazette* 27(6):1931–1937
3. Hemer A, Sedmak S, Milović Lj, Grbović A, Sedmak A (2020) FEM simulation of welded joint geometry influence on fatigue crack growth resistance. *Procedia Struct Integrity* 28:1827–183
4. Milović Lj, Vuherer T, Radaković Z, Petrovski B, Janković M, Zrilić M, Daničić D (2011) Determination of fatigue crack growth parameters in welded joint of HSLA steel. *Struct Integrity Life* 11(3):183–187
5. Mlikota M, Schmauder S, Božić Ž, Hummel M (2017) Modelling of overload effects on fatigue crack initiation in case of carbon steel. *Fatigue Fract Eng Mater Struct* 40(8):1182–1190
6. Čamagić I, Sedmak S, Sedmak A, Burzić Z (2019) Influence of temperature on fracture toughness values in different regions of A-387 Gr B welded joint. *Procedia Struct Integrity* 18:205–213
7. Sedmak A, Hemer A, Sedmak S, Milović Lj, Grbović A, Čabrilo A, Kljajin M (2021) Welded joint geometry effect on fatigue crack growth resistance in different metallic materials. *Int J Fatigue* 150:106298
8. Arandjelović M et al (2021) Numerical and experimental investigations of fracture behaviour of welded joints with multiple defects. *Materials* 14(17), special issue numerical and experimental analysis of fracture behaviour of heterogeneous welded structures. <https://doi.org/10.3390/ma14174832>
9. Berković M, Maksimović S, Sedmak A (2004) Analysis of welded joints by applying the finite element method. *Struct Integrity Life* 4(2):75–83
10. Arandjelović M et al (2021) Numerical simulation of welded joint with multiple various defects. *Struct Integrity Life* 21(1):103–107

Chapter 2

Calculation of the Stress State in Coatings by Analytical and Numerical Methods Considering Thermal Loads



Nikolay Dolgov , Leonid Vinogradov , Ilmars Blumbergs ,
and Rafal Chatys 

Abstract The aim of this paper is to provide an analytical solution for the stress distribution in a coated substrate under tensile and thermal loads. An analytical model for coated substrate is derived in order to evaluate the distribution of interface shear stress. The stress distributions in the coating-substrate interface show concentration of interface shear stress near free edge of the coating, which must be taken into account when developing coatings for aircraft and increasing their service life since the results of numerical simulation are in good agreement with the stresses obtained by the analytical method, except for the regions in which the stress singularity arises and exists. The magnitude of these stresses depends both on the level of the load applied to the substrate and on the thermal stresses arising from the difference in the coefficients of thermal expansion of the substrate and the coating. These features in the operation of materials with high-temperature coatings should be taken into account in the design and manufacture of thermal barrier coatings for gas turbine engine blades. This paper is a part of work that has been started in Riga Technical University in project supported by the European Regional Development Fund “High-Performance Erosion Resistant Multifunctional coatings for Aircraft Composite Structures (PEROMACS)”.

Keywords Coating-substrate system · Stress distribution · Analytical model · Thermal loading · Shear stress

N. Dolgov

G.S.Pisarenko Institute for Problems of Strength, Nat. Ac. Sci. of Ukraine, Timiryazevska Str,
Kyiv 01014, Ukraine

National Transport University, 1 Omelianovycha-Pavlenka Str, Kyiv 01010, Ukraine

L. Vinogradov · I. Blumbergs (✉)

Institute of Aeronautics, Riga Technical University, 1 Kalku Street, Riga 1658, Latvia
e-mail: ilmars.blumbergs@rtu.lv

R. Chatys

Kielce University of Technology, al. Tysiąclecia Państwa Polskiego 7, 25-314 Kielce, Poland

2.1 Introduction

The coatings increase the wear resistance, corrosion resistance, and thermal barrier properties of various structures. Plasma spraying of ceramic coatings is widely used in shipbuilding, automobile, and aircraft industry. To increase the adhesion strength of the ceramic coating, a plasma-sprayed metal sublayer is used [1–5].

The properties of plasma-sprayed coatings depend, first of all, on the structure, composition, and morphology of the initial powders, porosity, as well as micro- and macro-cracks. One of the most important causes of component failure is cracking and detachment of the top ceramic layer during service [6]. In this regard, studies of the strength properties, processes of delamination, and cracking of coatings are necessary to increase their reliability and improve the design. There are various approaches to assessing the stress state in multilayer materials under various types of force loading [7–12] and thermal loads [13–16].

The paper presents an analysis of the stress state, obtained by the analytical approach, using the example of coatings that are used to protect the blades of aircraft gas turbine engines. The effect of thermal loads on the stress state in the plane of the adhesive contact between the substrate and the coating is considered. The studies carried out are necessary for the development of modern ideas about the peculiarities of the delamination of high-temperature ceramic coatings under the influence of power and thermal loads. The purpose of this study is to develop an analytical model to predict the interfacial stresses for the coating-substrate systems.

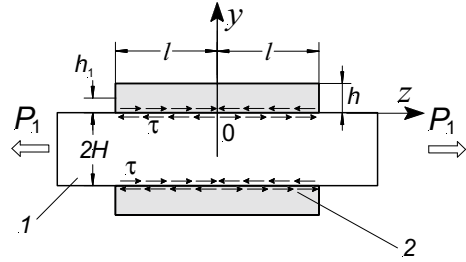
2.2 Development of an Analytical Model to Determine the Stress State in the Coating

When exposed to an external load in the coatings, due to the different characteristics of the coating and substrate, an inhomogeneous stress state arises. These features of multilayer materials must be taken into account in the development and design of coated structural elements. Below is the output of analytical equations that allow you to determine the shear stresses in the substrate-coating interface when tensile forces are applied to the substrate together with thermal loads.

Consider a plate with a coating applied to the top and bottom surfaces of a substrate that is being stretched (Fig. 2.1). Loads are applied to the substrate 1. Consider the section at a distance $h_1 = h/2$ from the substrate-coating interface. In the planes of adhesive contact between the substrate 1 and the coating 2, as well as at a distance $h/2$ from the substrate-coating interface, shear stresses τ and τ_1 arise, respectively. The substrate is the subject to a thermal load ΔT .

We assume that the shear stresses τ and τ_1 are proportional to the difference in displacements in adjacent layers of materials that make up the substrate-coating system:

Fig. 2.1 Calculation scheme of a coated specimen: 1—the substrate, 2—the coating



$$\begin{aligned}\tau &= S_1 \cdot (u_1 - u_2) \\ \tau_1 &= S_2 \cdot (u_2 - u_3)\end{aligned}\quad (2.1)$$

where S_1 , S_2 are some coefficients of the substrate-coating system; u_1 , u_2 , u_3 —displacements of the centers of gravity of the substrate, the lower and upper layers of the coating, respectively.

Longitudinal forces in the lower and upper parts of the coating, respectively, are determined from the equations:

$$N_2 = N_2^0 - Q_2 + Q_1;$$

$$N_3 = N_3^0 + Q_2,$$

where N_2^0 is the longitudinal force in the lower part of the coating arising from the effect of an external load P_1 ; Q_1 and Q_2 —shearing forces in the planes of adhesive contact between the substrate 1 and the coating 2, as well as at a distance $h/2$ from the substrate-coating interface, respectively; N_3^0 —the longitudinal force in the upper part of the coating arising from the action of the external load P_1 .

Since the shift in the planes of adhesive contact between the substrate 1 and the coating 2, as well as at a distance $h/2$ from the substrate-coating interface depends on the difference between the displacements of the center of gravity of the substrate, the lower and upper parts of the coating, the derivative of these differences will be equal to the difference between the corresponding deformations:

$$\frac{\partial}{\partial z}(u_1 - u_2) = \frac{N_2}{E_2 F_2} - \frac{P_1}{E_1 F_1} + (\alpha_s - \alpha_c) \Delta T;$$

$$\frac{\partial}{\partial z}(u_2 - u_3) = \frac{N_3}{E_2 F_3} - \frac{N_2}{E_2 F_2} + (\alpha_c - \alpha_c) \Delta T;$$

where E_1 , E_2 —elasticity modules of the substrate and coating, respectively; F_1 , F_2 , F_3 —cross-sectional areas of the substrate, bottom, and top of the coating, α_s , α_c are

the thermal expansion coefficients of the substrate and coating; ΔT is the temperature change.

Consequently, the difference between the elongations of adjacent layers of the substrate-coating system for the planes of adhesive contact between the substrate 1 and the coating 2, as well as at a distance $h/2$ from the substrate-coating interface depends both on the external tensile load and on the shear forces equivalent to the effect of the corresponding layers and temperature changes:

$$\begin{aligned}\frac{\partial}{\partial z}(u_1 - u_2) &= C_{11}Q_1 + C_{12}Q_2 + \varepsilon_0 + (\alpha_s - \alpha_c)\Delta T \\ \frac{\partial}{\partial z}(u_2 - u_3) &= C_{21}Q_1 + C_{22}Q_2 + (\alpha_c - \alpha_c)\Delta T\end{aligned}\quad (2.2)$$

where C_{11} , C_{21} and C_{12} , C_{22} —the compliance of the cross-sections, which are affected by the shearing forces Q_1 and Q_2 , respectively, ε_0 —strain under the action of an external load on an uncoated substrate.

The value ε_0 equals:

$$\varepsilon_0 = -\frac{P_1}{E_1 F_1}$$

The values C_{11} , C_{12} , C_{21} and C_{22} , respectively are equal:

$$C_{11} = \frac{2}{E_1 F_1} + \frac{1}{E_2 F_2}; \quad C_{12} = -\frac{1}{E_2 F_2}; \quad C_{21} = -\frac{1}{E_2 F_2}; \quad C_{22} = \frac{1}{E_2} \left(\frac{1}{F_2} + \frac{1}{F_3} \right).$$

The cross-sectional areas are calculated from the following equations:

$$F_1 = 2H \cdot b;$$

$$F_2 = F_3 = h_1 \cdot b;$$

where $2H$ is the thickness of the substrate; b is the width of the substrate and coating; h_1 —thickness of the lower and upper parts of the coating, respectively.

Differentiating Eq. (2.1) and substituting (2.2) into them, we get:

$$\begin{aligned}\frac{1}{S_1} \frac{\partial \tau}{\partial z} &= C_{11}Q_1 + C_{12}Q_2 + \varepsilon_0 + (\alpha_s - \alpha_c)\Delta T; \\ \frac{1}{S_2} \frac{\partial \tau_1}{\partial z} &= C_{12}Q_1 + C_{22}Q_2 + (\alpha_c - \alpha_c)\Delta T.\end{aligned}$$

The shear stresses τ and τ_1 in the planes of adhesive contact between the substrate 1 and the coating 2, as well as at a distance $h/2$ from the substrate-coating interface are determined from the equations:

$$\begin{aligned}\tau &= \frac{1}{b} \frac{\partial Q_1}{\partial z}; \\ \tau_1 &= \frac{1}{b} \frac{\partial Q_2}{\partial z}\end{aligned}\quad (2.3)$$

Thus, the system of differential equations for determining the shear forces in the planes of adhesive contact between the substrate 1 and the coating 2, as well as at a distance $h/2$ from the substrate-coating interface can be transformed as follows:

$$\begin{aligned}\frac{1}{S_1 \cdot b} \frac{\partial^2 Q_1}{\partial z^2} &= C_{11} Q_1 + C_{12} Q_2 + \varepsilon_0 + (\alpha_s - \alpha_c) \Delta T; \\ \frac{1}{S_2 \cdot b} \frac{\partial^2 Q_2}{\partial z^2} &= C_{12} Q_1 + C_{22} Q_2 + (\alpha_c - \alpha_s) \Delta T.\end{aligned}\quad (2.4)$$

The solution to the inhomogeneous system of differential Eq. (2.4) consists of a particular solution of this system and the general solution of the corresponding homogeneous system. Using a linear transformation of the functions Q_1 and Q_2 , we introduce such functions and for which the system of differential Eq. (2.4) turns into two independent differential equations:

$$\begin{aligned}Q_1 &= \alpha_{11} Q_1^* + \alpha_{12} Q_2^*; \\ Q_2 &= \alpha_{21} Q_1^* + \alpha_{22} Q_2^*,\end{aligned}$$

where $\alpha_{11}, \alpha_{12}, \alpha_{21}, \alpha_{22}$ —certain constant multipliers.

If the solution to the homogeneous system of equations is sought in the form:

$$\begin{aligned}Q_1^* &= A_1 \sinh(k_1 z) + B_1 \cosh(k_1 z); \\ Q_2^* &= A_2 \sinh(k_2 z) + B_2 \cosh(k_2 z),\end{aligned}$$

where A_1, B_1, A_2, B_2 —constants defined from border conditions, then finding the roots k_1 and k_2 of characteristic equation we get such the equation as:

$$\begin{vmatrix} S_1 b C_{11} - k^2 & S_1 b C_{12} \\ S_2 b C_{21} & S_2 b C_{22} - k^2 \end{vmatrix} = 0$$

where from:

$$k^4 - k^2(S_1 b C_{11} + S_2 b C_{22}) + S_1 S_2 b^2 (C_{11} C_{22} - C_{12}^2) = 0 \quad (2.5)$$

Equation (2.4) has the roots k_1 and k_2 :

$$k_1^2 = \frac{1}{2} \left(S_1 b C_{11} + S_2 b C_{22} + \sqrt{(S_1 b C_{11} - S_2 b C_{22})^2 + 4 C_{12}^2 S_1 S_2 b^2} \right)$$

$$k_2^2 = \frac{1}{2} \left(2S_1bC_{11} + 2S_2bC_{22} - 2\sqrt{(S_1bC_{11} + S_2bC_{22})^2 - 4S_1S_2b^2(C_{11}C_{22} - C_{12}^2)} \right)$$

The coefficients α_{11} , α_{12} , α_{21} , α_{22} are defined from homogeneous systems of linear equations, the determinant of which equals zero:

$$\begin{aligned} (S_1bC_{11} - k_i^2)\alpha_{1i} + S_1bC_{12}\alpha_{2i} &= 0; \\ S_2bC_{21}\alpha_{1i} + (S_2bC_{22} - k_i^2)\alpha_{2i} &= 0, \end{aligned} \quad i = 1, 2.$$

with number $i = 1$ acquired:

$$\begin{aligned} (S_1bC_{11} - k_1^2)\alpha_{11} + S_1bC_{12}\alpha_{21} &= 0; \\ S_2bC_{21}\alpha_{11} + (S_2bC_{22} - k_1^2)\alpha_{21} &= 0, \end{aligned} \quad (2.6)$$

where from:

$$\frac{\alpha_{21}}{\alpha_{11}} = \frac{k_1^2 - S_1bC_{11}}{S_1bC_{12}} = \frac{S_2bC_{12}}{k_1^2 - S_2bC_{22}}.$$

To make the solution of Eq. (2.6) nontrivial, we set the following normalization condition for the coefficients α_{i1} :

$$\sum_{i=1}^2 \frac{\alpha_{i1}^2}{S_i b} = 1 \quad (2.7)$$

Entering definition:

$$\frac{\alpha_{21}\sqrt{S_1}}{\alpha_{11}\sqrt{S_2}} = \frac{\sqrt{S_1}S_2bC_{12}}{k_1^2 - S_2bC_{22}} = \operatorname{tg}\beta$$

where from:

$$\alpha_{21} = \alpha_{11}\sqrt{\frac{S_2}{S_1}} = \operatorname{tg}\beta$$

In accordance with the Eq. (2.7) acquired:

$$\frac{\alpha_{11}^2}{S_1b} + \frac{\alpha_{21}^2}{S_2b} = \frac{\alpha_{11}^2}{S_1b} + \frac{\alpha_{11}^2}{S_1b} \tan^2 \beta = 1$$

therefore:

$$\frac{\alpha_{11}^2}{S_1 b} = \frac{1}{1 + \tan^2 \beta} = \cos^2 \beta$$

The final record is:

$$\alpha_{11} = \sqrt{S_1 b} \cos \beta$$

$$\alpha_{21} = \sqrt{S_2 b} \sin \beta.$$

similarly, $i = 2$ gives:

$$\alpha_{12} = -\sqrt{S_1 b} \sin \beta;$$

$$\alpha_{22} = \sqrt{S_2 b} \cos \beta.$$

The expressions for the unknowns Q_1^* and Q_2^* will look like:

$$\begin{aligned} Q_1^* &= \frac{\alpha_{11}}{S_1} Q_1 + \frac{\alpha_{21}}{S_2} Q_2 = \sqrt{\frac{b}{S_1}} \cos \beta \cdot Q_1 + \sqrt{\frac{b}{S_2}} \sin \beta \cdot Q_2; \\ Q_2^* &= \frac{\alpha_{12}}{S_1} Q_1 + \frac{\alpha_{22}}{S_2} Q_2 = -\sqrt{\frac{b}{S_1}} \sin \beta \cdot Q_1 + \sqrt{\frac{b}{S_2}} \cos \beta \cdot Q_2. \end{aligned}$$

The system of Eq. (2.4) will be transformed as follows:

$$\begin{aligned} \frac{\partial^2 Q_1^*}{\partial z^2} &= k_1^2 Q_1^* + \varepsilon_{01}^*; \\ \frac{\partial^2 Q_2^*}{\partial z^2} &= k_2^2 Q_2^* + \varepsilon_{02}^*, \end{aligned} \quad (2.8)$$

where

$$\begin{aligned} \varepsilon_{01}^* &= \alpha_{11}(\varepsilon_0 + (\alpha_s - \alpha_c)\Delta T) = \sqrt{S_1 b} \cos \beta \cdot (\varepsilon_0 + (\alpha_s - \alpha_c)\Delta T) \\ \varepsilon_{02}^* &= \alpha_{12}(\varepsilon_0 + (\alpha_c - \alpha_s)\Delta T) = -\sqrt{S_1 b} \sin \beta \cdot (\varepsilon_0 + (\alpha_c - \alpha_s)\Delta T) \end{aligned}$$

The solution of equation system (2.8) will be recorded as follows:

$$\begin{aligned} Q_1^* &= A_1 \sinh(k_1 z) + B_1 \cosh(k_1 z) + Q_{01}^* \\ Q_2^* &= A_2 \sinh(k_2 z) + B_2 \cosh(k_2 z) + Q_{02}^* \end{aligned}$$

Where Q_{01}^* , Q_{02}^* —particular solutions of the system (2.8),

$$Q_{01}^* = -\frac{\varepsilon_{01}^*}{k_1^2}$$

$$Q_{02}^* = -\frac{\varepsilon_{02}^*}{k_2^2}$$

As soon as Q_1^* is symmetric in reference to the axis $z = 0$ so $A_1 = 0$.
From the border condition $Q_1^*(l) = 0$ acquired:

$$B_1 \cosh(k_1 l) - \frac{\varepsilon_{01}^*}{k_1^2} = 0$$

where from:

$$B_1 = \frac{\varepsilon_{01}^*}{k_1^2 \cosh(k_1 l)}$$

Accordingly, it will be found that:

$$A_2 = 0 \text{ and } B_2 = \frac{\varepsilon_{02}^*}{k_2^2 \cosh(k_2 l)}$$

The shearing forces Q_1 and Q_2 are defined from the equations:

$$Q_1 = \sqrt{S_1 b} \cos \beta \cdot Q_1^* - \sqrt{S_1 b} \sin \beta \cdot Q_2^*$$

$$Q_2 = \sqrt{S_2 b} \sin \beta \cdot Q_1^* + \sqrt{S_2 b} \cos \beta \cdot Q_2^*$$

In accordance with Eq. (2.3) the shear stresses τ and τ_1 are calculated in the equations:

$$\tau(z) = \frac{1}{t} \sqrt{S_1 b} \cos \beta \cdot B_1 \cdot k_1 \cdot \sinh(k_1 z) - \frac{1}{t} \sqrt{S_1 b} \sin \beta \cdot B_2 \cdot k_2 \cdot \sinh(k_2 z);$$

$$\tau_1(z) = \frac{1}{t} \sqrt{S_2 b} \cos \beta \cdot B_1 \cdot k_1 \cdot \sinh(k_1 z) + \frac{1}{t} \sqrt{S_2 b} \sin \beta \cdot B_2 \cdot k_2 \cdot \sinh(k_2 z).$$

After suitable transformations we acquire:

$$\begin{aligned} \tau(z) &= S_1 \left(\frac{\cos^2 \beta \cdot \sinh(k_1 z)}{k_1 \cosh(k_1 l)} + \frac{\sin^2 \beta \cdot \sinh(k_2 z)}{k_2 \cosh(k_2 l)} \right) [\varepsilon_0 + (\alpha_s - \alpha_c) \Delta T]; \\ \tau_1(z) &= \sqrt{S_1 S_2} \sin \beta \cdot \cos \beta \cdot \left(\frac{\sinh(k_1 z)}{k_1 \cosh(k_1 l)} - \frac{\sinh(k_2 z)}{k_2 \cosh(k_2 l)} \right) \\ &[\varepsilon_0 + (\alpha_c - \alpha_c) \Delta T]. \end{aligned} \quad (2.9)$$

The coefficients S_1 and S_2 are determined in accordance with the approach proposed in Ref. [17].

We assume that the shear stresses in the plane of the adhesive contact between the base and the coating damp linearly, and the distribution of normal stresses in the coating does not change over the thickness:

$$S_1 = \frac{2}{\left(\frac{h}{G_1} + \frac{h_1}{G_2}\right)}; S_2 = \frac{G_2}{h_1}.$$

2.3 Verification of the Developed Model

Let us compare the stresses obtained from the developed analytical model using numerical simulation. In the calculations, we used the modulus of elasticity of AISI316L stainless steel equal to 193 GPa, Poisson coefficient of the substrate—0.25, coefficient of thermal expansion (CTE) $\alpha_s = 17.2 \times 10^{-6} \text{ K}^{-1}$. Calculations were carried out for zirconia-based coating, which is widely used in aviation as thermal barrier coatings on blades of gas turbine engines [18, 19].

For calculations, the modulus of elasticity of the coating of the plasma-sprayed yttria-stabilized zirconia coating was 40 GPa, Poisson's ratio was 0.22, and the coefficient of thermal expansion $\alpha_c = 10.7 \times 10^{-6} \text{ K}^{-1}$ [20].

Figure 2.2 shows the distribution of shear stresses in the coating-substrate interface in accordance with the developed analytical model. For the numerical calculation of stresses in the coated specimen, the graph model of the elastic body was used [21, 22].

Since the design scheme of the coated specimen has two axes of symmetry, it is possible to restrict ourselves to solving the problem in a symmetric formulation and considering only a quarter of the specimen section. In the simulation, the mesh of elementary cells was reduced as it approached the area of the free edge of the coating. Figure 2.3 shows an enlarged fragment of the mesh in the vicinity of the free edge of the coating. Figure 2.4 shows the distributions of shear stresses in the coating-substrate interface, obtained by the method of numerical simulation. Analysis of the data in Fig. 2.2 shows that the distribution of shear stresses in the coating-substrate interface is in good agreement with the numerical calculation. It should be noted that the numerical calculations coincide with the analytical calculations along the entire length of the coating, except for the regions in the vicinity of the free edge of the coating, in which there is a singularity of the stress fields [23].

2.4 Discussion

Changes in the elastic characteristics and geometric dimensions of coatings can lead to both a decrease and an increase in the level of shear stresses in the coating-substrate interface. The optimal selection of the design parameters of the substrate-coating system is an urgent scientific and technical problem and is of practical interest.

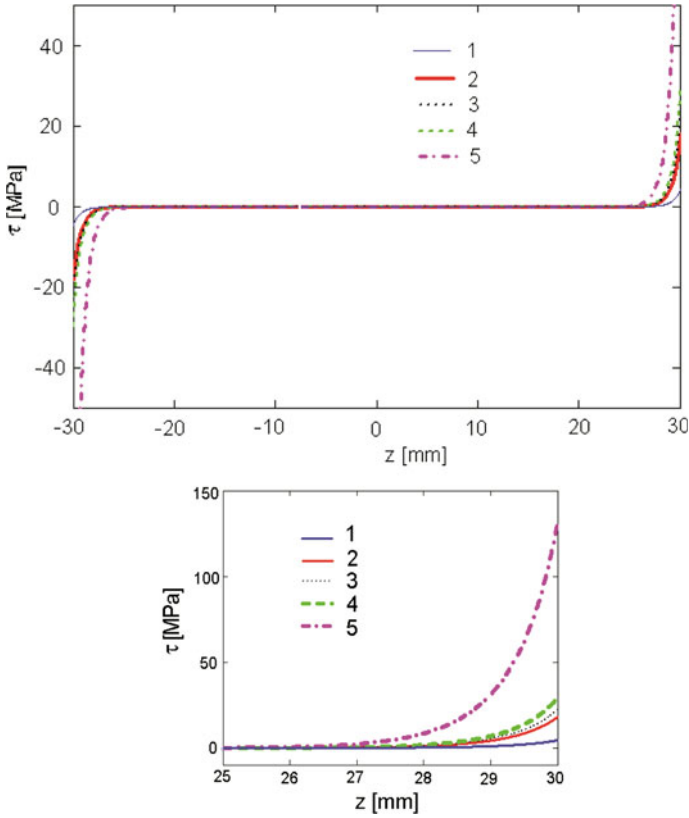


Fig. 2.2 Distribution of shear stresses $\tau(z)$ in the coating-substrate interface **a** and its enlarged fragment **(b)**: 1—without mechanical loads (at $\Delta T = 20$ K); 2—without thermal loads (at $\Delta T = 0$ K); 3—at $\Delta T = 20$ K; 4—at $\Delta T = 50$ K; 5—at $\Delta T = 500$ K

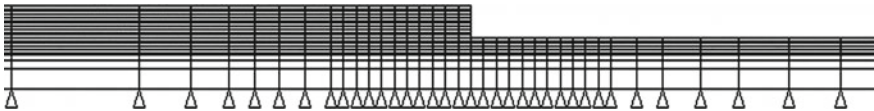


Fig. 2.3 Fragment of the numerical model of the coated specimen in the vicinity of the free edge of the coating

With a decrease in the elastic modulus of the coating, the level of shear stresses in the coating-substrate interface decreases. The elastic modulus of plasma-sprayed ceramic coatings is a technologically dependent characteristic of the material [24–26].

The application of porous ceramics reduces the Young’s modulus [27]. With an increase in the thickness of the coatings, their porosity increases [28]. With an increase in the thickness of the plasma-sprayed coatings, their Young’s moduli

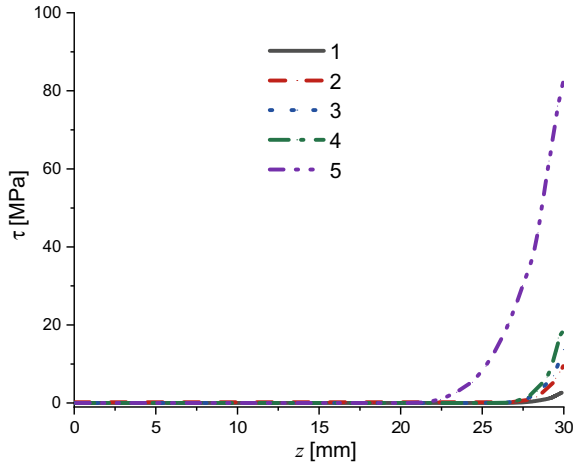


Fig. 2.4 Distribution of shear stresses $\tau(z)$ in the coating-substrate interface, obtained by the numerical method

decrease [29]. Segmentation of plasma-sprayed coatings also reduces their elastic modulus [30].

Reducing shear stresses can also be achieved by reducing the difference in thermal expansion coefficients of the substrate and the coating. Thus, there are various ways to reduce the level of interface shear stresses. Reducing shear stresses reduces the probability of coating delamination and increases the lifetime of component with coatings.

2.5 Conclusions

Thus, we have analyzed the stress state of a rectangular plate, the upper and lower surfaces of which are coated. Analytical equations are obtained for determining the distribution of shear stresses in the coating-substrate interface, depending on both on the elastic characteristics of the substrate and coating, and on their geometric dimensions and thermal expansion coefficients. The shear stresses in the coated specimen obtained by the analytical approach are consistent along the length of the interface with the numerical simulation, except for the areas near the free edge of the coating, where there is a singularity of the stress fields.

References

1. Takahashi S, Harada Y (2010) In situ observation of creep and fatigue failure behavior for plasma-sprayed thermal barrier coating systems. *J. Solid Mechanics Mater Eng* 4(2):235–243
2. Golosnoy IO, Cipitria A, Clyne TW (2009) Heat transfer through plasma-sprayed thermal barrier coatings in gas turbines: a review of recent work. *J Thermal Spray Technol* 18(5):809–821
3. Wang YQ, Sayre G (2009) Commercial thermal barrier coatings with a double-layer bond coat on turbine vanes and the process repeatability. *Surf Coat Technol* 203:2186–2192
4. Tarel'nik VB, Konoplyanchenko EV, Kosenko PV et al (2017) Problems and solutions in renovation of the rotors of screw compressors by combined technologies. *Chem Petrol Eng* 53:540–546
5. Grigoriev S, Gershman E, Gershman I, Mironov A (2021) Properties of cold spray coatings for restoration of worn-out contact wires. *Coatings* 11(6):626
6. Bose S, DeMasi-Marcin J (1997) Thermal barrier coating experience in gas turbine engines at Pratt & Whitney. *J Thermal Spray Technol* 6(1):99–104
7. Dolgov NA, Lyashenko BA, Rushchitskii YY et al (1995) Effects of differences in elastic characteristics between substrate and coating on the stress and strain state in a composite. 1. Estimating tensile stresses in the coating. *Strength Mater* 27(9):525–530
8. Agrawal DC, Raj R (1989) Measurement of the ultimate shear strength of a metal-ceramic interface. *Acta Metall* 37(4):1265–1270
9. Dolgov NA (2016) Analytical methods to determine the stress state in the substrate-coating system under mechanical loads. *Strength Mater* 48(5):658–667
10. Bulbuk O, Bulbuk O, Mazurenko V, Ropyak L, Pryhorovska T (2019) Analytical estimation of tooth strength, restored by direct or indirect restorations. *Eng Solid Mech* 7(3):193–204
11. Rizov V (2020) Analyses of delaminations in non-linear elastic multilayered inhomogeneous beam configurations. *Eng Rev* 40(3):65–77
12. Rizov V (2018) Analysis of cylindrical delamination cracks in multilayered functionally graded non-linear elastic circular shafts under combined loads. *Frattura ed Integrità Strutturale* 46:158–177
13. Shevchuk VA (2017) Thermoelasticity problem for a multilayer coating/half-space assembly with undercoat crack subjected to convective thermal loading. *J Therm Stress* 40(10):1215–1230
14. Shevchuk VA (2019) Problem of thermoelasticity for a cylinder with thin multilayer coating. *J Math Sci* 243:145–161
15. Lin E, Nault I, Champagne VK et al (2020) Analysis of interface fracture of cold-sprayed coatings due to thermal cycling. *J Thermal Spray Technol* 29:158–172
16. Falope FO, Lanzoni L, Radi E, Marcello Tarantino A (2016) Thin film bonded to elastic orthotropic substrate under thermal loading. *J Strain Anal Eng Des* 51(4):256–269
17. Dolgov NA, Lyashenko BA, Rushchitskii YY et al (1996) Effects of elasticity differences between substrate and coating on the state of stress and strain in a composite. Part 2. Coating tensile stress distribution. *Strength Mater* 28(5):373–375
18. Bakan E, Vaßen R (2017) Ceramic top coats of plasma-sprayed thermal barrier coatings: materials, processes, and properties. *J Thermal Spray Technol* 26(6):992–1010
19. Viswanathan V, Dwivedi G, Sampath S (2015) Multilayer, multimaterial thermal barrier coating systems: design, synthesis, and performance assessment. *J Am Ceram Soc* 98(6):1769–1777
20. Cao XQ, Vaßen R, Stöver D (2004) Ceramic materials for thermal barrier coating. *J Eur Ceram Soc* 24(1):1–10
21. Kuzovkov EG (1996) Axisymmetric graph model of an elastic solid. *Strength Mater* 28(6):470–485
22. Tyrymov AA (2016) Graph model of three-dimensional elastic solids in cartesian coordinates. *PNRPU Mech Bullet* 3:282–303
23. Dolgov NA, Soroka EB (2004) Stress singularity in a substrate-coating system. *Strength Mater* 36(6):636–642

24. Sobhanverdi R, Akbari A (2015) Porosity and microstructural features of plasma sprayed Ytria stabilized Zirconia thermal barrier coatings. *Ceram Int* 41(10):14517–14528
25. Bakan E, Mack DE, Mauer G, Mücke R, Vaßen R (2015) Porosity–property relationships of plasma-sprayed $Gd_2Zr_2O_7/YSZ$ thermal barrier coatings. *J Am Ceram Soc* 98(8):2647–2654
26. Lamuta C, Di Girolamo G, Pagnotta L (2015) Microstructural, mechanical and tribological properties of nanostructured YSZ coatings produced with different APS process parameters. *Ceram Int* 41(7):8904–8914
27. Manjunatha SS, Basavarajappa S (2015) Effect of coating thickness on properties of Mo coatings deposited by plasma spraying. *Tribol Mater Surfaces Interfaces* 9(1):41–45
28. Koutsomichalis A, Vardavoulias M, Lontos A, Vaxevanidis N (2018) Tensile and bend behaviour of nanostructured HVOF and flame sprayed stellite coatings. In: *MATEC Web Conf.*, 188. EDP Sciences, pp 04015
29. Dolgov NA (2004) Method for determining the modulus of elasticity for gas thermal spray coatings. *Poroshkovaya Metallurgiya* 7–8:110–115
30. Chen X, Honda H, Kuroda S et al (2016) Highly segmented thermal barrier coatings deposited by suspension plasma spray: effects of spray process on microstructure. *J Thermal Spray Technol* 25:1638–1649

Chapter 3

Numerical Simulation and Constructral Design Applied to Perforated Plate Subjected to Biaxial Buckling



Guilherme Ribeiro Baumgardt, Eysler Queiroz De Sousa,
Leonardo Willian Barbosa Pinto, Elizaldo Domingues Dos Santos,
Thiago Da Silveira, and Liércio André Isoldi

Abstract Thin plates are widely employed as structural components in different industries, like naval and civil. They are often subjected to loadings that can generate the unwanted phenomenon called buckling. In this sense, the present work analyzes the elasto-plastic buckling behavior of perforated thin steel plates, under biaxial compression. To obtain the ultimate load of the plates, a computational model via finite element method was used. In order to find the type and geometry of the hole that allows the perforated plate to achieve the best mechanical behavior, the Constructral Design method associated with the Exhaustive Search technique were employed. For that, the adopted degrees of freedom were the hole geometry (varied by its aspect ratio, given by b_0/a_0) and hole type (rectangular, oblong longitudinal, and elliptical). As performance indicator this work adopted the Normalized Ultimate Stress (ratio between the ultimate stresses of the perforated plate and the reference plate with no hole). As constraints the length, width and hole volume fraction of $\phi = 0.15$ were considered, being ϕ the ratio between the hole volume and the total plate volume with no hole. Based on the obtained results, the best hole type was the longitudinal oblong, leading to the best mechanical behavior with a slight superiority of 1.08 and 0.34% in relation to the best behavior of the elliptical and rectangular holes, respectively.

Keywords Elasto-plastic buckling · Biaxial compression · Computational modeling · Constructral design

3.1 Introduction

The study of thin plates has been carried out due to its wide use as structural components in the aeronautical, naval, and civil industries; being, generally, subjected to

G. R. Baumgardt (✉) · E. D. Dos Santos · L. A. Isoldi
Federal University of Rio Grande - FURG, km 8 Itália Ave, Rio Grande, RS, Brazil

E. Q. De Sousa · L. W. B. Pinto · T. Da Silveira
Federal University of Pampa - UNIPAMPA, 810 Tiarajú Ave, Alegrete, RS, Brazil

transverse loads and/or loads in its plane [1]. In many cases, these plates are subjected to axial compressive loads that can cause an undesired instability phenomenon, known as buckling, which can occur in two ways: elastic buckling, when the instability happens in the elastic regime of the material, and elasto-plastic buckling, which occurs when the load reaches the material's plastic deformation regime [2].

In addition, in several practical situations these structures may require material removal through perforations, which directly affects their mechanical behavior. For instance, the use of perforated plates in the naval industry and offshore structures are made to enable access points or for the weight reduction of the structure [3]. In this sense, it is necessary to investigate the effects of perforations in plates when subjected to elasto-plastic buckling since the insertion of the hole affects its ultimate load.

Therefore, to numerically simulate the mechanical behavior of a thin perforated steel plate submitted to elasto-plastic biaxial buckling, a computational model developed in ANSYS Mechanical APDL, which is based on the Finite Element Method (FEM), was adopted.

For the geometric optimization, a methodology allying the Constructal Design method and the Exhaustive Search technique was employed. The Constructal Design performs a geometric evaluation aiming to identify the geometry influence over the performance of a system subjected to some kind of flow [4]. To do so, performance indicators must be improved while the geometry is subject to global constraints (constant parameters throughout the process) and varies according to the defined degrees of freedom (parameters changed throughout the process) [5]. In recent studies, it was proven that the Constructal Design is an effective approach for the geometric analysis in structural engineering [6]. Therefore, the possible geometric configurations proposed by Constructal Design were compared among each other, defining a geometric optimization by Exhaustive Search.

3.2 Computational Model

The computational model was developed in the ANSYS Mechanical APDL, employing the finite element SHELL281 that is suitable for analyzing thin to moderately thick shell/plate structures. The element has eight nodes with six degrees of freedom in each node: translations on the x , y and z axes and rotations on the x , y and z axes, being its formulation based on the first-order shear-strain theory (Reissner–Mindlin Theory) [7].

For the elastic buckling analysis, the eigenvalue buckling approach was adopted [8]. In this analysis, a perturbation load P is used as a reference load. So, the critical buckling load is P_{cr} calculated by the multiplication of the previous with a buckling load factor λ . This factor stems from a buckling eigenvalue problem where the lowest eigenvalue λ_{cr} obtained from eigenvalue buckling analysis is used for the calculation of the critical load.

After, the numerical simulation of the post-buckling behavior of plates was carried out assuming an elastic-perfectly plastic behavior, i.e., without strain hardening. It is considered an initial geometric imperfection for the plate, which was derived from the first elastic buckling mode with a maximum displacement of $b/2000$, being b the plate width [2]. From this initial imperfect configuration, the ultimate load of the plate is obtained if, at a specific loading step, convergence cannot be achieved in the iterative process. In this case, a finite increment in the displacement vector cannot be defined so that the out-of-balance load vector is nullified. This is because no matter as large as the strains and displacements can be, the internal forces and stresses cannot increase as it would be needed to balance the external loads, which indicates that the plate material achieved its ultimate strength [9–11]. Thus, the final load of the plate is defined using as a reference the load $P_y = \sigma_y \cdot t$, where σ_y is the material yield stress and t is the plate thickness [2]. More details of this computational model can be found in Helbig et al. [9] and Lima et al. [12]. The verification and validation of this computational model can be found in Da Silveira et al. [6] and [13], respectively.

It is worth to mention that in all simulated cases the plate was considered as simply supported in its four edges, having as building material the AH-36 steel with $\sigma_y = 355$ MPa, Young's modulus $E = 210$ GPa and Poisson's coefficient $\nu = 0.30$.

3.3 Constructal Law and Constructal Design Application

Constructal Design is based on the Constructal Law, which corresponds to the foundations of Constructal Theory and states that “for a finite size flow system to persist in time (to live), its configuration must evolve in such a way as to provide greater and greater access to the currents that cross it” [4, 5, 14–16]. According to Rocha et al. [17], the Constructal Law can be understood as a unifying design principle. According to Rocha et al. [18], when applying Constructal Design, there is no “best” in the evolutionary system, but there is “better” today, which ends up not being so good tomorrow. It is worth to highlight that the Constructal Design is not a mathematical optimization method. However, the Constructal Design method can be applied associated with some optimization method, such as the Exhaustive Search technique. In this case, the Constructal Design is responsible to define the search space of the possible geometric configurations.

To the Constructal Design application is necessary to define at least one performance indicator (to be improved), the degrees of freedom (variables) and the geometric constraints (fixed parameters). The degrees of freedom are free to vary, as long as the imposed restrictions are respected [9].

In agreement with [13], as performance indicator this work used the Normalized Ultimate Stress (NUS). The parameter NUS is obtained from the ratio between the ultimate stress of the perforated plate (σ_U) and the ultimate stress (σ_{UR}) of the reference plate (without cutout).

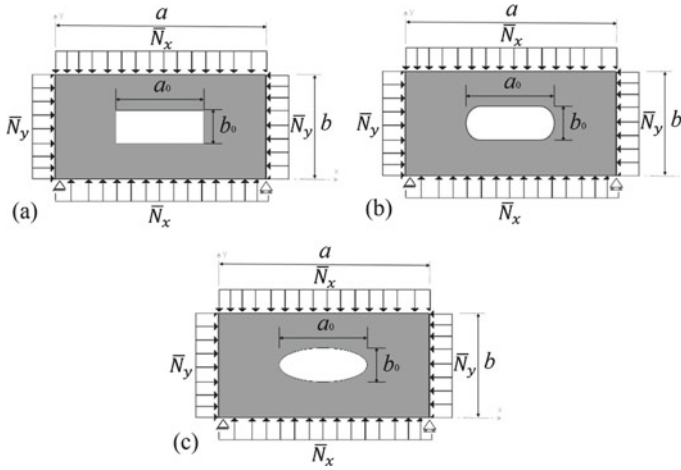


Fig. 3.1 Perforated plates studied: **a** rectangular hole, **b** longitudinal oblong hole and **c** elliptical hole

Taking into account the Fig. 3.1, the adopted degrees of freedom were the hole type, being considered the rectangular, longitudinal oblong and elliptical perforations; and the hole geometry, by means the hole aspect ratio (b_0/a_0).

As restriction a fixed value for the ratio between the plate cutout volume and its total volume, known as volume fraction (ϕ), of 0.15 was used. Also, the shape of the plate would have a height-to-length (b/a) ratio of 0.5, keeping the thickness (t) fixed. As in [7], the adopted values were $a = 2000$ mm, $b = 1000$ mm, and $t = 12$ mm, both for the perforated plates as reference plate. In addition, other imposed constraint was that the edge of the hole must be at least 100 mm away from the edge of the plate, to avoid the effect of boundary conditions, i.e.

$$b - b_0 \geq 200 \text{ mm}; \quad a - a_0 \geq 200 \text{ mm} \quad (3.1)$$

3.4 Results and Discussion

First, the reference plate (without cutout) was numerically simulated. The ultimate biaxial buckling stress obtained through this analysis of $\sigma_{UR} = 47.90$ MPa was used to calculate the NUS factor, as above mentioned. The obtained results for NUS in relation to the hole aspect ratio (b_0/a_0), for each studied hole type, are presented in Fig. 3.2.

From Fig. 3.2 it is possible to observe that, for each hole type a maximized NUS_m is obtained, allowing to define the optimal geometry, i.e., the geometric configuration that provides the highest value for the performance indicator. The results demonstrate

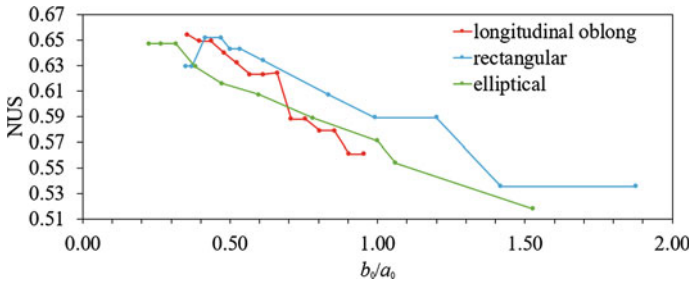


Fig. 3.2 Normalized ultimate stress of plates with centered hole

that for the elliptical hole with $(b_0/a_0)_o$ of 0.316 promotes the maximization of the NUS_m , reaching a mechanical behavior approximately 24.90% better than the worst geometry with $b_0/a_0 = 1.528$. Evaluating the rectangular hole, it is observed that the maximum NUS_m reached occurs for the aspect ratio values $(b_0/a_0)_o$ of 0.469, being 21.67% higher than the worst rectangular geometry. For the longitudinal oblong hole, the maximized NUS_m value is displayed for a $(b_0/a_0)_o$ ratio of 0.436, which is 16.58% larger than the geometry with the lowest NUS value for this hole type.

Still regarding Fig. 3.2, it can be seen that for the vast majority of the analyzed aspect ratio values, the rectangular hole has a higher NUS value. However, comparing the values of NUS_m , one can note that the longitudinal oblong hole has the best global performance. In other words, the twice maximized NUS_m is 0.654, obtained by the twice optimized longitudinal oblong hole geometry with $(b_0/a_0)_{oo}$ of 0.356.

3.5 Conclusion

The development of this work presented allied the computational modeling, Constructal Design method, and Exhaustive Search technique for the analysis of simply supported rectangular plates under biaxial compressive load, considering different types of centered holes. The results indicated that the variation of the hole aspect ratio can promote improvements in the ultimate buckling stress of 24.90, 21.67, and 16.58%, respectively, for the elliptical, rectangular, and longitudinal oblong hole types. In addition, comparing the performance of the optimized geometry for each hole type, the longitudinal oblong hole achieves a slight superiority of 1.08–0.34%, respectively, than the elliptical and rectangular hole types.

Acknowledgements G.R. Baumgardt thanks to the *Coordenação de Aperfeiçoamento de Pessoal de Nível Superior*—Brazil (CAPES)—Finance Code 001. E.D. dos Santos and L.A. Isoldi thank to the *Conselho Nacional de Desenvolvimento Científico e Tecnológico*—Brazil (CNPq)—Processes: 306024/2017-9, and 306012/2017-0, respectively. All authors thank to FURG and Unipampa.

References

1. Birman V (2011) *Solid mechanics and its applications: plate structures*. Springer, Netherlands
2. El-Sawy KM, Nazmy AS, Martini MI (2004) Elasto-plastic buckling of perforated plates under uniaxial compression. *Thin-Walled Struct* 42:1083–1101
3. Paik JK (2007) Ultimate strength of perforated steel plates under combined biaxial compression and edge shear loads. *Thin-Walled Struct* 46:207–213
4. Bejan A, Zane JP (2012) *Design in nature: how the constructal law govern evolution in biology, physics, and social organization*. Doubleday, New York
5. Bejan A (2000) *Shape and structure from engineering to nature*. Cambridge University Press, Cambridge
6. Da Silveira T, Pinto VT, Neufeld JPS, Pavlovic A, Rocha LAO, Dos Santos ED, Isoldi LA (2021) Applicability evidence of constructal design in structural engineering: case study of biaxial elasto-plastic buckling of square steel plates with elliptical cutout. *J Appl Comput Mech* 7:922–934
7. ANSYS Help Viewer. Release 18.1—© ANSYS, Inc. All rights reserved
8. Vu QV, Papazafeiropoulos G, Graciano C, Kim SE (2019) Optimum linear buckling analysis of longitudinally multi-stiffened steel plates subjected to combined bending and shear. *Thin-Wall Struct* 136:235–245
9. Helbig D, Da Silva CCC, Real MV, Dos Santos ED, Isoldi LA, Rocha LAO (2016) Study about buckling phenomenon in perforated thin steel plates employing computational modeling and constructal design method. *Latin Am J Solids Struct* 13:1912–1936
10. Madenci E, Guven I (2015) *The finite element method and applications in engineering using ANSYS®*, 2nd edn. Springer, Boston
11. Lima JPS, Rocha LAO, Dos Santos ED, Real MV, Isoldi LA (2018) Constructal design and numerical modeling applied to stiffened steel plates submitted to elasto-plastic buckling. *Proceedings of the Romanian Academy—Series A: Mathematics, Physics, Technical Sciences, Information Science*, 19(Special Issue):195–200
12. Lima JPS, Cunha ML, Dos Santos ED, Rocha LAO, Real MV, Isoldi LA (2020) Constructal design for the ultimate buckling stress improvement of stiffened plates submitted to uniaxial compressive load. *Eng Struct* 203:109883
13. Da Silveira T, Neufeld JPS, Rocha LAO, Dos Santos ED, Isoldi LA (2021) Numerical analysis of biaxial elasto-plastic buckling of perforated rectangular steel plates applying the constructal design method. *IOP Conf Ser Mater Sci Eng* 1048:012–017
14. Bejan A, Lorente S (2004) The constructal laws and the thermodynamics of flow systems with configuration. *Int J Heat Mass Transfer* 47:3073–3083
15. Bejan A, Lorente S (2005) *La Loi Constructale*. L'Harmattan, Paris
16. Bejan A, Lorente S (2008) *Design with constructal theory*. Hoboken, New Jersey
17. Rocha LAO, Lorente S, Bejan A (2013) *Constructal law and the unifying principle of design*. Springer, New York
18. Rocha LAO, Lorente S, Bejan A (2017) Constructal theory in heat transfer. *Hand-book of thermal science and engineering*, 1st edn., 1, 1–32 (2017)

Chapter 4

Fatigue Damage Simulation of a Metal Sandwich Panel Under Four-Point Bending Conditions



M. K. Faidzi, S. Abdullah, M. F. Abdullah, S. S. K. Singh, A. H. Azman, José A. F. O. Correia , and D. Hui

Abstract This paper presents the effect of a variety of dimple core designs of a metal sandwich panel simulated using four-point bending under different cyclic loading spectrums of high-low and high-low–high loading sequences. This core design was vulnerable to delamination when subjected to cyclic loading conditions. The variable amplitude loading data from random number sets have been equivalent in terms of damage to produce the constant amplitude loading data, which was used as cyclic loading data for all models. The simulation results indicated the loading sequences of high-low and high-low–high had a significant effect on the fatigue performance of the sandwich panel. Dimples 6.0/3.0 mm in size showed exceptional performance, possessing the highest number of cycles before failure. The coefficient of determination for this dimple was $0.8921 < R^2 < 0.9828$ for all damage modeling conditions. It is highlighted that dimple size plays an important role since the largest dimple size made the sandwich panel vulnerable to early delamination under the simulated cyclic loading conditions.

Keywords Sandwich panel · Dimple design · Four-point bending · Fatigue damage

M. K. Faidzi · S. Abdullah (✉) · S. S. K. Singh · A. H. Azman
Department of Mechanical and Manufacturing Engineering, Faculty of Engineering and Built Environment, Universiti Kebangsaan Malaysia, UKM, 43600 Bangi, Selangor, Malaysia
e-mail: shahrum@ukm.edu.my

M. F. Abdullah
Department of Mechanical Engineering, Faculty of Engineering, Universiti Pertahanan Nasional Malaysia, Kem Perdana Sg. Besi, 57000 W.P Kuala Lumpur, Malaysia

J. A. F. O. Correia
INEGI, Faculty of Engineering, University of Porto, Porto 4200-465, Portugal

D. Hui
Composite Material Research Laboratory, Faculty of Engineering, University of New Orleans, New Orleans, LA, USA

4.1 Introduction

Sandwich panels are used in many engineering applications within the building construction, automotive and aircraft industries. Based on previous researches, most metal sandwich panels were developed using lightweight materials such as aluminum alloy and ceramics [1, 2]. However, the use of magnesium alloy in sandwich panel applications as outer skins and/or the main core has increased due to its special characteristics; for instance, it is lightweight and adaptable enough to be reinforced [3]. Recent research shows that the bonding area of the sandwich panel experiences the most critical failure when subjected to high loading, resulting in unstable structural integrity and delamination [4, 5].

Modifications of the sandwich panel surface at the bonding area is vital to improve the bonding strength and structural integrity of sandwich panel. This reduces the risk of pre-delamination occurring between the bonding layer of the sandwich panel, which may lead to delamination. The type of loading condition plays an important role in determining the strength and capability of sandwich panels [6]. It is crucial to identify their capabilities under certain conditions such as constant and variable cyclic loading in order to determine the delamination effect which usually occurs between the bonding surface layer of the sandwich panel.

This study aims to evaluate the performance of a metal sandwich panel under constant and variable cyclic loading with different loading sequences, high-low and high-low-high using four-point bending simulation to assess the delamination effect, which is the main contributor to the failure mechanism of a sandwich panel. The half spectrum of variable amplitude loading (VAL) data produced from a random number of 10,000 data points was simulated using a fatigue data analysis package to produce an equivalent damage value of constant amplitude loading (CAL) as the loading data used in this simulation. The influence of surface modifications on the main core of the sandwich panel is investigated and the fatigue damage due to bending is displayed through the hotspot contour on the surface core and fatigue damage plot.

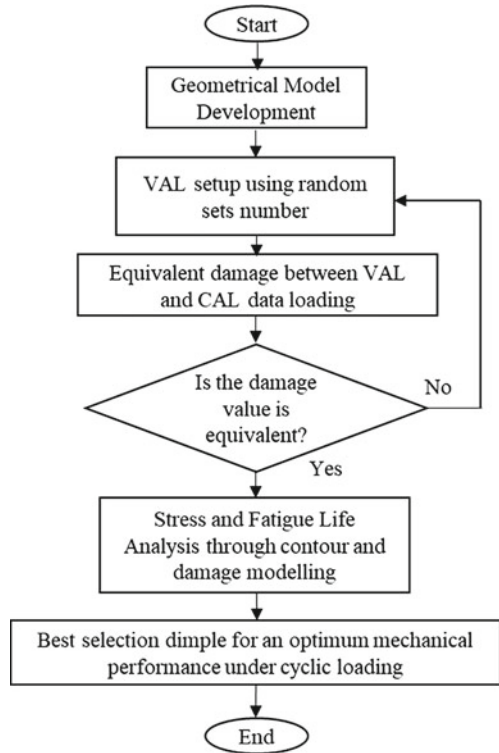
4.2 Materials and Methods

The three-dimensional geometrical metal sandwich panel was developed and simulated using the finite element software package based on ASTM C393 [7]. The flowchart for this study is shown in Fig. 4.1.

4.2.1 Geometrical Metal Sandwich Panel

The upper and lower skins were made of AR500 steel while the main core was magnesium alloy AZ31B. The adhesive material used for the sandwich panel models

Fig. 4.1 The methodology flowchart for the simulation work in this study



was epoxy resin. The size and dimension of the geometrical model, including the hemisphere dimple core design are shown in Fig. 4.2. An adaptive uniform mesh type 1.0 mm in size and with a fine span angle center was chosen since this size is a reliable value to ensure stability and reduce the time taken for the simulation [5]. A hemisphere dimple design was chosen to reduce residual stress at the dimple area due to its sharp-edged design. An enhanced design of the sandwich panel core surface was used to produce lightness and better bonding strength without reducing the structural integrity.

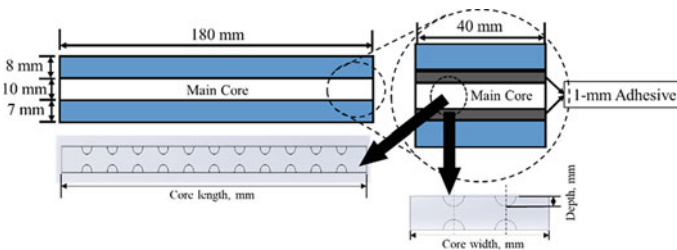


Fig. 4.2 The schematic diagram of geometrical metal sandwich panel with main core panel

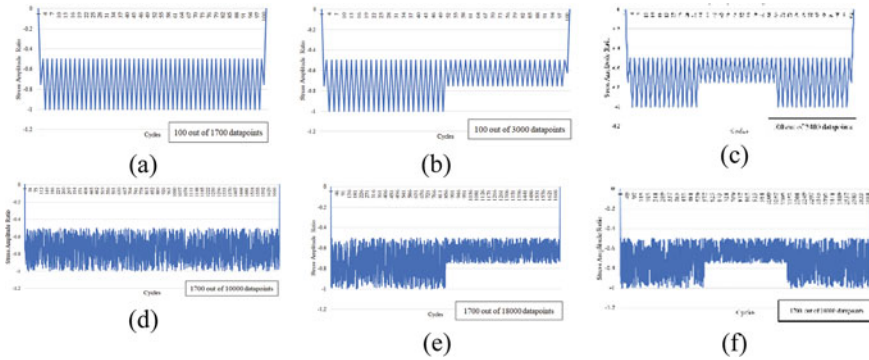


Fig. 4.3 The loading data used in this simulation **a** CAL with $R = 2$, **b** CAL high-low; $R = 2$ to 1.5, **c** CAL high-low-high; $R = 2, 1.5$ and 2 **d** VAL with $R = 2$, **e** VAL high-low; $R = 2$ to 1.5, and **f** VAL high-low-high; $R = 2, 1.5$ and 2

4.2.2 Loading Conditions

The maximum loading, F was calculated using the properties of the lowest strength material for this sandwich panel (magnesium alloy) based on its ultimate tensile strength and was determined using Eq. (4.1) [8]:

$$\sigma_{\max,x} = \frac{1}{12}FL, \frac{1}{2}h, \left(-\frac{12}{bh^3}\right) = \frac{FL}{-2bh^2} \quad (4.1)$$

Three types of sequence cyclic loading conditions with half spectrum were applied to the sandwich panel. These were constant, high-low and high-low-high sequence loading, as shown in Fig. 4.3.

Variable amplitude loading (VAL) was set as a random number of 10,000 points using the fatigue data analysis package and was ensured its damage value was equivalent to that of CAL. This process is crucial as the VAL data have more inconsistency in peak amplitude compared to CAL data and also to avoid over-prediction in the fatigue damage modeling. Therefore, in order to produce an equivalent damage value for CAL high-low, VAL high-low, CAL high-low-high and VAL high-low-high, the CAL damage value became the main reference since it was equivalent to the VAL damage value at the first stage.

4.3 Result and Discussion

Figure 4.4 shows the fatigue contour on the sandwich panel at 90% of loading for all types of cyclic loading conditions. It can be observed that the number of cycles before failure has increased as the cyclic loading spectrum changes from constant

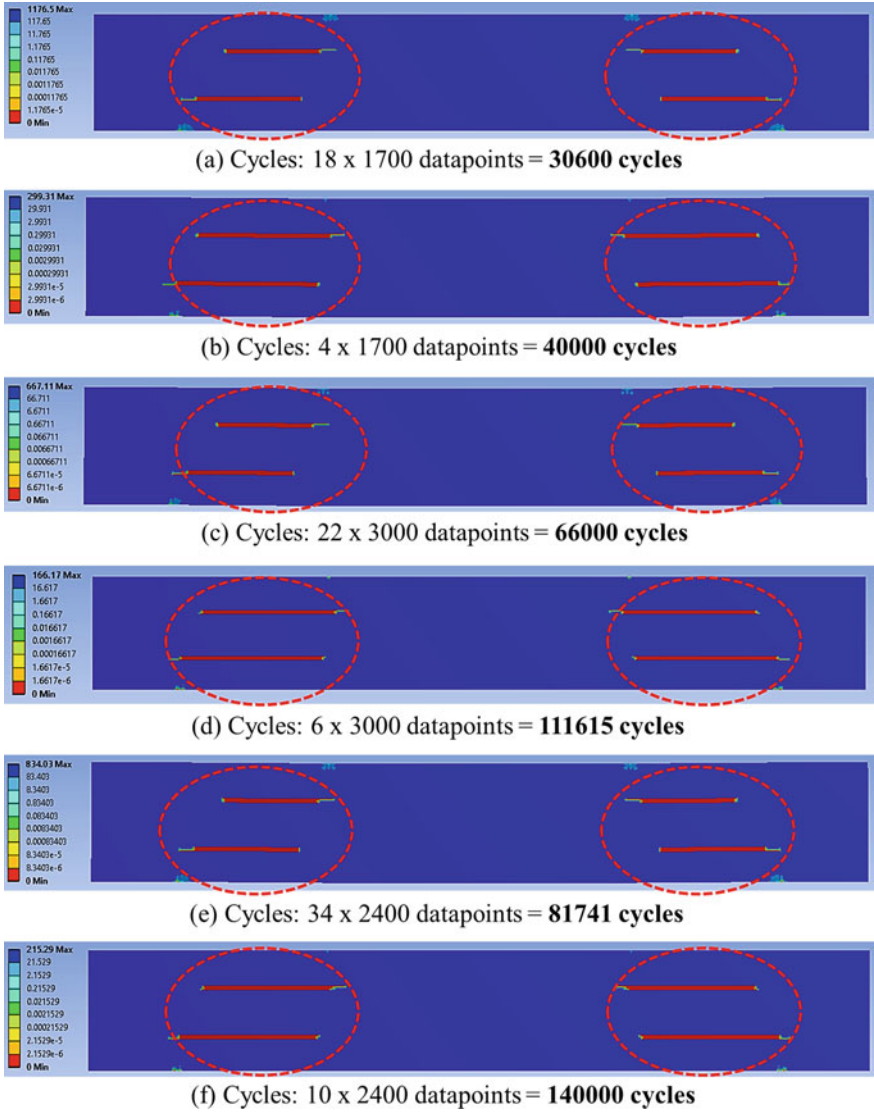


Fig. 4.4 The sandwich panel with dimple of 6 mm diameter and 3 mm depth, at 90% loading with maximum number of cycles to failure **a** CAL, **b** VAL, **c** CAL high-low, **d** VAL high-low, **e** CAL high-low-high and **f** VAL high-low-high. The red circle indicated that delamination take place at the bonded layer of sandwich panel at this loading condition

to the high-low and lastly to the high-low-high loading sequence. At 90% loading, the delamination effect was clearly seen in the bonding area. At 50% loading, none of the sandwich panels displayed any red marks at the bonding layer, as shown in Fig. 4.5. However, there was still the possibility for the red marks, known as hotspot points, to appear on the main core surface panel near the dimple area.

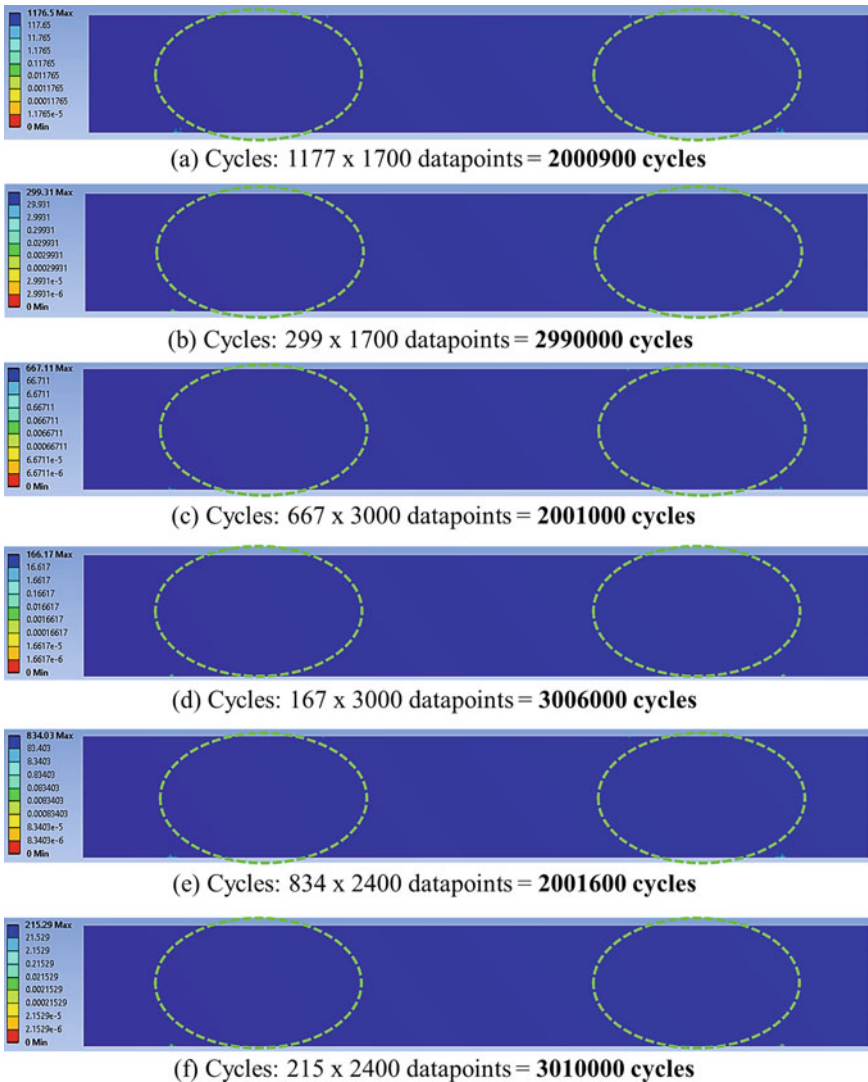


Fig. 4.5 The sandwich panel with dimple of 6 mm diameter and 3 mm depth, at 50% loading with number of cycles to failure **a** CAL, **b** VAL, **c** CAL high-low, **d** VAL high-low, **e** CAL high-low-high and **f** VAL high-low-high. The green circle indicated that there is no delamination take place at the bonded layer of sandwich panel under this condition

Further analysis was conducted at the hotspot area of the main core panel. Figures 4.6, 4.7, 4.8 show the damage plot for the maximum damage value against the number of cycles to failure in log scale for sandwich panels with different dimple core designs under CAL and VAL conditions. The damage plot shows that the dimple sizes of 6.0/3.0–8.0/4.0 mm exhibited significant trendline for all figures. For both CAL and VAL conditions, it was observed that the dimple with size of 6.0/3.0 mm experienced a higher number of cycles before failure compared to the dimple sizes of 5.0/2.5, 7.0/3.5 and 8.0/4.0 mm.

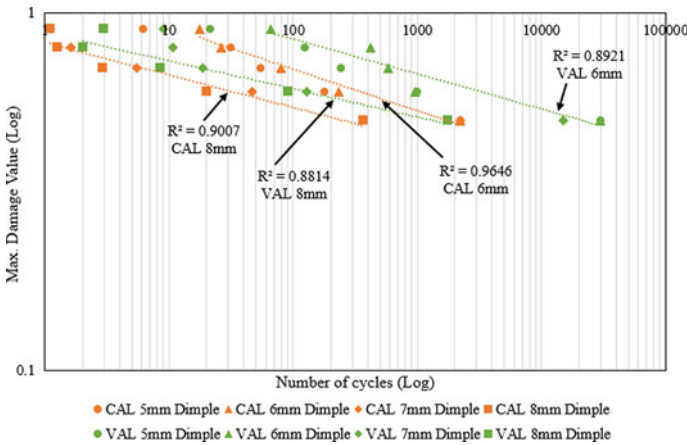


Fig. 4.6 The damage plot for maximum damage value against number of cycles to failure for sandwich panel with different dimple specifications under CAL and VAL conditions

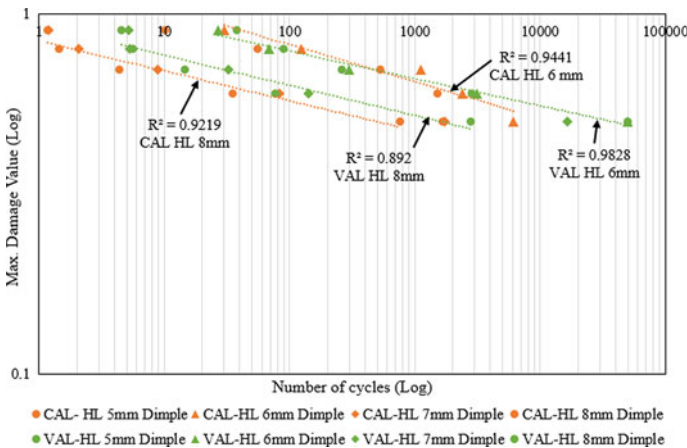


Fig. 4.7 The damage plot for maximum damage value against number of cycles to failure for sandwich panel with different dimple specifications under CAL High-Low and VAL High-Low conditions

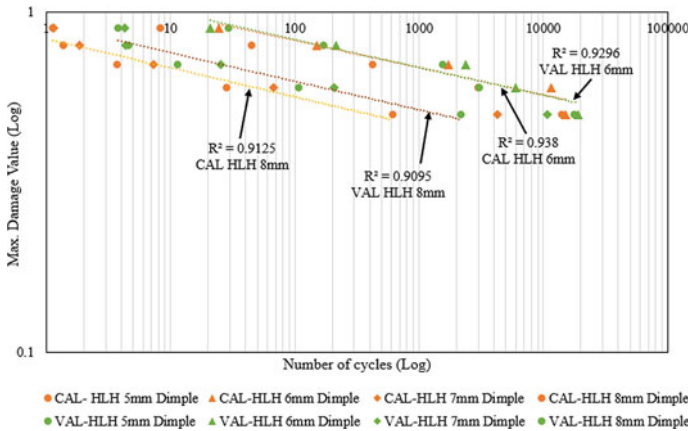


Fig. 4.8 The damage plot for maximum damage value against number of cycles to failure for sandwich panel with different dimple specifications under CAL High-Low-High and VAL High-Low-High conditions

The range coefficient of determination for the dimple size 6.0/3.0 mm was between $0.8921 < R^2 < 0.9828$ for all cyclic loading conditions, as shown in Figs. 4.6, 4.7 and 4.8. For the dimple size of 8.0/4.0 mm, the range coefficient of determination was $0.892 < R^2 < 0.9219$ for all cyclic loading conditions, as shown in Figs. 4.6, 4.7 and 4.8. Based on this range, the dimples of 6.0/3.0 mm showed the highest accuracy for the fatigue damage plot trendline, compared to the dimples of 8.0/4.0 mm. However, both ranges were acceptable as they were beyond the 0.85 limit value, based on the engineering statistical value [5]. At the lowest maximum damage value, a large dimple size experienced lower cycle fatigue than a small dimple size.

4.4 Conclusion

The effects of different dimple core designs of a metal sandwich panel were evaluated and analyzed using four-point bending simulation under constant amplitude loading (CAL) and VAL conditions, with different loading sequences of high-low and high-low-high. The results show that under CAL and VAL loading conditions, the difference in dimple size produced a significant effect on sandwich panel performance in terms of fatigue damage modeling. The dimple size of 6.0/3.0 mm showed a greater potential to be selected as the optimum design for a dimple core design, compared to the others. From the fatigue damage plot modeling, the dimple size of 6.0/3.0 mm reached the highest number of cycles before failure, with the lowest average in maximum damage value on the hotspot area of the core panel. The coefficient of determination for all the damage plot modeling in log scale for this dimple was between $0.8921 < R^2 < 0.9828$ under CAL and VAL loading conditions. This

shows that it is acceptable and has proven the correlation between the maximum damage value at the hotspot area of the core panel and the number of cycles before failure. It was also noticed that a large dimple size has disadvantages in terms of the bonding strength of the sandwich panel.

References

1. Rahman NA, Abdullah S, Abdullah MF, Zamri WFH, Omar MZ, Sajuri Z (2018) Experimental and numerical investigation on the layering configuration effect to the laminated aluminium/steel panel subjected to high speed impact test. *Metals* 8(732):1–16
2. Wang Z, Li Z, Xiong W (2018) Experimental investigation on bending behavior of honeycomb sandwich panel with ceramic tile face-sheet. *Compos B* 164:280–286
3. Xu T, Yang Y, Xiaodong P, Jiangfeng S, Fusheng P (2019) Overview of advancement and development trend on magnesium alloy. *J Magnes Alloys* 7(3):536–544
4. Pan Y, Wu G, Huang Z, Li M, Ji S, Zhang Z (2017) Effect of surface roughness on interlaminar peel and shear strength of CFRP/Mg laminates. *Int J Adhes Adhes* 79:1–7
5. Faidzi MK, Abdullah S, Abdullah MF, Singh SSK, Azman AH (2021) Evaluating an adhesive effect on core surface configuration for sandwich panel with peel simulation approach. *J Mech Sci Technol* 35:2431–2439
6. Sun G, Yu H, Wang Z, Xiao Z, Li Q (2019) Energy absorption mechanics and design optimization of cfrp/aluminium hybrid structures for transverse loading. *Int J Mech Sci* 150:767–783
7. ASTM Standard C393 (2000) Standard test method for flexural properties of sandwich construction. In: American society for testing and materials annual book of ASTM standards. ASTM International, West Conshohocken, PA
8. Mujika F, Arrese A, Adarraga I, Osés U (2016) New correction terms concerning three-point and four-point bending tests. *Polym Test* 55:25–37

Chapter 5

Analysis of Pulse Load of a Steel Roller in the Numerical Simulation Method



Dariusz Pyka, Kayode Olaleye, Adam Kurzawa, Tetiana Roik, Grzegorz Ziolkowski, Mirosław Bocian, and Krzysztof Jamroziak

Abstract This article presents the tests of EN C45 steel as a result of the impulse load of the detonation wave of the explosive charge. This process was carried out on a specially prepared test stand using a 75 g Tri-Nitro-Toluene (TNT) drilling cartridge. Two series of tests were carried out with the explosive charge placed in direct contact with the sample and the charge away from the sample at a distance of 30 mm. As a result of detonation, the samples were fragmented or visibly deformed. The main purpose of the work was to verify the impact resistance of EN C45 steel, which is commonly used in technical facilities. The results of research on the impact of the shock wave on the morphology and internal structure of the tested material in the areas subjected to dynamic deformation are presented. The results of computed tomography and light microscopy analyzes as well as numerical analyzes are presented to describe in detail the phenomenon of destruction under the influence of the pressure impulse.

Keywords Impulse load · Blast shock wave · Swelling phenomenon · Numerical analysis · SPH method

D. Pyka · K. Olaleye (✉) · M. Bocian · K. Jamroziak
Department of Mechanics, Materials and Biomedical Engineering, Wrocław University of Science and Technology, Smoluchowskiego 25, 50-370 Wrocław, Poland
e-mail: kayode.olaleye@pwr.edu.pl

A. Kurzawa
Department of Lightweight Elements Engineering, Foundry and Automation, Wrocław University of Science and Technology, Smoluchowskiego 25, 50-370 Wrocław, Poland

T. Roik
National Technical University of Ukraine “Igor Sikorsky Kyiv Polytechnic Institute”, 37 Peremogy Ave, Kyiv 03057, Ukraine

G. Ziolkowski
Department of Laser Technology, Automation and Production Organization, Wrocław University of Science and Technology, ul. Łukasiewicza 5, 50-371 Wrocław, Poland

5.1 Introduction

The shock wave, which is a consequence of the explosion process, is the main burden on the objects of technical infrastructure or people in contact with the epicenter of the explosive explosion (MW). When forecasting the fatigue strength of a material for shock loads generated by an explosive explosion, an important approach is to capture the material load with a pressure impulse or the pressure of the blast (shock) wavefront [1]. Based on the study [2], a shock wave and rapidly expanding gases are generated near the source of the explosive explosion. This phenomenon is accompanied by high temperatures. We can distinguish three types of explosions here, namely free explosions (in the air), closed explosions (in a closed medium), and explosions in which the explosive is attached to a structure (object). Nevertheless, the common feature of a closed explosion, and an explosion of material applied to an object, is the formation of strong stress waves in the material, which affects its destruction in the form of crushing this material [3]. Therefore, in order to estimate the effects of a blast wave, knowledge about the pressure generated by the blast wave on its forehead and the phenomena related to its amplification is needed. This amplification is the resultant of the incident and reflected wave presented, inter alia, in [4]. The literature on the subject is quite extensive in this regard. In the works of Baker [5], Bulson [6], Henrych [7] or Włodarczyk [8], as well as other authors, analytical methods for determining explosive loads have been presented.

In this paper, the authors presented the impact of the use of the numerical method to describe the pulse load generated by the blast wave of the explosion on selected elements used in the construction of structural components of machines and devices. The aim of the work was to reproduce the destruction process of a selected structural element in the form of a shaft made of EN C45 steel, loaded with a cylindrical TNT explosive charge, using explicit ABAQUS/Explicit integration codes. The explosion process was modeled using three methods, SPH, ALE, and FEM. In the description of the cylinder fracture, the limit deformation parameter was introduced, based on which the qualitative evaluation of the numerical method was performed. The obtained results were validated experimentally.

5.2 Materials and Methods

5.2.1 *Materials*

The subject of the research was samples made of structural steel EN C45 (1.0503), which is mainly used for medium-loaded elements of machines and devices in the automotive industry, as well as for die forgings and hot rolling of products such as bars, sheets, and wires. The samples were made as cylinders with a diameter of 25 mm and a height of 30 mm. Two series of samples, five each, were made (Fig. 5.1).



Fig. 5.1 General view of the samples

Before carrying out basic tests on the impact resistance to the impact of an explosion blast wave, the material from the samples was analyzed in terms of mechanical properties and metallographic structure.

5.2.2 Methods

The shock wave load tests for C45 samples were carried out in a proving ground laboratory, where a test stand was designed for this purpose. The research material in the form of samples (cylinders with dimensions $d = 25$ mm, $h = 30$ mm) was tested in two series (Fig. 5.2). The damage distribution of the tested shaft element was used to perform numerical analyzes in the ABAQUS/Explicit environment.

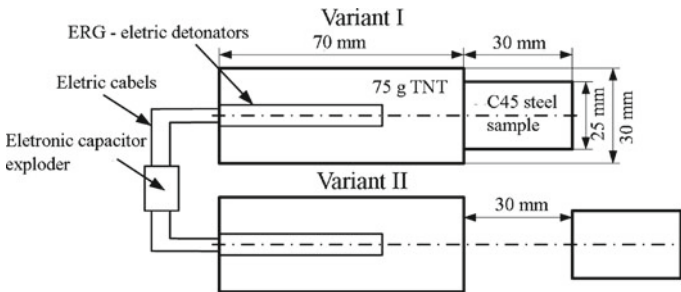


Fig. 5.2 Diagram of the test stand

5.3 Results and Discussion

5.3.1 Microscopic and Tomographic Analysis

After the detonation test, the samples were also subjected to microstructure analysis using light microscopy using the Nikon Eclipse MA200 microscope and scanning on the Hitachi TM3000 microscope (see Fig. 5.3).

The cracks in this area show a brittle character without clear plastic deformations of the structure in the immediate vicinity of the cracks. The propagation of cracks in this area frequently proceeds in a staggered manner (Fig. 5.4a), which leads to the crack coalescence effect (Fig. 5.4b).

Further analysis was performed using the VG Studio MAX 2.0 Volume Graphics GmbH software. In order to obtain the three-dimensional geometry of the analyzed fragment, the grayscale data were thresholded, separating the grayscale recorded for

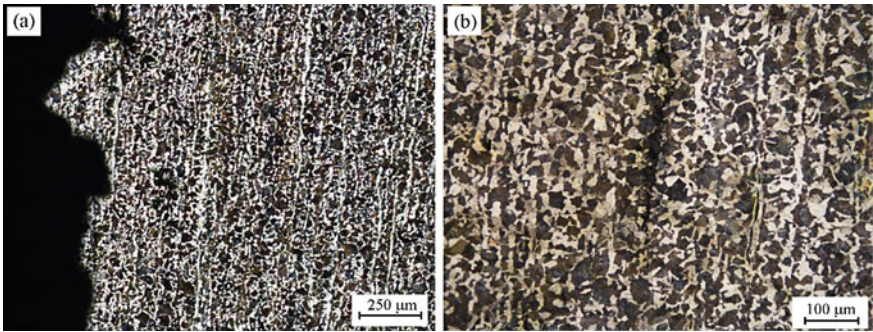


Fig. 5.3 Material structure: fracture edge (a), near the fracture edge (b). Light microscopy. Etching: 4% Nital

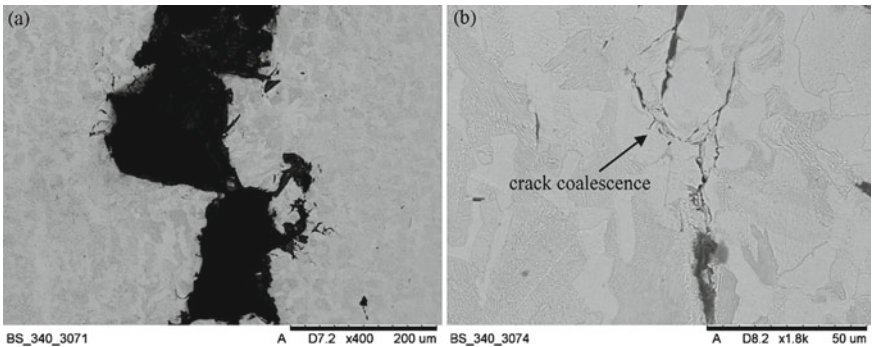
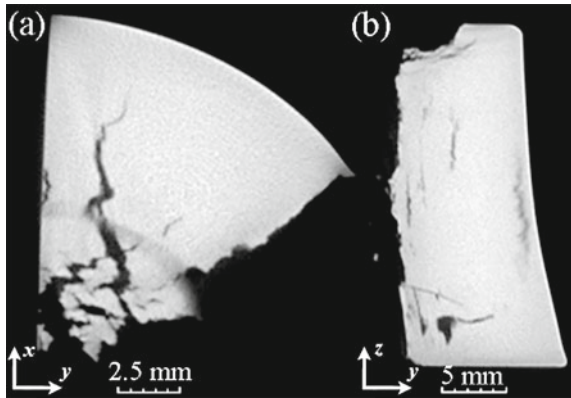


Fig. 5.4 SEM—longitudinal fracture: fracture edge (a), fracture merging (b)

Fig. 5.5 Sample I—CT cross-sections: **a** in the XY plane, **b** in the YZ plane



the background from the grayscale for the material. In order to determine the geometry of the cracks, a defect analysis was carried out, which allowed the determination of the volume of the discontinuity inside the reconstructed fragment.

The reconstruction was performed with the use of the technical computed tomography (CT) method that allows for the reconstruction of the three-dimensional model of discontinuity distribution as shown in Fig. 5.5.

5.3.2 Numerical Analysis

Numerical analysis was performed in the ABAQUS program. The tested system was modeled as to what volumetric elements were. Three methods of modeling an explosive are presented below. The first FEM, the second SPH, and CEL (see Fig. 5.6).

The thresholding result in the form of the reconstructed volume is shown in Fig. 5.7a, and the defect analysis, allowing to determine the volume of the discontinuity inside the reconstructed fragment, is shown in Fig. 5.7b. Exemplary results of numerical simulations are presented in Fig. 5.8.

The analysis of the exemplary results allows to determine the physical process of cracking in the structure of the steel shaft. As shown, the ALE method (Fig. 5.8b) most reliably approximates the failure of a steel element loaded with impulse.

5.4 Conclusion

The use of a specific numerical method to describe the explosion phenomenon determines the obtained results. The use of computed tomography for crack analysis allows to obtain a map of the crack distribution along with its surface. The comparison of

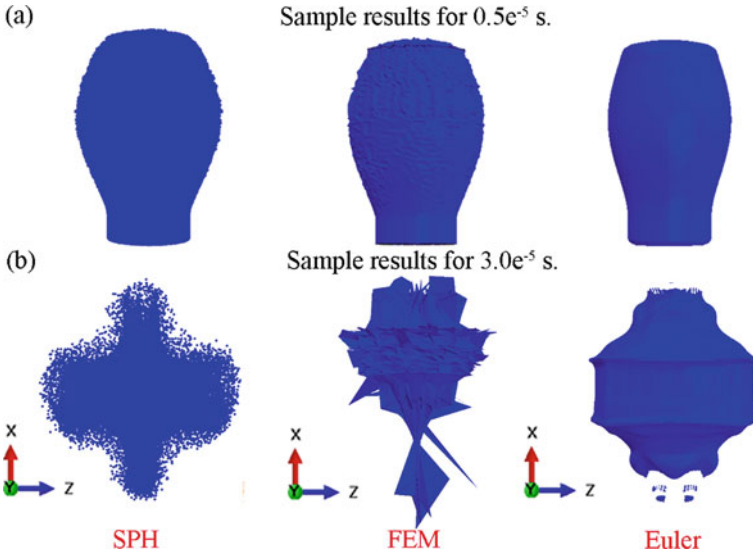


Fig. 5.6 Numerical modeling methods: **a** the initial phase of the explosion, **b** the final phase of the explosion, clear discrepancies in the results obtained

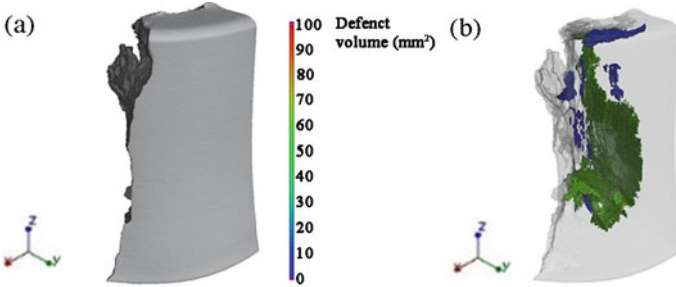


Fig. 5.7 Example results: **a** data thresholding result, **b** transparent view with marked discontinuities. The color of the cracks is marked

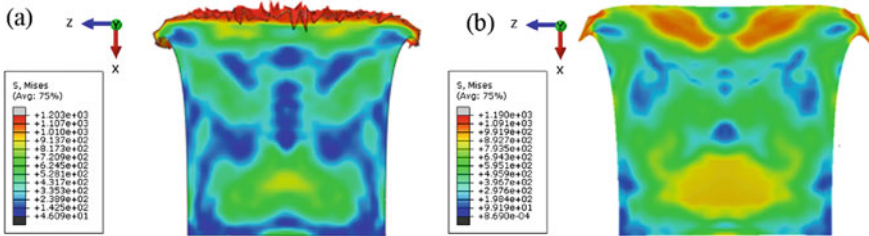


Fig. 5.8 Examples of simulation results include hybrid simulation methods: **a** SPH/FEM method, **b** ALE/FEM

the scrap formed because of the impulse load of the shaft is the essence of the validation of numerical results and the possibility of qualitative assessment of the methods used to describe the mechanism of damage to the structure of steel loaded with the pressure of the detonation wave of the explosion. Such imaging of the results makes us aware of the physical process of destruction of selected elements of the structure in the assessment of the critical infrastructure exposed to undesirable threats.

References

1. Structures to resist the effects of accidental explosions (1990) Departments of the army, the Navy, and the air force. Washington, DC. TM 5-1300/NAVFAC P-397/AFR 88-22
2. Yandzio E, Gough M (1999) Protection of buildings against explosions. SCI Publication, Berkshire UK
3. Smith PD, Hetherington JG (1994) Blast and ballistic loading of structures. Taylor & Francis, London and New York
4. Mays GC, Smith PD (1995) Blast effects on buildings: design of buildings to optimize resistance to blast loading. Thomas Telford Publications, London
5. Baker WE, Cox PA, Weslina PS, Kulesz JJ, Strehlow RA (1983) Explosion hazards and evaluation. Elsevier, Amsterdam-Oxford-New York
6. Bulson PS (1997) Explosive loading of engineering structures. Taylor & Francis, London and New York
7. Henrych J (1979) The dynamics of explosion and its use. Elsevier, New York
8. Włodarczyk E (2012) The basic physics of explosion. WAT, Warsaw (in polish)

Part II
Fatigue and Fracture Assessment of Joints
and Complex Structures

Chapter 6

Fatigue Analysis of Thin-Walled Welded Hollow Section Joints



Martin Machač, Jan Papuga, Karel Doubrava, and Jakub Fišer

Abstract This paper describes experiments and computational fatigue analysis regarding two types of thin-walled hollow section joints. Due to the thickness of the tubes used, the standard hot-spot FAT curves of IIW for plates of 25 mm thickness are not suitable. The most appropriate definition is sought.

Keywords Thin-walled welded hollow section joints · Structural stress approach

6.1 Introduction

The IIW standard for evaluating the fatigue life of welded structures [1] was originally built and was intended for large structures with a basic reference thickness of 25 mm. The thickness correction in Hobbacher [1] is defined to deal with even thicker plates. Such values are not applicable in the transportation industry, and therefore some improvement is necessary in this regard. A relatively general advice there could be to use the effective stress approach (known also as the notch stress approach), which introduces artificial notches into the toe and root of the weld in the finite element model (FEA). IIW recommends that the root radius of the notch be 1 mm as a value usable for the thickness of the plate greater than or equal to 5 mm. Some other documents from IIW [2] postulate that the notch radius should decrease to 0.05 mm for plates thinner than 5 mm.

The case discussed in this paper focuses on section joints from cylindrical tubes intended originally as a component test for one version of an engine bed for L 410 NG aircraft produced by Aircraft Industries, a.s. The thickness of 1.24 mm of the thinner elements, and the relative complexity of the engine bed call rather for the application of the hot-spot approach than of the notch stress solution. Although this

M. Machač · J. Papuga (✉) · K. Doubrava
Faculty of Mechanical Engineering, Czech Technical University in Prague, Technická 4, 166 07
Prague 6, Czech Republic
e-mail: jan.papuga@fs.cvut.cz

J. Fišer
Aircraft Industries, a.s., Na Záhonech 1177, 686 04 Kunovice, Czech Republic

design project was abandoned, the already manufactured samples were found to be suitable for the evaluation of whether this type of approach could be used for other cases in the future. This is the reason why the applicability of the findings of the report [3] was evaluated on the experiments performed. This report covers various section joints of cylindrical or rectangular profiles and focuses especially on tube thicknesses less than 25 mm up to 4 mm. Below this level (and thus also for our case), it states that the current evidence shows a too large potential for manufacturing defects to affect the fatigue life of such structures.

6.2 Description of the Experimental Campaign

Acorn Welding produced two configurations of welded joints, each with the central hollow section of interest with an outer diameter of 31.75 mm and an inner diameter of 29.25 mm. In the axial configuration of I-type specimens (see Fig. 6.1, left), the central tube was inserted into the machined hollow sections to simulate the intended joint between the rolled tube and the machined connection items. The H-type specimen (Fig. 6.1, right) was used to analyze the behavior of the tube-tube connection. The material used for all parts of the samples is the AISI 4130-N specification AMS 6360.

The Quality Control in Aircraft Industries performed the check for imperfections in fillet welds and for geometrical tolerations. Of the 12 I-type specimens, three cases with pores or tungsten particles were detected in the weld by radiographic testing (RT). In the case of H-specimens, the number of imperfections was substantially higher—no issue was found on three specimens from 14 only. The imperfections found again concern the pores above all, but also cases of incomplete penetration were detected. The absolute majority (9) of defects concern the crown location, where the stress concentration is about one-half of the stress concentration expected

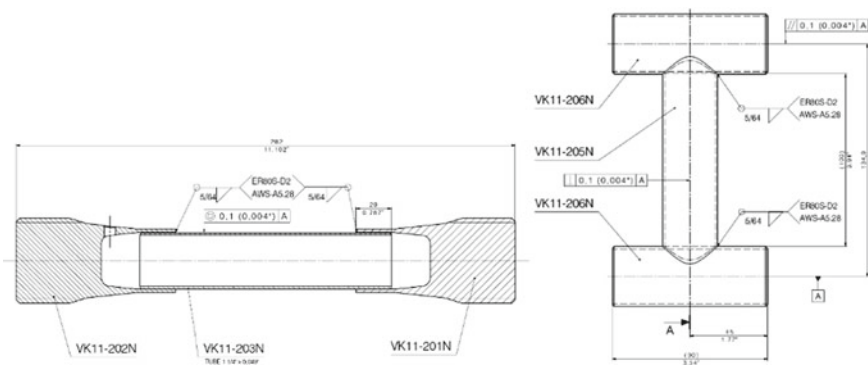


Fig. 6.1 The specimen designs. Type I (left) and Type H (right) samples. In both cases, the central tube is 31.75 mm in diameter and 1.24 mm in wall thickness

at the saddle position (see Fig. 6.3 for terminology). Two cases of pore defects were detected approximately in the middle between the saddle and crown points.

The fatigue tests were carried out on Amsler HFP422 with a load capacity of 100 kN under force control at $R = 0.1$ coefficient of load asymmetry. In the case of I-type specimens, the hole in the specimen head was used to fill the specimen with oil under a pressure of three bar in a closed circuit checked by a pressure sensor. Any crack through the entire wall of the central tube caused a decrease in pressure that indicated this moment. Due to the use of the pulsator for fatigue testing, this moment was, however, very similar to the end condition of the test set to the 5 Hz frequency decrease. The H-type specimens run approximately between 75 and 90 Hz, while the I-type specimens run at 130 Hz. In the case of H-type specimens, a special fixture was manufactured and the load was transmitted to the specimens through 31.5 mm diameter pins inserted into both chords. The pin was thinned in the middle section so that the contact between the pin and the tube was established only 14 mm in length at each end of the chord.

6.3 Experimental Results

The test results for both specimen configurations are shown in Fig. 6.2. The graphs also include the description of the defects detected by the output quality check performed in Aircraft Industries. Quality criteria follow: Any occurrence of a pore larger than 0.8 mm, a tungsten particle larger than 0.8 mm, any incomplete penetration, or a row of pores (less than 4 mm apart from each other) is deemed unacceptable.

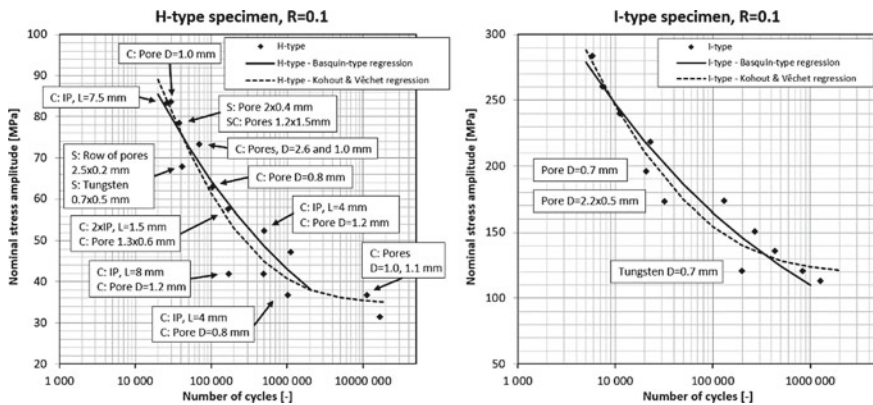


Fig. 6.2 Results of the S–N curves include the description of the defects detected by radiographic testing in Aircraft Industries. Abbreviations: S—close to the saddle, C—close to the crown, SC—between S and C positions, IP—incomplete penetration

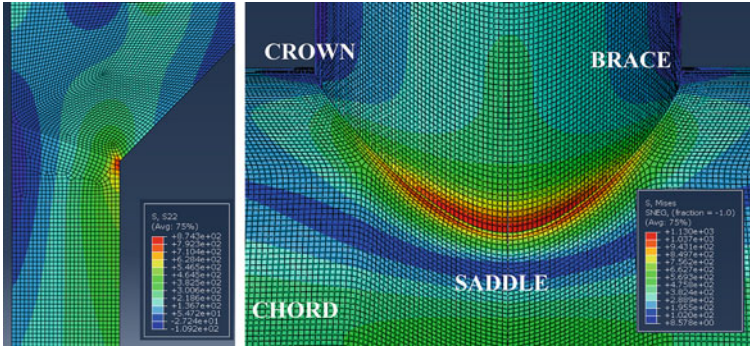


Fig. 6.3 Finite element models of the assemblies—I-type specimen left, H-type specimen right

In the case of axial I-type specimens, the influence of detected defects is obvious in Fig. 6.2. All three cases represent outliers of the general trend, although only the largest pore of them would cause rejection of the item. In the case of H-type samples, the legend also states the location of the defects. The only case where the defect is detected in a close vicinity to the saddle point is an outlier as well. The other outliers are, however, related to defects in the crown position or even no defect was detected at all.

The regression curves used to deal with the experimental data are the Basquin power-law model and the Kohout-Vechet curve [4], which better follows the observed trend in the region of the transition to the fatigue limit; see Fig. 6.2, left. For the same reason, two data points with the longest lifetime were not used for the Basquin-type regression.

Although the outliers, at least in the axial specimens, are clearly related to the weld imperfections, they are included in the regression analyzes. Theoretically, the output control should routinely detect them, but the fact that a company regularly involved in aircraft engine bed production releases them to its customers is a mild warning. Second, this greater potential for weld imperfections is also commented on in Anon [3] as the main reason for not decreasing to thinner thicknesses than 4 mm.

6.4 Fatigue Life Estimation

The IIW hot-spot concept is used to model the welded joints. The FEA models of both cases differ substantially in their complexity. The I-type specimen is modeled as an axisymmetric task with 2D elements to represent the meridian cut of the connection; see Fig. 6.3, left. This solution was preferred over modeling the specimen by the shell structure as a result of the varying thickness of the turned end.

The H-type specimen was modeled by shell elements according to the IIW recommendation [1], i.e., the midsection surfaces were extended at the weld location up

to the position where they meet, see Fig. 6.3, right. The task was prepared as a non-linear analysis involving the contact between the friction pin and the chord, with the coefficient of friction 0.15. Due to the very different stiffnesses of the pin and the hollow sections, the pin was modeled as rigid. The non-linearity of the system meant that upper and lower loads of each load case had to be modeled and evaluated.

The critical locality of the I-type model is without any doubt. In case of the H-type model, the IIW report [3] recommends the calculation of the stress concentration factor (SCF) based on geometrical characteristics. In such a case, the question of the fixity of the chord ends is considered (the general case with $C = 0.7$ was chosen). The SCF s calculated based on Anon [3] show an interesting difference between the outputs of these analytical formulas and the FEA calculation represented in Fig. 6.3, right. It concerns the definition of the critical locality, which according to Anon [3] should be the chord saddle, while the FEA model predicts damage in the position of the brace saddle. It should be explicitly mentioned that crack initiation was generally observed at the saddle weld toe on the brace, from which the crack grew along the weld toe line further to the crown.

Another interesting observation concerns the magnitude of the stress ranges of the hot spots. The SCF values obtained from this evaluation are between 7.5 and 9.8 for the highest and lowest load levels tested, respectively. These values are obviously much higher than any values obtained in Table 6.1.

The solution proposed in Anon [3] relies on the SCF factors derived from the topological parameters of the joint, and not on the FE model. Its application leads to results presented in Fig. 6.4, left for two different cases differing by the wall thickness for which the FAT curve is intended. The first is related to the wall thickness of 4 mm, which corresponds to the applicable bottom thickness limit [3], the other to the actual thickness of the chord, on which the maximum SCF is predicted by the report.

The graph on the right in Fig. 6.4 corresponds to the application of the hot-spot approach based on the FE model analysis. This time, the brace on which the local stress maximum is detected defines the lower thickness, for which the FAT curve is defined (thus exceeding the allowed range of its defined use), while the other presented curve is related to the FAT curve representing the 4 mm wall thickness.

The confidence intervals shown by the thinner dashed lines are defined on the basis of the actual scatter of the experimental data to make the estimates compared with the same probability of fracture. Both types of analysis show that the use of the

Table 6.1 Definition of stress concentration factors [3] based on the boundary conditions of the chord ends

Item	Position	Stress concentration factors (SCF) based on the chord end conditions		
		Chord ends fixed	Chord ends pinned	General condition
Chord	Saddle	4.948	5.644	5.644
	Crown	2.821	2.821	3.217
Brace	Saddle	3.391	3.868	3.868
	Crown	1.838	1.838	1.996

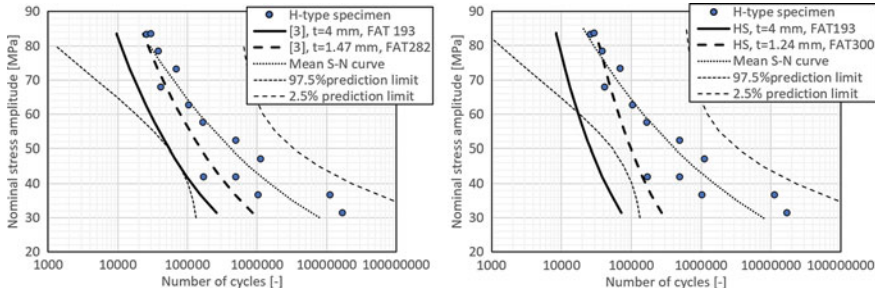


Fig. 6.4 S–N fatigue prediction curves for the H-type sample based on the Z&P SCF approach ([3], here left) and based on the hot-spot approach that includes FEM (right)

limit 4 mm thickness is reasonably conservative if compared with the experimental data, though the additional margin available for the hot-spot approach could be a bit smaller. If there were no outliers to the trends caused by welding defects, even proper wall thickness could provide an acceptable prediction. However, the potential for weld defects is precisely the reason why it is not recommended to use the formulas in Anon [3] to define the FAT curves for structures of wall thickness below 4 mm.

There is no hint in Anon [3] about the axial I-type specimen design. In such a case, this report recommends using $SCF = 2.0$ in the analysis. Its results are as non-conservative as presented in Fig. 6.5, left. Obviously, the report [3] does not focus on such simple geometries. To solve such a problem, the logical process heads to the application of the hot-spot method, results of which are presented in Fig. 6.5, right. Compared to H-type specimens, the FAT curve deduced from Anon [3] on the thickness of the real tube is obviously unsafe, while the application of the thickness of the FAT curve related to the 4 mm thickness leads to a reasonably conservative output.

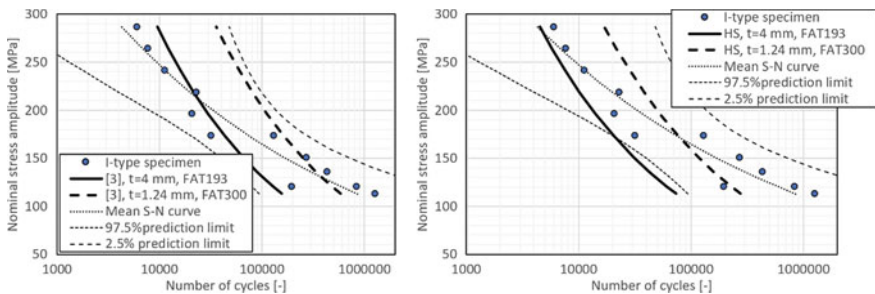


Fig. 6.5 S–N fatigue prediction curves for the I-type specimen based on the Z&P SCF approach ([3], here left) and based on the hot-spot approach including FEM (right)

6.5 Conclusions

The paper describes the experimental results of two different thin-walled hollow welded sections with a relevant wall thickness of 1.24 mm. The prediction obtained by applying [3] is shown to provide a reasonably conservative output if the FAT curves are deduced for a thickness of 4 mm, and the real smaller thickness is not used. This output is apparently caused, among others, by the higher probability of welding defects, whose occurrence does not justify the further increase in the FAT parameter.

Acknowledgements The support from the Grant Agency of the Czech Technical University in Prague (SGS20/158/OHK2/3T/12) is gratefully acknowledged.

References

1. Hobbacher A (2008) The IIW recommendations for fatigue design of welded joints and components. [IIW-1823-07 ex XIII-2151r4-07/XV-1254r4-07]. The International Institute of Welding, Paris
2. Fricke W (2010) Guideline for the fatigue assessment by notch stress analysis for welded structures. [IIW-Doc. XIII-2240r2-08/XV-1289r2-08]. Hamburg University of Technology, Hamburg
3. Anon (2000) Fatigue design procedure for welded hollow section joints. [IIW document XIII-1804-99 and IIW document XV-1035-99]. In: Zhao X-L, Packer JA (eds). Abington Publishing (2000).
4. Kohout J, Věchet S (2001) A new function for fatigue curves characterization and its multiple merits. *Int J Fatigue* 23:175–183

Chapter 7

Analytical Solutions of Water Hammer in Metal Pipes. Part I—Brief Theoretical Study



Kamil Urbanowicz , Anton Bergant , Michał Stosiak ,
and Marek Lubecki 

Abstract The work presents known analytical solutions concerning the unsteady phenomenon, the so-called water hammer that takes place in pressurized lines. The final form of the presented and discussed solutions has been unified. As can be seen from the final form of the presented formulas, they strongly depend on a dimensionless number, the so-called water hammer number Wh , which is a function of the viscosity of the fluid, the length of the pipe, the inner radius of the pipe and the pressure wave speed. The paper shows that there is no complete analytical solution of water hammer known to date, which would be correct in any dimensionless range of the water hammer number and include the frequency-dependent friction losses. The analysis of all the collected analytical solutions also revealed that the formulas determining the flow velocity and wall shear stress in the model represented the greatest consistency in the initial time period of this transient flow (in the Muto-Takahashi model) are not known. To fill this gap, the missing analytical solutions have been developed. This work is devoted to their derivation.

Keywords Water hammer · Frequency-dependent friction · Unsteady flow · Transient flow · Water hammer number · Analytical solution

K. Urbanowicz (✉)

Faculty of Mechanical Engineering and Mechatronics, West Pomeranian University of Technology, Szczecin, Szczecin, Poland
e-mail: kamil.urbanowicz@zut.edu.pl

A. Bergant

Litostroj Power d.o.o. (Full-Time) and Faculty of Mechanical Engineering, University of Ljubljana (Part-Time), Ljubljana, Slovenia
e-mail: anton.bergant@litostrojpower.eu

M. Stosiak · M. Lubecki

Faculty of Mechanical Engineering, Department of Technical Systems Operation, Wrocław University of Science and Technology, Wrocław, Poland
e-mail: michal.stosiak@pwr.edu.pl

M. Lubecki

e-mail: marek.lubecki@pwr.edu.pl

7.1 Introduction

The water hammer is one of those phenomena that continues to electrify the scientific community. These flows are often accompanied by various accompanying phenomena: unsteady hydraulic resistances, retarded strains (occurring in plastic pipes), liquid column separation (cavitation), fluid–structure interaction, etc. Every year, with each new scientific work, the accompanying phenomena are better understood and thus simulated with greater accuracy. A thorough, extensive review of the literature, carried out for the purposes of this work, shows that until today the complete analytical solution of the system of partial equations describing the unsteady water hammer flow occurring in a metal pipes is still unknown. Due to the fact that recently in many studies the topic of analytical solutions of transient flows is very popular, this topic will also be examined in this paper by us. The works of Joukowsky [1] and Allevi [2] that include mathematical analysis of basic equations are treated by the scientific community, dealing with pressure pulsation in hydraulic systems, as initiating research on this subject. However, due to the fact that both Joukowsky and Allevi did not take into account the hydraulic resistance, which determines the dynamics of damping of this phenomenon, these formulas are not suitable for common applications. The exception is the popular formula for the pressure increase that occurs just after the valve instantaneous closure, which was defined by Joukowsky [1]:

$$p = p_0 + \rho c \Delta v \quad (7.1)$$

where $p = p(x,t)$ —pressure in the pipe cross-section, x —axial coordinate along the pipe, t —time, ρ —density of the liquid, c —pressure wave speed, $v = v(x,t)$ —mean velocity of the liquid in the pipe cross-section.

In the first years of the twentieth century, the main focus was on development of graphical methods of analyzing this phenomenon. It was only in 1939 that Wood [3] presented a work that initiated research into analytical solutions to this phenomenon. Due to the fact that Wood presented only solutions in the Laplace domain, a work by Rich [4] appeared not long later as in year 1945; the author presented a number of solutions in the time domain. It is in this work that we find solutions in the form of infinite sums of water hammers excluding friction and taking it into account in a quasi-steady manner. The transient nature of the resistance was first noticed by Iberall in 1950 [5]. Research into a model that took into account the frequency-dependent nature of resistance emerged in the 1960s. Then Nichols [6], Brown [7], Holmboe [8], and Zielke [9] try to find a complete time-domain solution that would take into account the transient nature of resistance. None of them succeeded, but the closest was Holmboe, who proposed to use Brown’s asymptotic extension of wave propagation function, which determines the nature of the resistance for high frequencies. This Holmboe’s solution was an inspiration for Muto and Takahashi [10], who in 1985 presented a very interesting work, the most important point of which was the solution of the pressure in the time domain. The formula obtained by Muto and Takahashi is

very consistent, in particular for the flows of liquids characterized by relatively low viscosity (e.g., water) and in the range of the water hammer number [11] to its value of 0.1. Relatively recently, Mei and Jing [12] presented an interesting solution taking into account frequency-dependent friction, the assumption of which was to model blood flow in the veins. Another analytical solution that may allow for the analytical analysis of turbulent flows (including water hammers) concerned accelerated and delayed flows was presented just recently by García-Alvariño [13, 14].

In the first part of this two-part paper, known analytical solutions (for pressure, flow velocity, and wall shear stress) will be briefly discussed, as well as new solutions derived from the approach initiated by Holmboe and developed later on by Muto and Takahashi. In the second part of this work [15], comparative studies of dynamic pressure, velocity, and shear stresses will be carried out, for which the formulas presented in this part will be used. The results of analytical tests will be compared to the results obtained from the numerical model (method of characteristics algorithm) and, in selected cases, to the results of experimental tests (pressure oscillations).

7.2 Analytical Solutions

The set of partial differential equations of hyperbolic type that describes the unsteady flow in horizontal pipes is of the following form [11]:

$$\begin{cases} \frac{\partial p}{\partial t} + \rho c^2 \frac{\partial v}{\partial x} = 0 \\ \rho \frac{\partial v}{\partial t} + \frac{\partial p}{\partial x} + \frac{2}{R} \tau_w = 0 \end{cases} \quad (7.2)$$

where R —inner diameter of the pipe, τ —wall shear stress.

The solutions of above system of equations by assuming sudden (instantaneous) downstream end valve closure in a simple horizontal pipeline (constant head reservoir-pipeline-valve system) will be the topic of our work (water hammer event). The solutions in time domain presented in this paper differ from the solutions presented in the original scientific works. It was our intention to maximally simplify the mathematical notation so that the solutions could be easily used in engineering practice.

7.2.1 Frictionless Solution

For the frictionless simple horizontal pipeline, i.e., $\tau_w = 0$, it was Rich [4] who first presented the correct time-domain solution for pressure and velocity, respectively:

$$p(x, t) = p_0 + 2\mathbb{Z} \sum_{n=1}^{\infty} \frac{\sin\left(\frac{k_n ct}{L}\right) \sin\left(k_n \left(1 - \frac{x}{L}\right)\right)}{k_n \sin(k_n)} \quad (7.3)$$

$$v(x, t) = 2v_0 \sum_{n=1}^{\infty} \frac{\cos\left(\frac{k_n ct}{L}\right) \cos\left(k_n\left(1 - \frac{x}{L}\right)\right)}{k_n \sin(k_n)} \quad (7.4)$$

where $k_n = (n - 0.5)\pi$ and $\mathbb{Z} = \rho cv_0$ is the Joukowsky pressure rise formula [1], L —pipe length. Above two solutions are the modified Fourier square wave solutions.

7.2.2 Quasi-steady Friction Solution

Again, it was Rich [4] who first presented the solution that include the quasi-steady frictional effects $\tau_w = \tau_q = \frac{4\mu}{R} v(x, t)$. The simplified solution for pressure and velocity is:

$$p(x, t) = p_0 + 2\mathbb{Z} \cdot \text{Wh} \cdot e^{-4\hat{t}} \sum_{n=1}^{\infty} \frac{\sin\left(k_n\left(1 - \frac{x}{L}\right)\right) [8\psi_n \cos(\psi_n \hat{t}) + (16 - \psi_n^2) \sin(\psi_n \hat{t})]}{\psi_n k_n^2 \sin(k_n)} \quad (7.5)$$

$$v(x, t) = 2v_0 e^{-4\hat{t}} \sum_{n=1}^{\infty} \frac{\cos\left(k_n\left(1 - \frac{x}{L}\right)\right) \left[\cos(\psi_n \hat{t}) + \frac{4 \sin(\psi_n \hat{t})}{\psi_n}\right]}{k_n \sin(k_n)} \quad (7.6)$$

where $\psi_n = \sqrt{\left(\frac{k_n}{\text{wh}}\right)^2 - 16}$, $\hat{t} = \frac{\nu}{R^2} t$ is a dimensionless time and $\text{Wh} = \frac{\nu L}{cR^2}$ is a water hammer number [11], ν = kinematic viscosity. The same solution was recently presented by Jović and Lucić as well [16]. The authors solved electromagnetic transients on a single electrical transmission line using the double Laplace transform. Since Telegrapher's equations have the same structure as water hammer equations, final result was obtained just by rearranging of variables from electrical to hydrodynamic ones.

7.2.3 Unsteady Friction Solution

In unsteady friction solution the wall shear stress is a sum of quasi-steady and unsteady terms: $\tau_w = \tau_q + \tau_u$. Brown [7], Holmboe [8], Zielke [9], and others based on Iberall's work [5] developed a frequency-dependent function M in frequency-domain, the value of which is determined by the viscosity of the flowing liquid and the internal radius of the pipe:

$$M = \sqrt{\left(1 - \frac{2J_1(i\sqrt{\frac{s}{v}}R)}{(i\sqrt{\frac{s}{v}}R)J_0(i\sqrt{\frac{s}{v}}R)}\right)^{-1}} = \sqrt{\frac{-J_0(i\sqrt{\frac{s}{v}}R)}{J_2(i\sqrt{\frac{s}{v}}R)}} = \sqrt{\frac{I_0(\sqrt{\frac{s}{v}}R)}{I_2(\sqrt{\frac{s}{v}}R)}} \quad (7.7)$$

where s = complex-valued frequency.

The above function Eq. 7.7 affects the wave propagation operator. Brown derived an asymptotic expansion of it. From this expansion, it follows that for large s arguments:

$$M = 1 + \left(\frac{v}{R^2s}\right)^{1/2} + \left(\frac{v}{R^2s}\right) + \frac{7}{8}\left(\frac{v}{R^2s}\right)^{3/2} \quad (7.8)$$

Holmboe [8] used above expansion to present the valve cross-section solution of pressure valid only for first complete water hammer cycle (period $\hat{t} < 4Wh$):

$$p(0, t) = p(0, 0) - \mathbb{Z} \left[\begin{array}{l} 1 + \frac{2}{\sqrt{\pi}}\sqrt{\hat{t}} + \hat{t} + \frac{7}{6\sqrt{\pi}}\hat{t}^{3/2} \\ -2e^{-2Wh} \left\{ \begin{array}{l} \text{erfc}\left[Wh(\hat{t} - 2Wh)^{-1/2}\right] \\ +2(\hat{t} - 2Wh)^{1/2}i\text{erfc}\left[Wh(\hat{t} - 2Wh)^{-1/2}\right] \\ +4(\hat{t} - 2Wh)i^2\text{erfc}\left[Wh(\hat{t} - 2Wh)^{-1/2}\right] \\ +7(\hat{t} - 2Wh)^{3/2}i^3\text{erfc}\left[Wh(\hat{t} - 2Wh)^{-1/2}\right] \end{array} \right\} \end{array} \right] \quad (7.9)$$

where: $i^n \text{erfc}$ is the n th integral of the complementary error function and Wh is the water hammer number, discussed by Urbanowicz et al. [11]. Just the first four terms in the square bracket are needed to represent the initial stage of pressure surge, a half of the water hammer period to be exact. To obtain a more complete solution that is correct also for the initial state, the square bracket of the above equation should be multiplied by the step Heaviside function $H(t)$, which for time $t = 0$ should assume the value $H(t = 0) = 0$.

As Holmboe's solution is limited only to the first water hammer cycle at valve cross-section Muto with Takahashi [10] presented an important improvement of it. They analyzed transient responses to sudden changes of pressure or flow rate in both single and series pipelines. For single pipeline, Muto and Takahashi derived the transfer function which relates either the input variable P_1 or Q_1 with the output variable P_x (the pressure at pipe coordinate x). The final time-domain solutions are:

(a) for a sudden change of pressure:

$$p(x, t) = \sum_{k=1}^2 \sum_{l=1}^{\infty} (-1)^{l+1} R_L^{k+l-2} e^{-\lambda \cdot Wh} \operatorname{erfc} \left(\frac{\lambda}{2} \sqrt{\frac{Wh}{T}} \right) \mathbb{H} \left(T \frac{L}{c} \right) \quad (7.10)$$

(b) for a sudden change of flow rate:

$$p(x, t) = p(x, 0) - \mathbb{Z} \sum_{k=1}^2 \sum_{l=1}^{\infty} (-1)^{k+l-2} e^{-\lambda \cdot Wh} \left\{ \begin{array}{l} (2 - \lambda \cdot Wh) \sqrt{\frac{T \cdot Wh}{\pi}} e^{-\frac{\lambda^2 \cdot Wh}{4T}} \\ + \left[1 + Wh \left(T - \lambda + \frac{\lambda^2 \cdot Wh}{2} \right) \right] \operatorname{erfc} \left(\frac{\lambda}{2} \sqrt{\frac{Wh}{T}} \right) \end{array} \right\} \mathbb{H} \left(T \frac{L}{c} \right) \quad (7.11)$$

where:

$\lambda = 2(k+l-2) + \frac{x}{L} (-1)^{k+l-1}$; $T = t \frac{c}{L} - \lambda$; $p(x, 0) = p(0, 0) - 8Wh \cdot \mathbb{Z} \cdot \frac{x}{L}$ and $p(0, 0)$ —is the valve pressure (note that $\mathbb{Z} < 0$ as $v_0 < 0$).

From presented solutions (Eqs. 7.10 and 7.11), the second one (step response to flow rate) corresponds to a typical instantaneous valve closure scenario in water hammer event. A relation between the Muto and Takahashi dimensionless numbers T , λ and those known from Holmboe and Rich studies \hat{t} , Wh as follows:

$$\frac{\hat{t}}{Wh} = T + \lambda \quad (7.12)$$

Recently Mei and Jing [12] presented analytical solution for blood hammer in a long and stiffened artery due to sudden (instantaneous) blockage. Based on the model of a viscous fluid in laminar flow, they derived explicit expressions of oscillatory pressure and wall shear stress. A small error was found in the original equations presented in paper [12], consisting in omitting the line packing effect. The revised solutions take the following form [17]:

$$p(x, t) = p(L, 0) \sin \left(k_n \left(1 - \frac{x}{L} \right) \right) + 2\mathbb{Z} \sum_{n=1}^{\infty} \frac{\left[\sin \left(\hat{t} \left(\frac{k_n}{Wh} - \sqrt{\frac{k_n}{2Wh}} \right) \right) - \frac{8Wh}{k_n} \cos \left(\hat{t} \left(\frac{k_n}{Wh} - \sqrt{\frac{k_n}{2Wh}} \right) \right) \right]}{k_n \sin(k_n)} e^{-\hat{t} \sqrt{\frac{k_n}{2Wh}}} \quad (7.13)$$

where $p(L, 0)$ —is a reservoir pressure.

$$v(x, t) = 2v_0 \sum_{n=1}^{\infty} \frac{\cos(k_n(1 - \frac{x}{L})) \left[\begin{array}{l} \cos\left(\hat{t}\left(\frac{k_n}{Wh} - \sqrt{\frac{k_n}{2Wh}}\right)\right) \\ + \frac{8Wh}{k_n} \sin\left(\hat{t}\left(\frac{k_n}{Wh} - \sqrt{\frac{k_n}{2Wh}}\right)\right) \end{array} \right]}{k_n \sin(k_n)} e^{-\hat{t}\sqrt{\frac{k_n}{2Wh}}} \quad (7.14)$$

A dimensional solution for the wall shear stress is:

$$\tau(x, t) = \frac{2\mu v_0}{R} \sum_{n=1}^{\infty} \frac{\sqrt{\frac{k_n}{2Wh}} \cos(k_n(1 - \frac{x}{L})) \left[\begin{array}{l} \left(1 + \frac{8Wh}{k_n}\right) \cos\left(\hat{t}\left(\frac{k_n}{Wh} - \sqrt{\frac{k_n}{2Wh}}\right)\right) \\ + \left(\frac{8Wh}{k_n} - 1\right) \sin\left(\hat{t}\left(\frac{k_n}{Wh} - \sqrt{\frac{k_n}{2Wh}}\right)\right) \end{array} \right]}{k_n \sin(k_n)} e^{-\hat{t}\sqrt{\frac{k_n}{2Wh}}} \quad (7.15)$$

7.3 Novel Solution of Velocity and Wall Shear Stress

In this section, we will derive solutions for dynamic change of flow and shear stress to complete the work of Muto and Takahashi [10] which presents solution for dynamic change of pressure only.

In the Laplace-domain Holmboe [8] presented the following solution for pressure:

$$\begin{aligned} \tilde{v}(x, s) &= \left(\frac{1}{s\rho} \frac{\partial \tilde{p}}{\partial x} - \frac{8v_0 v}{s^2 R^2} \right) \left(\frac{2J_1(i\sqrt{\frac{s}{v}}R)}{(i\sqrt{\frac{s}{v}}R)J_0(i\sqrt{\frac{s}{v}}R)} - 1 \right) \\ - \frac{v_0}{s} &= \left(\frac{8v_0 v}{s^2 R^2} - \frac{1}{s\rho} \frac{\partial \tilde{p}}{\partial x} \right) \left(\frac{1}{M^2} \right) - \frac{v_0}{s} \end{aligned} \quad (7.16)$$

The derivative of Eq. 7.16 with respect to x is:

$$\frac{\partial \tilde{p}(x, s)}{\partial x} = v_0 \rho M^2 \left[\begin{array}{l} -e^{-\frac{x}{c}Ms} - e^{-\frac{(2L-x)}{c}Ms} + e^{-\frac{(2L+x)}{c}Ms} \\ + e^{-\frac{(4L-x)}{c}Ms} - e^{-\frac{(4L+x)}{c}Ms} - \dots \end{array} \right] + \frac{8v_0 v \rho}{sR^2} \quad (7.17)$$

If the above derivative (Eq. 7.17) is inserted into the velocity equation in Laplace domain:

$$\begin{aligned} \tilde{v}(x, s) &= \left(\frac{1}{s\rho} \frac{\partial \tilde{p}}{\partial x} - \frac{8v_0\nu}{s^2 R^2} \right) \left(\frac{2J_1\left(i\sqrt{\frac{x}{v}}R\right)}{\left(i\sqrt{\frac{x}{v}}R\right)J_0\left(i\sqrt{\frac{x}{v}}R\right)} - 1 \right) \\ &- \frac{v_0}{s} = \left(\frac{8v_0\nu}{s^2 R^2} - \frac{1}{s\rho} \frac{\partial \tilde{p}}{\partial x} \right) \left(\frac{1}{M^2} \right) - \frac{v_0}{s} \end{aligned} \tag{7.18}$$

then one obtains the final velocity formula in Laplace domain:

$$\tilde{v}(x, s) = -\frac{v_0}{s} \left[\begin{aligned} &-e^{-\frac{x}{c}M \cdot s} - e^{-\frac{(2L-x)}{c}M \cdot s} + e^{-\frac{(2L+x)}{c}M \cdot s} \\ &+ e^{-\frac{(4L-x)}{c}M \cdot s} - e^{-\frac{(4L+x)}{c}M \cdot s} - \dots \end{aligned} \right] - \frac{v_0}{s} \tag{7.19}$$

Using the first three terms of Brown’s asymptotic expansion of Eq. 7.8 in the powers of exponential terms one obtains:

$$M \cdot s = s + \sqrt{\frac{\nu}{R^2}}\sqrt{s} + \frac{\nu}{R^2} \tag{7.20}$$

Then for the first product term of velocity an infinite sum solution (Eq. 7.19):

$$F_v = v_0 \frac{e^{-\frac{x}{c}\left(s + \sqrt{\frac{\nu}{R^2}}\sqrt{s} + \frac{\nu}{R^2}\right)}}{s} = v_0 \frac{e^{-as} \cdot e^{-b\sqrt{s}} \cdot e^{-a\frac{\nu}{R^2}}}{s} = C \frac{e^{-as} \cdot e^{-b\sqrt{s}}}{s} \tag{7.21}$$

where: $a = \frac{x}{c}$; $b = \frac{x}{c}\sqrt{\frac{\nu}{R^2}} = a\sqrt{\frac{\nu}{R^2}}$ and $C = v_0 \cdot e^{-a\frac{\nu}{R^2}} = const.$

Noting that in the remaining terms of the obtained Laplace solution, only the sign in front of subsequent terms and the value of the a constant changes (first term $a_1 = \frac{x}{c}$, second $a_2 = \frac{(2L-x)}{c}$, third $a_3 = \frac{(2L+x)}{c}$, fourth $a_4 = \frac{(4L-x)}{c}$, etc. please note that all values are positive), a solution in the time domain is obtained after calculating the inverse Laplace transform of the following function (using second shift theorem):

$$\mathcal{L}^{-1} \left\{ \frac{e^{-as} \cdot e^{-b\sqrt{s}}}{s} \right\} = H(t - a) \cdot \operatorname{erfc} \left(\frac{b}{2\sqrt{t - a}} \right) \tag{7.22}$$

then the final novel time-domain solution for velocity is:

$$v(x, t) = v_0 \left(1 + \sum_{k=1}^2 \sum_{l=1}^{\infty} (-1)^l e^{-\lambda \cdot \text{Wh}} \operatorname{erfc} \left(\frac{\lambda}{2} \sqrt{\frac{\text{Wh}}{T}} \right) H \left(T \frac{L}{c} \right) \right) \tag{7.23}$$

where: $T \frac{L}{c} = t - \lambda \frac{L}{c}$.

In a similar way, the missing wall shear stress solution can be determined in this work. The function describing the dynamic velocity distribution in the pipe cross-section has the form [8]:

$$\tilde{u}(x, r, s) = \left(\frac{1}{s\rho} \frac{\partial \tilde{p}}{\partial x} - \frac{8v_0\nu}{s^2 R^2} \right) \left(\frac{J_0(i\sqrt{\frac{s}{\nu}}r)}{J_0(i\sqrt{\frac{s}{\nu}}R)} - 1 \right) - \frac{2v_0}{s} \left(1 - \frac{r^2}{R^2} \right) \quad (7.24)$$

Due to the fact that $\tilde{\tau}(x, s) = -\mu \frac{\partial \tilde{u}}{\partial r}$, μ = dynamic viscosity, the derivative from the above function (in respect to r) was first calculated:

$$\frac{\partial \tilde{u}}{\partial r} = \left(\frac{1}{s\rho} \frac{\partial \tilde{p}}{\partial x} - \frac{8v_0\nu}{s^2 R^2} \right) \frac{-i\sqrt{\frac{s}{\nu}} \cdot J_1(i\sqrt{\frac{s}{\nu}}r)}{J_0(i\sqrt{\frac{s}{\nu}}R)} \Big|_{r=R} + \frac{4v_0r}{sR^2} \Big|_{r=R} \quad (7.25)$$

then

$$\tilde{\tau}(x, s) = -\mu \frac{\partial \tilde{u}}{\partial r} = -\frac{R}{2} \left(\frac{\partial \tilde{p}}{\partial x} - \frac{8v_0\nu\rho}{sR^2} \right) \frac{2J_1(i\sqrt{\frac{s}{\nu}}R)}{i\sqrt{\frac{s}{\nu}}R \cdot J_0(i\sqrt{\frac{s}{\nu}}R)} - \frac{4\mu v_0}{sR} \quad (7.26)$$

$$\begin{aligned} \tilde{\tau}(x, s) &= \frac{Rv_0\rho}{2} \left(-e^{-\frac{x}{c}Ms} - e^{-\frac{(2L-x)}{c}Ms} + e^{-\frac{(2L+x)}{c}Ms} + \dots \right) \\ &\quad (1 - M^2) - \frac{4\mu v_0}{sR} \end{aligned} \quad (7.27)$$

Now inserting the derivative from (Eq. 7.17):

$$\begin{aligned} \tilde{\tau}(x, s) &= \frac{Rv_0\rho}{2} \left(-e^{-\frac{x}{c}Ms} - e^{-\frac{(2L-x)}{c}Ms} + e^{-\frac{(2L+x)}{c}Ms} + \dots \right) \\ &\quad (1 - M^2) - \frac{4\mu v_0}{sR} \end{aligned} \quad (7.28)$$

Taking the first three terms of M (for high frequencies) into account, one gets

$$M^2 = 1 + \frac{2}{\sqrt{s}} \sqrt{\frac{\nu}{R^2}} + \frac{3}{s} \frac{\nu}{R^2} + \frac{2}{s^{3/2}} \left(\frac{\nu}{R^2} \right)^{3/2} + \frac{1}{s^2} \left(\frac{\nu}{R^2} \right)^2 \quad (7.29)$$

and:

$$(1 - M^2) = \left(-\frac{2}{\sqrt{s}} \sqrt{\frac{\nu}{R^2}} - \frac{3}{s} \frac{\nu}{R^2} - \frac{2}{s^{3/2}} \left(\frac{\nu}{R^2} \right)^{3/2} - \frac{1}{s^2} \left(\frac{\nu}{R^2} \right)^2 \right) \quad (7.30)$$

Thus, the final solution in the Laplace frequency-domain is as follows:

$$\begin{aligned} \tilde{\tau}(x, s) = & -\frac{Rv_0\rho}{2} \left(\frac{2}{\sqrt{s}} \sqrt{\frac{v}{R^2}} + \frac{3}{s} \frac{v}{R^2} + \frac{2}{s^{3/2}} \left(\frac{v}{R^2} \right)^{3/2} + \frac{1}{s^2} \left(\frac{v}{R^2} \right)^2 \right) \\ & \left(-e^{-\frac{x}{c}Ms} - e^{-\frac{(2L-x)}{c}Ms} + e^{-\frac{(2L+x)}{c}Ms} + \dots \right) - \frac{4\mu v_0}{sR} \end{aligned} \quad (7.31)$$

Finding the Laplace inverse for the above function by using the following inverse Laplace transforms:

$$\begin{aligned} \mathcal{L}^{-1} \left\{ \frac{e^{(-b\sqrt{s})}}{\sqrt{s}} \right\} &= \frac{e^{-\frac{b^2}{4t}}}{\sqrt{\pi t}}; \mathcal{L}^{-1} \left\{ \frac{e^{(-b\sqrt{s})}}{\sqrt{s}} \right\} \\ &= \operatorname{erfc} \left(\frac{b}{2\sqrt{t}} \right); \mathcal{L}^{-1} \left\{ \frac{e^{(-b\sqrt{s})}}{s^{3/2}} \right\} = \frac{2\sqrt{t}}{\sqrt{\pi}} e^{-\frac{b^2}{4t}} - b \cdot \operatorname{erfc} \left(\frac{b}{2\sqrt{t}} \right) \\ \mathcal{L}^{-1} \left\{ \frac{e^{(-b\sqrt{s})}}{s^2} \right\} &= \left(\frac{b^2}{2} + t \right) \operatorname{erfc} \left(\frac{b}{2\sqrt{t}} \right) - \frac{b\sqrt{t}}{\sqrt{\pi}} e^{-\frac{b^2}{4t}} \end{aligned} \quad (7.32)$$

provides the following final time-domain solution:

$$\begin{aligned} \tau(x, t) = & \frac{v_0\mu}{2R} \sum_{k=1}^2 \sum_{l=1}^{\infty} (-1)^l \\ & \left\{ \begin{aligned} & (4 - \lambda \cdot Wh) \sqrt{\frac{T \cdot Wh}{\pi}} e^{-\frac{\lambda^2 \cdot Wh}{4T}} \\ & + \left[3 + Wh \left(T + \frac{\lambda^2 \cdot Wh}{2} - 2\lambda \right) \right] \operatorname{erfc} \left(\frac{\lambda}{2} \sqrt{\frac{Wh}{T}} \right) \\ & + \frac{2e^{-\frac{\lambda^2 \cdot Wh}{4T}}}{\sqrt{\pi \cdot Wh \cdot T}} \end{aligned} \right\} \\ & H \left(T \frac{L}{c} \right) - \frac{4v_0\mu}{R} \end{aligned} \quad (7.33)$$

The asymptotic time-domain solutions for pressure is:

$$\begin{aligned} p(x, t) = & 4\mathbb{Z} \sum_{k=1}^2 \sum_{l=1}^{\infty} (-1)^{k+l-2} \\ & \left\{ \sqrt{\frac{2Wh(T+\lambda)}{\pi}} e^{-\frac{2Wh\lambda^2}{T+\lambda}} - 2\lambda \cdot Wh \cdot \operatorname{erfc} \left(\lambda \sqrt{\frac{2Wh}{T+\lambda}} \right) \right\} + p(x, 0) \end{aligned} \quad (7.34)$$

and the asymptotic solution for flow velocity:

$$v(x, t) = v_0 \left(1 + \sum_{k=1}^2 \sum_{l=1}^{\infty} (-1)^l \operatorname{erfc} \left(\lambda \sqrt{\frac{2Wh}{T + \lambda}} \right) \right) \quad (7.35)$$

The above solutions have been written using the coefficients found in the previous solutions. The formulas presented above (Eqs. 7.34 and 7.35) will allow us to make comparisons of asymptotic solutions with the complete solutions for the initial water hammer impact period (Eqs. 7.11 and 7.23).

7.4 Conclusions

In this prequel paper, the important analytical solutions for water hammers taking place in a simple horizontal metal pipe are presented in new simplified forms. The analysis of all collected solutions in the second section showed that there are no solutions for the dynamic change of velocity and wall shear stress in an interesting analytical model originally developed by Muto and Takahashi. The missing solutions have been presented. The detailed derivation procedure is described as well. Comparisons of simulation calculations made with the help of the presented analytical solutions and with the help of a numerical solution based on the use of the method of characteristic will be presented in the sequel paper.

Acknowledgements Bergant gratefully acknowledges the support of the Slovenian Research Agency (ARRS) conducted through the project L2-1825 and the program P2-0126.

References

1. Joukowsky N (1900) Über den hydraulischen stoss in wasserleitungsröhren. Memoires de L'academie Imperiale des Sciences de St.-Petersbourg, IX(5): 1–71
2. Allievi L (1902) Teoria generale del moto perturbato dell'acqua nei tubi in pressione (colpo d'ariete). Annali della Società degli Ingegneri ed Architetti Italiani 17(5):285–325
3. Wood FM (1937) The application of heaviside's operational calculus to the solution of problems in water hammer. Trans. A.S.M.E 59:707–713
4. Rich GR (1945) Water hammer analysis in the Laplace–Mellin transformation. Trans ASME 67(5):361–376
5. Iberall AS (1950) Attenuation of oscillatory pressures in instrument lines. J Res Nat Bureau Standards 45:85–108
6. Nichols NB (1962) The linear properties of pneumatic transmission lines. Trans Instrum Soc Am 1:5–14
7. Brown FT (1962) The transient response of fluid lines. J Fluids Eng 84(3):547–553
8. Holmboe EL (1964) Viscous distortion in wave propagation as applied to waterhammer and short pulses. Doctoral Thesis, Carnegie Institute of Technology
9. Zielke W (1968) Frequency-dependent friction in transient pipe flow. ASME J Basic Eng 90:109–115
10. Muto T, Takahashi K (1985) Transient responses of fluid lines (Step responses of single pipeline and series pipelines). Bullet JSME 28(244):2325–2331

11. Urbanowicz K, Bergant A, Karadzić U, Jing H, Kodura A (2021) Numerical investigation of the cavitation flow for constant water hammer number. *J Phys Conf Ser* 1736:012040
12. Mei CC, Jing H (2016) Pressure and wall shear stress in blood hammer —analytical theory. *Math Biosci* 280:62–70
13. García García FJ, Alvariño PF (2019) On an analytic solution for general unsteady/transient turbulent pipe flow and starting turbulent flow. *Eur J Mech B Fluids* 74:200–210
14. García García FJ, Alvariño PF (2020) On the influence of Reynolds shear stress upon the velocity patterns generated in turbulent starting pipe flow. *Phys Fluids* 32:105119. doi:<https://doi.org/10.1063/5.0019180>
15. Urbanowicz K, Bergant A, Stosiak M, Lubecki M (2021) Analytical solutions of water hammer in metal pipes. Part II—comparative study. *Structural Integrity and Fatigue Failure Analysis*, Springer
16. Jović V (2013) *Analysis and modelling of non-steady flow in pipe and channel networks*. Wiley
17. Urbanowicz K, Jing H, Bergant A, Stosiak M, Lubecki M (2021) Progress in analytical modeling of water hammer. Proceedings of the fluids engineering division summer meeting *FEDSM 2021*, August 10–12, paper 65920

Chapter 8

Analytical Solutions of Water Hammer in Metal Pipes. Part II—Comparative Study



Kamil Urbanowicz , Anton Bergant , Michał Stosiak ,
and Krzysztof Towarnicki 

Abstract The newly derived analytical solutions of water hammer for dynamic flow velocity and wall shear stress, as well as the previously known albeit corrected pressure solutions, have been studied in detail. Their correctness was verified with the help of comparative tests with the results obtained with the use of a numerical solution in which a model of frequency-dependent hydraulic friction was implemented. The dynamic pressure courses were compared with the results of the experimental tests. The performed comparisons showed that the analytical models based on Brown's asymptotic extension of frequency-dependent friction function are very compatible with experimental studies for small values of water hammer number Wh . Due to the fact that the majority of unsteady water flows occur for small values of $Wh < 0.1$, it can be concluded that the new solutions can be safely used in engineering practice (excluding wall shear stress solution), i.e., when calculating unsteady water hammer wave dependent flows occurring in water supply systems.

Keywords Water hammer · Frequency-dependent friction · Unsteady flow · Transient flow · Water hammer number · Analytical solution

K. Urbanowicz (✉)

Faculty of Mechanical Engineering and Mechatronics, West Pomeranian University of Technology, Szczecin, Szczecin, Poland
e-mail: kamil.urbanowicz@zut.edu.pl

A. Bergant

Litostroj Power d.o.o. (Full-Time) and Faculty of Mechanical Engineering, University of Ljubljana (Part-Time), Ljubljana, Slovenia
e-mail: anton.bergant@litostrojpower.eu

M. Stosiak · K. Towarnicki

Faculty of Mechanical Engineering, Department of Technical Systems Operation, Wrocław University of Science and Technology, Wrocław, Poland
e-mail: michal.stosiak@pwr.edu.pl

K. Towarnicki

e-mail: krzysztof.towarnicki@pwr.edu.pl

8.1 Introduction

The main component of a number of industrial systems (hydraulic, water supply, transmission lines, etc.) is the liquid-filled pipe. If there is a sudden change in the selected parameter describing the flow (velocity or pressure) a transient state occurs. The most dangerous scenario of possible pressure pulsations is so-called water hammer phenomenon, in which the valve installed at the pipe far end is suddenly closed. In order to effectively estimate and to be able to protect systems in the future against excessive pressure rise (which may damage pipeline components), this phenomenon should be carefully examined. Analytical and numerical models are used to carry out the research. Until now, the system of equations describing the water hammer has not been solved in an entire analytical manner, hence, the numerical methods are very important as well. The numerical method of characteristics (MOC) is today considered to be the most important one for solving differential equations describing the unsteady flow of a liquid in pressurized conduits. This is not a method that was originally invented for unsteady fluid flows in conduits. Its foundations were defined by Paul Charpit de Villecourt, who presented his lecture on the integration of partial differential equations at the French Academy of Sciences in 1784 [1]. At the same time, Lagrange and Monge [2] had a great influence on its development. The MOC was initially used for unsteady fluid flow problems in the 1950s and 1960s [3–8]. The two partial differential equations (of momentum and continuity) are transformed into four total differential equations, which are next expressed in a finite difference form.

Initially, during the numerical modeling, unsteady hydraulic resistance was not taken into account. Thanks to the work of Zielke [9, 10] this situation was changed. Due to the fact that Zielke's solution is based on a convolutional integral, finding the solution initially required the use of an ineffective numerical procedure. Over time, a number of researchers (Triakha [11], Kagawa et al. [12], Schochl [13], Vítkovský et al. [14], Urbanowicz [15]) managed to modify the computational procedure so that it would be effective and bring the determined hydraulic resistance closer to its real physically observed value. Zielke's solution has been developed for laminar flow only. Solutions for turbulent flow were presented independently by Zarzycki [16, 17] and Vardy and Brown [18, 19] in early 90s of the previous century. Relatively recently, Vardy and Brown [20] noticed that the ineffective original solution of the wall shear stress according to Zielke, which is an ineffective numerical way is defined by the convolutional integral, is characterized by an error and it was corrected by the authors [20]. However, the new corrected solution was presented in an ineffective form. An effective solution representing the Vardy and Brown correction was presented by Urbanowicz in [15]. It is this solution that will be used in numerical simulations of dynamic changes of wall shear stress presented in this paper.

In this sequel work, the main emphasis was given to the analysis of dynamic wall shear stress and flow velocity histories in selected cross-sections of the tested pipeline. The results obtained with the use of analytical models discussed in Vardy and Brown [21] will be compared with the results of numerical tests. In addition, to

confirm the compliance of the analytical method analyzed in this work, the results of experimental pressure pulsation tests are compared to the results calculated with use of discussed analytical models, showing their very good compliance.

8.2 Numerical Solution of Transient Pipe Flow

The role of numerical methods is to transform partial differential equations into algebraic equation systems. The transformation is carried out by dividing the integration area of the analyzed equations into small elements called calculation cells (reaches). In this work the MOC is used which (1) perfectly interprets the physical essence of the transient flow phenomenon, (2) is characterized by fast convergence, (3) offers possibility to have use of various boundary conditions, and (4) gives high accuracy of calculation results. It is the only method, in which there is no problem with the correct reproduction of the steep pressure wavefronts that propagate along the pipe during transient events [22, 23]. The governing system of quasi-linear hyperbolic partial differential equations describing the unsteady flow in a horizontal pipe (Eq. 8.2 from work [21]) is transformed to equivalent system of four ordinary differential equations:

$$C^+ : \begin{cases} \frac{dx}{dt} = +c \\ \frac{1}{c\rho} \frac{dp}{dt} + \frac{dv}{dt} + \frac{2}{\rho R} \tau = 0 \end{cases} \quad (8.1)$$

$$C^- : \begin{cases} \frac{dx}{dt} = -c \\ -\frac{1}{c\rho} \frac{dp}{dt} + \frac{dv}{dt} + \frac{2}{\rho R} \tau = 0 \end{cases} \quad (8.2)$$

where c —pressure wave speed, ρ —liquid density, p —pressure, v —liquid velocity, R —pipe inner radius, τ —wall shear stress.

Above two equations (Eqs. 8.1 and 8.2) are solved with the use of finite differences [24]. The pressure and mean cross-sectional velocity solutions are:

$$p_X = \frac{1}{2} \left[(p_A + p_B) + c\rho(v_A - v_B) + \frac{2c\Delta t}{R} (\tau_B - \tau_A) \right] \quad (8.3)$$

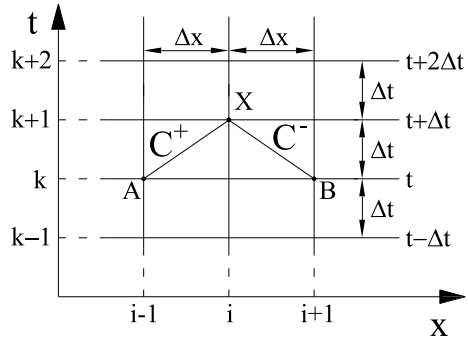
$$v_X = \frac{1}{2} \left[(v_A + v_B) + \frac{1}{c\rho} (p_A - p_B) - \frac{2\Delta t}{\rho R} (\tau_A + \tau_B) \right] \quad (8.4)$$

where: Δt —numerical time step.

The subscripts X , A , and B indicate the computational points on a characteristic grid—see Fig. 8.1. The wall shear stress is calculated from equation [9, 10]:

$$\tau = \tau_q + \tau_u = \frac{f\rho v|v|}{8} + \frac{2\mu}{R} \int_0^t w(t-u) \cdot \frac{\partial v(u)}{\partial t} du \quad (8.5)$$

Fig. 8.1 Rectangular grid of characteristics



where: f —Darcy-Weisbach friction factor, μ —dynamic viscosity of liquid, $w(t)$ —dimensionless weighting function.

The unsteady component of wall shear stress τ_u in Eq. 8.5 is calculated with use of the recently developed effective solution of the above convolutional integral [15]:

$$\tau_{u,(t+\Delta t)} = \frac{2\mu}{R} \sum_{i=1}^3 \underbrace{[A_i y_{i,(t)} + \eta B_i [v_{(t+\Delta t)} - v_{(t)}] + C_i [1 - \eta] [v_{(t)} - v_{(t-\Delta t)}]]}_{y_{i,(t+\Delta t)}} \tag{8.6}$$

The above new approach eliminates the error noticed by Vardy and Brown [20]. Coefficients A_i , B_i , C_i and the weighting function correction factor η is calculated from the following formulas:

$$\eta = \frac{\int_0^{\Delta \hat{t}} w_c(u) du}{\int_0^{\Delta \hat{t}} w_e(u) du}; A_i = e^{-n_i \Delta \hat{t}}; B_i = \frac{m_i}{n_i \Delta \hat{t}} [1 - A_i]; C_i = A_i B_i \tag{8.7}$$

In the above equation $w_c(u)$ is a classical laminar weighting function (developed by Zielke [9, 10]), and $w_e(u)$ is the computationally effective approximate form of the weighting function, written as a sum of only three exponential terms:

$$w_e = \sum_{i=1}^3 m_i e^{-n_i \hat{t}} \tag{8.8}$$

As we are using only three exponential terms, the coefficients m_i and n_i are filtered. Their values are a function of the used numerical grid; strictly speaking, they are numerically time step dependent (Δt)—see [25] for details.

8.3 Comparative Study

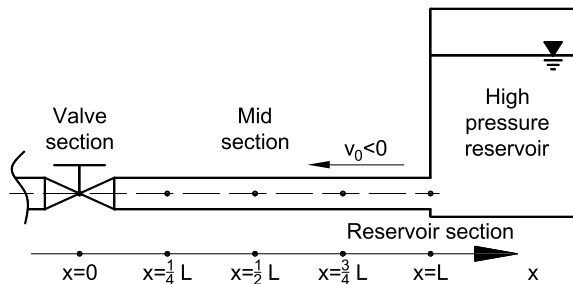
All comparisons presented in this paper are for a single pipeline which represents a simplified reservoir-pipe-valve system RPVS (Fig. 8.2). Considering such an elementary system and assuming the sudden valve close scenario (no additional reflected waves), enables the analysis of the influence of the most important accompanying phenomena: unsteady friction, cavitation, retarded strain (in plastic pipes), and fluid-structure interaction (FSI). In this work, only the effect of the unsteady hydraulic resistance that occurs in laminar flows through metal pipes is studied. We hope that a thorough understanding of the nature of the resistance and the new ways of modeling it discussed in this paper will enable an analytical turbulent flow solution to be found in the near future. An interesting solution recently proposed by Garcia-Alvarino [26, 27] could be useful for this matter. All discussed analytical solutions in the prequel paper [21] were presented in the simplest way as possible form. Earlier attempts in simplifying the original analytical solutions can be found in the works [28, 29].

Analytically calculated results (quasi-steady Rich A-QS; unsteady: Mei-Jing A-MJ and Muto-Takahashi A-MT) will be compared with MOC results NUM, and in the pressure case also with experimental results EXP. In order to make comparisons at the five characteristic cross-sections of the tested system ($x = 0$; $x = 0.25L$; $x = 0.5L$; $x = 0.75L$ and $x = L$; $L = \text{pipe length}$), it is necessary to meet the following condition concerning the discretization of the analyzed pipe along its length:

$$N = 4q \tag{8.9}$$

where: N is a number of reaches and $q = 1,2...n$. The division of the pipe in our study was not accidental. To fulfill the computational compliance criteria [30] it is suggested that $q \geq 4$. For all comparisons in this paper $q = 10$, which gives $N = 40$. The number of nodal points is then $i_t = N + 1 = 41$. The nodal point represents a characteristic cross-section in which the dynamical velocity and wall shear stress histories will be analyzed:

Fig. 8.2
Reservoir-pipe-valve system



$$\begin{cases} x = 0i = 0q + 1 \\ x = 0.25Li = 1q + 1 \\ x = 0.5Li = 2q + 1 \\ x = 0.75Li = 3q + 1 \\ x = Li = 4q + 1 \end{cases} \quad (8.10)$$

Consequently for $q = 10$; $i_{x=0} = 1$; $i_{x=0.25L} = 11$; $i_{x=0.5L} = 21$; $i_{x=0.75L} = 31$ and $i_{x=L} = 41$.

8.3.1 Simulation of Pressure Pulsations

The pressure simulations are treated today as the most important ones when a transient flow is being analyzed. This is related to the fact that pressure is a parameter that can be recorded experimentally with high accuracy. In this subsection a comparison of experimental results with the analytical ones obtained by using the part I paper equations is presented [21]. Additionally, we will compare the simulation results received with use of the numerical model described in subsection 8.2. For our comparison two experimental results of transient laminar pipe flow (Reynolds number $Re_0 < 2320$) were selected. The experiments were conducted by Bergant et al. [31] and Adamkowski and Lewandowski [32]. The initial simulation data needed to perform comparisons are collected in Table 8.1.

Typically several authors compare pressure pulsations at the valve-cross-section. This approach is governed by the fact that at this cross-section, the increased pressure lasts for the longest time, to be exact a half of water hammer period ($4L/c$). At the remaining cross-sections, the pressure of the same peak of the amplitude is kept for a shorter time. Naturally, the duration of the increased pressure is shorter toward the

Table 8.1 Data of the experimental cases

Parameter	Bergant et al.	Adamkowski and Lewandowski
L [m]	37.23	98.11
R [m]	0.01105	0.008
ν [m ² /s]	1.13×10^{-6}	9.5×10^{-7}
c [m/s]	1302	1308
p_R [Pa]	4.15×10^5	1.265×10^6
v_0 [m/s]	0.1	0.066
ρ [kg/m ³]	999.1	997.65
Wh [-]	2.65×10^{-4}	0.0011
Re [-]	1956	1112

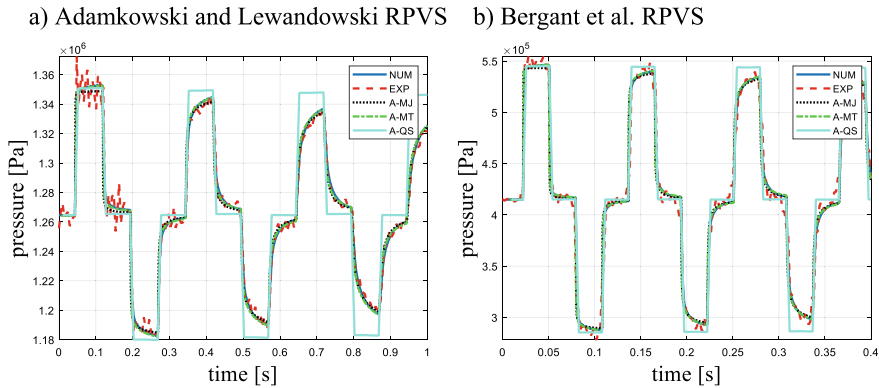


Fig. 8.3 Analytical versus numerical and experimental pressure results—at midpoint section of RPVS

reservoir. The comparisons made in another paper [29] concerned only the cross-section at the valve, therefore, in order to further confirm the effectiveness of the presented analytical solutions presented in the first part of this work, results of test runs are presented at the midpoint cross-section (Fig. 8.3). At this section, the elevated pressure is maintained for half the time of that at the valve section (exactly during $\frac{1}{4}$ of the full water hammer period). Results of comparisons at the midpoint of two exemplary experimental RPVS are presented in Fig. 8.3.

The performed comparative simulations of pressure pulsations at the midpoint section of the RPVS show that:

- for relatively small values of water hammer number $Wh < 0.01$, the differences between the numerical simulation NUM results and calculated with help of analytical models A-MJ and A-MT are small. It can be seen from Figs. 8.3a and b that the A-MJ model simulates the pressure values at the first amplitudes slightly lower than those obtained with the A-MT model;
- both analytical models taking into account the unsteady nature of hydraulic resistance (A-MJ and A-MT) as well the numerical solution reflect the real shape and damping speed of the modeled pressure waveforms;
- the results obtained with the quasi-steady friction model do not reflect the experimental pressure histories;
- it is advisable to analyze not only the initial water hammer period (first amplitude) but also the later phase. The discrepancies between the models and the experimental results are revealed depending on the value of the water hammer number Wh also in the later phase of the transient event;
- analytical models and a numerical solution based on the method of characteristics are highly effective. Therefore, with the help of these solutions, it is possible to analyze pressure changes occurring at any cross-section of the pipeline.

Table 8.2 Data of the numerical cases

WH	ν [m ² /s]	v_0 [m/s]
0.001	1×10^{-6}	-0.05
0.01	1×10^{-5}	-0.5
0.1	1×10^{-4}	-5

Other: $L = 100$ [m]; $R = 0.01$ [m]; $c = 1000$ [m/s], $\rho = 1000$ [kg/m³]; $p_R = 1 \cdot 10^8$ [Pa]; $Re = 1000$ [-]

The models that were used for research presented in this subsection are available in the literature, however, for the purposes of this work the formulas have been maximally simplified and unified. Their final forms are depended on the water hammer number Wh. Although the presented comparisons did not show problems with the quality of matching the results calculated with the aid of the A-MT or A-MJ analytical models with the experimental results, such problems are noticeable in tests performed for large values of dimensionless water hammer number $Wh > 0.1$. One can read more about these problems in the recent paper [29].

8.3.2 Simulation of Velocity and Wall Shear Stress Pulsations

This subsection presents the results of the comparisons of the velocity waveforms (averaged value at the pipe cross-section) and the wall shear stresses occurring on the conduit wall for different values of the dimensionless water hammer number Wh. In the present work, the results for the following three values of the Wh number were compared: 0.1, 0.01, and 0.001. Appropriate water hammer number values were obtained by modifying the liquid kinematic viscosity value. The value of $Wh = 0.001$ in tested R-P-V system corresponds to the flow of water, $Wh = 0.01$ to the flow of water-oil emulsion, and $Wh = 0.1$ to the flow of oil. Other data of the analyzed R-P-V system, which are necessary for the simulation, are presented in Table 8.2.

Pressure is not the only parameter that should be analyzed during water hammer event, the remaining ones are the flow velocity and the wall shear stress, which is closely related to the friction force. Velocity is the basic parameter while wall shear stress is a dependent quantity which is a function of velocity (Eqs. 8.5 and 8.6). In the new analytical studies in this section, the explicit dependence of wall shear stress and velocity occurs only in the Laplace domain. The final form of the analytical formula for τ in the time-domain is, like the solution for pressure and velocity, a function of: (1) water hammer number Wh, (2) position x , and (3) time t .

During the preparation of this work, simulation tests were carried out at five cross-sections defined by Eq. (8.10). Key results will be presented and discussed, i.e., at cross-sections $x = L$ and $x = 0.5L$ (Figs. 8.4, 8.5, 8.6, 8.7, 8.8, 8.9).

Unfortunately, as shown by the comparisons carried out (Figs. 8.4a and 8.7a), the final velocity determined with the help of A-MT model does not always approach

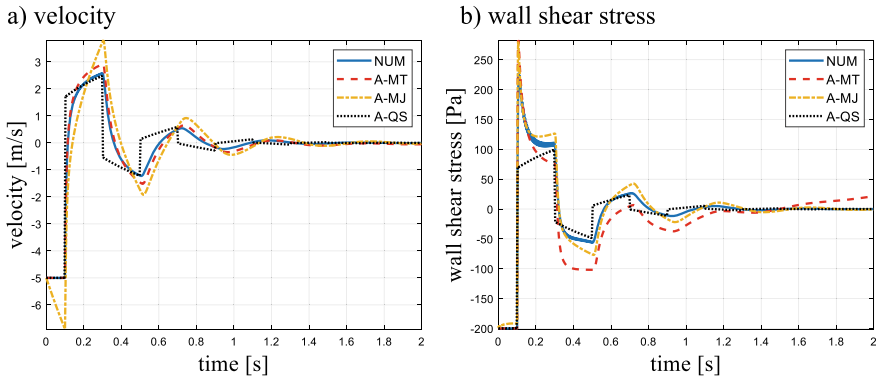


Fig. 8.4 Analytical versus numerical results for $Wh = 0.1$ for $x = L$ (reservoir section)

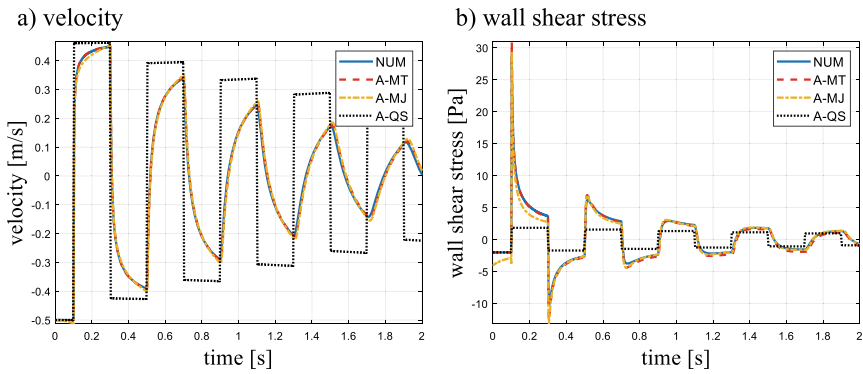


Fig. 8.5 Analytical versus numerical results for $Wh = 0.01$ for $x = L$ (reservoir section)

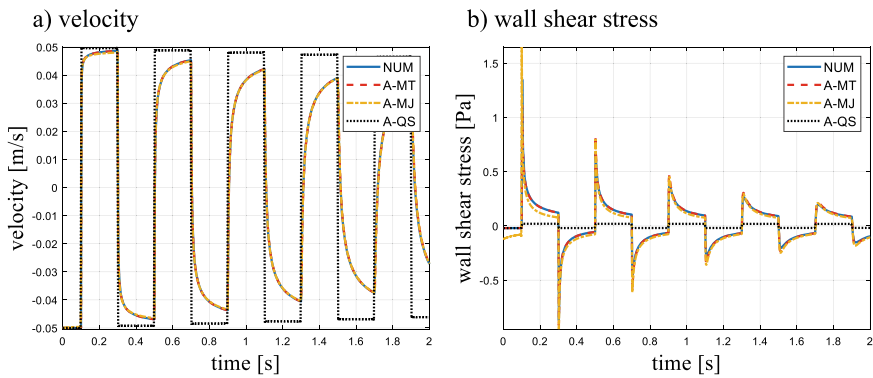


Fig. 8.6 Analytical versus numerical results for $Wh = 0.001$ for $x = L$ (reservoir section)

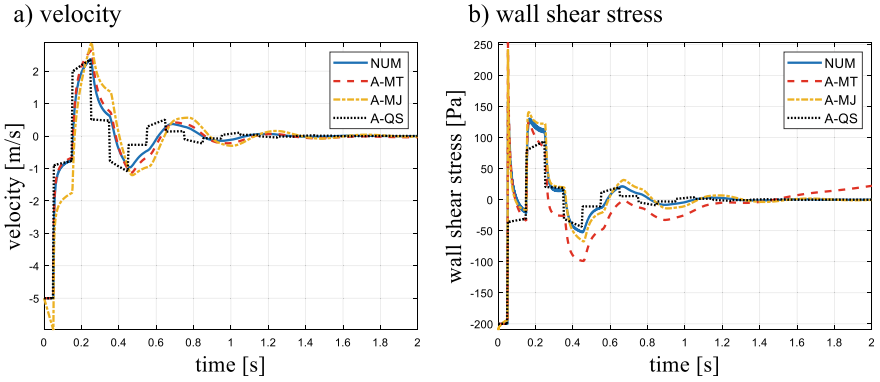


Fig. 8.7 Analytical versus numerical results for $Wh = 0.1$ for $x = 0.5L$ (midpoint section)

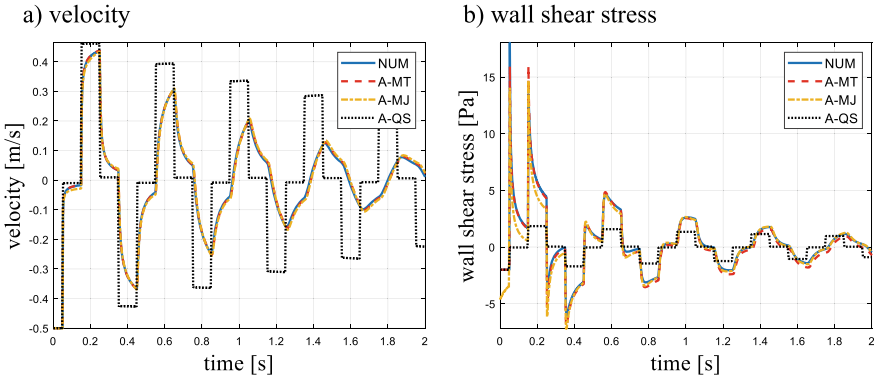


Fig. 8.8 Analytical versus Numerical results for $Wh = 0.01$ for $x = 0.5L$ (midpoint section)

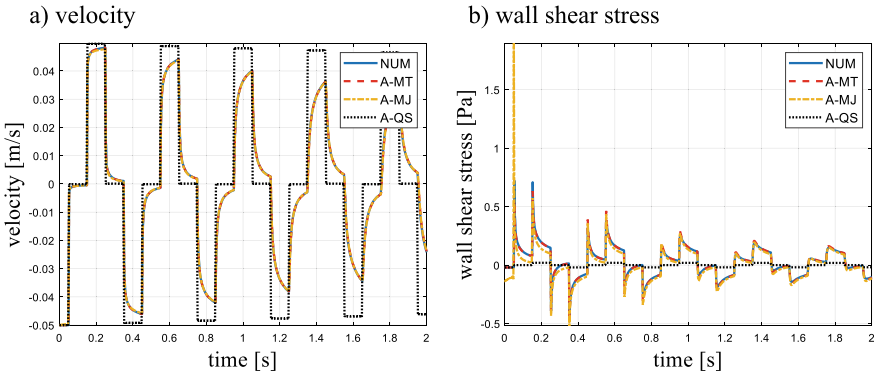


Fig. 8.9 Analytical versus numerical results for $Wh = 0.001$ for $x = 0.5L$ (midpoint section)

zero. This indicates an error in the model, which is especially visible for higher values of the water hammer number Wh . For the numbers $Wh > 0.1$, this error systematically increases for the A-MT model with increase of Wh value. Within the same range of Wh numbers, the A-MJ model simulates the final asymptotic velocity values correctly (i.e., they tend to zero over time). However, in A-MJ model, significant errors are visible at the initial phase of the water hammer event, which prevents its practical use in the range of relatively large values of $Wh > 0.05$.

Figure 8.4b evidently confirms that the quasi-steady hydraulic resistance model is responsible for a significant simulation error in the initial phase of the water hammer event. With its use, the wall shear stress value increases from 60 to 100 MPa in the initial impact period, which is evident from the analytical models taking into account the unsteady nature of friction (A-MJ and A-MT) and the numerical solution NUM that the wall shear stress at the pipe wall increases abruptly to values exceeding 200 MPa, and then gradually drops to the value about 100 MPa ($t = 0.3$ s) in the early water hammer phase. This graph shows that for such a large value of the number $Wh = 0.1$, the A-MT model cannot cope with the simulation of the further period of the wall shear stress from time $t = 0.2$ s. Additionally, from the time $t > 1.4$ s, the value modeled with the use of this model begins to systematically increase. In connection with the above, it should be emphasized that this model can be applied only to the corresponding value of dimensionless times $\hat{t} = \frac{v}{R\hat{c}}t$. The research showed that this time can be expressed as a function of the water hammer number.

Figure 8.5a depicts the results of velocity changes for $Wh = 0.01$. It shows that the analytical A-MT solution enables velocity calculation with very good consistency over the entire time range. The differences between the analytical and numerical results are practically imperceptible for the first three amplitudes. Both analytical models (A-MT and A-MJ) produced a slight time delay of velocity and wall shear histories.

Figure 8.5b shows that the A-MT model simulates the wall shear stresses at the first two amplitudes, i.e., at the initial period of the water hammer, with sufficient compliance. However, starting from the third amplitude, the A-MJ model begins to simulate these dynamic waveforms better than A-MT. This is manifested in a significantly closer results obtained with use of A-MJ model to the numerical results with increasing time. At the peaks of the first wall shear stress amplitudes, the results obtained by the appropriate models taking into account unsteady friction were as follows: NUM 28.8 Pa, A-MJ 29.3 Pa, and A-MT 30.9 Pa. However, the initial stress value of the A-MJ model (time $0 < t < 0.1$ s) as well as the stress drop after the first peak ($t \approx 0.3$ s) significantly differ from the simulation results obtained with the numerical model. The above indicates that this model incorrectly simulates the initial period of water hammer. Until the increased pressure wave reaches this cross-section, the stress should be as high as it was in the steady motion, i.e., before the occurrence of the transient state.

Figure 8.6a shows that for the water hammer number $Wh < 0.001$, both analyzed analytical models are strictly consistent with the numerical results. Interestingly, the A-MJ model, which for the number $Wh = 0.01$ and $Wh = 0.1$ in the initial phase of the impact (before the arrival of the first pressure wave) modeled increase in flow

velocity, in this case simulating its slight decrease in the same period, i.e., for a time $t < (L/c)$ s. Figure 8.6b shows the comparisons of wall shear stress results received for $Wh = 0.001$. It shows that the maximum wall shear stress at the first stress amplitude, occurring just after the arrival of the increased pressure wave, estimated with the analyzed models had the following values: NUM 1.35 Pa, A-MJ 1.65 Pa, and A-MT 1.11 Pa. The A-MT model, more precisely than the A-MJ model, simulates in this case the wall shear stress drop from the instantaneous peaks for all analyzed amplitudes in initial period of water hammer lasting for two seconds. Starting from the fifth amplitude, the results simulated with the A-MT and A-MJ models remain convergent to each other.

Figure 8.7 compares analytical and numerical results at the pipe midpoint for the water hammer number $Wh = 0.1$. The only significant difference between the analytical and numerical results is the peak velocity value at the first amplitude. The fit of the A-MJ model is definitely worse, as evident by the significant deviation of the results during the first velocity amplitude. It can also be seen (Fig. 8.7a) that the quasi-steady model A-QS has problems with maintaining the phase compliance. From Fig. 8.7b the interesting behavior of the wall shear stress at the midpoint section is worth noting. After reaching the pressure wave, the stress increases abruptly, and then it relaxes until time $t \approx 0.15$ s, at which point the pressure wave reflected from the pressure reservoir reaches this cross-section again (a second stress amplitude shows up). Figure 8.7b also shows that the A-MJ model with acceptable compliance simulated the wall shear stresses (except for the initial impact period).

Figures 8.8a and 8.9a show the simulation results for dynamic velocity runs when $Wh = 0.01$ and $Wh = 0.001$. For $Wh = 0.01$ it can be seen (Fig. 8.8a) that there are slight discrepancies in the first amplitude between the numerical solution NUM and the A-MJ solution. However, when $Wh = 0.001$, these differences are imperceptible (Fig. 8.9a). It can be seen from Figure 8.8b that for such a value of Wh , two peaks of shear stress appear during the first impact period. At the first peak the results are as follows: NUM 18 Pa, A-MT 16 Pa, and A-MJ 14 Pa and at the second one A-MT 16 Pa, A-MJ 14.7 Pa, and NUM 13.5 Pa. Thus, it can be seen that in the numerical model, a decrease in stress was observed at successive increments whereas the results from the analytical model did not indicate this decrease. Moreover, in the A-MJ model, there was even a slight increase in stress. In the further phase, it is noticed that the A-MT model tends to values other than zero, exactly to -0.3 Pa, which again indicates the imperfection of the derived wall shear stress model (for large values of Wh number) [21].

For the wall shear stress history for $Wh = 0.001$ (Fig. 8.9b) the A-MT model performs well in the initial phase of the water hammer event. The model is better than the A-MJ model, which again incorrectly models the initial value, which should be -0.02 Pa.

During the preparation of this work, simulation tests were carried out also at other cross-sections too ($x = 0$; $x = 0.25L$ and $x = 0.75L$). The presentation of these results is beyond the space limitation of this paper.

8.4 Conclusions

The paper compares the known and newly developed analytical solutions supporting the analysis of unsteady pipe flows in pressurized lines, which were triggered by the instantaneous closure of the valve in a simplified reservoir-pipeline-valve system. The conducted comparisons showed:

- significant influence of unsteady hydraulic resistance on the modeling of pressure, velocity, and wall shear stress waveforms;
- disadvantages of analytical models which, due to the simplifying assumptions, do not comply with the basic system of equations for a wide range of water hammer numbers Wh ;
- the need for further modification of shear stress Muto and Takahashi model (A-MT) for high frequencies. In the next stage of research on this model, the influence of the complete viscosity function $M(s)^2$, for which the inverse Laplace transform was found during the finalization of this work, will be investigated:

$$\mathcal{L}^{-1} \left\{ M(s)^2 = \frac{I_0\left(\sqrt{\frac{s}{\nu}}R\right)}{I_2\left(\sqrt{\frac{s}{\nu}}R\right)} \right\} = \delta(t) + 8\frac{\nu}{R^2} + 4\frac{\nu}{R^2} \sum_{i=1}^{\infty} \exp\left(-\eta_i^2 \frac{\nu}{R^2} t\right) \quad (8.11)$$

where: η_i are consecutive zeros of the Bessel function $J_2(\eta_i)$;

- dimensionless time $\hat{t} = 1.4[-]$ after which the novel model of wall shear stresses A-MT is not anymore applicable. The knowledge of such a dimensionless time allows for the determination of the critical real-time $t \leq \hat{t} \frac{R^2}{\nu}$ that should not be exceeded during simulation (this time is getting longer with a decrease of the fluid viscosity).
- the remaining test results for dynamic velocity histories as well as dynamic wall shear stress histories (for $x = 0$; $x = 0.25L$ and $x = 0.75L$) are the subject of the extended version of the work.

Acknowledgements Anton Bergant gratefully acknowledges the support of the Slovenian Research Agency (ARRS) conducted through the project L2-1825 and the program P2-0126.

References

1. Grattan-Guinness I, Engelsman S (1982) The manuscripts of Paul Charpi. *Hist Math* 9(1):65–75
2. Fische H, Kaul H (2014) *Mathematik für Physiker Band 2*. Springer Fachmedien Wiesbaden
3. Gray CAM (1953) The analysis of the dissipation of energy in water hammer. *Trans Am Soc Civ Eng* 119:259–274

4. Gray CAM (1954) Analysis of water hammer by characteristics. *Trans Am Soc Civ Eng* 119:1176–1189
5. Ezekial FD, Paynter HM (1957) Computer representation of engineering systems involving fluid transients. *Trans ASME* 79:1840–1850
6. Lister M (1960) The numerical solution of hyperbolic partial differential equations by the method of characteristics. In: Ralston A, Wiley HS (eds) *Mathematical methods for digital computers*, edited by John Wiley & Sons, New York, Chap. 15, pp 165–179
7. Streeter VL, Lai C (1962) Water hammer analysis including fluid friction. *J Hydr Div Am Soc Civ Eng*, May, pp 79–112
8. Streeter VL (1962) Water hammer analysis with nonlinear frictional resistance, hydraulics and fluid mechanics. *Proceedings of the first Australasian conference held at the university of Western Australia*, 6–13 Dec, pp 431–452
9. Zielke W (1966) Frequency-dependent friction in transient pipe flow. *Doctoral Thesis, University of Michigan*
10. Zielke W (1968) Frequency-dependent friction in transient pipe flow. *ASME J Basic Eng* 90:109–115
11. Trikha AK (1975) An efficient method for simulating frequency-dependent friction in transient liquid flow. *J Fluids Eng ASME* 97(1):97–105
12. Kagawa T, Lee I, Kitagawa A, Takenaka T (1983) High speed and accurate computing method of frequency-dependent friction in laminar pipe flow for characteristics method (in Japanese). *Trans Japan Soc Mech Eng Part A* 49(447):2638–2644
13. Schohl GA (1993) Improved approximate method for simulating frequency—dependent friction in transient laminar flow. *J Fluids Eng ASME* 115:420–424
14. Vítkovský J, Stephens M, Bergant A, Lambert M, Simpson A (2004) Efficient and accurate calculation of Zielke and Vardy-Brown unsteady friction in pipe transients. In: *Proceedings of the 9th international conference on pressure surges*. Chester, UK, 24–26 March, pp 405–419
15. Urbanowicz K (2018) Fast and accurate modelling of frictional transient pipe flow. *Z Angew Math Mech* 98(5):802–823
16. Zarzycki Z (1994) A hydraulic resistance of unsteady fluid flow in pipes. Published by Technical University of Szczecin, 516, Szczecin (in Polish)
17. Zarzycki Z (2000) On weighting function for wall shear stress during unsteady turbulent flow. In: *Proceedings of 8th international conference on pressure surges*. BHR Group, Hague, Holland, 39, pp 529–534
18. Vardy AE, Hwang KL, Brown JMB (1993) A weighting function model of transient turbulent pipe friction. *J Hydraul Res* 31(4):533–548
19. Vardy AE, Brown JMB (2003) Transient turbulent friction in smooth pipe flows. *J Sound Vib* 259(5):1011–1036
20. Vardy AE, Brown JMB (2010) Evaluation of unsteady wall shear stress by Zielke’s method. *J Hydraul Eng* 136:453–456
21. Urbanowicz K, Bergant A, Stosiak M, Lubecki M (2022) Analytical solutions of water hammer in metal pipes. Part II—brief theoretical study. Grzegorz Lesiuk et al. (Eds): *Fatigue and Fracture of Materials and Structures*, vol. 24, 978-3-030-97821-1, 522626_1_En, (Chapter 7). Springer
22. Chaudhry MH (2014) *Applied hydraulic transients*. Springer, New York
23. Tijsseling AS, Bergant A (2007) Meshless computation of water hammer, *Scientific Bulletin of the “Politehnica” University of Timișoara. Transactions on Mechanics* 52(66):65–76
24. Wylie EB, Streeter VL (1993) *Fluid transients in systems*. Prentice-Hall Inc., Englewood Cliffs, New Jersey
25. Urbanowicz K (2017) Analytical expressions for effective weighting functions used during simulations of water hammer. *J Theor Appl Mech* 55(3):1029–1040
26. García García FJ (2017) Transient discharge of a pressurised incompressible fluid through a pipe and analytical solution for unsteady turbulent pipe flow, Ph.D. thesis. Higher Polytechnic College-University of a Coruña

27. García García FJ, Alvariño PF (2019) On an analytic solution for general unsteady/transient turbulent pipe flow and starting turbulent flow. *Eur J Mech B Fluids* 74:200–210
28. Urbanowicz K, Firkowski M, Bergant A (2018) Comparing analytical solutions for unsteady laminar pipe flow. In: *Proceedings of 13th international conference pressure surges*. Bordeaux, pp 283–303
29. Urbanowicz K, Jing H, Bergant A, Stosiak M, Lubecki M (2021) Progress in analytical modeling of water hammer. *Proc Fluids Eng Div Summer Meeting FEDSM 2021(August)*:10–12
30. Urbanowicz K (2017) Computational compliance criteria in water hammer modelling. *E3S Web of Conferences*, 19, 03021
31. Bergant A, Simpson AR, Vítkovský J (2001) Developments in unsteady pipe flow friction modelling. *J Hydraul Res* 39(3):249–257
32. Adamkowski A, Lewandowski M (2006) Experimental examination of unsteady friction models for transient pipe flow simulation. *J Fluids Eng* 128:1351–1363

Chapter 9

Experimental and Theoretical Analysis of Hydraulic Cylinder Loads



Marek Lubecki , Michał Stosiak , Michał Banaś , Piotr Stryczek , and Kamil Urbanowicz 

Abstract The use of composite materials in mechanical engineering allows to significantly reduce the weight of elements. However, the process of designing elements made of such materials is more complex than conventional ones and requires a thorough knowledge of the distribution of loads acting on the element. The paper presents experimental research on deformation of a barrel of tie-rod hydraulic cylinder as well as mathematical calculations of axial and circumferential strains. The existence of an axial force so far not included in the calculations of this type of actuator was identified. It has been shown that omitting the axial force when designing a composite barrel may lead to a significant reduction in its strength.

Keywords Classical lamination theory · Strain gauge · CFRP

9.1 Introduction

One of the most common types of drive used in mechanical engineering is hydrostatic drive. The reason is a number of advantages, such as an excellent power-to-weight ratio of the system, the possibility of precise control of receivers and automation, as well as the possibility of almost any arrangement of the system elements on the machine. The actuators in the hydrostatic system can be cylinders or rotary motors. Reciprocating hydraulic cylinders are usually solid components made of metal alloys. The reason is the necessity to ensure stiffness and resistance to working pressure (in standard designs up to 35 MPa).

Composite materials and plastics are increasingly used in many industries to reduce the weight of the structure [1, 2]. Their advantages include a very high strength to weight ratio, the possibility of free shaping of material properties, the ease of

M. Lubecki (✉) · M. Stosiak · M. Banaś · P. Stryczek
Wrocław University of Science and Technology, Wrocław, Poland
e-mail: marek.lubecki@pwr.edu.pl

K. Urbanowicz
West Pomeranian University of Technology, Szczecin, Poland

manufacturing complex shapes and increased resistance to corrosion and electro-magnetic field. Recently, there has been an increase in interest in the development of composite hydraulic cylinders, the operational parameters of which would be similar or better than conventional designs, but their mass would be significantly reduced [3–5]. Designing components from composite materials requires a good knowledge of the distribution of loads acting on the component. Due to the strong anisotropy of the mechanical properties of the material, slight deviations in the direction of the force action may lead to a significant decrease in the strength of the element [6–8]

The paper presents experimental tests of a tie-rod hydraulic cylinder with a steel barrel and compares the results with theoretical calculations obtained with the use of the theory of thick-walled pipes. The obtained results were used for the preliminary design of the composite cylinder, the strength calculations of which were also presented.

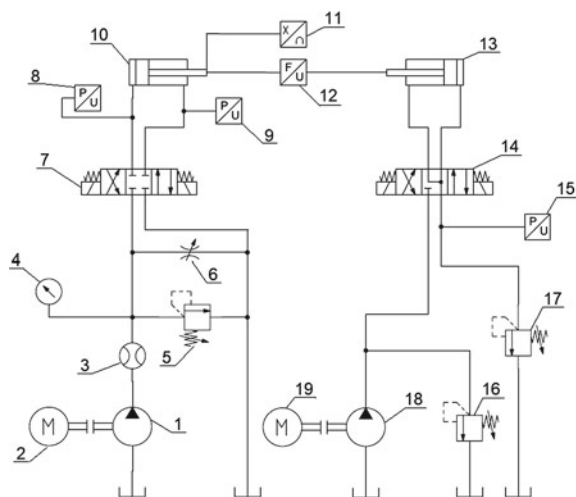
9.2 Materials and Methods

9.2.1 Experimental Research

The barrel of the tested cylinder was made of St 52.3 steel. The inner diameter of the barrel was 40 mm, and the wall thickness was 5 mm. The base and the head were made of PET plastic. Measurements of linear deformations in the axial and circumferential directions were carried out using strain gauges. The diagram of the hydraulic system of the test stand is shown in Fig. 9.1.

During the test, the pressures in the cylinder chambers and the axial force loading the piston rod were also recorded. The value of pressure and temperature of the

Fig. 9.1 Hydraulic testing system: 1, 18—pump; 2, 19—electric motor; 3—flow metre; 4—pressure gauge; 5, 16, 17—pressure relief valve; 7, 14—directional control valve; 8, 9, 15—pressure sensor; 10—tested actuator; 11—position sensor; 12—force sensor; 13—loading cylinder



working fluid was kept at the constant level of 30 °C. This allowed to determine the state of stresses in the steel barrel of the cylinder and contributed to the parameterization of the numerical model of the element. This data was then used to design and model a composite barrel using classical lamination theory. The values of stresses and strains were determined in the global coordinate system of the laminate and in its individual layers. The aim of the work is to be able to reliably design and model a barrel made of a composite material intended for a hydraulic cylinder operating in commonly encountered conditions, i.e. at operating pressures not lower than 16 MPa.

9.2.2 Mathematical Modelling

In order to calculate the axial deformations ε_x and circumferential deformations ε_ϕ of a steel barrel, the relationships known in the literature were used for thick-walled pipes with open ends loaded with internal pressure [9, 10]

$$\varepsilon_\phi = \frac{1}{E} \left[A(1 - \nu) + \frac{B}{r_i^2}(1 + \nu) \right] \tag{9.1}$$

$$\varepsilon_x = -\frac{2\nu A}{E} \tag{9.2}$$

where

$$A = \frac{p_i r_i^2}{r_e^2 - r_i^2}, \quad B = \frac{p_i r_i^2 r_e^2}{r_e^2 - r_i^2}$$

p_i is internal pressure, r_i is internal radius, r_e is external radius, E is Young’s modulus and ν is Poisson’s ratio.

Composite barrel strength calculations were performed with the use of the classical lamination theory. Assumptions have been made that the laminate consists of perfectly bonded plies, that the deformations in the laminate are continuous (no slip occurs) and that the parallel planes before deformation remain parallel after deformation. It was also assumed that because composite cylinders are thin-walled, radial stresses are negligible. The relationship between stress and strain for a single ply can be written as follows [11]:

$$\begin{bmatrix} \sigma_x \\ \sigma_\phi \\ \tau_{x\phi} \end{bmatrix} = [Q] \begin{bmatrix} \varepsilon_x^0 \\ \varepsilon_\phi^0 \\ \gamma_{x\phi}^0 \end{bmatrix} + z [Q] \begin{bmatrix} k_x \\ k_\phi \\ k_{x\phi} \end{bmatrix} \tag{9.3}$$

where $\varepsilon_x^0, \varepsilon_\phi^0, \gamma_{x\phi}^0$ is midplane strains, z is distance from the midplane, $k_x, k_\phi, k_{x\phi}$ is curvatures, $[\bar{Q}]$ is reduced, transformed stiffness matrix, created by rotating the stiffness matrix of the ply by an angle equal to the angle of the fibres arrangement in the layer.

Laminate deformation depends on the applied loads, which can be summarized as follows:

$$\begin{bmatrix} N \\ M \end{bmatrix} = \begin{bmatrix} A & B \\ B & D \end{bmatrix} \begin{bmatrix} \varepsilon^0 \\ k \end{bmatrix} \quad (9.4)$$

where $[N]$ is forces per unit length, $[M]$ is moments per unit length, $[A]$ is extensional stiffness matrix, $[B]$ is coupling stiffness matrix, $[D]$ is bending stiffness matrix, $[\varepsilon^0]$ is midplane strains matrix, $[k]$ is curvatures matrix.

For an internal pressure load only, the matrices $[N]$ and $[k]$ are as follows:

$$\begin{bmatrix} N_x \\ N_\phi \\ N_{x\phi} \end{bmatrix} = \begin{bmatrix} 0 \\ p_i r_i \\ 0 \end{bmatrix} \quad (9.5)$$

$$\begin{bmatrix} k_x \\ k_\phi \\ k_{x\phi} \end{bmatrix} = \begin{bmatrix} 0 \\ -\frac{\varepsilon_x^0}{r_i} \\ -\frac{\gamma_{x\phi}^0}{r_i} \end{bmatrix} \quad (9.6)$$

In order to assess the strength of the element, the Tsai–Hill criterion was used [12]:

$$\left(\frac{\sigma_1}{(\sigma_1^T)_{ult}} \right)^2 - \left(\frac{\sigma_1 \sigma_2}{(\sigma_1^T)_{ult}^2} \right) + \left(\frac{\sigma_2}{(\sigma_2^T)_{ult}} \right)^2 + \left(\frac{\tau_{12}}{(\tau_{12})_{ult}} \right)^2 = R < 1 \quad (9.7)$$

where σ_1 is stress along the fibres in the ply, σ_2 is stress perpendicular to the fibres, τ_{12} is in-plane shear stress and R is strength ratio.

9.3 Results

Figure 9.2 shows the results of experimental tests of a steel barrel. The points mark the results obtained from the measurements, and the continuous line marks the strains resulting from calculations carried out in accordance with the theory of thick-walled pipes. It can be noticed that while the values of the circumferential deformations both obtained experimentally and computationally agree, the actual values of the axial strains are smaller in terms of values than it would appear from the theoretical

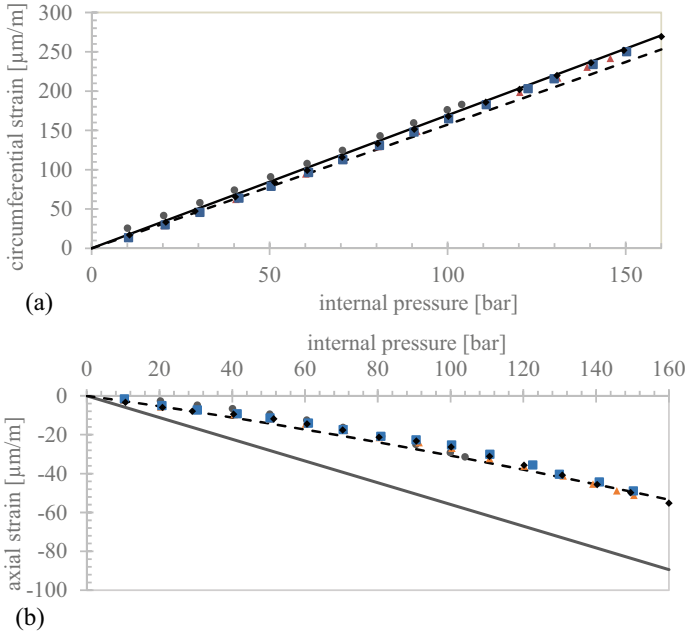


Fig. 9.2 Results of experimental studies on strains of a steel barrel (scatter plot), results of theoretical calculations under internal pressure load (solid line) and under internal pressure and axial force (dashed line): **a** circumferential strain, **b** axial strain

relations. This may be due to the additional axial force acting on the element. It was not possible to measure this force directly, so it was determined by adjusting the model parameters. In this case, the axial force depended nonlinearly on the internal pressure acting on the element. This force was taken into account in the mathematical model, and the results of the calculations are shown in Fig. 9.2 by a dashed line.

Acquired results were used to carry out the strength calculations of the composite cylinder the material properties of which are presented in Table 9.1. Table 9.2 shows the values of the strength ratio R for a hoop wound carbon-epoxy pipe with wall thickness of 0.6 mm, loaded in the first case only with internal pressure of 16 MPa. In the second case, the load distribution took into account the axial force identified in the experimental tests value of which, for 16 MPa of internal pressure, was 7 kN. As can be seen in the first case, the ratio R is well below 1, which corresponds to no damage to the element. However, taking into account the axial force causes the ratio R to increase to 1.69, which is synonymous with the failure of the element.

Table 9.1 Material parameters of a carbon/epoxy composites used for calculations

Parameter	E_1 [GPa]	E_2 [GPa]	ν_{12}	G_{12} [MPa]	$\sigma_1^{T_{ult}}$ [MPa]	$\sigma_2^{T_{ult}}$ [MPa]	$\sigma_2^{C_{ult}}$ [MPa]	$\sigma_2^{T_{ult}}$ [MPa]
Value	141	13.4	0.3	3.9	3265	71	71	37

Table 9.2 Value of the strength ratio R when the composite barrel is loaded with internal pressure and additional axial force

	Pure internal pressure	Internal pressure with axial force
Strength ratio R	0.028	1.69

9.4 Conclusion

The paper presents the results of experimental research and mathematical calculations of strains of a steel barrel of a tie-rod hydraulic cylinder. The experimental results have shown the existence of an axial force that has so far not been taken into account in the strength calculations of this type of actuator. In steel structures, it is indeed possible to omit it. However, as shown, not taking it into account when designing a composite barrel can lead to a significant reduction in its strength. The study shows that the knowledge of the exact distribution of loads acting on the cylinder barrel of a composite cylinder is necessary to ensure the appropriate strength of the element.

References

1. Lubecki M, Stosiak M, Gazińska M (2021) Numerical and experimental analysis of the base of a composite hydraulic cylinder made of PET. In: Lecture notes in mechanical engineering. Springer Science and Business Media Deutschland GmbH, pp 396–405
2. Stryczek P, Przystupa F, Banas M (2018) Research on series of hydraulic cylinders made of plastics. In: 2018 global fluid power society PhD Symposium (GFPS). IEEE, pp 1–7
3. Solazzi L (2020) Design and experimental tests on hydraulic actuator made of composite material. *Compos Struct* 232:111544. <https://doi.org/10.1016/j.compstruct.2019.111544>
4. Solazzi L (2021) Stress variability in multilayer composite hydraulic cylinder. *Compos Struct* 259:113249. <https://doi.org/10.1016/j.compstruct.2020.113249>
5. Mantovani S (2020) Feasibility analysis of a double-acting composite cylinder in high-pressure loading conditions for fluid power applications. *Appl Sci* 10:826. <https://doi.org/10.3390/app10030826>
6. Kaw AK (2005) *Mechanics of composite materials*. CRC Press, Boca Raton
7. Reddy JN (2003) *Mechanics of laminated composite plates and shells*. CRC Press, Boca Raton
8. Dato MH (1999) *Mechanics of fibrous composites*
9. Annaratone D (2007) *Pressure vessel design*
10. Vullo V (2014) *Circular cylinders and pressure vessels*. Springer International Publishing, Cham
11. Rosenow MWK (1984) Wind angle effects in glass fibre-reinforced polyester filament wound pipes. *Composites* 15:144–152. [https://doi.org/10.1016/0010-4361\(84\)90727-4](https://doi.org/10.1016/0010-4361(84)90727-4)
12. Kassapoglou C (2013) *Design and analysis of composite structures: with applications to aerospace structures*, second edition

Chapter 10

A New Anti-fatigue Design Method for Welded Structures Based on Stiffness Coordination Strategy and Its Application



Chunliang Niu, Suming Xie, and Tao Zhang

Abstract In order to effectively improve the anti-fatigue performance of welded structures in the design stage, a new anti-fatigue design method of welded structures oriented to stiffness coordination strategy is proposed, based on the structural stress theory which can effectively identify the stress concentration, which is a three-stage anti-fatigue design method of welded structures, namely, stress concentration identification, stress concentration analysis and stress concentration mitigation. The effectiveness of the stiffness coordination strategy in the design of welded joints is verified by the test of welded joints in IIW. The application of the method in the design of engineering welding parts verifies the engineering significance of the method. This study has reference value for the optimization design of load-bearing joint welding structure and the improvement of fatigue resistance.

Keywords Complex welding structure · Stress concentration · Stiffness coordination · Structural stress method · Anti-fatigue design

10.1 Introduction

BS7608 points out that the key to determining the fatigue performance of welded structures is stress concentration, which is caused by sudden change of stiffness [1]. It is difficult to predict the fatigue life in the design stage. Therefore, the anti-fatigue design of welded structures is still mainly based on various fatigue tests, but in the design stage of product development, there is often no fatigue test carrier available. The welding structure design concept of engineering and technical personnel is still

C. Niu · S. Xie (✉)

School of Locomotive and Rolling Stock Engineering, Dalian Jiaotong University, Dalian 116028, China

e-mail: sumingxie@163.com

C. Niu

School of Mechanical and Power Engineering, Dalian Ocean University, Dalian 116023, China

T. Zhang

National Innovation Center of High Speed Train, Qingdao 266109, China

based on static strength, lacking forward-looking anti-fatigue design ideas [2, 3]. Therefore, it has important engineering application value to study the anti-fatigue method of welded structure in the design stage.

10.2 A New Method of Three-Stage Anti-fatigue Design and Numerical Analysis of Core Parameters

10.2.1 Mechanical Explanation of Stress Concentration

The influence of geometric details of different joints on fatigue life is clearly reflected in BS7608. Due to different joint details, the corresponding S–N curves are also different. As shown in Fig. 10.1a, the corresponding S–N curves are also different due to different geometric details of butt joint welds.

The mechanical explanation of stress concentration is based on the steel butt joint with reinforcement. The joint geometry is shown in Fig. 10.1b, and the axial tensile load is applied to the joint. The simulation results show that the reinforcement leads to a sharp increase of stress in the local area near the weld, while in the distance,

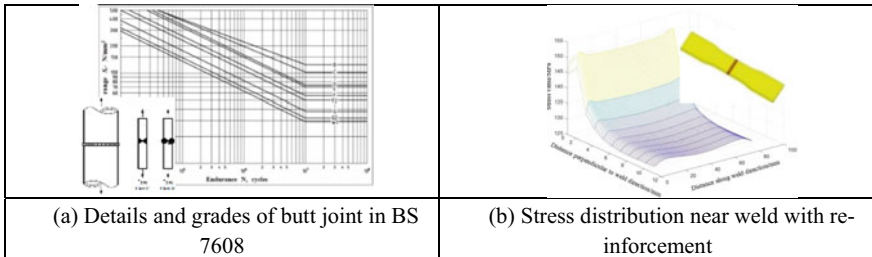


Fig. 10.1 Stress concentration analysis of welds

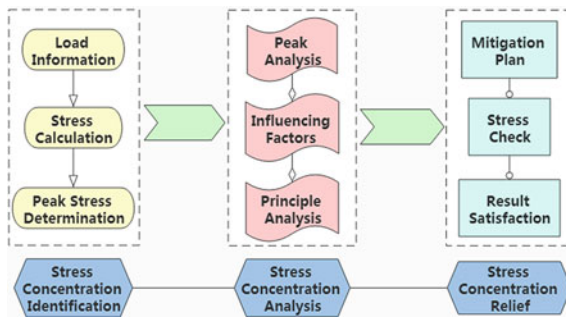


Fig. 10.2 A new anti-fatigue design method for three-stage complex welded joints

the stress decreases rapidly and tends to be uniform. The local increase of stress caused by the change of weld details is called stress concentration. The ratio of the maximum stress σ_{max} near the weld to the average stress σ on the same section is expressed by a , as shown in Formula 10.1.

$$a = \sigma_{max}/\sigma \tag{10.1}$$

where: a is called the theoretical stress concentration factor, which reflects the degree of stress concentration and is a factor greater than 1.

At the location of stress concentration, the peak stress is related to geometry, weld arrangement, and loading mode. However, stress concentration is only the representation of the problem, and the fundamental reason is the sudden change of structural stiffness.

10.2.2 The Execution Flow of Fatigue Resistance Design Method

10.2.3 Numerical Analysis of Structural Stress

Suppose that the weld is divided into n units, and the node number is from 1 to n , as shown in Fig. 10.3. Elements along the weld toe (such as (1), (2) ...) are used to extract nodal forces from the finite element solution in the global coordinate system (x, y, z) . Through coordinate transformation, the nodal force vector of each element is transformed to the local coordinate system (x', y', z') , where the local coordinate axis x' is the direction along the welding line [4].

The distance of each node on the welding line is l_1 to l_{n-1} . According to the force balance equation, the corresponding relationship between the nodal force F_{yn} and the line force f_{yn} can be obtained.

$$\begin{aligned} \{F_{y1}, F_{y2} \dots F_{yn}\}^T &= L \{f_{y1}, f_{y2} \dots f_{yn}\}^T, \{f_{y1}, f_{y2} \dots f_{yn}\}^T \\ &= L^{-1} \{F_{y1}, F_{y2} \dots F_{yn}\}^T \end{aligned} \tag{10.2}$$

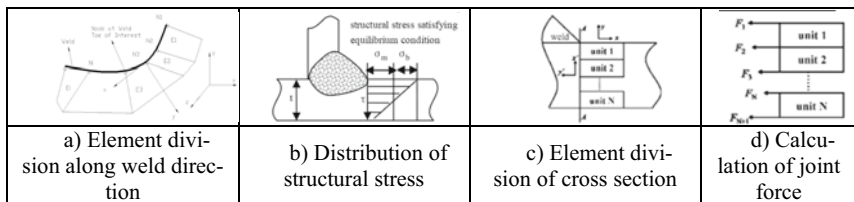


Fig. 10.3 Core idea of weld structure stress calculation

Similarly, the linear moment m_x and joint moment M_x have the same form as the above expression, so that when there are n joints with the same element thickness t , the structural stress σ_n of each node, as well as the force F_{yn} and moment M_{xn} of each node can be expressed in the form of matrix (3): Formula (4) is the general formula for structural stress calculation.

$$\sigma_n = \frac{1}{t} \cdot \mathbf{L}^{-1} \left(\mathbf{F}_{yn} + \frac{6}{t} \cdot \mathbf{M}_{xn} \right) \tag{10.3}$$

10.3 Verification of Welded Joint Fatigue Test with Stiffness Coordination in Standard

This paper studies the fatigue test of steel butt flat weld and analyzes the influence of stiffness coordination at weld joint on fatigue life. IIW standard points out that different undercut levels lead to different fatigue strength grades (FAT grades) of welded joints [5] because the existence of undercut makes the longitudinal tensile stiffness at weld toe inconsistent.

The basis of undercut evaluation in IIW standard is u/t value, that is, the ratio of undercut depth u to plate thickness t , which is regarded as a limited range in fatigue strength table of classified components.

10.3.1 Specimen Preparation and Fatigue Test

The test piece adopts the double-sided forming welding process of three layers, three passes, and single face groove, forming the undercut defect at the junction of the cover layer and the base metal, as shown in Fig. 10.4a. Q345E steel is used as the test piece, and the size and welding of the test piece are shown in Fig. 10.4b.

According to GB/T 13,816 “Pulsating tensile fatigue test method for welded joints”, the fatigue test of specimens with undercut defects is carried out, and the

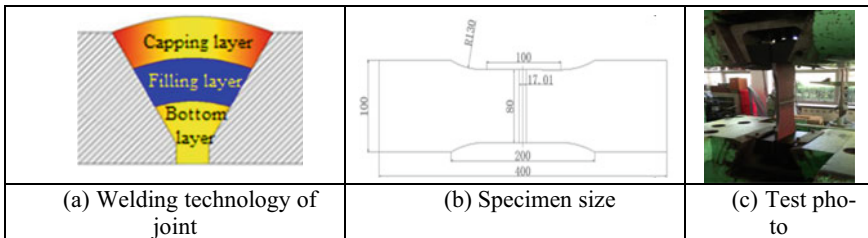


Fig. 10.4 Fatigue test of specimens

influence of undercut defects on fatigue life is evaluated based on structural stress method.

From the fracture morphology of the specimen, it can be seen that the fatigue crack growth starts from the weld toe at the bottom of the groove and gradually extends to the inside of the weld.

10.3.2 Analysis of Fatigue Test Results

There are five smooth V-groove specimens, and the fatigue test results show that the average fatigue life is 530000 times. There are six groups of V-groove specimens with undercut, and each group has five specimens. The test results of V-groove specimens with undercut are shown in Table 10.1.

The fatigue test results show that the peak stress increases with the increase of undercut depth.

10.4 Engineering Application of Method

The engineering verification of the method is based on the anti-fatigue design of the fillet weld between the flange and the pipe of the air compressor. The yield strength of the material is 345 MPa. Each bolt hole is applied with 1500 N tension in the horizontal direction, and the displacement constraint is applied on the bottom surface of the lower flange with a diameter of 160 mm. As shown in Fig. 10.5a.

Table 10.1 Fatigue test results of welded specimens with undercut

Group	Undercut depth (mm)	Stress range (MPa)	Average test fatigue life of five specimens in each group (10^4 times)
1	0.28	220.75	44
2	0.41	220.75	38
3	0.45	220.75	36
4	0.46	220.75	34
5	0.55	220.75	30
6	0.60	220.75	26

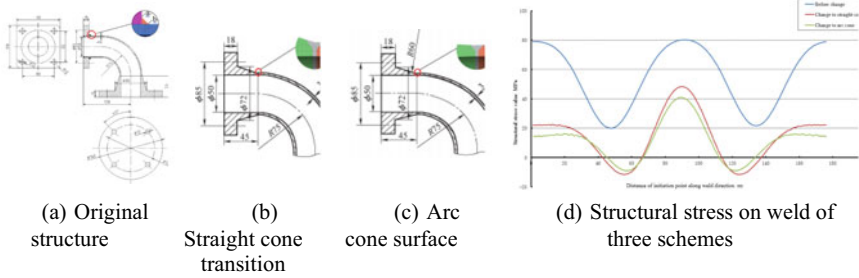


Fig. 10.5 Fatigue test of specimens weld details after modification and structural stress before and after modification

10.4.1 *The First Stage—Identification of Stress Concentration in Welded Joint*

The maximum structural stress peak (stress concentration) of the original structure is 80.1 MPa. The peak stress occurs in the middle of the wire *b*.

10.4.2 *The Second Stage—Analysis of Stress Concentration in Welded Joint*

The reason for the obvious stress concentration in the fatigue behavior of the structure is that the connection between the upper flange and the elbow of the compressor is realized by a fillet weld with high-stress concentration factor, which greatly reduces the anti-fatigue performance in the service process.

10.4.3 *The Third Stage—Stress Concentration Relief of Welded Joint*

Two solutions to relieve stress concentration are proposed for this case. Scheme 1: The original fillet weld joint is replaced by the butt straight cone joint.

In the load direction, the welded joint realizes the coordination of the stiffness of the weld joint as shown in Fig. 10.5b and relieves the stress concentration at the weld joint. Scheme 2: Change the straight cone joint of the first improvement scheme to the arc cone joint as shown in Fig. 10.5c. According to the calculation process of structural stress, the structural stress of each node of the weld is calculated.

It can be seen from Fig. 10.5d that the stress concentration at the weld is relieved after the fillet weld joint is changed to butt joint. The maximum structural stress of fillet weld joint is 80.1 MPa, and the maximum structural stress of butt joint with

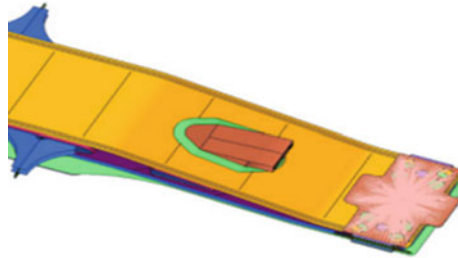


Fig. 10.6 Fatigue test of specimens partial view of bolster

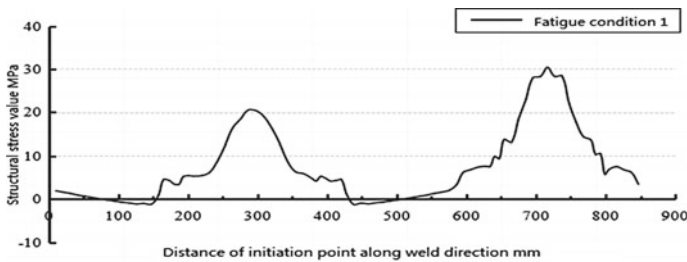


Fig. 10.7 Fatigue test of specimens stress curve of weld structure at transverse stop seat

straight cone is 48.3 Mpa, which is reduced by 40%. After changing to arc cone, the maximum structural stress on the weld is 41.0 MPa, which decreases by 50%.

The method is also applied to the design of the welded bolster of the railway freight car, which is a complex welded structure. As shown in Figs. 10.6 and 10.7.

Through the stiffness coordination design of the local welded structure of the bolster, the weld stress concentration in the local area is effectively alleviated. For example, after the optimization of the weld between the transverse stop seat and the lower cover plate, the peak value of the structural stress is reduced by 16.01%. Therefore, the fatigue resistance of the welded structure is improved at the source.

10.5 Conclusion

- (1) The stress concentration of welded structure makes the anti-fatigue performance decline, so the stiffness coordination is of great significance in the anti-fatigue design of welded structure.
- (2) The stress concentration relief is completed in the design stage, which is conducive to the transformation of fatigue resistance design of welded structure from passive state to active state. This method has guiding value for practical engineering applications.

Acknowledgements Project supported by the Research Project of National Innovation Center of High-Speed Train (No. CXKY-02-01-01(2020))

References

1. BS7608:2014+A1 (2015) Fatigue design and assessment of steel structures[S]. BSI, London
2. EN15085 European standard (2007) EN15085-3-2007 Railway applications—welding of railway vehicles and components part 3: design requirements [S]. European Committee for standardization: CEN
3. ASME BPVC VIII-2-2015 (2015) ASME boiler and pressure vessel code [S]. The American Society of Mechanical Engineers, New York
4. Dong P, Hong JK, Osage DA, Dewees D, Prager M (2010) The master S-N curve method: an implementation for fatigue evaluation of welded components in the ASME B&PV code section VIII, Division 2 and API579-1/ASME FFS-1[M]. WRC Bulletin 523
5. IIW Joint Working Group (2008) XIII1539-07/XV-1254r4-07 IIW document recommendations for fatigue design of welded joints and components[S]. IIW/IIS, England (2008)

Chapter 11

Characterization of Multiaxial Strain Road Loads in Assessing the Durability of Automotive Coil Spring



N. M. Hazmi, S. S. K. Singh, S. Abdullah, L. Abdullah, A. H. Azman, and M. R. M. Rasani

Abstract This paper presents the multiaxial fatigue life characteristics under random strain loads from rural road load conditions. Random loads during operating conditions cause fatigue failure of automotive components. Uniaxial fatigue analysis is reasonable when the system is in a simple state of loading. However, multiaxial fatigue analysis must be included for material response, such as variation of the principal stress directions associated with random loads. Critical region of the coil spring is assessed based on finite element analysis. Multiaxial strain signals of random road loads were captured at a sampling rate of 500 Hz in 150 s. The time history of rural road load strain signal demonstrates high amplitude on uneven surface roads. Kurtosis and root mean square value is extracted from the multiaxial strain signal to evaluate the statistical characteristic of the signal. Fatigue life is assessed using the Brown-Miller, Fatemi-Socie, and Wang-Brown strain-life models. The fatigue life was estimated to be 4.32×10^4 , 1.39×10^4 , and 1.87×10^4 cycles/block for Brown-Miller, Fatemi-Socie, and Wang-Brown, models, respectively. The Brown-Miller model is identified as the suitable model for the predicted fatigue life data, as it has the highest cycles block-to-failure value.

Keywords Multiaxial fatigue life · Finite element · Coil spring · Durability

11.1 Introduction

Coil spring experiences vertical axial loading at the mounting during their service that results in tension-compression force. The helical coil spring shape is complex, generating internal reactions of direct shear force, normal stress, and a torsion due to its movement when subjected to cyclic loading [1]. The helical shape of coil spring causes the main failure due to torsion during its operating condition. Fatigue analyses have focused on the uniaxial loading condition and a number of successful prediction methods for uniaxial fatigue lives. However, conventional uniaxial fatigue

N. M. Hazmi · S. S. K. Singh (✉) · S. Abdullah · L. Abdullah · A. H. Azman · M. R. M. Rasani
Department of Mechanical and Manufacturing Engineering, Universiti Kebangsaan Malaysia,
UKM, 43600 Bangi, Selangor, Malaysia
e-mail: salvinder@ukm.edu.my

approaches usually overestimate fatigue life of these components [2]. The fatigue crack is expected to initiate and propagate from the high-stress concentration surface to the non-high-stress concentration surface, where the direction is parallel to the cross-sectional area of the coil spring [3]. Nevertheless, a real case of crack propagation on coil spring shows that it is not parallel to the plane of a cross-sectional area of the coil spring when it fails [4]. Variation of crack propagation direction showed that the failure of a coil spring is not only caused by simple uniaxial stress, but also by multiaxial stress state. The variation of stress direction makes it necessary to assess the fatigue life of coil springs based on multiaxial fatigue analysis approach.

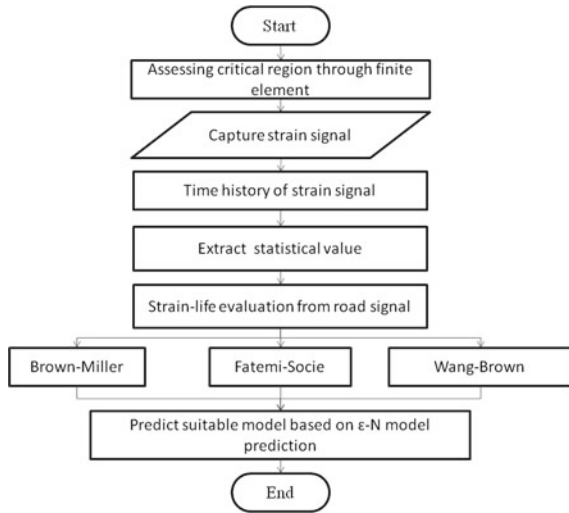
Identification of component failure was done based on multiaxial fatigue life, which includes strain-based criteria, stress-based criteria, and energy-based criteria. Multiaxial fatigue models, such as Brown-Miller, Wang-Brown, Kandil-Brown-Miller, and Fatemi-Socie criteria are strain-based criteria [5]. There are several previous studies that are related to the multiaxial fatigue of the mechanical components. Freitas et al. [6] predicted multiaxial fatigue lives by using Stress Scale Factor (SSF) method and made its comparison with the critical plane approach. Meanwhile, Xu et al. [7] characterized the influence of shear stress and non-proportional hardening by using a new critical plane multiaxial fatigue model parameter in order to assess the multiaxial fatigue life of material alloys. There has been increasing works on fatigue life assessment based on mechanical components, especially coil spring, as demonstrated by Abdullah et al. [8], Prawoto et al. [9], and Yan et al. [10]. However, the aspect of multiaxial fatigue is not fully explored and the aforementioned studies had mainly focused on uniaxial fatigue life prediction under random load.

Therefore, the aim of this study is to characterize the multiaxial random strain loading signal to assess the durability of the coil spring for fatigue life prediction. A coil spring experiences a fatigue failure when traveling on uneven road conditions. The fatigue life was analyzed by using multiaxial strain-life model, Brown-Miller, Fatemi-Socie, and Wang-Brown. Brown-Miller criteria analyzed two different crack growth patterns at the surface of materials, which are subjected to multiaxial loading that is based on the orientation of the planes, normal and shear strain on the maximum shear plane [11]. Fatemi-Socie criteria substituting normal strain amplitude with maximum normal stress on critical plane and the analysis include material cyclic hardening effect [12]. Both Brown-Miller and Fatemi-Socie criteria defined the critical plane as maximum shear strain plane as failure crack occurs at near to maximum shear strain plane. Wang-Brown criteria defined the critical plane as the angular strain range and normal strain range that reached the maximum value in the plane [13].

11.2 Methodology

Figure 11.1 shows the process flow for characterization of multiaxial strain road loads in assessing the durability of an automotive coil spring. Multiaxial fatigue strain loading data were used in this study, in which they were collected from a vehicle coil spring. The rosette strain gauge was used to extract and measure the multiaxial strain

Fig. 11.1 Process flow for durability assessment of multiaxial fatigue life of vehicle coil spring

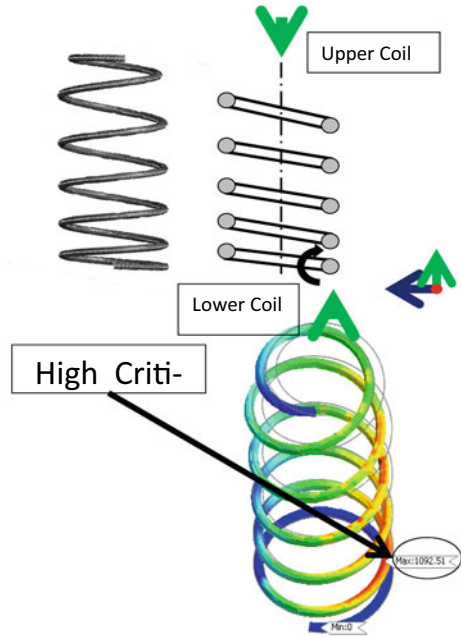


signal of rural roads. The rosette strain gauge was placed at the critical region of the coil spring that was determined based on finite element analysis. Meanwhile, kurtosis and root mean square is extracted from the multiaxial strain signal to analyze the statistical characteristic of the signal. Subsequently, the fatigue life of the strain signal was computed by using Brown-Miller, Fatemi-Socie, and Wang-Brown models.

11.2.1 Finite Element Analysis

Figure 11.2 shows the finite element analysis of the vehicle coil spring model. SAE 5160 carbon steel was employed as material cyclic properties. The bottom of the coil spring model was fixed with rigid body and load is applied from the top of coil spring model. Then, the four-node tetrahedral elements were applied for solid mesh. Therefore, 17,285 and 32,450 elements and nodes, respectively, were obtained from the model. The load of the coil spring is based on the curb weight of the vehicle together with load of passenger [14]. In this finite element analysis, the load (3500 N) was subjected to the top of the coil spring model. The maximum von Mises stress is 1092 MPa, which is below the yield strength of the coil spring (1487 MPa). The critical region of the coil spring is at the maximum von Mises stress region where the maximum stress is localized.

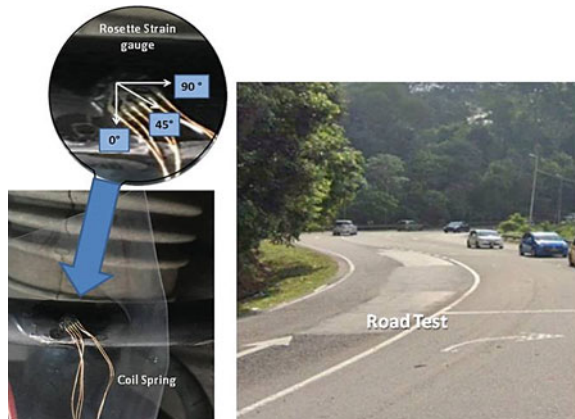
Fig. 11.2 Assessment of critical region of the vehicle coil spring



11.2.2 Experimental Setup

The experimental setup is illustrated in Fig. 11.3. In this study, the rosette strain gauge is used to capture the signals in x -axis, 45° , and y -axis, as shown in Fig. 11.3. The multiaxial strain signal is analyzed to evaluate the multiaxial fatigue behavior of the coil spring. Strain signal in x -axis refers to 0° , while strain signal in y -axis refers to 90° . All strain signals in 0° , 45° , and 90° axis are on the same plane. The rosette strain

Fig. 11.3 Experimental setup for extracting multiaxial strain



gauge is placed at the critical region of the vehicle coil spring. The vehicle traveled on the rural road, where the road condition is of somewhat irregular surface and curvy roadway. The road conditions were selected based on uneven road conditions, where coil spring failure usually occurs [15]. To collect sufficient information for strain data, the frequency of sample must be higher than 400 Hz [8]. Therefore, data were captured with a sampling rate of 500 Hz in 150 s.

11.2.3 Statistical Characterization

The multiaxial strain signal is characterized based on the kurtosis value, where value above three indicates the data as non-stationary, whereas kurtosis value below three indicates the data as stationary [8]. Kurtosis above three also indicates that the data have high amplitude, therefore, contributing to high damage of the signal data [8]. The kurtosis value is represented in the equation below:

$$K = \frac{1}{n(\text{rms})^4} \sum_{j=1}^n (x_j - \bar{x})^4 \quad (11.1)$$

Root mean square (RMS) describes the total vibrational energy contained in the signal data and quantifies the mean value of the signal without negative data [8]. RMS value can be computed as follows:

$$\text{rms} = \left\{ \frac{1}{n} \sum_{j=1}^n x_j^2 \right\}^{\frac{1}{2}} \quad (11.2)$$

11.2.4 Multiaxial Life Prediction

Brown-Miller model was applied for multiaxial fatigue life calculation. Generally, fatigue life is assumed as in-phase loading and non-linear function of the strain state. Brown-Miller algorithm considers that the fatigue damage is dominated by the combination of normal strain and maximum shear of the multiaxial strain signal [3]. Brown-Miller model proposed that critical plane is the plane with maximum shear strain amplitude combined with the shear strain and maximum normal strain or normal stress. The Brown-Miller prediction model is written as below:

$$\frac{\gamma_{\max}}{2} + \frac{\varepsilon_N}{2} = 1.65 \frac{\sigma_{f'}}{E} (2N_f)^b + 1.75 \varepsilon_{f'} (2N_f)^c \quad (11.3)$$

where, γ_{\max} and ε_n are maximum shear strain amplitude and normal strain amplitude, respectively. Meanwhile, σ_f' and b are fatigue strength coefficients and fatigue strength exponent, respectively. The ε_f' and c are fatigue ductility coefficient and fatigue ductility exponent, respectively.

Fatemi–Socie model introduced a concept of equivalent shear strain amplitude, which reflects the effects of mean stress and additional hardening. This is achieved by substituting the normal strain amplitude for maximum normal stress on the critical plane. The critical plane of the FS model is usually considered to be the maximum shear strain plane. The Fatemi–Socie model [12] is represented as follows:

$$\frac{\Delta\gamma}{2} \left(1 + k \frac{\sigma_{n,\max}}{\sigma_y} \right) = \frac{\tau_f'}{G} (2N_f)^{b\gamma} + \gamma_f' (2N_f)^{c\gamma} \quad (11.4)$$

where $\Delta\gamma$ and $\sigma_{n,\max}$ is shear strain amplitude and maximum normal stress, respectively. Wang-Brown model proposed a similar linear criterion, which modifies the definition of the normal strain range to consider the variable-amplitude strains. The Wang-Brown model [12] is represented by the equation below:

$$\frac{\Delta\gamma_{\max}}{2} + s\varepsilon_n^* = [1 + v + (1 - v)s] \frac{\sigma_f' - 2\sigma_n^0}{E} (2N_f)^b + (1.5 + 0.5s)\varepsilon_f' (2N_f)^c \quad (11.5)$$

where, $\Delta\gamma_{\max}$ and σ_n^0 are shear strain range and mean normal stress, respectively; v refers to Poisson's ratio; and σ_f' , ε_f' , b , c , and s refer to fatigue properties of the material that are determined from axial and torsional fatigue tests.

11.3 Results and Discussion

Figure 11.4 illustrates the multiaxial strain signal history and probability density function curves of rural roads at 0°, 90°, and 45° axis. Figure 11.4 shows random multiaxial strain signals that were extracted for 150 s with 75,000 discrete data points per block. The history strain signal data ranged between -774.9 and $442.2 \mu\varepsilon$. The probability density function curve for strain signal at 0° axis data shows a narrow bell-shaped with negative mean value ($-3343 \mu\varepsilon$). However, the probability density function curves for strain signal at 90° and 45° axis data are broad bell-shaped with negative mean values of -3115 and $-3228 \mu\varepsilon$, respectively. On the other hand, the strain signal at 45° axis shows high-range amplitude due to the helical shape of the coil spring, as highlighted in Fig. 11.4. The behavior of random strain amplitude data signal at 0°, 90°, and 45° axis can be attributable to the internal stress in the coil spring.

Figure 11.5 shows the statistical parameter of the multiaxial strain signal, root mean square, and kurtosis. Root mean square value of strain signal at 45° axis has

Fig. 11.4 Multiaxial strain signal history and probability density function curves at 0°, 90°, and 45° axis

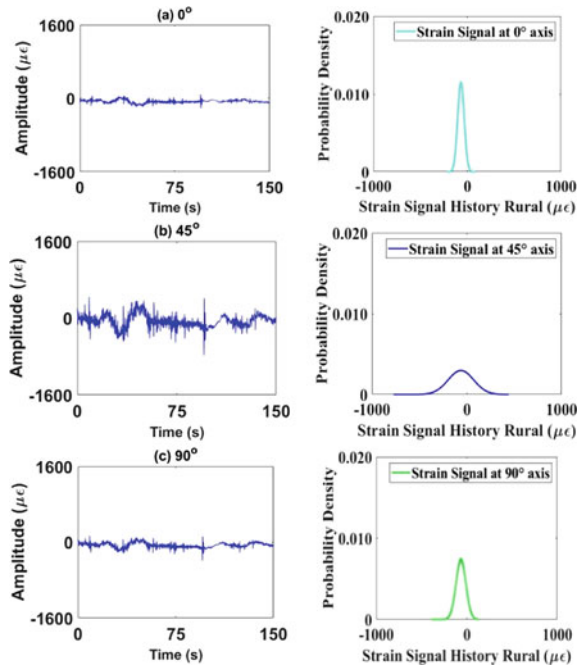
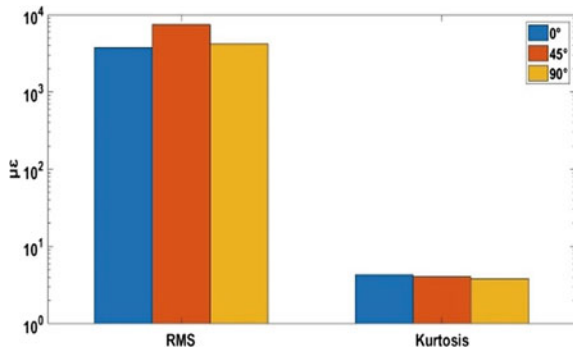


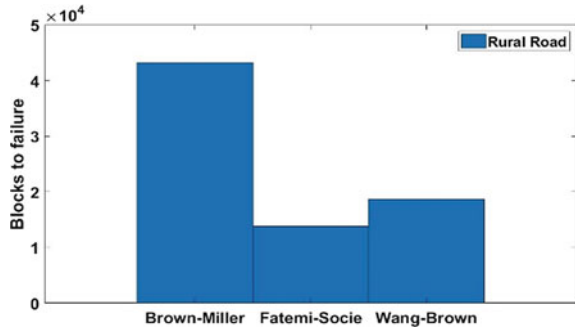
Fig. 11.5 Root mean square and kurtosis value for strain signal at 0°, 90°, and 45° axis



the highest value, compared with the strain signal at 0° and 90° axis. The total vibrational energy contained for strain signal at 45° axis is higher due to torsion behavior of the helical shape coil spring. Meanwhile, kurtosis value for strain signal at 0° axis is the highest, compared with the strain signal at 0° and 90° axis. However, all three kurtosis values for strain signal at 0°, 90°, and 45° axis are above three at 4.3 μϵ, 4.1 μϵ, and 3.8 μϵ, respectively. This could be attributable to the strain signal experiencing high-amplitude events on rural roads with irregular road surfaces.

Figure 11.6 illustrates the multiaxial fatigue life of rural roads for Brown-Miller, Fatemi-Socie, and Wang-Brown models. Strain-life from Brown-Miller model is

Fig. 11.6 Fatigue life of strain signal based on Brown-Miller, Fatemi–Socie, and Wang-Brown models



the highest at 4.32×10^4 cycles/block, followed by Fatemi–Socie at 1.39×10^4 cycles/block, and Wang-Brown at 1.87×10^4 cycles/block. The multiaxial fatigue life prediction from Brown-Miller model is the highest due to non-linear strain of the helical coil spring. Both Brown-Miller and Fatemi–Socie models include crack propagation mechanism effect, where fatigue life is a non-linear function of the strain state [3]. However, Fatemi–Socie is superior when describing the effect of additional hardening caused by non-proportional loadings [2]. Meanwhile, Wang-Brown model is superior when shear strain and normal strain are considered and the effect of mean stress on fatigue life is characterized [2].

11.4 Conclusion

This paper aims to assess the characterization of multiaxial random strain loads signal to evaluate the durability of the coil spring. There are several conclusions that can be made based on the durability assessment of the multiaxial strain loads. Strain signal data at 0° axis possessed narrow probability density curve compared to strain data at 90° axis and 45° axis. However, strain signal data at 45° axis possessed high-amplitude event, compared with strain data at 0° axis and 90° axis. The highest total vibrational energy contained for strain signal and kurtosis are at 45° axis and 0° axis, respectively. The fatigue life prediction for the Fatemi–Socie is the lowest, followed by Wang-Brown and Brown-Miller models.

Acknowledgements The authors would like to express their gratitude to the Universiti Kebangsaan Malaysia (Research funding: FRGS/1/2019/TK03/UKM/02/1) for the support given for this research.

References

1. Nishimura Y, Yanase K, Ikeda Y, Tanaka Y, Miyamoto N, Miyakawa S, Endo M (2018) Fatigue strength of spring steel with small scratches. *Fatigue Fract Eng Mater Struct* 41(7):1514–1528

2. Zhu S, Yu Z, Correia J, Jesus A, Berto F (2018) Evaluation and comparison of critical plane criteria for multiaxial fatigue analysis of ductile and brittle materials. *Int J Fatigue* 112:279–288 (2018)
3. Kong YS, Abdullah S, Schramm D, Omar MZ, Haris SM (2020) Correlation of uniaxial and multiaxial fatigue models for automobile spring life assessment. *Exp Tech* 44(2):197–215
4. Pastorcic D, Vukelic G, Bozic Z (2018) Coil spring failure and fatigue analysis. *Eng Fail Anal* 99(1):310–318
5. Feng ES, Wang XG, Jiang C (2019) A new multiaxial fatigue model for life prediction based on energy dissipation evaluation. *Int J Fatigue* 122:1–8
6. Freitas MD, Reis L, Meggiolaro MA, Castro J (2017) Stress scale factor and critical plane models under multiaxial proportional loading histories. *Eng Fract Mech* 174:104–116
7. Xu S, Zhu SP, Hao YZ, Liao D, Qian G (2018) A new critical plane-energy model for multiaxial fatigue life prediction of turbine disc alloys. *Eng Fail Anal* 93:55–63
8. Abdullah L, Singh SSK, Abdullah S, Azman AH, Ariffin AK (2020) Fatigue reliability and hazard assessment of road load strain data for determining the fatigue life characteristics. *Eng Fail Anal* 123:105314 (2020)
9. Prawoto Y, Manville S, Sakai T, Lee L, Tanaka M, Gnaupel-Herold T (2019) Fracture mechanics approach to splitting in low spring index cold coiling process. *J Fail Anal Prev* 19(3):738–751
10. Yan S, Wang Q, Chen X, Zhang C, Cui G (2019) Failure analysis of an automobile coil spring in high-stress state. *J Fail Anal Prev* 19(2):361–368
11. Portugal I, Olave M, Urresti I, Zurutuza A, López A, Muñiz-Calvente M, Fernández-Canteli A (2019) A comparative analysis of multiaxial fatigue models under random loading. *Eng Struct* 182:112–122
12. Yu ZY, Zhu SP, Liu Q, Liu Y (2017) Multiaxial fatigue damage parameter and life prediction without any additional material constants. *Materials* 10(8) (2017)
13. Tobajas R, Elduque D, Ibarz E, Javierre C, Gracia L (2020) A new multiparameter model for multiaxial fatigue life prediction of rubber materials. *Polymers* 12(5) (2020)
14. Tarek Musalli TA, Ali TK, Esakki B (2021) Fatigue analysis of helical spring subjected to multi-axial load. In: *Innovative design, analysis and development practices in aerospace and automotive engineering*, pp 377–387
15. Kong YS, Abdullah S, Haris SM, Omar MZ, Schramm D (2018) Generation of artificial road profile for automobile spring durability analysis. *J Kejurut* 30(2):123–128

Chapter 12

Identification of Key Fatigue Welds of Bogie Welded Frame



Suming Xie, Zhipeng Xu, Chunliang Niu, Chungue Nie, and Tao Zhang

Abstract Based on the EN 13749-2011 standard and the master S–N curve method, the fatigue strength of the welded frame of the rail vehicle bogie is analyzed. First, based on the master S–N curve method, the influence of weld leg size and penetration on the failure mode of fillet welds is studied. The results show that the two failure modes of weld toe failure and weld throat failure when the fillet weld is not penetrated need to be considered at the same time, and only the weld toe failure needs to be considered for full penetration. Secondly, the fatigue load and fatigue conditions of the welded frame are determined based on the EN 13749-2011 standard, the cumulative damage of the frame welds is obtained according to the master S–N curve method, and the key fatigue welds of the frame are determined by the cumulative damage value. The cumulative damage value of the throat of the key fatigue welds is smaller than that of the weld toe. Among them, the cumulative damage of the annular fillet weld between the vertical plate of the motor hanger and the beam is the largest, with a value of 0.59.

Keywords Welded frame · Fillet weld failure · Master S–N curve method

12.1 Introduction

The complex and severe fatigue loads experienced by bogies during the operation of rail vehicles have led to fatigue failures at key positions of the bogie welded frame. Therefore, the research on the fatigue strength of the rail vehicle welded frame has great practical significance.

S. Xie (✉) · Z. Xu · C. Niu · C. Nie

School of Locomotive and Rolling Stock Engineering, Dalian Jiaotong University, Dalian 116028, China

e-mail: sumingxie@163.com

C. Niu

School of Mechanical and Power Engineering, Dalian Ocean University, Dalian 116023, China

T. Zhang

National Innovation Center of High Speed Train, Qingdao 266109, China

Fillet weld joints are the most common form of welded joints in welded structures. So first, based on the master S–N curve method, the influence of weld leg size and weld penetration on the stress distribution and failure mode of fillet welds is explored. The law provides help for the design of the fillet weld of the welded frame. Then, with a certain bogie welded frame as the research object, the fatigue load and fatigue working conditions of the frame are determined according to the EN 13749-2011 standard, and the master S–N curve method is used to calculate the cumulative damage of the frame welds to identify the key fatigue welds.

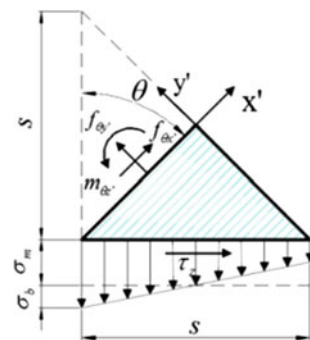
12.2 Stress Analysis of Fillet Weld Joint Structure

Due to the stress concentration at the joint weld toe and weld throat, the failure modes of fillet welds are mainly divided into weld toe failure and weld throat failure. The two failure modes are mainly affected by the size of the weld leg and weld penetration. The failure section of the weld toe failure is relatively clear, and the location of the failure section of the weld throat failure is affected by the weld penetration, so the location of the weld throat failure section is not clear in practice. In the finite element analysis, the imaginary section can be modeled by the finite element method, and the structural stress distribution in the section can be obtained based on the master S–N curve method [1]. In order to summarize the relevant laws of the failure section of the weld throat, the structural stress of any section of the weld throat should be analyzed.

12.2.1 Stress Analysis of Weld Throat Section

Literature [2] believes that only normal structural stress and transverse shear structural stress exist in the section of the weld throat of the fillet weld subjected to the tensile force perpendicular to the weld, as shown in Fig. 12.1. Based on the master

Fig. 12.1 Stress analysis model of weld throat section



S–N curve method, the normal structural stress σ_s (including membrane stress σ_m and bending stress σ_b) and transverse shear structural stress τ_z can be obtained when the imaginary section of the weld throat is 90° to the horizontal plane. When the fillet weld penetration depth p is 0, based on the static equilibrium condition, the following relationship can be established between the normal structural stress $\sigma_s(\theta)$ and transverse shear structural stress $\tau_z(\theta)$ of any section and the structural stress component at 90° :

$$\sigma_s(\theta) = \sigma_m(\theta) + \sigma_b(\theta) \quad (12.1)$$

$$\sigma_m(\theta) = \frac{\sigma_m \cdots \sin \theta + \tau_m \cdots \cos \theta}{a_\theta} \quad (12.2)$$

$$\sigma_b(\theta) = \frac{\sigma_b s^2 - 3\sigma_m \cdots}{a_\theta^2} + 3\sigma_m(\theta) \quad (12.3)$$

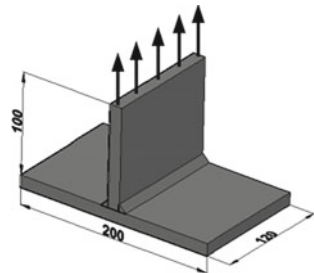
$$\tau_z(\theta) = \frac{\sigma_m \cdots \cos \theta - \tau_z \cdots \sin \theta}{a_\theta} \quad (12.4)$$

In the formula, a_θ is the weld throat size when the imaginary section of the weld throat is at an angle θ to the horizontal plane, which can be expressed as a function of θ , $a_\theta = s/(\sin \theta + \cos \theta)$, and s is the weld leg size. When the fillet weld has penetration, just replace s in the formula with $s + p$.

12.2.2 Numerical Analysis of Structural Stress of Double-Sided Fillet Welds

According to the joint details in Appendix B of EN 15085-3:2007 [3], a T-shaped double-sided fillet weld is designed, as shown in Fig. 12.2. The size unit in the figure is mm, the plate thickness is 12.0 mm, and the material is steel. The fillet weld leg size s is 4.2 mm, 5.6 mm, 7.0 mm, and the penetration value p is 0 mm, 3.0 mm, 6.0 mm, corresponding to non-penetration, semi-penetration, and full penetration.

Fig. 12.2 Schematic diagram of T-shaped double-sided fillet weld geometry



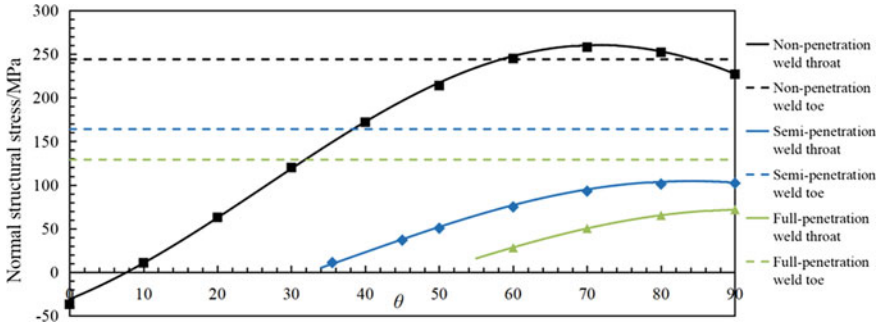


Fig. 12.3 The structural stress of the fillet weld when the weld leg size is 4.2 mm

When the size of the fillet weld leg is 4.2 mm, the conditions of non-penetration, semi-penetration, and full penetration are considered, respectively. The normal structural stresses of the different sections of the weld throat and weld toe are shown in Fig. 12.3. It can be seen from Fig. 12.3 that the normal structural stress of the not penetrated weld throat is greater than that at the weld toe, and the joint may fail in the weld throat at this time.

When the fillet weld leg size is 5.6 mm and 7.0 mm, the conditions of non-penetration, semi-penetration, and full penetration are considered, respectively. The normal structural stresses of different sections of the weld throat and weld toe are shown in Figs. 12.4 and 12.5. It can be seen from Figs. 12.4 and 12.5 that as the size of the weld leg increases, the normal structural stress of the not penetrated weld throat begins to be smaller than that at the weld toe, and the weld failure mode has changed from throat failure to weld toe failure.

It can be seen from Figs. 12.3, 12.4 and 12.5 that the normal structural stress of the fully penetrated and partially penetrated weld throat is much smaller than that at the weld toe, and there is no throat failure at this time; the maximum structural stress of the not penetrated weld throat resulting cross-sectional angle is about 70°. As

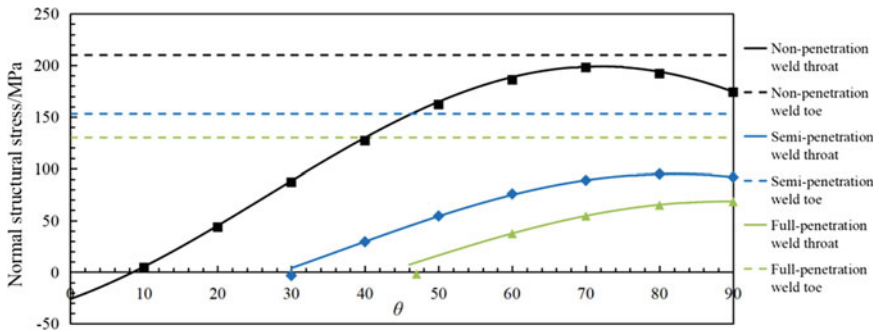


Fig. 12.4 The structural stress of fillet weld when the weld leg size is 5.6 mm

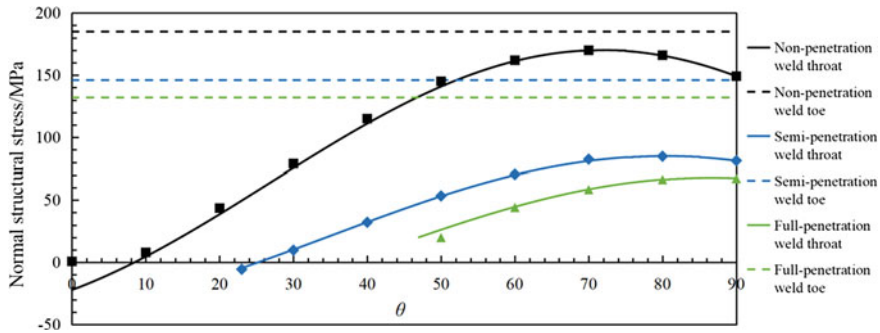


Fig. 12.5 The structural stress of fillet weld when the weld leg size is 7.0 mm

the penetration depth increases, the cross-sectional angle of the maximum structural stress of the weld throat gradually increases, and it tends to 90° at full penetration.

12.3 Identification of Key Welds for Fatigue of Welded Frames

Taking a rail vehicle welded frame as the research object, according to the relevant requirements in the EN 13749–2011 standard [4], the fatigue load condition of the welded frame is determined. The fatigue load of the welded frame mainly includes vertical load (vertical quasi-static force and vertical dynamic force), lateral load (lateral quasi-static force and lateral dynamic force), track twist load, and motor inertial load. According to the number of dynamic cycles of each load in the standard, the dynamic force, quasi-static force, track twist load, and motor inertial load are combined into seven fatigue analysis conditions. Fatigue loads are applied in three stages, the second stage load is 1.2 times that of the first stage; the third stage load is 1.4 times that of the first stage. Figure 12.6 shows the structure and load diagram of the welded frame. Table 12.1 is a summary table of fatigue analysis conditions.

Under the action of fatigue analysis conditions, according to the master S–N curve method and the Miner cumulative damage principle, the toe, and throat of the welded frame weld are calculated for cumulative damage. According to the cumulative damage value, five key fatigue welds are screened out. As shown in Fig. 12.7. Weld_1 is the circular fillet weld between the crossbeam and the inner vertical plate of the longitudinal beam; Weld_2 is the circular fillet weld between the auxiliary longitudinal beam and the crossbeam; Weld_3 is the circular fillet weld between the motor suspension stand and the crossbeam; Weld_4 is the lap fillet weld between the auxiliary longitudinal beam and the crossbeam; Weld_5 is the fillet weld between the short gusset plate and the crossbeam; except for Weld_4, the rest are single-sided grooved full penetration fillet welds. When calculating the normal structural stress at the weld throat of these key welds, according to the previous

Fig. 12.6 Schematic diagram of the structure and load of the welded frame

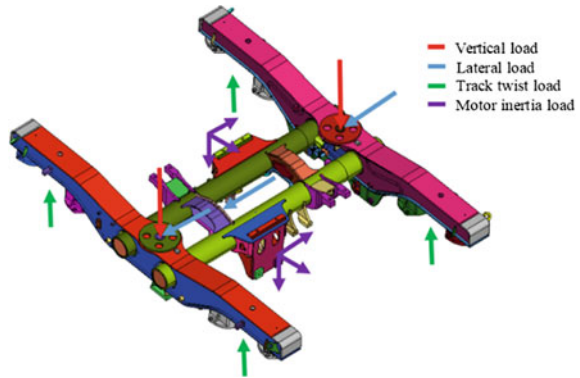


Table 12.1 Fatigue analysis conditions of frame

Condition	Load	Load times (10^4)		
		First	Second	Third
1	Vertical dynamic load + lateral dynamic load (+)	270	90	90
2	Vertical dynamic load + lateral dynamic load (-)	270	90	90
3	Vertical dynamic load + lateral dynamic load (+) + Track twist load	30	10	10
4	Vertical dynamic load + lateral dynamic load (-) + Track twist load	30	10	10
5	Vertical quasi-static load + lateral quasi-static load (+)	7.5	2.5	2.5
6	Vertical quasi-static load + lateral quasi-static load (-)	7.5	2.5	2.5
7	Motor inertia load	120	40	40

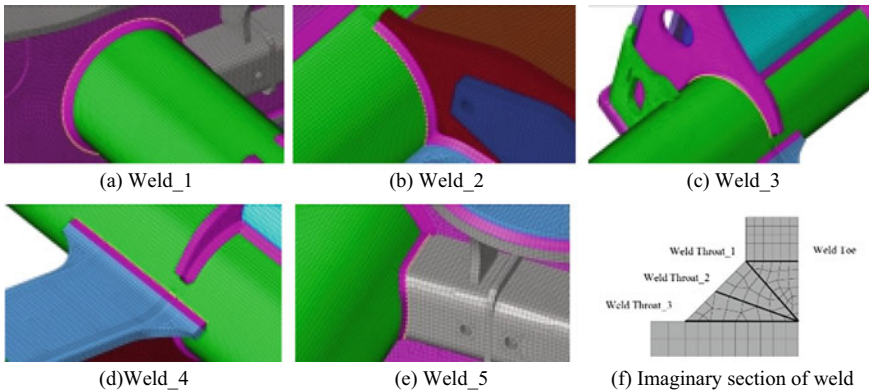


Fig. 12.7 Key fatigue welds of frame and imaginary section of weld

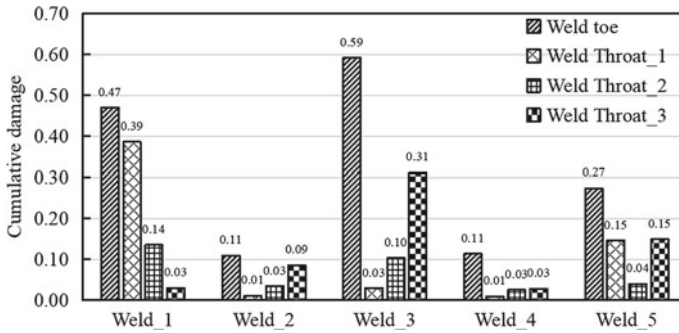


Fig. 12.8 Cumulative fatigue damage at the key fatigue welds

analysis, three imaginary sections with greater structural stress are selected at the weld throat (1-weld and base metal connection surface, 2-weld middle area and the 3-weld connection surface with the base metal), as shown in Fig. 12.8g.

Figure 12.8 shows the cumulative damage of the weld toe and weld throat at the key fatigue welds. The cumulative damage of Weld_3 is the largest, the cumulative damage value at the weld toe is 0.59, and the cumulative damage of Weld_1 is the second, with the value of 0.47. The cumulative damage at the throat of the key fatigue welds is less than that at the weld toe. Therefore, the failure mode of the key fatigue welds is mainly the failure of the weld toe.

12.4 Conclusion

1. Under different weld leg sizes, when the fillet weld is not penetrated, the structural stress at the weld toe and the weld throat is at a relatively high level, so weld toe failure and weld throat failure when the fillet weld is not penetrated are required at the same time; when full penetration, only the failure of the weld toe needs to be considered. As the weld leg size increases, the normal structural stress of the not penetrated weld throat begins to be smaller than that at the weld toe, and the failure mode of the weld is changed from weld throat failure to weld toe failure.
2. According to the BS EN 13749-2011 standard, seven fatigue analysis conditions of the welded frame were determined, and the cumulative damage analysis was carried out on the weld toe and throat of the welded frame, five key fatigue welds of the frame were screened out, of which the cumulative damage at the weld toe of Weld_3 was the largest, with a value of 0.59; the cumulative damage at the weld toe of the welds was greater than that at the weld throat.

Acknowledgements Project supported by the Research Project of National Innovation Center of High Speed Train, China (No. CXKY-02-01-01(2020)).

References

1. Mei J, Dong P (2017) An equivalent stress parameter for multi-axial fatigue evaluation of welded components including non-proportional loading effects. *Int J Fatigue* 101:297–311
2. Xing S, Dong P, Threstha A (2016) Analysis of fatigue failure mode transition in load-carrying fillet-welded connections. *Mar Struct* 46:102–126
3. BS EN 15085-3 (2007) Railway applications-welding of railway vehicles and components-part 3: design requirements. BSI, London
4. BS EN 13749 (2011) Railway applications—wheelsets and bogies—methods of specifying structural requirements of bogie frames

Chapter 13

Susceptibility of Steel Sucker Rods Operated in Oil Well to Environmentally Assisted Fatigue



Olha Zvirko , Oleksandr Tsyruynyk , and Nataliya Kret

Abstract Sucker rod is one of the most important elements of the sucker rod pump system in oilfield, operated often under severe conditions. This may lead to premature failures of sucker rods with negative consequences. Therefore, it is important to assess susceptibility of operated sucker rod steel to corrosion and environmentally assisted fatigue in order to seek effective ways of mitigation and extension of their service life. In the paper, operational degradation of sucker rod steels was observed using corrosion, fatigue and corrosion fatigue testing. It was shown that long-term operation of the low-alloyed 20H2M and 35XM steels of sucker rods caused 10–15% decrease in corrosion resistance and approximately 25% decrease in corrosion fatigue resistance in CO₂-containing formation water with pH = 3.1. Fatigue crack growth acceleration in the 20H2M steel in acid formation water was revealed in the medium-amplitude region of loading due to a combination of mechanisms of fatigue and stress corrosion cracking (stress corrosion fatigue). The operated 20H2M steel was revealed to be more susceptible to environmentally assisted fatigue than that in the unoperated state. Corrosion fatigue crack growth acceleration in the operated 20H2M steel in acid formation water occurred at lower values of ΔK compared to that in the unoperated one. The effectiveness of protection of the operated 20H2M steel in formation water with pH = 3.1 against corrosion and corrosion fatigue failure with environmentally friendly inhibitor was demonstrated.

Keywords Steel · Sucker rod · Operation · Corrosion · Corrosion fatigue · Stress corrosion fatigue · Inhibitor

13.1 Introduction

Sucker rod is one of the most important elements of the sucker rod pump system in oil well since it is often operating under severe conditions, including cyclic loads, corrosive environments, high pressure and temperature [1–6]. This leads to frequent

O. Zvirko (✉) · O. Tsyruynyk · N. Kret
Karpenko Physico-Mechanical Institute of the National Academy of Sciences of Ukraine, 5
Naukova St., Lviv 79060, Ukraine

sucker rod failures and, consequently, to significant negative environmental, technological and economic impacts. Therefore, it is important to assess susceptibility of operated sucker rod steel to corrosion and environmentally assisted fatigue in order to seek effective ways of mitigation and extension of their service life.

The service life of steel structures is governed by time-dependent deterioration process, mainly influenced by mechanical and environmental factors, which change the steel properties. Therefore, serviceability of steels and structural integrity can be influenced by in-service steel degradation. It implies deterioration of corrosion resistance [7–9], plasticity [7, 10], resistance to brittle fracture [7–11] and resistance to fatigue and corrosion fatigue crack propagation [12–17].

The main objectives of the study were to assess degradation of corrosion resistance, fatigue and corrosion fatigue failure resistance of the sucker rod steels as a result of operation and to identify effective and green inhibitor as sustainable inhibitor for protection of degraded steel rods against corrosion and corrosion fatigue in CO₂-containing acid chloride solution, modelling formation water.

13.2 Experimental

13.2.1 Materials

The work done is consisted in characterisation of the sucker rod steels with different strength. Two low-alloyed 20H2M and 35XM (Ukrainian codes) steels were studied. The chemical composition of the investigated steels is presented in Table 13.1. Sucker rods, being investigated in the study, were operated for 5.5 years. For comparison purpose, the steel of the sucker rod end was considered as that in the unoperated state since it was exposed to much less stress under operation than the sucker rod body.

The 20H2M steel in unoperated state was characterised by ultimate strength σ_{UTS} of 1004 MPa, yield strength σ_Y of 807 MPa, reduction in area RA of 55% and elongation of 16%. The 35XM steel in unoperated state was characterised by σ_{UTS} of 793 MPa, σ_Y of 473 MPa, RA of 69% and elongation of 21%.

Tannin as environmentally friendly inhibitor was used with the purpose to assess a possibility to protect the operated steel of sucker rods against corrosion and corrosion fatigue failure in acid formation water.

Table 13.1 Chemical composition of the investigated steels, mass %

Steel	C	Si	Mn	Ni	S	P	Cr	Mo	Cu
20H2M	0.17–0.25	0.17–0.37	0.4–0.7	1.5–1.9	<0.035	<0.035	<0.3	0.2–0.3	<0.3
35XM	0.32–0.4	0.17–0.37	0.4–0.7	<0.3	<0.035	<0.035	0.8–1.1	0.15–0.25	<0.3

13.2.2 Electrochemical Investigations

Corrosion resistance of steels was evaluated using electrochemical polarisation potentiodynamic method at a sweep rate of 1.0 mV s^{-1} . Electrochemical tests were carried out on IPC-Pro potentiostat, using a standard three-electrode electrochemical cell consisting of working electrode made of the investigated steel, Ag/AgCl (saturated KCl) reference electrode and auxiliary Pt electrode. The basic electrochemical characteristics of steels, corrosion potential E_{corr} and corrosion current density i_{corr} , were determined by the graph-analytic method.

Corrosive environment was a 1% NaCl solution + CH_3COOH ($\text{pH} = 3.1$), bubbled with CO_2 , simulating acid formation water in oilfield. The test solution was prepared from analytical-grade reagents. The steels were tested under temperature $20 \pm 2^\circ\text{C}$.

13.2.3 Fatigue Testing

Fatigue and corrosion fatigue crack growth behaviour of steels was investigated in air and simulated formation water using beam specimens $8 \times 18 \times 160 \text{ mm}$ in size with V -concentrator. Specimens were loaded by means of cantilever bending for a load ratio $R = 0.1$ and a frequency $f = 5$ and 1 Hz in air and solution, respectively. Fatigue crack growth curves (fatigue crack growth rate da/dN vs. stress intensity factor range ΔK) were plotted. The number of cycles for crack initiation N_i in the studied steels was defined, when crack was propagated to crack length of 0.1 mm at stress $\sigma = 350 \text{ MPa}$, which is almost twice higher than the fatigue limit σ^{-1} of steels in air ($\sim 200 \text{ MPa}$).

13.3 Results of Experimental Studies and Discussion

Analysing susceptibility of steels to in-service corrosion degradation as reported in researches [8, 9], electrochemical behaviour of steels in the unoperated state and after 5.5 years of operation was investigated in 1% NaCl solution + CH_3COOH ($\text{pH} = 3.1$), bubbled with CO_2 , simulating formation water. Based on the determined polarisation curves, electrochemical properties were defined (Table 13.2).

The 35XM steel in both investigated states was characterised by lower corrosion current density i_{corr} and more positive values of corrosion potential E_{corr} than the 20H2M steel (Table 13.2). Corrosion resistance of the investigated steels was deteriorated during operation. Thus, corrosion current density i_{corr} was increased by 10–15% for the investigated steels as a result of operation. In the presence of 1.0 g/dm^3 inhibitor in 1% NaCl solution + CH_3COOH ($\text{pH} = 3.1$), bubbled with CO_2 , corrosion current density i_{corr} of the operated 20H2M steel was decreased in 6 times ($1.3 \times 10^{-5} \text{ A/cm}^2$), and the degree of protection was $\sim 85\%$.

Table 13.2 Electrochemical properties of the studied steels in 1% NaCl solution + CH₃COOH (pH = 3.1), bubbled with CO₂, simulating formation water

Steel	Steel state	$-E_{\text{corr}}$ (V)	i_{corr} ($\times 10^{-5}$ A/cm ²)
20H2M	Unoperated	0.672	7.2
20H2M	Operated	0.676	8.0
35XM	Unoperated	0.644	4.9
35XM	Operated	0.638	5.7

Table 13.3 presents data on the number of cycles to crack initiation in the studied steels determined in ambient air. Higher resistance to fatigue crack initiation was inherent to the 20H2M steel in comparison with the 35XM steel (Table 13.3). Operation of sucker rods caused deterioration of fatigue resistance at crack initiation stage: number of cycles to crack initiation N_i decreased in 1.14 (from 500 to 440 cycles) and 1.32 (from 330 to 250 cycles) times for the 20H2M and 35XM steels, respectively.

The 20H2M steel in both investigated states was characterised by higher resistance to corrosion fatigue failure at the stage of crack initiation (Table 13.4) in the test solution, than the 35XM steel. The resistance to corrosion fatigue failure of both steels in the post-operated state was lower by almost 25% compared to that for unoperated steels. In the presence of inhibitor (1.0 g/dm³ tannin), the number of cycles for crack initiation in the operated 20H2M steel was higher in 4.7 times ($N_i = 160 \times 10^3$ cycles) than in the environment without inhibitor, and the degree of protection was ~80%.

Figure 13.1 presents fatigue crack growth diagrams for the 20H2M steel in air and in 1% NaCl solution + CH₃COOH (pH = 3.1), bubbled with CO₂, simulating formation water: (a) in the unoperated state; (b) after 5.5 years operation.

Table 13.3 Number of cycles for crack initiation N_i in the studied steels in air

Steel	Steel state	N_i ($\times 10^3$ cycles)
20H2M	Unoperated	500
20H2M	Operated	440
35XM	Unoperated	330
35XM	Operated	250

Table 13.4 Number of cycles for crack initiation N_i in the studied steels in 1% NaCl solution + CH₃COOH (pH = 3.1), bubbled with CO₂, simulating formation water

Steel	Steel state	N_i ($\times 10^3$ cycles)
20H2M	Unoperated	45
20H2M	Operated	34
35XM	Unoperated	36
35XM	Operated	28

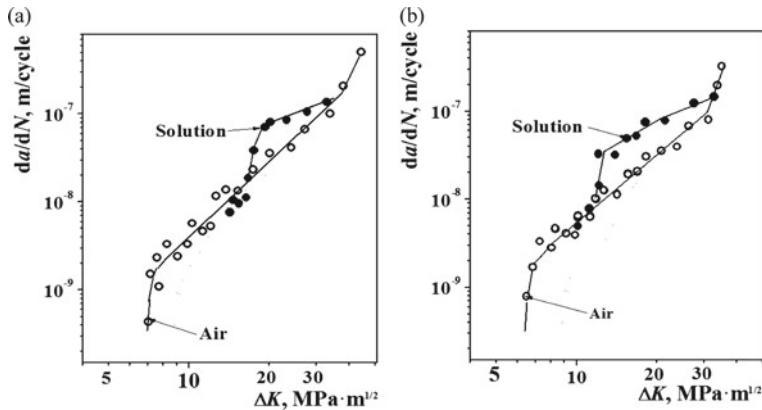


Fig. 13.1 Fatigue crack growth diagrams for the 20H2M steel in air and in 1% NaCl solution + CH_3COOH ($\text{pH} = 3.1$), bubbled with CO_2 , simulating formation water: **a** in the unoperated state; **b** after 5.5 years operation

The effect of operational degradation of the 20H2M steel on fatigue crack propagation rate in air was only revealed in the near-threshold region of the fatigue crack growth curves da/dN — ΔK (Fig. 13.1). Thus, a slight decrease in the corrosion fatigue threshold ΔK_{thc} was observed.

It was revealed that formation water with $\text{pH} = 3.1$ intensified fatigue crack growth in the 20H2M steel in both investigated states (unoperated and post-operated) in the medium-amplitude region of loading (the Paris region) due to a combination of mechanisms of fatigue and stress corrosion cracking, as indicated by the tendency to form a plateau on fatigue crack growth diagrams (Fig. 13.1). It means that stress corrosion fatigue is realised under such circumstances: fatigue crack growth is significantly influenced by sustained load (predominantly a stress-dependent process [18]).

Acceleration of fatigue crack growth in the operated 20H2M steel in the corrosive environment is more intensive than in the unoperated steel. Moreover, fatigue crack growth acceleration in the operated 20H2M steel in acid formation water occurs at lower values of ΔK compared to that in the unoperated steel.

It should be also noted that a crack tip in the investigated acid solution can be hydrogenated as a result of hydrogen evolution during electrochemical interaction, and therefore, fatigue crack propagation can be influenced by hydrogen [19, 20].

13.4 Concluding Remarks

Long-term operation of the low-alloyed 20H2M and 35XM steels of sucker rods caused decrease in corrosion resistance by 10–15% and in corrosion fatigue resistance in approximately 25% in CO_2 -containing formation water with $\text{pH} = 3.1$. Fatigue crack growth acceleration in the 20H2M steel in both investigated states

(unoperated and post-operated) in acid formation water was revealed in the medium-amplitude region of loading due to a combination of mechanisms of fatigue and stress corrosion cracking (stress corrosion fatigue). Acceleration of fatigue crack growth in the operated 20H2M steel in acid formation water occurred at lower values of ΔK compared to that in the unoperated steel. Environmentally friendly inhibitor was proposed to protect the operated steel of sucker rods against corrosion and corrosion fatigue failure in acid formation water.

References

1. Kopei BV, Zvirko OI, Venhrynyuk TP, Slobodyan ZV, Shtoiko IP (2020) Elevation of the fatigue strength of pump rods as a result of treatment with a special medium. *Mater Sci* 56(1):125–131
2. Liang H, Li XM (2014) Analysis on failure mechanism of sucker rod pumping system. *Adv Mater Res* 875–877:1219–1224
3. Du H, Qi Y, He Y, Zhu H, Li Z, Yang Y, Meng S (2018) Study on stress corrosion characteristics of different Grade H sucker rods. *Chem Eng Trans* 66:145–150
4. Duan DL, Geng ZL, Jiang SL, Li S (2014) Failure mechanism of sucker rod coupling. *Eng Fail Anal* 36:166–172
5. Popoola LT, Grema AS, Latinwo GK, Gutti B, Balogun AS (2013) Corrosion problems during oil and gas production and its mitigation. *Int J Ind Chem* 4(35):1–15
6. Ding H, Xie JF, Bai ZQ, Li Y, Long Y, Qi DT, Li HB (2009) Fracture analysis of a connecting rod for oil pumping unit in China western oilfield. *Eng Fail Anal* 105:313–320
7. Kharchenko EV, Polishchuk LK, Zvirko OI (2014) Estimation of the in-service degradation of steel shapes for the boom of a clamp-forming machine. *Mater Sci* 49(4):501–507
8. Pustovoi VM, Reshchenko IO, Zvirko OI (2015) Influence of long-term cyclic deformation on the electrochemical behavior of steels of marine gantry cranes. *Mater Sci* 51(1):125–130
9. Zvirko O, Nykyforchyn H, Tsyruynyk O (2019) Evaluation of impact toughness of gas pipeline steels under operation using electrochemical method. *Proc Struct Integr* 22:299–304
10. Dzioba I, Zvirko O, Lipiec S (2021) Assessment of operational degradation of pipeline steel based on true stress–strain diagrams. *Lect Notes Civ Eng* 102:175–187
11. Zvirko O, Gabetta G, Tsyruynyk O, Kret N (2019) Assessment of in-service degradation of gas pipeline steel taking into account susceptibility to stress corrosion cracking. *Proc Struct Integr* 16:121–125
12. Lesiuk G, Szata M (2015) Kinetics of fatigue crack growth and crack paths in the old puddled steel after 100-years operating time. *Frat Integrita Strutt* 9(34):290–299
13. Polishchuk LK, Kharchenko HV, Zvirko OI (2015) Corrosion-fatigue crack-growth resistance of steel of the boom of a clamp-forming machine. *Mater Sci* 51(2):229–234
14. Lesiuk G, Kucharski P, Correia JAFO, De Jesus AMP, Rebelo C, Simões da Silva L (2016) Mixed mode (I+II) fatigue crack growth of long term operating bridge steel. *Proc Eng* 160:262–269
15. Voloshyn VA (2020) Cyclic corrosion crack resistance of an exploited welded joint of 17G1S pipe steel. *Mater Sci* 56(1):119–124
16. Okipnyi I, Poberezhny L, Zapukhliak V, Hrytsanchuk A, Poberezhna L, Stanetsky A, Kravchenko V, Rybitskyi I (2020) Impact of long-term operation on the reliability and durability of transit gas pipelines. *Strojnický Cas* 70(1):115–126
17. Chmielewski R, Muzolf P (2021) Analysis of degradation process of a railway steel bridge in the final period of its operation. *Struct Infrastruct Eng*. <https://doi.org/10.1080/15732479.2021.1956550>
18. McEvily AJ, Wei RP (1972) Corrosion fatigue: chemistry, mechanics and microstructure. *NACE, Houston*, pp 381–395

19. Nykyforchyn HM (1997) Effect of hydrogen on the kinetics and mechanism of fatigue crack growth in structural steels. *Mater Sci* 33(4):504–515
20. Dmytrakh I, Leshchak R, Syrotyuk A (2021) Effect of environmental composition on fatigue crack growth and hydrogen permeation in carbon pipeline steel. *Lect Notes Civ Eng* 102:145–159

Chapter 14

Increasing the Durability of Critical Parts in Heavy-Duty Industrial Machines by Deep Cryogenic Treatment



Pavlo Krot , Serhii Bobyr , Ivan Zharkov , Ihor Prykhodko ,
and Przemysław Borkowski 

Abstract This paper provides a brief overview and results of conducted studies on the increasing wear resistance and durability of heavy-duty machines in different branches of industry. The proposed approach is based on the Deep Cryogenic Treatment (DCT) of parts made of alloy steel. Although this physical phenomenon has been known for ages, it still has contradictory opinions among practitioners and therefore is not widely used. In our studies, technological schedules and corresponding cryogenic equipment were developed and tested. It was shown that DCT is not substitutive but a complementary stage of the standard heat treatment procedures. In distinction from different surface hardening technologies, DCT has a permanent effect on the whole volume of parts. Wear reduction is achieved due to a complete transformation of retained austenite to martensite as well as fine carbides precipitation at the sub-zero temperature range. Additional effects are stress release and hardness homogenisation over the whole large-scale parts subjected to DCT. Particular features of this technology are considered as a time of parts holding at cryogenic temperatures, preferable cooling medium, heating/cooling rates. Recommendations are given for successful DCT implementation in the mining industry depending on steel chemical composition and pre-treatment quenching schedules.

Keywords Heavy-duty machines · Wear · Deep cryogenic treatment (DCT)

P. Krot (✉) · P. Borkowski
Faculty of Geoen지니어ing, Mining and Geology, Wrocław University of Science and Technology,
50-421, Wrocław, Poland
e-mail: pavlo.krot@pwr.edu.pl

P. Borkowski
e-mail: przemyslaw.borkowski@pwr.edu.pl

S. Bobyr · I. Prykhodko
Iron and Steel Institute of Z.I. Nekrasov, National Academy of Sciences of Ukraine, Dnipro
49107, Ukraine
e-mail: isi@ukr.net

I. Zharkov
Cryogenic Technologies Laboratory, Institute of Physics, National Academy of Sciences of
Ukraine, Kyiv 03028, Ukraine
e-mail: zharkov@iop.kiev.ua

14.1 Introduction

The demands for productivity and reliability of heavy-duty machines are constantly increasing in different industries such as mining and minerals processing, metallurgy, transport, energetics, aviation and military branches. Excessive wear causes high dynamic loads and further degradation of machines under non-stationary loading [1–3].

The designers and producers of machines need to satisfy the contradictory requirements to the weight and size and simultaneously provide the carrying capacity under the high specific mechanical loads of critical parts (gears, bearings, rolls, springs, cutting tools, etc.).

In this paper, several examples of DCT technology applications are considered for different alloy steels used in metal cutting tools, bearings, large rolls and gun barrels. Perspectives of DCT implementation in highly loaded mining machinery are discussed along with issues of this technology application in industry.

14.2 Theoretical Basis of DCT

To provide contact wear resistance of highly loaded elements, the appropriate heat treatment in conjunction with surface hardening technologies are usually used. However, quite different mechanical properties of the coating layer and the main material create internal stresses and subsequent initiation of cracks. One of the efficient methods to increase durability is the deep cryogenic treatment (DCT). The permanent effect after metals cooling was observed yet at the beginning of the twentieth century [4, 5]. Practical aspects of DCT are given in [6–8]. The main factors affecting steel properties are retained austenite transformation into martensite and later defined fine carbides precipitation [9]. Some additional positive effects of DCT are reported in [10, 11]. Initially used for cutting tools [12, 13], DCT was later spread out for cooling in machining [14] and cold rolling [15]. The majority of known studies are well categorised in [16] by the materials (including non-ferrous metals) and treated parts.

Relations of carbon content and alloy elements on the critical points of martensite transformation M_s , M_f are given in Fig. 14.1.

Hence, using highly alloyed steels is not only an expensive solution but also leads to a higher percentage of retained austenite (A_r) right after quenching. Depending on the chemical composition of steel, A_r content and the expected effect of DCT can be roughly estimated by the M_f value. Prolonging steel cooling below zero allows achieving the unique combination of increased hardness, wear-resistance and high impact toughness within a whole volume of alloy steel parts.

Nevertheless, some aspects of DCT are still not clarified to the end. In some papers, DCT is called “cryogenic quenching” that is due to understanding this process as the next stage of quick cooling process, which has been interrupted at the room

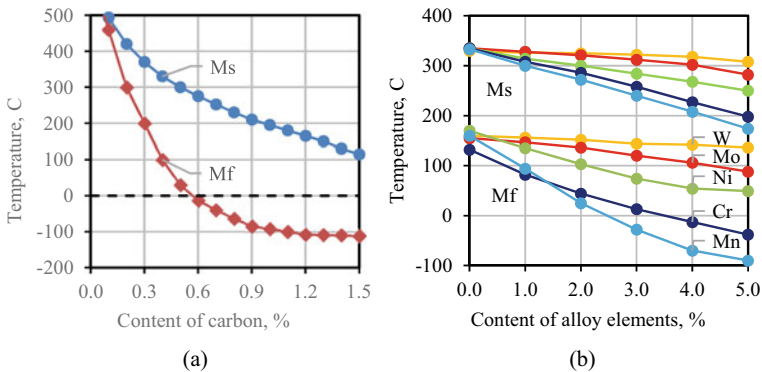


Fig. 14.1 The dependence of M_s , M_f on the amount of carbon (a) and alloying elements (b)

temperature, but when parts are immersed directly into liquid nitrogen. However, high cooling rates below zero are rather harmful because of restricting full martensite transformation and creating additional stresses especially for parts containing 10–20% of retained austenite.

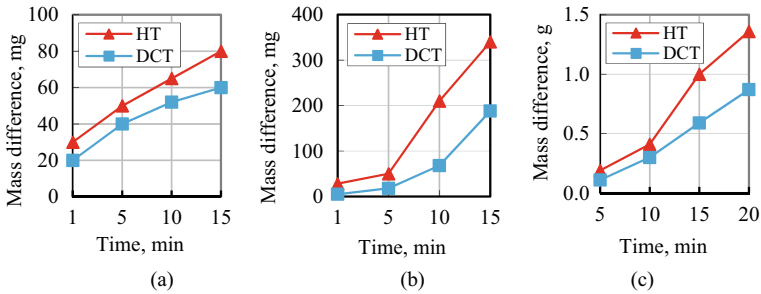
Some authors reported on the existence of optimal holding time for the DCT process, which is estimated to be about 24 h for their cooling schedules and steel grades [17]. In practice, it was observed that less effect can be achieved from “shallow” cooling (up to -70 °C but below the M_f) in contrast to “deep” (-196 °C) cooling, while the most intensive isothermal martensitic transformation was observed in the vicinity of -150 °C [18]. One more subject for detailed theoretical research is multistage DCT, which is less reported but has a greater effect with fewer total holding time and coolant consumption [19]. Hence, this phenomenon needs further investigation including temperatures for subsequent tempering, which may influence the overall DCT effect.

14.3 Results of Research

Theoretical and experimental research on DCT is conducted by the collaboration of several institutions aimed at the development of technological regimes and computer-controlled chambers (cryogenic processors) for programmable treatment of large-scale parts within the range ± 190 °C having minimum liquid nitrogen consumption (patents UA 84214, 106517). Different aspects of DCT are investigated, e.g. optimal time of parts holding in a nitrogen atmosphere, cooling/heating rates, cyclic treatment at different lowest temperatures and subsequent tempering. To investigate the internal stresses and temperature fields, the finite-element models (FEM) are developed [20] combined with Continuous Cooling Transformation (CCT) diagrams and analytical models of phase transformations [21, 22]. Based on these studies, the optimal heat treatment (HT) schedules are determined.

Table 14.1 Results of DCT implemented on different alloy steels

Parameters	M2 (cutter)	90CrSi (drill)	100Cr6 (bearing)
Microhardness, $\Delta\%$	170	3	25
Wear resistance, $\Delta\%$	26	65	59

**Fig. 14.2** Mass lost in abrasive wear tests: M2 cutter (a); 90CrSi drill (b); 100Cr6 bearing (c)

14.3.1 Cutting Tools and Bearings

Cutting tools and bearings made of different alloy steels were subjected to DCT. The total processing time was 26 h, holding time at gaseous nitrogen was 18 h. The cooling rate was 1 °C/min, and the heating rate was 2 °C/min. Results of abrasive wear testing are given in Table 14.1 and summarised in Fig. 14.2.

Changes in the microhardness of tool steels after DCT do not correlate with the wear resistance of the samples. For the M2 steel, microstructure homogenisation and the precipitation of fine carbides prevails as a mechanism for increasing the operational properties of tools, while in steels 90CrSi and 100Cr6, the transformation of retained austenite into martensite is the main mechanism due to the lower temperature of preliminary quenching and the absence of high-temperature tempering.

14.3.2 Steel Rolling Mills

The complicated alloy steels 50Cr5NiMoV, 65Cr2Si3MoV, 70Cr3MnNiMoV were investigated, which are used for large-scale rolls subjected to severe contact stresses in rolling mills. With increasing carbon and silicon content, the retained austenite fraction in the microstructure after quenching increases from 1 to 5%. Experiments showed wear resistance improvement by about 40% for 65Cr2Si3MoV even after short 2×60 min cycles of DCT [20]. The problems related to small quantities of retained austenite measurement are solved by the ultrasound technique [23].

14.3.3 Gun Barrels

Investigation of gun barrels made of 38Ni3CrMoV (AISI 4340) alloy steel subjected to DCT showed a small increase of macro hardness (2–3 HRC) but its full homogenisation over a length. The achieved increase in wear resistance is about 17–22% while a required level of impact toughness is ensured [24]. The variation of holding time at the DCT stage from 1 to 24 h did not affect the final results.

14.3.4 Perspectives of DCT in Mining Machines

Mining equipment is operated at the combination of cyclic fatigue, abrasive wear, impact load and corrosion. Higher yield strength and abrasion-resistant materials are costly, therefore, standard solutions are thermal spray coating and surface hardening. However, heat-affected zones (HAZ) cause carbides precipitation across grains boundaries with subsequent corrosion. Based on the grades of alloy steels used in mining machines, the following critical parts are promising for DCT: slurry pumps impellers, protective liners and grinding balls in tumbling mills, crusher cones, rock drilling and cutting tools, bucket teeth of excavators and brakes disks of load-haul-dump (LHD) vehicles as well as bearings, gears, nozzles.

14.4 Conclusions

The main problem of DCT implementation is in fact that producers of industrial machines, spare parts and assembly units for repair do not encourage any interference into supplied equipment, otherwise, guaranty obligations are violated. Hence, only simple or internally produced parts are available for DCT in enterprises. Producers of equipment are rarely agreed to introduce novel technology although the greatest effect may be achieved if DCT is conducted right after quenching of parts to prevent stabilisation of austenite. Nevertheless, post-production treatment even after standard HT procedures may have a great influence on the mechanical properties of high carbon (case hardened) and alloy steels. Due to that, producers of heavy-duty machines can reduce a large share of internal costs for purchased costly cutting tools as well as energy for tempering cycles aimed at the elimination of retained austenite in the parts.

To overcome obstacles for the wide commercialisation of this technology, industrial customers can cooperate either with the third parties providing DCT, which can offer both services—parts processing and lab testing capabilities (microstructure, wear, strength, toughness) or engage their R&D and engineering departments for the creation or acquiring of appropriate facilities (cryogenic processors). This

promising green technology saves energy for heating, uses no chemicals, is non-toxic and generates no environmental wastes [25].

The slowly evaporated gaseous nitrogen (about 78% of the atmosphere) needs standard ventilation to prevent its higher concentration and no more changes in the production process. It is most beneficial to conduct DCT for lightweight and costly critical parts of machines to reduce specific expenditures. However, heavy rolls (5–10 tones) and crushers cones [26] are also available for DCT in big chambers.

References

1. Konat Ł, Pękalski G (2020) Overview of materials testing of brown-coal mining machines (years 1985–2017). In: Sokolski M (eds) Mining machines and earth-moving equipment. Springer, Cham, pp 21–58
2. Krot PV (2019) Dynamical processes in a multi-motor gear drive of heavy slabbing mill. *J Vibroeng* 21(8):2064–2081
3. Krot P, Prykhodko I, Raznosilin V, Zimroz R (2020) Model based monitoring of dynamic loads and remaining useful life prediction in rolling mills and heavy machinery. *Smart Innov Syst Technol* 166:399–416
4. Dowdell RL, Harder OE (1927) The decomposition of the austenitic structure in steel. Part II. The decomposition of the austenite in liquid oxygen. *Trans Am Soc Steel Treat* 11:391
5. Schroeter K (1928) Transformation of austenite to martensite in liquid air. *Z Anorg Allgem Chem* 169:157–160
6. Gulyaev AP (1937) Decomposition of retained austenite at temperatures below 0 °C. *Bull Eng Tech* 5:7–11
7. Vorobiev VG (1954) Heat treatment of steel at temperatures below zero. State Publishing House of the Defense Industry, Moscow
8. Petrosyan PP (1957) Heat treatment of steel by cold. Theory and practice. Publishing House “Mashgiz”, Kyiv
9. Gavriljuk VG et al (2014) Carbide precipitation during tempering of a tool steel subjected to deep cryogenic treatment. *Metal Mater Trans A* 45:2453–2465
10. Jovicevic-Klug P et al (2021) Effect of deep cryogenic treatment on surface chemistry and microstructure of selected high-speed steels. *Appl Surf Sci* 548:149257
11. Baldissera P, Delprete C (2008) Deep cryogenic treatment: a bibliographic review. *Open Mech Eng J* 2:1–11
12. Tóth L (2021) The possibilities of the retained austenite reduction on tool steels. *Eur J Mater Sci Eng Crystal Eng* 6:99–105
13. Krot PV, Bobyr SV, Zharkov IP et al (2013) Increasing the wear resistance of tool steels by cryogenic treatment. *Metal Proc Equip* 4(34):88–98
14. Zindani D, Kumar K (2020) A brief review on cryogenics in machining process. *SN Appl Sci* 2:1107
15. Prykhodko IY, Krot PV (2009) Actual areas of cryogenic technologies use in rolling production. *Metall Process Equip* 1:10–16
16. CTD—Cryogenic treatment database. <http://www.cryogenictreatmentdatabase.org>. Last accessed 21 Sept 2021
17. Amini K et al (2012) Investigating the effect of holding duration on the microstructure of 1.2080 tool steel during the deep cryogenic heat treatment. *Vacuum* 86:1534–1540
18. Gavriljuk VG et al (2015) A concept for deep cryogenic treatment of tool steels. *Int Conf Stone Concr Mach (ICSCM)* 3:236–244
19. Alava LA (2008) Multistage cryogenic treatment of materials: process fundamentals and examples of application. In: Proceedings of the 10th international conference “cryogenics 2008”. ICARIS, Praha, Czech Republic, pp 223–230

20. Krot P, Bobyr S, Dedik M (2017) Simulation of backup rolls quenching with experimental study of deep cryogenic treatment. *Int J Microstruct Mater Prop* 12(3–4):259–275
21. Bobyr SV (2108) Nonequilibrium thermodynamic model of diffusionless transformation of an austenite in alloys on the base of iron. *Metallofiz Noveishie Tekhnol* 40(11) 1437–1451 (in Russian)
22. Bobyr SV (2020) Kinetics of formation of martensitic crystals in iron-based alloys. *Metallofiz Noveishie Tekhnol* 42(11):1573–1582
23. Bobyr S et al (2020) Analysis of the amount of retained austenite in the structure of steel rolls for sheet rolling. *Fundam Appl Probl Ferrous Metal* 34:256–264
24. Bobyr S et al (2021) Influence of modes of thermal hardening and the subsequent cryogenic processing on structure and properties of steel 38Ni3CrMoV. *Metal Sci Treat Metal* 27(98):14–22
25. Cahn J (2019) Reducing wear with deep cryogenics. *Min Mag* 15:15–17
26. Cahn J (2021) Deep cryogenic treatment of crusher cones. *Canadian Mining Magazine*, <http://canadianminingmagazine.com/in-this-issue/>. Last accessed 21 Sept 2021

Chapter 15

Risk-Based Inspection Strategies of Miter Gates Based on Structural Health Monitoring



Thuong Van Dang and Philippe Rigo

Abstract All over the world, many existing gates are used for inland navigation infrastructures. Miter gates are widely used over 90% of navigation locks in the United States due to their well-proven design, economic and aesthetic advantages. The purpose of the inspection strategy is to ensure the safe operation and serviceability of these structures. Inspection and monitoring of hydraulic steel structures are costly and generally performed by visual inspection at approximately 5–10 year intervals. There are many factors leading to the extensive degradation of miter gates including fatigue failure caused by cyclic loading, effects of environmental conditions, increasing load or design requirements over time. Therefore, it is required to use continuous monitoring system of miter gates to obtain the changes of the structural status as a function of time using real-time data. This paper presents a framework where a heuristic rule is used for risk-based inspection planning of a miter gate based on Structural Health Monitoring (SHM).

Keywords Fatigue · Miter gate · Risk-based inspection planning · Dynamic Bayesian networks · Structural health monitoring

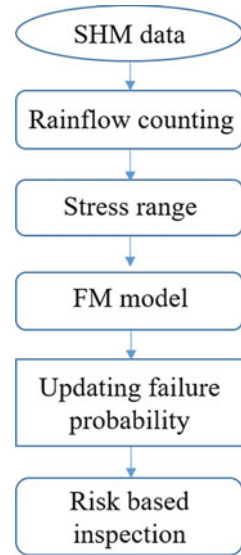
15.1 Introduction

There are presently a lot of miter navigation lock gates in operation along the inland waterways in the United States as well as all over the world. A lot of miter gates were fabricated a couple of decades ago and they are near or have reached their design life (>50 years). Fatigue is one of the major causes of failure of steel structures, particularly the welded steel structures. It reflects inherently poor and vulnerable fatigue performance of welded joints. Fatigue cracks are complicated, and they can be

T. Van Dang (✉)
Thuyloi University, 175 Tay Son, Dong Da, Hanoi, Vietnam
e-mail: thuongdv@tlu.edu.vn

P. Rigo
Department of ArGenCo/ANAST, Faculty of Applied Sciences, University of Liège, Liège, Belgium

Fig. 15.1 SHM optimal inspection methodology



developed from unexpected initial defects induced by the manufacturing processes. Miter navigation lock gates are susceptible to fatigue as they experience relatively large cyclic loads, multiple times every day, typically leading to 100,000–1000,000 cycles over the duration of the operation. Moreover, there are other factors leading to an extensive degradation of miter gates, such as effects of environmental conditions, increasing load or design requirements over time. SHM provides an update of the structural status and loading variation as a function of time using real-time data. This study presents a framework where a heuristic rule is used for risk-based optimal inspection strategies of a miter gate based on SHM data (Fig. 15.1).

15.2 Structural Health Monitoring

SHM is defined as the observation process of a structure for a specified period utilizing regularly spaced measurements to assess the health of a structure and predict its remaining life [1]. SHM has been utilizing in many fields, for example, aircraft, bridges, offshore structures for more than 30 years. For hydraulic steel structures, Commander et al. [2] performed tests of monitoring strain at over 30 locations on the Emsworth downstream miter gate. Their research provided additional occurrence of unexpected field data to further identify irregular lock gate behavior. Treece et al. [3] used SHM to detect the deterioration between the quoin and wall boundary on the downstream miter lock gates at Lock and Dam 27 on the Mississippi River, USA.

SHM is a useful technology and is considered to be crucial for the future. Recently, the United States Army Corps of Engineers (USACE) [4] has developed an SHM

program to monitor for changes in behavior of lock gates and this study utilizes SHM data of the Greenup miter gate from SMART Gate. Measured data are collected and extracted every 15 s. The sensors installed in the project are the strain gauge model HBWF-35-125-6-150GP-NT, 350 Ω , full-bridge, HiTec temperature-compensated gauges. Stress cannot be measured directly and it is inferred from the measure of strain and the Young's modulus of elasticity (Hooke's law).

15.3 Rainflow Counting

Rainflow cycle counting algorithm was developed by Japanese engineers, Endo and Matsuishi in 1968 [5]. It is used to determine the number of cycles for different mean stress and stress ranges in a complex load-time history. Standard practices for cycle counting in fatigue analysis E1049-85 have been published [6]. This standard is a compilation of acceptable procedures for rainflow cycle counting methods applied in fatigue analysis.

In the rainflow cycle counting process, it is essential to clean unrealistic, duplicated, and redundant points. A useful technique proposed by Mai [7] was utilized in this paper. Figure 15.2 shows rainflow counting result of a strain gauge at the Greenup miter gate over a 12 months duration.

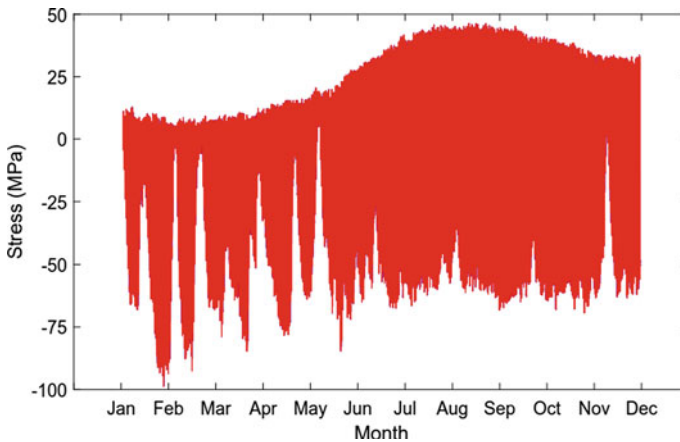


Fig. 15.2 Stress analysing of a measurement point

15.4 Methodology

Fatigue crack growth is a model based on fracture mechanics (FM) and can be used to analyze the crack propagation through the thickness. The most widely used model is the Paris–Erdogan law [8]. Crack depth at time t can be calculated by Eq. (15.1).

$$a_t = \left[a_{t-1}^{1-\frac{m}{2}} + \left(1 - \frac{m}{2}\right) C B_m^m B_y^m Y^m B_s^m \pi^{m/2} \sum_{j=1}^k \left(\Delta\sigma_j^{m_{SN}} n_j\right) \right]^{2/(2-m)} \tag{15.1}$$

where a_0 ($t = 1$) is the initial crack size. Y is geometry function. C and m are material parameters. $\Delta\sigma_j$ is stress range and n_j is number of cycles corresponding. B_m , B_s , B_y are measurement, load, and geometry uncertainties.

A Dynamic Bayesian network (DBN) is a special class of Bayesian network. It was developed in the early 1990s by extending static belief-network models to more general dynamic forecasting models [9]. DBN consists of a sequence of slices that are connected by direct links from nodes in slice i to nodes in slice $i + 1$. A framework for stochastic modeling of deterioration process and updating the failure probability was introduced by Straub [10]. In this paper, DBN is used to determine degradation modeling for a welded joint. The random variables, B_m , B_s , B_y (Fig. 15.3) are defined in order to reduce the dimensionality of the status space and consequently computation time. Therefore, the variables a_0 and q are discretized in 200 states. The discretization scheme for the random variables is shown in Table 15.1.

The DBN representation including inspection results (I_t) is shown in Fig. 15.3. By instantiating the inspection variables (I_t) in the DBN with the observed events at

Fig. 15.3 DBN for modelling of deterioration

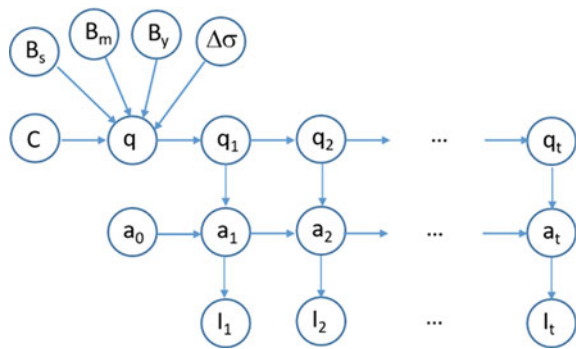


Table 15.1 Discretization scheme

Variable	Final interval boundaries
a_0	$\left[0, \exp\left(\ln(10^{-5}) : \frac{\ln(22) - \ln(10^{-5})}{200-2} : \ln(22)\right), +\infty\right]$
q	$\left[-\infty, \exp\left(0 : \frac{\ln(10^{-3})}{200-2} : \ln(10^{-3})\right), +\infty\right]$

the times of inspection, the failure probability can be updated by Eq. (15.2).

$$p(a_t, q_t | I_0, \dots, I_t) \propto p(a_t, q_t | I_0, \dots, I_{t-1}) p(I_t | a_t) \tag{15.2}$$

15.5 Risk-Based Inspection Strategies

Risk-based inspection is an interesting issue for hydraulic steel structures due to the increase of aging structures and that many failures are detected. The risk-based optimal inspection strategies are identified according to the collected SHM data for the heuristic decision rule “inspection performed when failure probability threshold is reached” [11].

The total expected cost during the lifetime E_{tot} maybe written as Eq. (15.3).

$$E_{tot} = \sum_{t=1}^T C_f P_f(t) \frac{1}{(1 + \alpha_r)^t} + \sum_{i=1}^{T_{insp}} \frac{C_r P_r(T_i) + C_{insp}}{(1 + \alpha_r)^{T_i}} + C_{SHM} \tag{15.3}$$

where P_f denotes the annual failure probability in year t and P_r is the probability that a repair is performed in year t after an inspection done in the same year. P_{fc} is the cumulative failure probability. C_f , C_r , C_{insp} and C_{SHM} are failure, repair, inspection, and SHM costs. The assumed failure cost C_f is 12×10^6 (\$) and the total time period is 100 years. The different costs are given in Table 15.3.

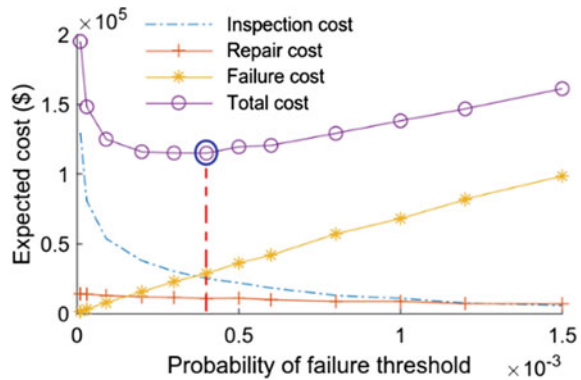
Figure 15.4 shows that the optimal annual failure probability threshold is $P_f = 4 \times 10^{-4}$ and the expected costs $E_{tot} = 1.15 \times 10^5$ (US\$).

In this paper, the risk-based inspection planning for the Greenup miter gate subject to fatigue based on SHM is carried out. Other factors that influence the integrity of miter gates, for example, corrosion may be considered in future work.

Table 15.3 Cost characteristics

Inspection cost, C_{insp}	0.0025 C_f
Repair cost, C_r	0.04 C_f
Failure cost, C_f	12×10^6
Discounting rate, α_r	0.03

Fig. 15.4 Optimal expected costs



Acknowledgements The authors acknowledge the financial support by the Wallonie-Bruxelles International (WBI), Belgium. Thanks also USACE for the data.

References

1. Gopalakrishnan S, Ruzzene M, Hanagud S (2010) Computational techniques for structural health monitoring. London, Springer
2. Commander BC, Schulz JX, Goble GG (1994) Detection of structural damage on miter gate. Technical report, U.S. Army Corps of Engineers
3. Treece Z, Smith M, Wierschem N, Sweeney S, Spencer B (2015) USACE SMART gate: structural health monitoring to preserve America's critical infrastructure. <https://doi.org/10.12783/shm2015/287>
4. USACE (2014) Lock characteristics general report. Vicksburg
5. Matsuishi M, Endo T (1968) Fatigue of metals subjected to varying stress. *Jpn Soc Mech Eng* 68(2):37–40
6. Standard ASTM (1997) Standard practices for cycle counting in fatigue analysis. ASTM E1049-85, Am Soc Test Mater. West Conshohocken, PA
7. Mai AQ (2018) Updating failure probability of a welded joint considering monitoring and inspection for offshore wind turbine substructures. University of Liege
8. Paris P, Erdogan F (1963) A critical analysis of crack propagation laws. *J Basic Eng.* <https://doi.org/10.1115/1.3656900>
9. Dagum P, Galper A, Horvitz E (1992) Dynamic network models for forecasting. In: Proceedings of the eighth annual conference on uncertainty in artificial intelligence, pp 41–48
10. Straub D (2010) Stochastic modeling of deterioration processes through dynamic Bayesian networks 135(10):1089–1099
11. Van Dang T, Mai QA, Morato PG, Rigo P (2019) Optimal inspection and repair scheduling for mitre lock gates. *Marit Eng* 1–9. <https://doi.org/10.1680/jmaen.2019.10>

Chapter 16

Fatigue Behavior of Re-tightened Bolted Joints Affected by Vibration-Induced Loosening



Baris Tanrikulu, Ramazan Karakuzu, Sarper Dogan, and Sezgin Yurtdas

Abstract Threaded fasteners are one of the most preferred joining methods today. Although there are many studies in this field, the number of researches on fatigue life as a result of the loosening behavior of fasteners is very limited. Within the scope of the study, the effects of preload loss due to transversal displacement for re-tightened bolted joints to their fatigue behaviors were investigated. The study was conducted by using $M8 \times 1.25$ 10.9 DIN 933 bolts and DIN 934 nuts with various preloads. Tightened bolts were subjected to repeated transversal displacement, and clamp load values were monitored and recorded for each cycle. Bolts subjected to preload loss were re-tightened to their desired clamp load values, and Junker vibration test was restarted. Increase on the tightening torque values after each usage was observed. This situation is caused by the friction coefficient change after reusing fasteners. Due to the increase in the friction coefficient, tightening torque values were increased as expected. Fastener subjected to repeated tightening failed during Junker vibration test due to fatigue. This phenomenon was mainly caused by high friction coefficient which prevents loosening and lead fasteners to take higher shear loads. A critical tightening-preload loss factor has been found for predicting early fatigue failure caused by loosening for re-tightened bolted joints.

Keywords Fastener · Loosening · Fatigue · Re-tightening

16.1 Introduction

Fasteners maintain their place as a basic component in many industries today. Although there are many types of threaded fasteners, in principle, they all work based on the same rule. Nowadays, many new studies are carried out to examine

B. Tanrikulu (✉)

The Graduate School of Natural and Applied Science, Dokuz Eylul University, Izmir, Turkey

R. Karakuzu

Department of Mechanical Engineering, Dokuz Eylul University, Izmir, Turkey

S. Dogan · S. Yurtdas

Norm Civata R&D Center, Norm Civata San ve Tic A.Ş.A.O.S.B., Izmir, Turkey

the behavior of fasteners, especially due to the increasing use of fasteners in vital applications. In a study conducted by Junker in 1969 [1], it was first discovered that bolts may lose their clamp loads under cyclic lateral loads. This study has formed the basis of vibration-induced relaxation studies today. In the following studies, it was revealed that cyclic loads acting perpendicular to the bolt axis caused micro-slippages in the bolt bearing surface and threaded region, and that there was a discrepancy in the clamp load over time. Within the scope of another study, the most effective parameters affecting the loosening mechanism were examined, and it was determined that the most effective parameters were clamp load, friction coefficient, and lateral displacement values [2, 3].

One of the most critical parameters in determining the service life of the fasteners has been the fatigue life. Although there are many different test and calculation methods in the industry, there are constant deviations in fatigue lives due to many variables affecting during assembly. Most basic reasons for fatigue-based damages encountered are that the insufficient clamp load values led to not obtain the desired number of lifetimes. Especially in the literature, studies have been started recently to examine the fatigue life of fasteners subjected to lateral displacement [4]. The obtained findings show that clamp load loss caused by vibrational loosening directly affects the fatigue behavior. As is known, fasteners are coated with special coatings in order to increase their corrosion resistance and to keep the friction coefficient value in a constant value. Although these coatings allow bolts to be used more than once, there are changes in the friction coefficient of the bolt after each use due to the wear. This situation reveals that even if the same bolt is tightened to the same torque value in the next time, it cannot show the same performance, and there will be a change in the clamp load. In a study conducted for this purpose, it was revealed that the coefficient of friction obviously changes depending on the number of tightening [5].

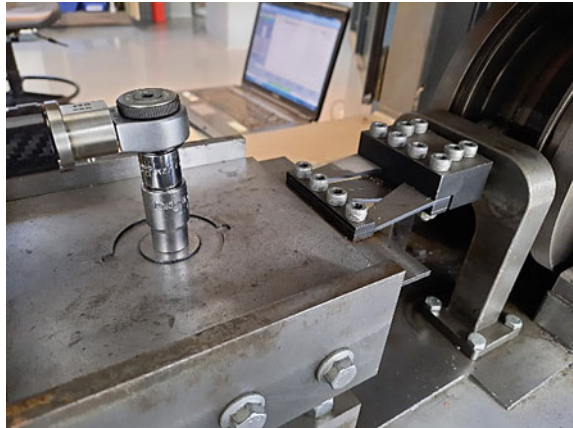
Within the scope of the study, the fatigue life of the reused bolts exposed to lateral load was investigated, and a comparison was made. Findings of the study combine two main sections of the literature with a new perspective, which is the effect of friction coefficient change under the combination of relaxation and fatigue.

16.2 Material and Method

Within the scope of the experimental studies, $M8 \times 1.25 \times 50$ 10.9 DIN 933 bolts and DIN 934 nuts, which are frequently used in the industry, were used. Since the behavior of the friction coefficients under repeated tightening will be examined, Delta Protect KL100 VH301 GZ Zinc Flake coating system with 0.09–0.14 friction coefficient is preferred as the surface coating. In the experimental part of the study, the Junker vibration device given in Fig. 16.1 is used to obtain cyclic loosening values.

During the tests, clamp load created by the bolt was instantly measured by the load cells, and cycle-based data were recorded. As a result, clamp load-cycle graphs were

Fig. 16.1 Junker vibration test device



obtained for each test. Since our aim is to determine the change in the coefficient of friction and to determine how this effect affects loosening and fatigue, the same bolt is tightened again after each test, and the torque values are recorded.

16.3 Experimental Results

Six experiments were conducted for each combination, and average of loosening curves was taken from the Junker vibration test device. Loosening rate values were obtained based on the slope of the clamp load-cycle graph for each combination. Clamp load-cycle graphs for 12.1 and 17.1 kN are shown in Figs. 16.2 and 16.3. For

Fig. 16.2 Clamp load-cycle graphs for 12.1 kN

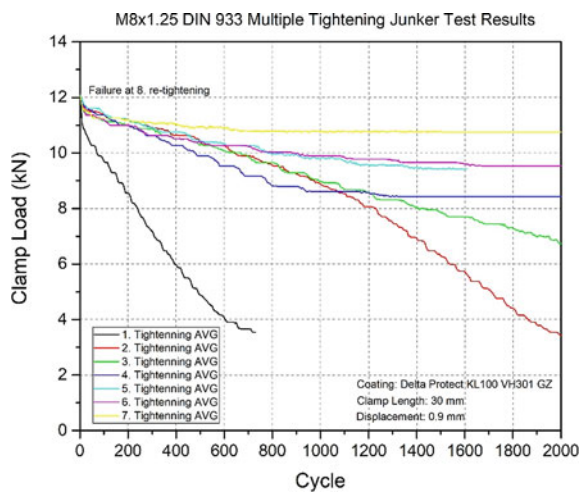
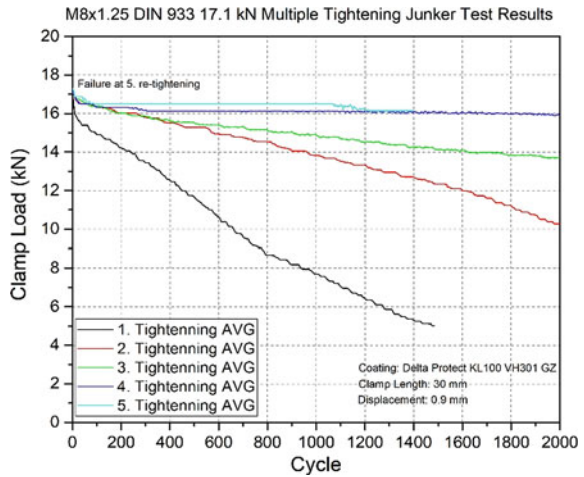


Fig. 16.3 Clamp load-cycle graphs for 17.1 kN



12.1 kN load set, fatigue failures of the bolts were observed at eighth re-tightening. On the other hand, for 17.1 kN bolts started to fail at fifth re-tightening. As expected, results reveal that higher initial clamp load values decrease fatigue life of the bolts under transverse loading as expected.

For bolts tested under 17.1 kN, it is clearly seen that slowing on the loosening behavior causes to fail fasteners after repeated tightening. In the first three tightening operations, due to friction coefficient increase, bolt loosening rates decrease drastically. Total locking occurs after fourth tightening which causes extra stress on the radius region of the bolt head and cause failures. For bolts tested under 12.1 kN, same loosening rate decrease was figured out for the first three tightening operations (Figs. 16.4 and 16.5).

Fig. 16.4 Critical failure zone for 17.1 kN

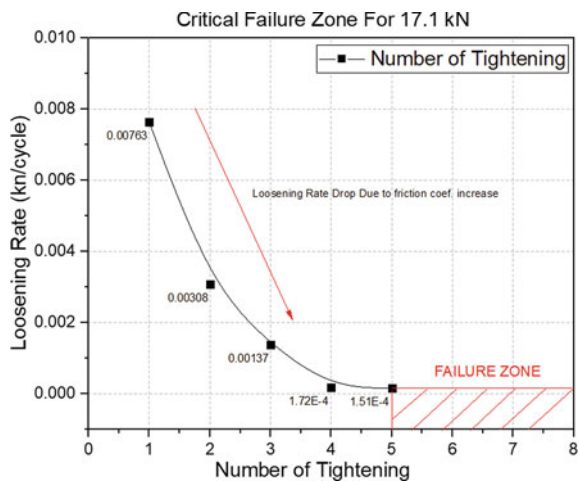
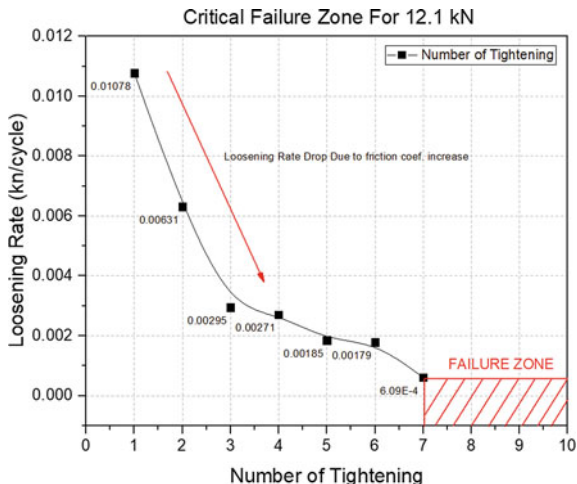


Fig. 16.5 Critical failure zone for 12.1 kN



Critical failure zones were determined based on the number of tightening and loosening rates obtained from the experimental test. Both load cases show similar behavior with parallel to friction coefficient change with a repeated tightening.

16.4 Conclusion

Findings showed that lateral displacement which is causing loosening on bolt preload values is the main reason of the fatigue failures. Due to the increase in friction coefficient, which is mainly caused by the repeated usage, bolts start to gain resistance to loosening which is also in good agreement with the literature. Having an increased friction coefficient value with a combination of high lateral loads causes some locking phenomena which reveals itself as a fatigue fracture due to the bending loads acting on under head radius. Findings also reveal that loosening of the bolt prevents an early fatigue failure phenomenon in case of a high lateral displacement, but with the increase of the friction coefficient value, initial clamp load value, and stress caused by bending loads, fatigue lives of bolts start to decrease drastically. A critical tightening-preload loss factor has been found for predicting early fatigue failure caused by loosening for re-tightened bolted joints with an enlarged experimental study. Ongoing experimental and simulation results which include an enlarged mapping show that there is a critical equilibrium point for high lateral displacements with an increased fatigue life.

References

1. Junker G (1969) New criteria for self-loosening of fasteners under vibration. SAE Technical Paper 690055
2. Hess DP, Keifer OP, Moody CB (2014) Tests on loosening of aviation threaded fasteners with different washer configurations. *J Fail Anal Prev*. <https://doi.org/10.1007/s11668-014-9873-8>
3. Sanclemente JAA, Hess DPP (2007) Parametric study of threaded fastener loosening due to cyclic transverse loads. *Eng Fail Anal* 14:239–249. <https://doi.org/10.1016/j.engfailanal.2005.10.016>
4. Yang L, Yang B, Yang G, Xu Y, Xiao S, Jiang S, Chen J (2021) Analysis of competitive failure life of bolt loosening and fatigue. *Eng Fail Anal* 129
5. Liu Z, Zheng M, Yan X, Zhao Y, Cheng Q, Yang C (2020) Changing behavior of friction coefficient for high strength bolts during repeated tightening. *Tribol Int*

Chapter 17

Friction Resistances in Internal Gear Pump with Modified Sickle Made of Plastic



Krzysztof Towarnicki , Michał Stosiak , Piotr Antoniak ,
Tadeusz Leśniewski , Kamil Urbanowicz , and Paweł Śliwiński 

Abstract This paper presents modifications of the sickle insert (constructional and material) made in a gear pump with internal meshing. The introduced design change consists in making an incision in the sickle insert. Due to this treatment, the races of the insert are pressed against the apex wheels of the gears. The introduced compensation causes a smaller drop in pump efficiency with increasing discharge pressure. The article describes the measuring stand and presents the measurement results. Measurements of the frictional resistance between the material of the gears and the insert material used during the measurements were carried out for the selected parameters of the pump operation. Differences in the frictional resistance were obtained between the POM material used for the sickle insert and the metal pin which reflects the material of the gear. The obtained results confirm that the increased pressure and speed of friction between cooperating elements causes increased frictional resistance, which was confirmed by measurements of torque changes on the pump shaft with the change of discharge pressure and different rotational speeds of the pump. The performed tests will allow to direct the work in order to make an optimal insert

K. Towarnicki (✉) · M. Stosiak · P. Antoniak · T. Leśniewski
Faculty of Mechanical Engineering, Wrocław University of Science and Technology, Wrocław,
Poland
e-mail: krzysztof.towarnicki@pwr.edu.pl

M. Stosiak
e-mail: michal.stosiak@pwr.edu.pl

P. Antoniak
e-mail: piotr.antoniak@pwr.edu.pl

T. Leśniewski
e-mail: tadeusz.lesniewski@pwr.edu.pl

K. Urbanowicz
Faculty of Mechanical Engineering and Mechatronics, West Pomeranian University of
Technology, Szczecin, Poland
e-mail: kamil.urbanowicz@zut.edu.pl

P. Śliwiński
Faculty of Mechanical Engineering and Ship Technology, Gdańsk University of Tech, Gdańsk,
Poland
e-mail: pawel.sliwinski@pg.edu.pl

that meets the requirements of the constructed (prototype) pump with increased efficiency at higher pumping pressures. This will allow the development of a pump with plastic displacement elements, so that the described pump will be able to be used in the future, inter alia, in the pharmaceutical and food industries.

Keywords Gear pump · Capacity · Internal gearing · Sickle insert · Friction resistances

17.1 Introduction

Owing to their many advantages, gear pumps are the displacement pumps most often used in industry. Nevertheless, efforts are still made to further reduce their weight and dimensions through the use of, e.g., novel lightweight materials [1] or plastics, such as polyoxymethylene (POM) [2]. Efforts are also made to reduce the noise emitted by gear pumps [3]. Currently hydraulic power systems are subject to miniaturization aimed at reducing the size of hydrostatic drives (the relevant discipline is called micro hydraulics) [4]. Micropumps must meet the following requirements: small unit capacity, ability to generate high pressures, small flow rate variation at rising pressure, low flow rate fluctuation, high performance and durability, resistance to working fluid impurities and relatively low production costs. For this reason, micropumps are modeled as classic gear pumps. They are used in hydrostatic drives and fluid dispensing in the automotive, chemical, food and pharmaceutical industries [5].

17.2 Test Methods and Materials

17.2.1 Hydraulic Tests

The research was performed in two stages. The first part concerned the determination of the hydraulic parameters of the pump depending on the design of the modified sickle insert. The second part related to the measurement of the frictional resistance of the material used for the modified sickle insert POM C (natural white) was used for the tests. The choice of research materials was also conditioned by the analysis of the literature and whether there were any previous attempts to use these materials in hydraulic systems. Measurements of hydraulic parameters were carried out on the measuring stand shown, in Fig. 17.1.

The following parameters were adopted: two rotational speeds and a pressure load of 6–20 bar with a step of 1 bar. The value of the parameters was selected taking into account the performance of the body part and the sickle-shaped insert made of plastic. Measurements were recorded after the indications of measuring instruments stabilized and at a constant temperature of the working medium of 333 [K]. The research was carried out for two materials of the sickle insert with two

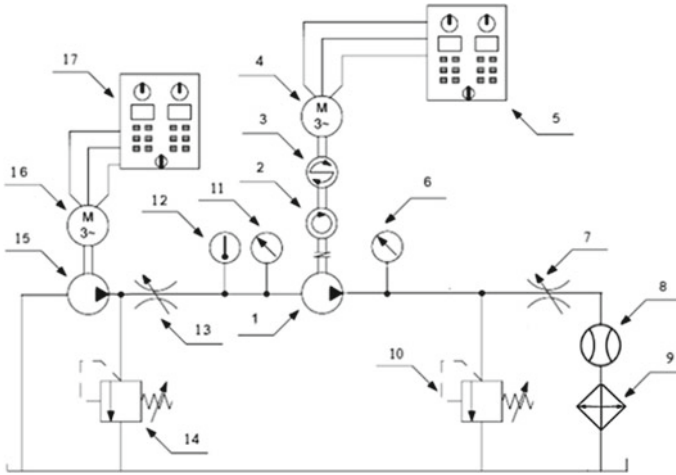


Fig. 17.1 Hydraulic diagram of test system. 1—tested gear pump, 2—tachometer, 3—torque meter, 4—electric motor, 5—control cabinet, 6—pressure transducer, 7—throttle valve, 8—flowmeter, 9—cooler, 10—safety valve, 11— pressure transducer, 12—thermometer, 13—throttle valve on feed pump discharge line, 14—safety valve on feed pump discharge line, 15—feed pump, 16—electric motor driving feed pump, 17—control cabinet of electric motor driving feed pump. *Source* [6]

different modifications—with cuts of a length equal to $1/4$ of the length of the insert in modification I and with a length equal to half the length of the insert in modification II, respectively. The purpose of the modifications was to determine their impact on the improvement in efficiency with increase in discharge pressure.

17.2.2 Tribological Tests

The tribological tests were performed with the ball on disk method using the T-11 tribotester produced by the Institute of Sustainable Technology in Radom. Measurements were carried out at the temperature of $21\text{ }^{\circ}\text{C}$. The samples used were disks $1''$ in diameter and 6 mm in height made of the test materials, and as counter-samples a pin made of 100Cr6 bearing steel, sized $1/4''$ was used. During the test, the value of the friction force was recorded. This method was chosen due to its simplicity and the ease of making samples. During determination of the range of input quantities, efforts were made to reproduce the actual operating conditions occurring in hydraulic cylinders and the ones that corresponded to the hydraulic tests were adopted. The study parameters were as follows:

- Load— 9.81 N and 14.72 N ,
- Linear speed— 0.26 m/s and 0.52 (which corresponded to 750 rpm and 1500 rpm),
- Friction distance— 250 m (which corresponds to the test time of 962 s),
- Renolin VG46 lubricant,

- Environmental conditions were constant throughout all tests and under control.

The initial (criterion) value was the friction force and the weighted wear. Weight loss due to the hygroscopic nature of some materials was not taken into account.

The tests were repeated four times for each measurement point. The results were statistically processed with a confidence level of 95% using the Student’s t-test.

17.3 Presentation and Discussion of Test Results

17.3.1 Hydraulic Tests

The results were made by making an incision in the sickle insert up to 1/4 of its length. After analyzing the data, it can be concluded that the introduced modification improved the pump performance. There is a significantly smaller drop in performance with increase in discharge pressure. Subsequently, measurements were made with the insert with a cut halfway down its length (Fig. 17.2). Measurements were made using the same pump construction, and only the sickle inserts were changed. Figure 17.3 shows exemplary results of the pump efficiency measurements with the second modification of the sickle insert.

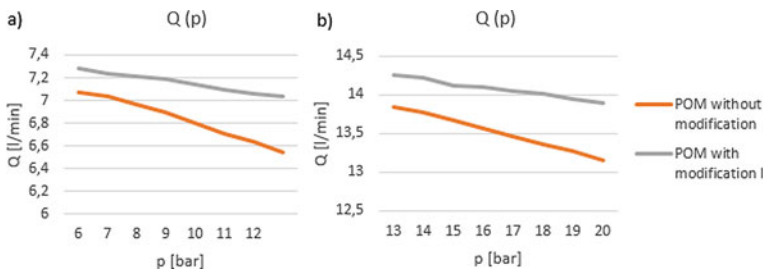


Fig. 17.2 Characteristics of internal gear pump with sickle insert modification I at different rotational speeds of pump shaft: **a** $n = 750$ [rpm] **b** $n = 1500$ [rpm]. Source [7]

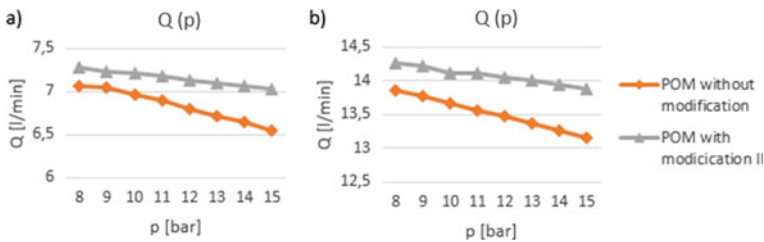


Fig. 17.3 Exemplary characteristics of internal gear pump with sickle insert modification II at different rotational speeds of pump shaft: **a** $n = 750$ [rpm] **b** $n = 1500$ [rpm]. Source [7]

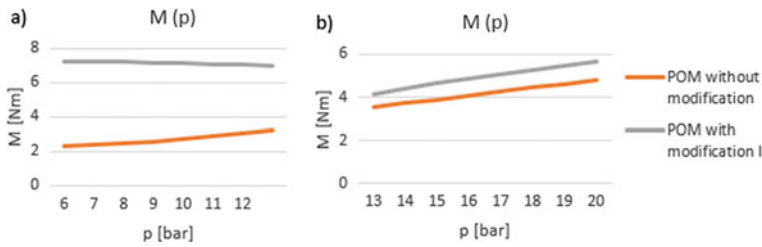


Fig. 17.4 Exemplary changes in pump shaft torque with increasing pressure for insert with modification I: **a** $n = 750$ [rpm], **b** $n = 1500$ [rpm]

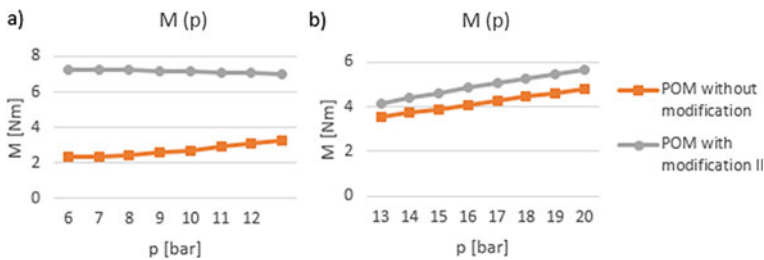


Fig. 17.5 Exemplary changes in pump shaft torque with increasing pressure for insert with modification II: **a** $n = 750$ [rpm], **b** $n = 1500$ [rpm]

Measurements were made in a narrow pressure range with a relatively low value, taking into account the average pressure obtained during the operation of hydrostatic drive systems. For this reason, the differences in the shape of the characteristics are not very clear.

Simultaneously, measurements of pump efficiency and changes of torque on the pump shaft were performed depending on the pump discharge pressure. Figures 17.4 and 17.5 show the results of measurements of the torque on the pump shaft, respectively, for the inserts with the 1st and 2nd modifications.

Taking into account the above-presented measurement results of the torque change on the pump shaft depending on the pump discharge pressure, it can be concluded that with the increase in the discharge pressure, the torque on the pump shaft increases. This applies to a system with and without modification. However, in a system with modification, a significant increase in torque is visible with increasing discharge pressure. This is due to the greater pressing force of the crescent insert raceway against the tips of the toothed wheel.

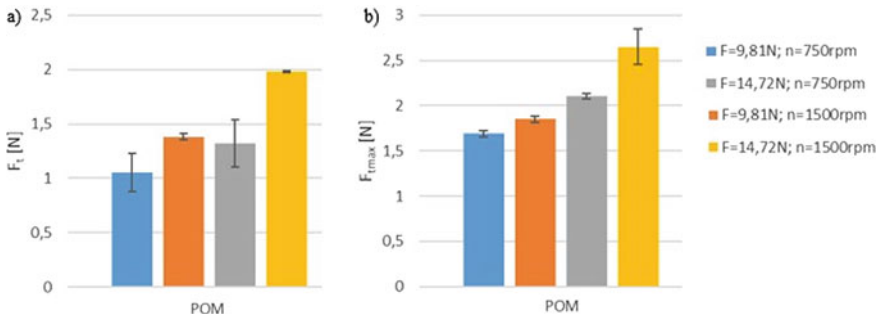


Fig. 17.6 **a** Average friction force of a steel mandrel against POM material, **b** Maximum friction force of a steel mandrel against POM material

17.3.2 Tribological Tests

Figure 17.6 shows the results of the measurements of the frictional resistance for POM C material.

As it can be noticed in Fig. 17.6, much lower frictional resistance is observed with less pressure and lower speed. The presented results reflect the results presented for the operational parameters of the pump, in particular, the change of torque on the pump shaft depending on the discharge pressure. Measurements should be made for other materials and the frictional resistance should be compared.

17.4 Conclusion

The current trend in the design of hydraulic power transmission system focuses on higher pressures. Due to it, smaller effectors can be used to generate the same forces. The changes are aimed to increase the power-to-weight ratio of hydrostatic drives. This leads to higher efficiency of the machines and devices equipped with this kind of drive. Consequently, it becomes necessary to build efficient pumps capable of generating higher pressures. Therefore, pumps with internal gearing are becoming increasingly popular [8], mainly owing to their lower noisiness due to the high tooth contact ratio resulting in quieter pump operation and lower pump filling losses. The modification consists in introducing an appropriate cut, whereby a radial compensation is obtained.

In addition to the appropriate shape of the insert, the material from which it is made is an important factor. The work uses POM C plastic. It was used to maintain the high efficiency of the pump and to obtain the smallest possible torque on the pump shaft needed to drive it. Based on the measurement results of the torque change on the pump shaft, it can be seen that the torque increases with increasing pressure. This is due to the greater pressure of the surface of the insert raceway against the tips of

the gears. More pressure is exerted in the modified inserts, therefore the torque is higher compared to the unmodified inserts. Owing to the modification, a significant improvement in pump efficiency at increasing discharge pressure has been achieved.

References

1. Błażejowski W, Lubecki M, Mayer P, Stosiak M, Towarnicki K (2018) The use of new materials in elements and hydraulic systems. In: NiSHP conference materials, centre for appraisal and personnel development of the SIMP branch in Wrocław, Wrocław, pp. 23–24
2. Stryczek J, Banaś M, Krawczyk J, Marciniak L, Stryczek P (2017) The fluid power elements and systems made of plastics. *Procedia Eng* 176:600–609
3. Fiebig W, Korzyb M (2015) Vibration and dynamic loads in external gear pumps. *Arch Civil Mech Eng* 15(3):680–688
4. Kollek W, Osiński P, Stosiak M, Wilczyńska A, Cichoń P (2014) Problems relating to high-pressure gear micropumps. *Arch Civil Mech Eng* 14:88–95
5. Kollek W (2011) Fundamentals of design, modelling, operation of microhydraulics components and systems. Oficyna wydawnicza PWr, Wrocław
6. Antoniak P, Stosiak M, Towarnicki K (2019) Preliminary testing of the gear pump with internal gearing with modifications of the sickle insert. In: Engineering mechanics 2019: 25th international conference: book of full text, 13–16 May 2019, Svratka, Czech Republic
7. Antoniak P, Stosiak M, Towarnicki K (2019) Preliminary testing of the internal gear pump with modifications of the sickle insert. *Acta Innovations* 32:84–90
8. Stryczek J, Bednarczyk S, Biernacki K (2014) Gerotor pump with POM gears: design, production technology, research. *Arch Civil Mech Eng* 14(3):391–397

Chapter 18

Defect Development in Ultra-Supercritical Steam Turbine Rotors According to British Standards



Mariusz Banasziewicz and Janusz Badur

Abstract The paper presents procedures for defect propagation assessment recommended by British standards and their application to rotating components. The way of applying these procedures was shown by an example of a steam turbine rotor with particular use of a characteristic strain model of creep. Calculations of the flaws located at the rotor axis have shown that their growth in the design life is small. The performed analyses have also shown that crack development due to low-cycle fatigue is comparable to that due to creep and cannot be ignored under typical service conditions. The presented results prove the usefulness of the methods included in the British standards for crack growth assessment in components subject to centrifugal load.

Keywords Fracture · Creep · Low-cycle fatigue · Steam turbine

18.1 Introduction

Steam turbine rotors operating at ultra-supercritical steam conditions are made of martensitic steel forgings that have diameters reaching 1300 mm. For such dimensions of forgings, the minimum detectable flaw size using ultrasonic methods is 2.2 mm [1]. At steam temperatures exceeding 600 °C defects of such sizes can propagate due to creep and, in addition, due to low-cycle fatigue induced by transient thermal stresses.

Defect propagation rate and the risk of brittle fracture can be assessed with the help of procedures recommended by British standards R5 [2] and BS7910 [3]. The procedures are based on a reference stress and their background has been set out in [4]. High-temperature defect assessment procedures are now well established and have been used in assessment of plant components [5], steel pipes [6, 7] and welds [8, 9].

M. Banasziewicz (✉) · J. Badur

The Szewalski Institute of Fluid-Flow Machinery Polish Academy of Sciences, Fiszerza 14, 80-231 Gdańsk, Poland

e-mail: mbanaszkiewicz@imp.gda.pl

The application of these procedures has been focused and validated on pressurized components of high-temperature plants. The present paper describes the way of applying these procedures to rotating components like turbine rotors with particular application of a characteristic strain model of creep [10].

18.2 Crack Growth Calculation Methodology

18.2.1 Creep Crack Growth

The development of a crack from a pre-existing crack-like defect in the rotor forging involves three stages [2–4]:

- an incubation period while the initial crack blunts without any significant crack extension
- a period of stress redistribution due to creep from the initial elastic state to widespread creep conditions during which creep crack growth occurs in unsteady creep conditions
- a period of steady-state creep crack growth under widespread creep conditions.

According to the R5 methodology [2], the incubation time, redistribution time and steady-state creep crack growth rate are all dependent upon the reference stress σ_s in the structure containing a crack of length a . The reference stress is defined to be the material yield stress σ_y at operating temperature divided by the limit load factor $L_r(a)$ of the structure [4]:

$$\sigma_{\text{ref}}(a) = \frac{\sigma_y}{L_r(a)} \quad (18.1)$$

The limit load factor is the factor by which the nominal load on the structure must be increased to produce plastic collapse.

Considering the case of a postulated crack-like defect existing at the time of manufacture of the rotor forging, BS7910 provides the following expression for the estimation of the incubation time t_i before which no creep crack growth occurs [3]:

$$t_i = 0.89 \left(\frac{\sigma_{\text{ref}}(a) t_{R,\text{ref}}}{(K^p)^2} \right)^{0.85} \quad (18.2)$$

where $t_{R,\text{ref}}$ is the time for creep rupture to occur at the reference stress and operating temperature, and K^p is the stress intensity factor under the primary loading on the structure.

The redistribution time may be estimated using the following expression which is given in both standards [2, 3]

$$\varepsilon_c(\sigma_{\text{ref}}(a), t_{\text{red}}) = \frac{\sigma_{\text{ref}}(a)}{E} \left(\frac{K^{(P+S)}}{K^P} \right)^2 \quad (18.3)$$

where the left-hand side of the equation is the creep strain accumulated over the redistribution time t_{red} at the reference stress, which is equated to the elastic strain obtained by dividing the reference stress by the elastic modulus E , factored by the square of the ratio of crack stress intensities under combined primary plus secondary loading to the primary loading alone.

For times in excess of the redistribution time, steady-state creep conditions exist and creep crack growth can be estimated using the C^* parameter, which is the creep equivalent of the J contour integral used to describe elastic-plastic fracture below the creep range. C^* is defined as the following function of creep strain rate [2]

$$C^* = \sigma_{\text{ref}} \dot{\varepsilon}_c(\sigma_{\text{ref}}(a), \varepsilon_c) \left(\frac{K^P}{\sigma_{\text{ref}}} \right)^2 \quad (18.4)$$

where $\dot{\varepsilon}_c(\sigma_{\text{ref}}(a), \varepsilon_c)$ is the creep strain rate at the reference stress and the current creep strain.

The crack growth rate \dot{a} is obtained from C^* by the relationship

$$\frac{da}{dt} = A(C^*)^q \quad (18.5)$$

where A and q are material constants obtained from creep crack growth tests.

If the total time over which the creep crack growth assessment is made is less than the redistribution time than [2] indicates that a more appropriate parameter for the evaluation of creep crack growth is $C(t)$ where $C(t)$ is related to C^* by the following expression:

$$\frac{C(t)}{C^*} = \frac{\left(1 + \frac{\varepsilon_c}{\varepsilon_e}\right)^{\frac{1}{1-q}}}{\left(1 + \frac{\varepsilon_c}{\varepsilon_e}\right)^{\frac{1}{1-q}} - 1} \quad (18.6)$$

where ε_c is the accumulated creep strain at time t , ε_e is the elastic strain and q is the exponent in the creep crack growth relation.

The crack extension occurring during the assessment period is then calculated from

$$\Delta a = \int_0^{t_a} A(C(t))^q dt \quad (18.7)$$

18.2.2 Fatigue Crack Growth

BS7910 provides three criteria to test the severity of fatigue loading which, if satisfied, permit the effect of the fatigue loading to be ignored. These criteria are [3]:

- crack growth due to fatigue alone must be shown to be small, and should not exceed one-tenth of the calculated creep crack growth
- the stress in the structure due to combined cyclic plus steady load should not exceed the material yield stress (except at the crack tip)
- the cyclic plastic zone size at the crack tip must be small in relation to the crack size or any other dimension characteristic of the structure.

Fatigue crack growth in service was calculated using the following relationship between crack growth rate and the cyclic range of stress intensity

$$\frac{da}{dN} = A_0 C_T (\Delta K)^n \quad (18.8)$$

where A_0 is the upper bound fatigue crack growth rate constant at 20 °C, C_T is a correction factor for the effect of temperature, determined from the elastic modulus at 20 °C and at operating temperature T from $C_T = (E_{20}/E_T)^3$, ΔK is the cyclic range of stress intensity factor and n is a material constant.

The cyclic plastic zone size r_p at the crack, tip was estimated from the following expression [3]

$$r_p = \beta \left(\frac{\Delta K}{2\sigma_y} \right)^2 \quad (18.9)$$

where β is $1/2\pi$ for plane stress and $1/6\pi$ for plane strain.

18.3 Characteristic Strain Model of Creep

18.3.1 Model Equations

The characteristic strain model (CSM) of creep developed by Bolton [10] is a simple model capable of predicting material creep deformation in primary, secondary and tertiary creep regimes. This is a very important and useful feature of the model as design calculations require mean creep behavior in primary and secondary regimes, and residual lifetime analyses are based on minimum creep behavior in secondary and tertiary regimes [11]. The use of the same creep model in design and remaining lifetime calculations facilitates comparisons of calculation results and model validation.

Using this model, Bolton [12] analyzed the behaviors of both simple structures, such as beams and pipes, and more complicated components, such as valve chests. The characteristic strain model was further examined by Boyle [13] using conventional creep mechanics. Three structures were analyzed, namely, a beam under bending, a pressurized thick cylinder and a notched bar, and it was shown that the characteristic strain model predicted stress distributions at steady-state creep similar to those obtained by traditional models, in particular Norton's power law. Also rotating components like a cylinder or a steam turbine rotor was analyzed in [14] where it was shown that the model predictions at steady state are similar to those of the Norton model. The CSM was also applied to online monitoring of steam turbine rotors life [15].

In the characteristic strain model, the equivalent creep strain ε_c is calculated from the following model equation [10]:

$$\varepsilon_c = \frac{\varepsilon_\chi}{\sigma_R/\sigma - 1} \quad (18.10)$$

where σ is the current stress, σ_R is the rupture stress and ε_χ is a characteristic creep strain that is assumed to be a material constant at a given time and temperature.

The characteristic creep strain ε_χ can be evaluated using Eq. (18.10) and by knowing two stresses, i.e., the creep rupture strength σ_{R1} at time t_1 and the stress σ_{D1} to produce datum creep strain ε_D at time t_1 :

$$\varepsilon_\chi = \varepsilon_D(\sigma_{R1}/\sigma_{D1} - 1) \quad (18.11)$$

The creep rupture strength σ_R is described by a simple power-law relationship:

$$\sigma_R = \sigma_{R1}(t_1/t)^{1/m} \quad (18.12)$$

where m denotes the exponent in the power-law relationship evaluated from two values of rupture strengths at t_1 and t_2 :

$$m = \frac{\log(t_2/t_1)}{\log(\sigma_{R1}/\sigma_{R2})} \quad (18.13)$$

The model is thus described by three constants: σ_{R1} , σ_{R2} and σ_{D1} which have clear physical significance and can be derived from readily available data from standard creep tests. This means that no special creep testing is required for using the model for available materials and the sensitivity of creep deformation to rupture and creep strength values exhibiting significant scatter (e.g., for steels typically $\pm 20\%$ of mean value) can be easily studied.

18.3.2 Model Validation

The characteristic strain model was evaluated by Bolton [10] using creep and rupture data of P91 9%CrMo steel produced by the European Collaborative Creep Committee. The measured creep strain against the ratio of the applied stress to the rupture strength at 550 °C and 600 °C for times between 300 and 30000 h were compared with the predictions of the creep model corresponding to the best-fit value of the characteristic strain. It was shown that the creep model curves are consistent with the test data and can accurately reproduce the continuously varying slope of the measured curves [10].

Test data published in [1] were used for independent validation of the creep model for 9%CrMoVNbNB steel. Tests specimens were taken from a trial melt, trial rotor forging and production rotor from the edge and near-center location. Creep tests were conducted at 600 °C and 160 MPa load for 1300 h. The test results plotted as creep strain versus time are presented in Fig. 18.1 together with the prediction of the characteristic strain model. The parameters of the model were evaluated using the Larson-Miller parameter and creep rupture strength data presented in [1, 16]. The creep strengths adopted for the validation represent mean creep properties of 9%CrMoVNbNB steel. As it is seen, the CSM model predicts creep strains that are within the strains measured at different specimens and represents average behavior of the material.

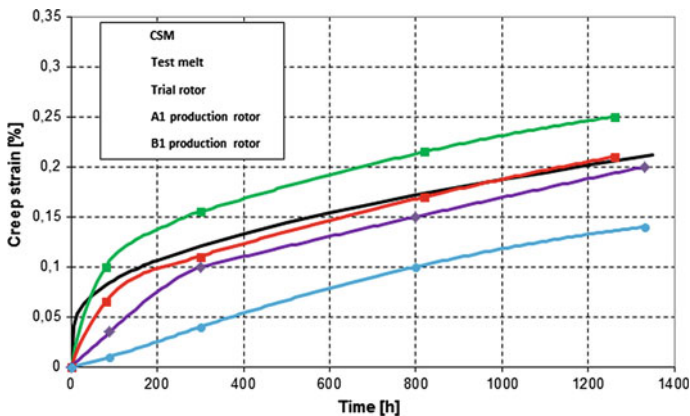


Fig. 18.1 Creep strain accumulation in rotor forgings

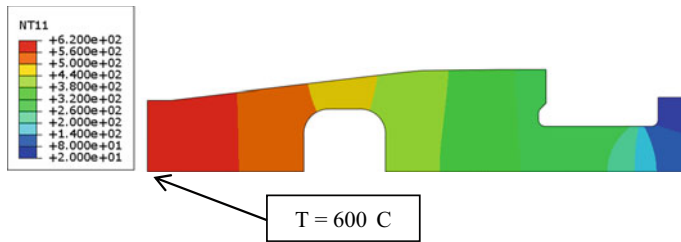


Fig. 18.2 Steady-state temperature distribution in the rotor

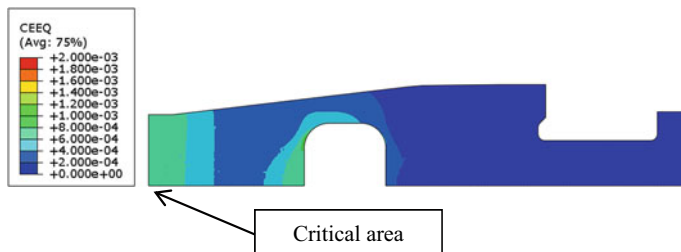


Fig. 18.3 Creep strain distribution in the rotor after 200 000 h

18.4 Defect Growth at Rotor Axis

18.4.1 Thermal and Creep Analysis

Finite element thermal and creep analyses of an ultra-supercritical rotor have been conducted using axisymmetric model to generate the basic results for creep crack growth calculation. Only half of the rotor was modeled due to symmetry of geometry and loads. Steady-state temperature and creep strain distribution in the rotor at the end of 200,000-h operation are shown in Figs. 18.2 and 18.3. The maximum creep strain at the rotor centreline occurs under inlet section due to the combination of high temperature ($T = 600\text{ }^{\circ}\text{C}$) and high centrifugal stress. This region was selected for creep crack growth investigation.

18.4.2 Calculation of Creep Crack Growth

Defect growth analysis was carried out assuming the likely extremes of crack geometry: a circular crack and an extended crack with the crack tips running parallel to the rotor axis. Both cracks are located at the rotor axis where temperature attains $600\text{ }^{\circ}\text{C}$ and maximum stresses are tensile. The rotor material is 9%CrMoVNbNB steel developed in COST522 program [1].

Table 18.1 Creep crack incubation times

Incubation time [hours]			
Circular crack		Extended crack	
Initial radius 2.2 mm	Initial radius 4.4 mm	Initial semi-depth 2.2 mm	Initial semi-depth 4.4 mm
3434	1905	1595	885

The reference stress required for determining the incubation time and the C^* parameter was calculated by performing finite element limit load analysis using a bi-linear elastic-plastic material model. The limit load was established by step-wise incrementation of the load beyond the normal rotational speed until plastic collapse of the section was calculated to occur.

Incubation times were calculated using Eq. (18.2) for both crack geometries and different initial crack sizes: 2.2 mm (minimum detectable flaw size) and 4.4 mm (for safety factor of 2 for crack size). The calculated incubation times under primary loading are given in Table 18.1. The incubation times are longer for circular cracks due to lower stress intensities as compared with extended cracks.

For determining the C^* parameter using Eq. (18.4), the instantaneous creep strain rate $\dot{\epsilon}_c$ must be first calculated for a given reference stress (as a function of crack size a) and accumulated creep strain ϵ_c . A time-stepping approach was proposed to apply to the characteristic strain model Eq. (18.10), starting at the end of incubation period for the assumed initial defect size. At a given time t beyond the incubation time, the reference stress at the current crack depth is used together with Eq. (18.10) to determine the creep strain at the current time and at a slightly later time $t + \delta$. The creep strain rate $\dot{\epsilon}_c$ is so determined and the value of C^* is calculated from Eq. (18.4) and $C(t)$ from Eq. (18.6).

The resulting redistribution times from Eq. (18.3) are calculated to be in excess of 200,000 h for both crack geometries and initial sizes. Therefore, according to the R5 procedure, since the total assessment time of 200,000 h is less than the redistribution time, the $C(t)$ parameter was used to evaluate creep crack growth.

Creep crack growth was calculated using Eq. (18.7) with material constants equal [2]: $A = 0.05$ and $q = 0.65$. The crack size development during rotor operation is shown in Fig. 18.4. The predictions show that extended cracks grow faster than circular cracks and after 200,000 h the difference in crack size is c.a. 1 mm. It is seen that the increase of crack sizes after such a long time is quite small and the final crack size is in the range of 2.9–3.6 mm for 2.2 mm initial crack and 5.5–6.6 mm for 4.4 mm initial crack. This gives a growth of 32–65% for the shorter crack and 26–51% for the longer crack over the entire lifetime of the rotor.

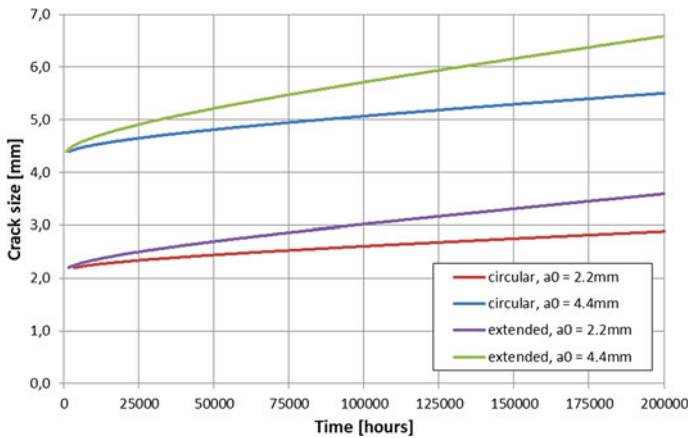


Fig. 18.4 Defect development at rotor axis under creep conditions

18.4.3 Calculation of Fatigue Crack Growth

Fatigue crack growth was calculated using Eq. (18.8) with $A_0 = 5.21E - 13$ and $n = 3$ [2]. The cyclic range of stress intensity factor ΔK was evaluated using stress ranges computed for cycles representing typical start-ups from a cold (CS), warm (WS) and hot (HS) state and a typical shutdown. A total of 3800 start-ups was assumed in the rotor lifetime with the start-ups' distribution according to IEC 60,045-1 [17], i.e., 100 cold, 700 warm and 3000 hot starts. The crack size development during rotor operation is shown in Fig. 18.5. Similar to the creep crack growth, the development of crack under low-cycle fatigue conditions was investigated for both crack geometries

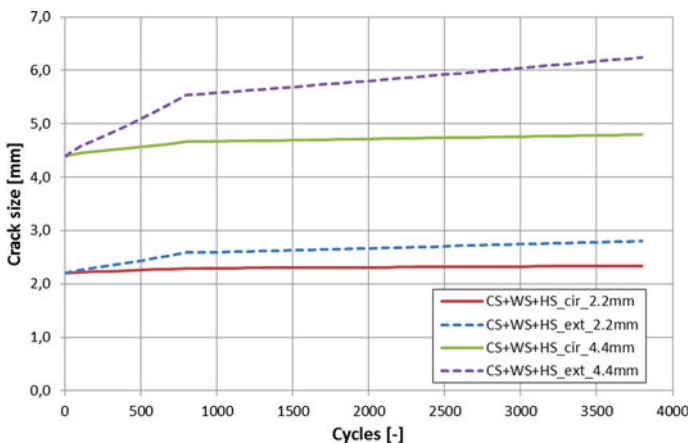


Fig. 18.5 Defect development at rotor axis under fatigue conditions

and initial sizes. As it is seen, also in case of fatigue, extended cracks grow faster than circular cracks and after 3800 cycles the difference in crack size is 0.5–1.5 mm. Similar to creep crack growth, the increase of crack sizes after such a high number of cycles is quite small and the final crack size is in the range of 2.3–2.8 mm for 2.2 mm initial crack and 4.8–6.2 mm for 4.4 mm initial crack. This gives a growth of 6–27% for the shorter crack and 9–42% for the longer crack over the entire lifetime of the rotor.

The size of plastic zone ahead of the circular crack tip estimated using Eq. (18.9) was 1.0% and 3.1% for plane strain and plane stress, respectively, while for the extended crack it was 2.6% and 7.7% of the initial crack size. These sizes of the plastic zone are not small and confirm the above results showing that fatigue crack growth cannot be ignored.

The final crack sizes obtained from creep and fatigue crack growth analyses can be assessed with respect to the critical crack sizes. For the worst combination of maximum principal stress and minimum fracture toughness at FATT50 [1] equal $K_{Ic} = 82\text{MPa}\sqrt{m}$, the critical crack size for circular and extended defects is 37 and 15 mm, respectively. These values are well above the crack sizes obtained at the end of rotor design life which proves defect tolerance of ultra-supercritical steam turbine rotors.

18.5 Summary

The presented methodology of crack growth assessment based on the calculation procedures given in the British standards R5 i BS7910 and the characteristic strain model of creep allows for effective assessment of the manufacturing flaws existing in ultra-supercritical steam turbine rotors. Calculations of the flaws located at the rotor axis, where their detection is most difficult, have shown that their growth in the design life is small and the final crack sizes calculated for different geometry and initial size are well below the critical crack sizes estimated for the rotor steel 9%CrMoVNbNB.

The performed analyses have also shown that crack development due to low-cycle fatigue is comparable to that due to creep and cannot be ignored under typical service conditions.

The presented results prove the usefulness of the methods included in the British standards for crack growth assessment in components subject to centrifugal load. In particular, the reference stress method in conjunction with the characteristic strain model of creep results in reasonable predictions of defect development and proves defect tolerance of ultra-supercritical steam turbine rotors.

References

1. Zeiler G (2017) Martensitic steels for rotors in ultra-supercritical power plants. In: Di Gianfrancesco A (ed) *Materials for ultra-supercritical and advanced ultra-supercritical power plants*. Elsevier, 143–174
2. An assessment procedure for the high temperature response of structures, R5 issue 3, British Energy Generation LTD (2003)
3. BS7910:2005 Guide to methods for assessing the acceptability of flaws in metallic structures, British Standards Institution (2005)
4. Webster GA, Ainsworth RA (1984) *High temperature component life assessment*. Chapman & Hall, London
5. Dean DW, Ainsworth RA, Booth SE (2001) Development and use of the R5 procedures for the assessment of defects in high temperature plant. *Int Journ Press Vess Piping* 85:108–116
6. Wasmer K, Nikbin KM, Webster GA (2003) Creep crack initiation and growth in thick section steel pipes under internal pressure. *Int Journ Press Vess Piping* 80:489–498
7. Gampe U, Seliger P (2001) Creep crack growth testing of P91 and P22 pipe bends. *Int Journ Press Vess Piping* 78:859–864
8. Nikbin KM (2013) Creep/Fatigue crack growth testing, modelling and component life assessment of welds. *Procedia Eng* 55:380–393
9. Samuelson LA, Segle P, Andersson P, Storesund J (2001) Creep crack growth in welded components—a numerical study and comparison with the R5 procedures. *Int Journ Press Vess Piping* 78:995–1002
10. Bolton J (2008) A ‘characteristic strain’ model for creep. *Mater High Temp* 25:197–204
11. Holdsworth SR (2008) Constitutive equations for creep curves and predicting service life. Abe F, Kern T-U, Viswanathan R (eds) *Creep resistant steels*. Woodhead Publishing Limited, Cambridge, 403–420
12. Bolton J (2008) Analysis of structures based on a characteristic-strain model of creep. *Int Journ Press Vess Piping* 85:108–116
13. Boyle JT (2011) The behaviour of structures based on the characteristic strain model of creep. *Int Journ Press Vess Piping* 88:473–481

Part III
Probabilistic Fatigue and Fracture
Approaches Applied to Materials
and Structures

Chapter 19

Fatigue Life Assessment Within the Frequency Domain for Explosive Cladded Joints Under Non-Gaussian Random Loading



Michał Böhmi 

Abstract The paper describes the problem of fatigue life assessment for the case of explosive cladded transition joints under random loading. Such elements are usually used in the lightweight automobile industry as well as in the marine industry. Due to this, they are undergoing random loading conditions in terms of road surface quality and the change of sea waves. The literature presents two domains in which one can approach this problem, which are the time domain and the frequency domain. The presented algorithm takes into account the residual stress effects which appear during the welding process in the form of the mean stress compensation with classical models such as the Gerber model. It also takes into account the effect of non-Gaussian loading by providing additional correction methods. The discussion on the use of strictly frequency domain estimates is provided and a number of probability density functions is presented.

Keywords Fatigue life assessment · Frequency domain · Probability density function · Spectral method

19.1 Introduction

19.1.1 Random Loading and Frequency Domain

Material fatigue is an important topic, especially due to the modern trend in the methodology of sustainable construction. This philosophy is aimed at preventing uncontrolled failures at various stages of production, as well as during the operation of the structure. Computational methods for estimating the fatigue life of metallic materials play an important role in the industry because bench fatigue tests require a lot of time and money. It is also very important to perform the tests with the use of a force profile that would simulate the actual load conditions, which is rare as

M. Böhmi (✉)

Department of Mechanics and Machine Design, Faculty of Mechanical Engineering, Opole University of Technology, ul. Mikołajczyka 5, 45-271, Opole, Poland
e-mail: m.bohm@po.edu.pl

usually bench tests are carried out under constant amplitude conditions. As we can read in the literature, the random variable loading conditions can be used in the process of fatigue lifetime estimation within the time and frequency domains [1–4]. The time domain requires specific information such as a full registration of loads appearing within a specific time frame. The frequency domain can be used to simulate the loading conditions according to probabilistic load distributions, which can be characterized for specific working conditions. In these terms only the frequency domain is a truly stochastic approach, as the loading history is not required. The paper presents the topic of fatigue life assessment of explosive cladded joints with the use of the frequency defined spectral method. The topic of estimation of the loads for non-stationary and non-Gaussian loading cases is widely discussed.

19.1.2 Explosive Cladded Materials

Many popular joining techniques are constantly evolving in terms of the accuracy and quality of the connections obtained. However, the problem of combining materials from different groups, such as, e.g., aluminum, titanium, copper and steel, using traditional techniques remains. That's why explosive welding remains an important technology for the problem of joining these materials. This method uses the force generated after the ignition of the explosive, causing a very high velocity and pressure of the air pushed out of the process zone between the joined plates in order to create a permanent connection between the materials. Such joined materials are used in many branches of the industry, where they are constantly being loaded with time varying forces such as the marine industry [5, 6]. In this respect, wind and sea conditions play a major role in this process. Characteristic for this method is the specific shape of the joint materials in the bonding zone, which is usually in the shape of a sine wave. For this reason, we are not able to completely calculate the stresses inside this type of joint, even for well-described tensile-compressive load cases, because due to the anisotropy of the joint, it is difficult to assess the cross-sectional area of individual materials. This fact is often simplified in terms of the loading description. An example of a transition joint has been presented in Fig. 19.1.

19.1.3 Explosive Cladded Materials Under Random Loading

Modern welding techniques cause various problems with the assessment of fatigue life. Problems arise from residual stresses, which can be assessed with advanced simulation methods such as the finite element method as well as other experimental bench tests with radiographic or borehole methods. Besides these, there is a problem with the assessment or generation of random loads influencing the material. The standard testing or simulation for such materials are rarely described exhaustively. Due to the high cost of such tests, it is advisable to use quick fatigue calculation methods

Fig. 19.1 Transition joint (steel + titanium + aluminium + aluminium) obtained with the use of the explosive welding method



such as those described in the frequency domain. These methods are operating on a Power Spectral Density (PSD), which can be generated on the basis of standardized Gaussian models as well as for specific conditions, which can include many real life effects such as the wind or sea forces. The PSD is used to calculate spectral moments which are used in order to calculate the probability density functions according to specific models. These functions are used in the process of fatigue damage accumulation and then used to calculate the fatigue lifetime. The main disadvantage of the frequency domain calculations is the fact that the PSD is always Gaussian. Therefore for the cases of non-Gaussian and non-stationarity, we need a set of compensation functions which are used in the process of the PSD modification before the actual spectral moments' calculations or during fatigue damage calculation. The methods presented in the literature have been discussed and compared in terms of their practical application in the case of materials connected with the technology of explosive welding under random loads.

19.1.4 Power Spectral Density Generation

The power spectral density should be obtained with the use of the Fourier transformation from the time domain data or directly by generating a given spectrum that can be described with the use of a deterministic model. Such direct PSDs can be generated for a certain wave height, wave period, etc. The most popular spectrum that is fitting to most areas around the world is called the Pierson-Moskowitz spectrum [7], which was developed for the North Sea. We can read all about the use of predefined spectrums in the process of fatigue damage estimation paper by Marquez et al. [8]. A standard spectrum can be generated with the use of the function:

$$G_x(f) = \lim_{\Delta f \rightarrow 0} \frac{\Psi_x(f, \Delta f)}{\Delta f} = \lim_{\Delta f \rightarrow 0} \frac{1}{\Delta f} \left[\lim_{T \rightarrow \infty} \frac{1}{T} \int_0^T x^2(t, f, \Delta f) dt \right], \quad (19.1)$$

where Ψ_x —mean square value of the signal $x(t)$, T —observation time, $x(t, f, \Delta f)$ —component of the function $x(t)$ in the frequency interval from f to $f + \Delta f$.

As for a spectrum for a certain sea state, we can use the Pierson-Moskowitz equation:

$$G_x(f) = \frac{H_s^2 \cdot T_D}{8\pi^2} (f \cdot T_D)^{-5} \cdot \exp \left[-\frac{1}{\pi} (f \cdot T_D)^{-4} \right], \quad (19.2)$$

where $G_x(f)$ —power spectral density expressed as the function of the frequency of the wave f , H_s —significant wave height with dominant period T_D .

19.1.5 Mean Stress Correction

The residual stresses, which can be experimentally verified with various methods such as the hole drilling method or simulations give us an additional information about the additional stresses. These stresses can be taken into account with the use of the mean stress effect correction. Due to this, we can use the method proposed by Niesłony and Böhm [9, 10], which takes into a transformation of the PSD due to mean stress with the use of classical mean stress compensation models. The transformed function can be described with the use of the equation:

$$G_{\sigma T}(f) = [K(\sigma_m, P)]^2 G_\sigma(f), \quad (19.3)$$

where $G_\sigma(f)$ is the power spectral density of a centered stress course and K is the transformation function, which can be defined, e.g., for the Gerber [9] model:

$$K_{Ge} = \frac{1}{1 - \left(\frac{\sigma_m}{R_m}\right)^2}, \quad (19.4)$$

where σ_m is the mean stress value, R_m is the ultimate stress.

19.1.6 Non-Gaussian Correction

As for one of the best approaches in terms of non-Gaussian frequency domain damage estimation methods, we can find many interesting approaches such as the one from Benasciutti and Tovo [11, 12]. Nevertheless, their methods do not allow to directly

use the PSD. In the case of most of natural phenomenon such as wind or sea waves, we have rather a non-Gaussian distribution. The spectral method of fatigue lifetime estimation causes any process to be Gaussian due to the Fourier transformation which gives us the PSD and is always Gaussian. In order to not lose the non-Gaussian information about a loading, we need to additionally add this information in the calculation process. This can be added with the use of the Braccesi et al. [3] approach, where we are using the kurtosis and skewness information in order to calculate the non-Gaussian correction factor. The factor can be presented in the form of the equation:

$$\lambda_{ng} = \exp\left(\frac{m^{\frac{2}{3}}}{\pi} \left(\frac{K-3}{5} - \frac{S^2}{4}\right)\right), \tag{19.5}$$

where S -skewness, K -kurtosis, m - is the Wöhler slope coefficient for the analyzed material.

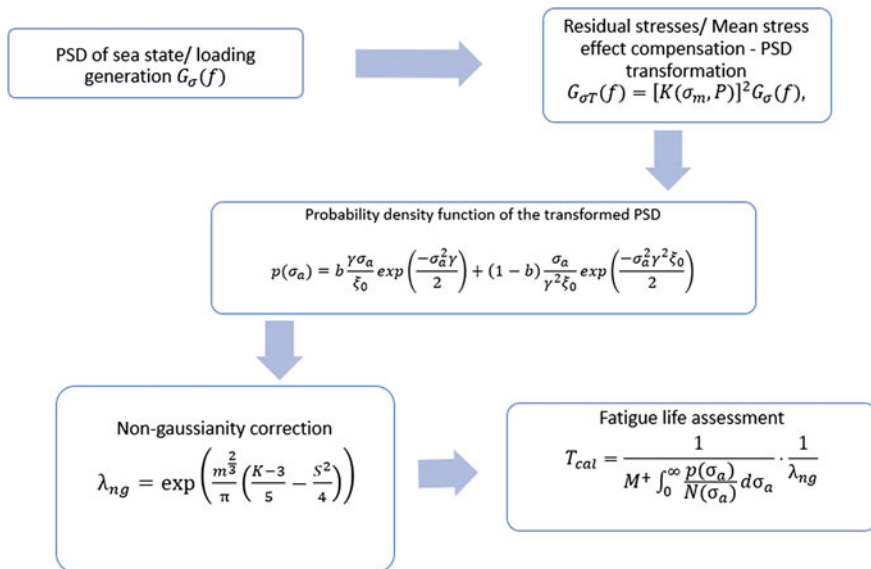


Fig. 19.2 Algorithm used in the process of fatigue life assessment of explosive clad materials

19.1.7 Fatigue Life Estimation in Frequency Domain

As for the most important part of the paper, a calculation algorithm is presented. In Fig. 19.2, we can see a fatigue life assessment algorithm for explosive cladded transition joints defined with the use of the frequency domain. The presented algorithm is using the Benasciutti-Tovo model for the probability density function [2]:

$$p(\sigma_a) = b \frac{\gamma \sigma_a}{\xi_0} \exp\left(\frac{-\sigma_a^2 \gamma}{2}\right) + (1 - b) \frac{\sigma_a}{\gamma^2 \xi_0} \exp\left(\frac{-\sigma_a^2 \gamma^2 \xi_0}{2}\right), \quad (19.6)$$

where σ_a —stress amplitude generated from the PSD, b —weight function dependent from the PSD and γ can be defined by the spectral moments ξ_i :

$$\gamma = \frac{\xi_2}{\sqrt{\xi_0 \cdot \xi_4}}. \quad (19.7)$$

The final formula for fatigue life is being completed with the material coefficients and the use of the non-Gaussian correction factor.

$$T_{cal} = \frac{1}{M^+ \int_0^\infty \frac{p(\sigma_a)}{N_0 \left(\frac{\sigma_a}{\sigma_{af}}\right)^m} d\sigma_a} \cdot \frac{1}{\lambda_{ng}}, \quad (19.8)$$

where σ_{af} —fatigue limit in fully reversed tension-compression, N_0 —number of cycles till failure and M^+ —is the expected number of peaks in a unit of time.

19.2 Conclusions and Observations

The presented work discusses the topic of fatigue life assessment of explosive cladded transition joints with the use of the spectral method which has been based on the past experiences of the author in this area. The approach can be used if we are operating on the power spectral density and we know that the loads have a non-Gaussian distribution. The presented algorithm explains the reader step by step on how to implement the mean stress correction as well as the simple non-Gaussian correction factor.

References

1. Niesłony A (2008) Determination of contour lines of fatigue damage by the spectral method (in Polish). Publishing House of the Opole University of Technology 2008.

2. Benasciutti D, Tovo R (2018) Frequency-based analysis of random fatigue loads: Models, hypotheses, reality. *Materialwiss Werkstofftech* 49:345–367
3. Braccesi C, Cianetti F, Lori G, Pioli D (2009) The frequency domain approach in virtual fatigue estimation of non-linear systems: the problem of non-Gaussian states of stress. *Int J Fatigue* 31:766–775
4. Gadolina I, Zaynetdinov R (2019) Advantages of the rain-flow method at the post-processing stage in comparison with the spectral approach. *IOP Conf Ser Mater Sci Eng* 481:012005
5. Boroński D, Skibicki A, Maćkowiak P, Płaczek D (2020) Modeling and analysis of thin-walled Al/steel explosion welded transition joints for shipbuilding applications. *Marine Struct* 74
6. Böhm M, Kowalski M (2020) Fatigue life estimation of explosive cladded transition joints with the use of the spectral method for the case of a random sea state. *Mar Struct* 71
7. Pierson WJ, Moskowitz L (1964) A proposed spectral form for fully developed wind seas based on the similarity theory of S. A. Kitaigorodskii. *J Geophys Res* (1896–1977) 69:5181–5190
8. Marques J, Benasciutti D, Tovo R (2020) Variability of the fatigue damage due to the randomness of a stationary vibration load. *Int J Fatigue* 141:105891
9. Niesłony A, Böhm M (2016) Universal method for applying the mean-stress effect correction in stochastic fatigue-damage accumulation. *Mater Perform Charact* 5(3):352–363
10. Niesłony A, Böhm M (2012) Determination of fatigue life on the basis of experimental fatigue diagrams under constant amplitude load with mean stress. In: Skibicki D (ed) *Fatigue failure and fracture mechanics*. Trans Tech Publications Ltd., Stafa-Zurich, Switzerland, vol 726, pp 33–38
11. Benasciutti D, Tovo R (2005) Cycle distribution and fatigue damage assessment in broad-band non-Gaussian random processes. *Probab Eng Mech* 20(2):115–127
12. Benasciutti D, Tovo R (2006) Fatigue life assessment in non-Gaussian random loadings. *Int J Fatigue* 28(7):733–746

Chapter 20

Cluster Analysis in the Choice of Operating Modes in Durability Analysis of Random Time-History Records



Irina Gadolina, Julian Marcell Enzweiler Marques, and Denis Benasciutti

Abstract Computational methods for assessing the structural durability of components under service loadings need, among other data, a detailed information about the service loading itself. Due to the usual non-stationary character of service loadings, the generalized loading block (GB) should be constructed based on the occurrence frequency of various service modes in the loading. A method for selecting the modes is proposed in this work, which proves to be particularly advantageous in those cases where it is difficult to distinguish the operating modes appropriately. The method is based on one of machine-learning tools called cluster analysis, which is here applied to representative loading time-histories recorded in a mountain-bike. To prove the correctness of the method, a posteriori comparison is made with known information about the service modes of the loading.

Keywords Service regimes · Rainflow counting · Cluster analysis · Durability

20.1 Introduction

To assess the fatigue strength and structural durability of machine components, it is necessary to have information about the operational loadings of structural elements. This information is formed on the basis of experimental service studies of loading conditions. To make a sound decision about all situations experienced by a machine during its service life with the aim of longevity prediction, one should construct the so-called generalized loading block (GB) [1]. The need to construct a GB is justified by: (i) unfeasibility to register all stress time-histories during the entire service life, (ii) necessity of considering the varied character of loading during service. This paper discusses the task of building the GB by means of cluster analysis. Specifically, cluster analysis was performed on time-series data (run-test) [2, 3].

I. Gadolina (✉)

Mechanical Engineering Research Institute of the Russian Academy of Sciences (IMASH RAN), Maly Kharitiniievsky 4, Moscow, Russia

J. M. E. Marques · D. Benasciutti

Department of Engineering, University of Ferrara, via Saragat 1, 44122 Ferrara, Italy

The problem of time-series clustering arises when a sample of time-series is observed and there is the need to gather more or less similar groups into different categories or clusters. Later, they are identified as the service modes and will serve to form the generalized block for longevity estimation. Cluster analysis has the capability of distinguishing the peculiarities of different parts of time-series, and it has already been applied in various research fields like as genetics, weather forecast, stock market etc. This paper presents the first attempt to use cluster analysis for analyzing the loading time-histories in machine parts.

Previous experiences of building the GB included applications to machine parts in various engineering fields: truck vehicles [4, 5], mooring lines [6], agriculture machines [7]. The problem of dividing a measured loading into segments is addressed in [8]; the problem is not simple as it requires one to consider specific traits of machine use. In this paper, as a first step, each almost stationary realization [9] is processed in time domain by using the rainflow cycle counting. Due to the specific character of the measured loading, and with the aim of durability estimation, the task of judging stationarity turns out to be non-trivial [9].

20.2 Method

It might be argued that the proposal of [4] to compare loading regimes by means of the accumulated damage is reasonable. The accumulated damage was estimated by the Palmgren-Miner rule as:

$$D = \sum S_i^b \quad (20.1)$$

(b is the fatigue exponent). This damage, based on a linear hypothesis, was further used for distinguishing the process modes. It is proposed that the load cycles S_i in (1) are determined from the force signal $x(t)$ by using the rainflow cycle counting. On the other hand, until now, the linear damage accumulation law as that in (1)—though being simplified—is far from being non-contradicted. When performing the cluster analysis, it was decided to explore an enlarged number of variables that characterize various estimates (attributes) of the parts of a random process, and which are thus supposed to be more or less responsible for fatigue damage accumulation. They are listed in Table 20.1, along with their notation. Note that the estimated durability, L , is a conventionally estimated value, as if the machine moves exclusively by this type of road.

In Table 20.1, S_m is the mean estimate on sub-realization, f is estimated as a number of local maximum of random process during an enough representative time period, S_{amax} is the maximum amplitude in the amplitude distribution obtained after rainflow counting, $I = N_o/N_e$ is the irregularity factor defined as the ratio of the number of mean level crossings, N_o , to the number of local extrema, N_e , in the random process; L is estimated based on amplitude distribution together with fatigue

Table 20.1 List of variables for cluster analysis

	Variable	Symbol
1	Mean value	S_m [MPa]
2	Effective frequency	f [Hz]
3	Rain-flow max amplitude	S_{amax} [MPa]
4	Root mean square value	RMS [MPa]
5	Efficient amplitude	$V S$ [MPa]
6	Irregularity factor	$I[-]$
7	Fullness ratio	$V[-]$
8	Estimated durability	L [months]

resistance data longevity (conditional). Finally, $V S = S_{amax} \cdot V$ is the equivalent amplitude, with:

$$V = \sqrt[b]{\left[\frac{1}{n} \sum h_i \left(\frac{S_{ai}}{S_{amax}} \right)^b \right]} \tag{20.2}$$

Here, n is the total number of cycles in the amplitude histogram, S_{ai} is the current stress amplitude in the histogram, h_i is the number of cycles with amplitude S_{ai} .

According to the proposed method, the random process is treated like as in the run-test [3]. This means that the whole realization is divided into equal parts (or subsequences) and mentioned parameters are estimated for each part. In cluster analysis, a closeness of parameters for some part allows selecting the specific operational modes and to distinguish them.

20.3 Case Study

An example of cluster analysis is performed on a loading time-series realization measured in a mountain bike [10], see Fig. 20.1. The whole realization (252,000 digital points) was divided into equal sub-segments (each with 20,000 digital points). The sample estimates of the variables in Table 20.1 were computed for each sub-set. Such estimates form the data set that was subsequently subjected to cluster analysis.

20.3.1 Preliminary Analysis

Prior to cluster analysis, some data mining procedures were performed. First, variables were checked for their pair correlation (Fig. 20.2). This allowed excluding some of them which are strongly correlated. Also, the time dependences of selected

Fig. 20.1 Loading history of the bicycle part [10]. Sub-sets were cut evenly

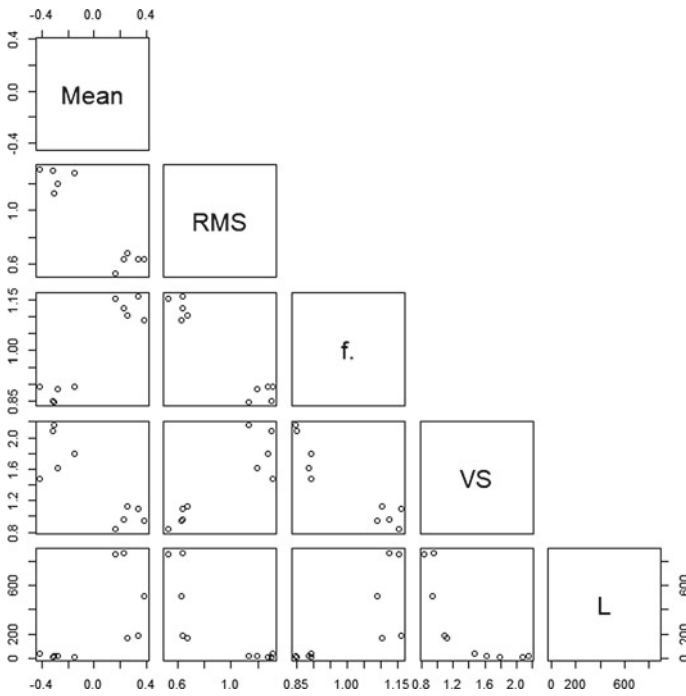
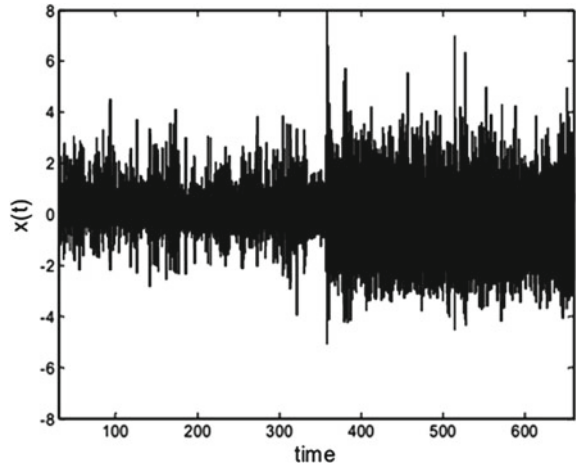


Fig. 20.2 Pair correlations of the selected variables

Fig. 20.3 Time dependences of chosen variables

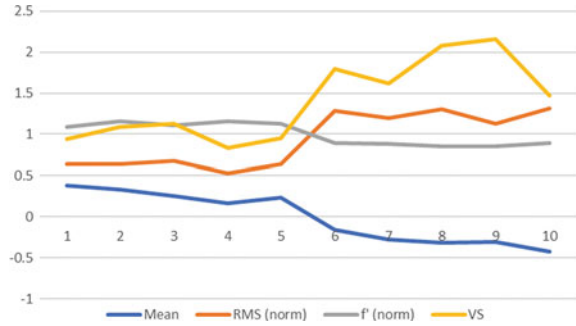
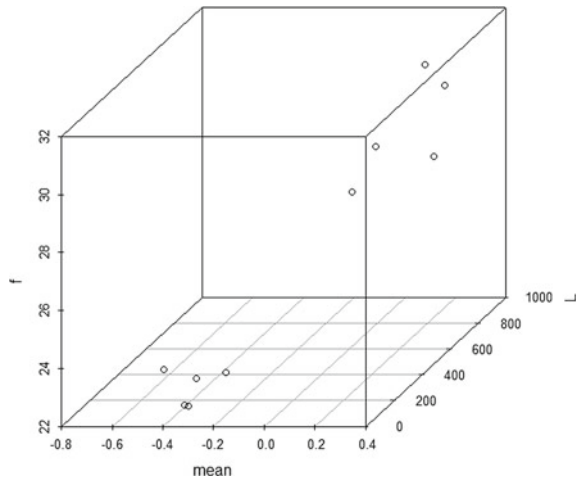


Fig. 20.4 3D representation of two clusters in the dataset



variables were investigated (Fig. 20.3). A visual representation of data clustering on a 3D graph (only for three variables) is shown in Fig. 20.4. Figure 20.3 and 20.4 give a hint that the analyzed data belong to two distinct clusters. To formulate this observation mathematically, the multivariable analysis by the *k*-mean cluster analysis was performed [11]. Based on analysis results (Fig. 20.3 and 20.4), as well on prior information on bicycle usage (the bike was moving on two types of roads), the number of clusters was taken as 2 during clustering calculations.

20.3.2 Cluster Analysis of the Dataset

Built according to the analysis of Sect. 20.2, the dataset—consisting of 10 rows (the number of sub-sets) and 6 columns (the number of finely chosen variables in this case, see Table 20.2)—was input into the *k*-mean standard program [11]. Given a set of observations $(x_1, x_2, \dots, x_{10})$, where each observation is a 6-dimensional real

Table 20.2 Results of cluster analysis

		Mean values of variables (cluster means)				
Variable:	RMS normalized	S_{amax} normalized	V	f' normalized	L (relative units)	Mean normalized
Cluster indexes:						
1	0.60	2.71	0.33	1.12	742	0.260
2	1.07	4.52	0.36	0.94	65	-0.127
Statistical data	Within cluster sum of squares by cluster:					
	Determination D (between_SS/total_SS) = 95.3%					
	Clustering vector: 1 1 1 1 1 2 2 2 2 2					

vector, k-means clustering aims to partition the 60 observations into 2 sets so as to minimize the within-cluster sum of squares (variance) and to maximize the outside sum of square to distinguish two clusters.

Table 20.2 summarizes the result of cluster analysis program after 10 iterations. Clustering statistics (95.3%) seems to be confident enough to justify two distinct clusters. The mean values of 6 dimensional vectors for 2 clusters are shown in Table 20.2.

20.4 Discussion, Conclusions and Future Plans

The aim of this work was to apply cluster analysis to distinguish more effectively the service loading modes with the aim to improve the accuracy of structural durability and longevity assessment. The proposed method is a first example of application of artificial intelligence to the problem of selecting loading modes in machine parts. The method of time-series clustering with the choice of specific parameters appeared to be efficient for the problems of longevity estimation. The efficiency of the proposed method was demonstrated by a case study concerning a real loading measured on a mountain-bike; the obtained results agreed with prior information on the bicycle usage.

It was however observed that, contrary to our preliminary idea of considering all the characteristics specific for fatigue damage accumulation, the case study has revealed that there was in fact no need to apply the complicated tools of random process analysis, like the selection of local extrema and rainflow cycle counting. Indeed, other more common characteristics of the random loading—like calculating the mean value and RMS—work just as well in this example.

A possible future development of this work aims:

- to consider more complicated loading cases with more service modes;
- to expand the proposed method into the field of spectral methods [3] by considering proper statistical parameters in the frequency-domain.

References

1. Kogaev V (1993) Strength calculations at stresses variable in time. Mashinostroenie, Moscow [in Russian]
2. Aghabozorgi S, Shirkhorshidi AS, Ying Wah T (2015) Time-series clustering—a decade review. *Inf Syst* 53:16–38
3. Marques JME (2021) Confidence intervals for the expected damage in random loadings: application to measured time-history records from a Mountain-bike. *IOP Conf Ser Mater Sci Eng* 1038:012025
4. Dreßler K, Speckert M, Müller R, Weber C (2009) Customer loads correlation in truck engineering. *Berichte des Fraunhofer ITWM* 151
5. Volmer M, Jicheng L, Shidong C, Siquan H, Lianlei W, Speckert M, Biedinger C, Weyh T (2020) Planning and conducting a measurement campaign and derivation of customer-specific load distribution for light trucks in China. In: 6th commercial vehicle technology symposium. Springer Fachmedien Wiesbaden
6. Dai J, Leira BJ, Moan T, Alsos HS (2021) Effect of wave inhomogeneity on fatigue damage of mooring lines of a side-anchored floating bridge. *Ocean Eng* 219:108304
7. Feijoo F, Gomez-Gil FJ, Gomez-Gil J (2020) Application of composite spectrum in agricultural machines. *Sensors* 20(19):5519
8. Burger M, Dreßler K, Speckert M (2021) Load assumption process for durability design using new data sources and data analytics. *Int J Fatigue* 145:106116
9. Gadolina I, Zaynetdinov R (2018) The estimation of the sufficient random loading realization length in the problem of machine parts longevity. In: 2018 IEEE 9th international conference on dependable systems, services and technologies (DESSERT 2018), pp 159–162
10. Benasciutti D, Tovo R (2007) Frequency-based fatigue analysis of non-stationary switching random loads. *Fatigue Fract Eng Mater Struct* 30(11):1016–1029
11. R Core Team (2020) R: a language and environment for statistical computing. R foundation for statistical computing

Chapter 21

Comparison of Different Fatigue Laws for Probabilistic Modeling of Mechanical Fatigue with Censored Data Using Maximum Likelihood Estimation Method



Ivan Rukavina, Faouzi Adjed, Charlotte Chabanas, Samuel Van De Hel, Mohcine Nfaoui, and Alexandre Dementiais

Abstract Mechanical fatigue, as one of the most common causes of structural failures, is of great interest in many industries. Modeling such a behavior is extremely difficult due to the random nature of fatigue. Therefore, the probabilistic approach is considered to be the most adequate choice. In order for the model to be valid, its parameters have to be estimated from obtained experimental data using statistical methods. In recent scientific literature, different fatigue laws and statistical methods have been proposed. However, only some of them are compared (Barbosa et al. in *Adv Mech Eng* 11(8), 2019, [1]), they are evaluated only on a few data sets, and their implementation details are often not provided. The consensus on the most appropriate fatigue law still does not exist. This work is based on parameter estimation of fatigue models in order to fit experimental data by using the maximum likelihood estimation method. Six different models are studied and implemented, based on Basquin (Castillo and Fernández-Canteli in *Science & business media*, 2009, [2]), Strohmeier (Castillo and Fernández-Canteli in *Science & business media*, 2009, [2]), Castillo and Fernández-Canteli (Castillo and Fernández-Canteli in *Science & business media* (2009); Toasa Caiza in *Consideration of runouts by the evaluation of fatigue experiments*. KIT Scientific Publishing 2019, [2, 3]) and Stüssi (Toasa Caiza et al. in *Pract Periodical Struct Des Constr* 25(4), 2020, [4]) fatigue laws. A software code and a web application have been built in order to facilitate their comparison. The models are compared on several fatigue data sets and the obtained results are presented here.

Keywords Probabilistic fatigue modeling · Censored data · Maximum likelihood estimation · Statistical tests

I. Rukavina (✉) · F. Adjed · C. Chabanas · S. Van De Hel · M. Nfaoui · A. Dementiais
Expleo France, 3 Avenue des Prés, 78180 Montigny-le-Bretonneux, France
e-mail: Ivan.Rukavina@expleogroup.com

M. Nfaoui
ENSEIRB-MATMECA, 1 Avenue du Dr Albert Schweitzer, 33400 Talence, France

A. Dementiais
IPSA, 7 Rue Maurice Grandcoing, 94200 Ivry sur Seine, France

21.1 Introduction

The fatigue phenomenon and its modeling are one of the challenging topics for researchers due to its dependence on several physical constraints, in terms of material composition and experimentation, but also due to mathematical complexity. Therefore, to model a realistic fatigue behavior with these constraints taken into account, several mathematical models were developed in literature based on different fatigue laws such as Basquin, Castillo and Fernández-Canteli, Strohmeyer, Bastenaire and Stüssi [2].

To obtain a functional model for mechanical fatigue, parameters of the fatigue law have to be estimated based on the experimental data. The main challenge is to take into account the random behavior of fatigue visible in the large dispersion of the experimental data. Additionally, the probabilistic models for S-N curves are not able to describe well the whole range of cycle regions [5], so they should be evaluated based on the region in focus. Fitting becomes more challenging when the model integrates censored data (the measurements for tests that were interrupted before failure, usually due to reaching the maximum testing time or the number of cycles in the experiment) [6].

In the literature, developed probabilistic approaches for fatigue use statistical and mathematical knowledge. In fact, in addition to the selection of fatigue law, compatibility conditions related to the number of cycles N and stress level S are required. These conditions are represented by two probability densities identifying the variabilities of the number of cycles to failure and stress level. Furthermore, statistical variables, such as fatigue limit, are used to identify the minimum and maximum of stress level [2]. In recent work by Harlow [6], the fatigue life estimation is presented by taking into account censored data by using 3-parameter Weibull distribution to compute and interpret the compatibility conditions. Also, the maximum likelihood estimation method is used to estimate the fatigue law parameters.

In our current work, we propose the following steps to model fatigue behavior and obtain S-N curves: (i) identification of the suitable fatigue law for a given objective, (ii) selection of the suitable probability distribution for the compatibility conditions by integrating statistical tests for residuals, (iii) selection of the optimization method to estimate several parameters of the fatigue law considering censored data.

21.2 Fatigue Models

In order to make a comparison between the most used fatigue models in the scientific community and industry, their theoretical formulations have been obtained from the literature, and rewritten using the same notation and following the same solution procedure. A short summary of the models is shown in Table 21.1, and the detailed theoretical development and comparison will be presented in our future work.

Table 21.1 Implemented fatigue models

Model name	Random variable	Distribution	Fatigue law
Basquin model with log-normal distribution	N	Lognormal(μ, σ)	$\ln(N) = C - m \ln(S)$
Basquin model with 2-parameter Weibull distribution	N	Weibull(λ, k)	$\ln(N) = C - m \ln(S)$
Strohmeyer model with number of cycles as random variable	N	Lognormal(μ, σ)	$\ln(N) = C - m \ln(S - E)$
Strohmeyer model with fatigue limit as random variable	E	Normal(μ, σ)	$\ln(N) = C - m \ln(S - E)$
Castillo and Fernández-Canteli model	$(\ln(N) - B)(\ln(S) - C)$	Weibull(a, b, c)	$S = \exp \left[\frac{[-\log(1-p)]^{\frac{1}{c}} b + a}{\log N - B} + C \right]$
Stüssi model based on 3-parameter Weibull distribution	$S - \frac{R_m + \alpha N^\beta E_c}{1 + \alpha N^\beta}$	Weibull(a, b, c)	$S = b \left[\log(1 - p)^{\frac{1}{c}} \right] + \frac{R_m + \alpha N^\beta E_c}{1 + \alpha N^\beta} + a$

It is important to mention that most of the models are not improved in any way in the scope of our work, and the main contribution is that their implementation details are systematized and implemented in a software code, and their performances compared. Furthermore, they are described from the statistical point of view, where concepts like statistical tests to check the normality of residuals, null hypothesis testing (if all input samples are from the populations with equal variances), and confidence intervals for estimated parameters are introduced.

The general procedure to estimate parameters for all the models by using the maximum likelihood estimation method consists of the following steps: (i) choice of the distribution for the random variable, (ii) definition of the relation between the number of cycles to failure and stress—choice of a fatigue law, (iii) development of log-likelihood function with censored data included, (iv) estimation of the parameters of the model based on the experimental data by maximizing the log-likelihood function.

In Table 21.1, N is the number of cycles to failure, S is the stress, E is the fatigue limit, B, C, α and β are geometrical parameters, C and m are parameters of the model, a, b and c are parameters of the Weibull distribution, p is probability of failure, R_m and E_c are parameters of the material, ultimate tensile strength and fatigue limit, respectively.

Basquin model is implemented with the number of cycles to failure having both log-normal and 2-parameter Weibull distribution [7]. In this way, the influence of the chosen distribution for the random variable is studied. Strohmeier law is an improvement of the Basquin law as it introduces the fatigue limit E . Two versions of Strohmeier models are implemented, one with the number of cycles to failure and the other with the fatigue limit taken as random variable.

The model developed in [2] by Castillo and Fernández-Canteli, introduces a random variable as a product of the number of cycles to failure and stress (with added geometrical parameters B and C that represent threshold value of the number of cycles and fatigue limit, respectively), and defines it to follow 3-parameters Weibull distribution [2, 3]. Stüssi model that is based on the model from Castillo and Fernández-Canteli is taken from [8].

21.3 Results

21.3.1 Composite Material Dataset

The dataset for a composite material is obtained from [9], and consists of 10 samples with three of them intact (runouts). The quantity and quality of the data allows to obtain a good approximation for all the models and to take care of the dispersion. The material used in the experiment is a composite with fiber.

In Fig. 21.1, a box plot with residuals is shown for all the implemented models. The difference between two statistical distributions used for the random variable for Basquin law can be seen in Fig. 21.2. In Fig. 21.3, two models with Strohmeier law are shown, while Fig. 21.4 shows the S-N curves for Castillo and Fernández-Canteli, and Stüssi models.

The S-N curves for both Basquin models converge to zero, while for the Strohmeier law, the curve converges to the estimated value of the fatigue limit. Castillo and Fernández-Canteli model also gives the estimation for fatigue limit, while in Stüssi, the fatigue limit is an input parameter. Additionally, we notice the existence of both fatigue limit and ultimate tensile strength in Stüssi model, which provide optimal solution for both low and high cycle regions.



Fig. 21.1 Box plot of residuals for a composite material for: (i) Basquin (log-normal distribution), (ii) Basquin (2-parameter Weibull), (iii) Castillo and Fernández-Canteli, (iv) Stüssi, (v) Strohmeier (fatigue limit) and (vi) Strohmeier (number of cycles)

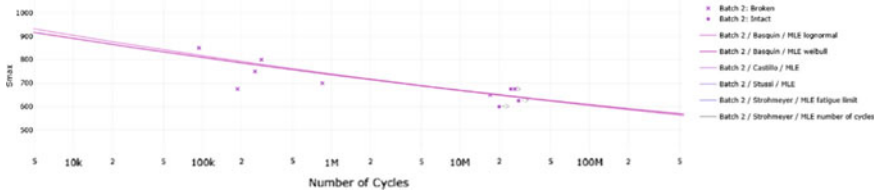


Fig. 21.2 S-N mean curves for a composite material for Basquin model with log-normal distribution and 2-parameteres Weibull distribution

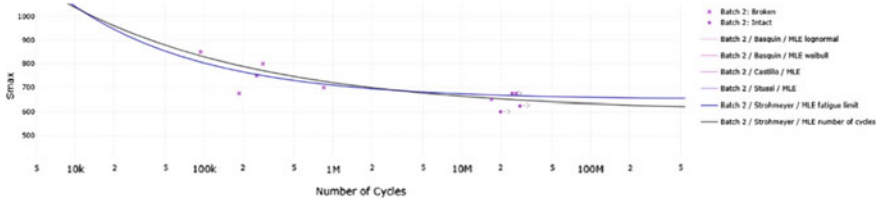


Fig. 21.3 S-N mean curves for a composite material for Strohmeier model with fatigue limit as random variable and Strohmeier model with number of cycles as random variable

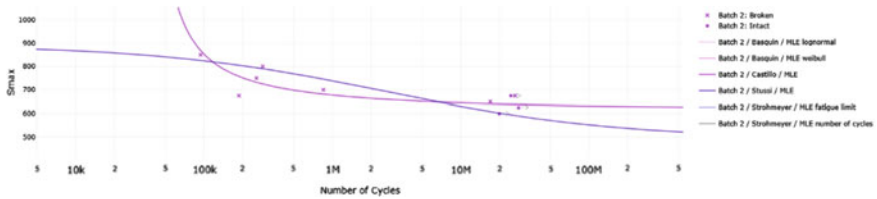


Fig. 21.4 S-N mean curves for a composite material for Castillo and Fernández-Canteli, and Stüssi model



Fig. 21.5 Box plot of residuals for steel for: (i) Basquin (log-normal distribution), (ii) Basquin (2-parameter Weibull), (iii) Castillo and Fernández-Canteli, (iv) Stüssi, (v) Strohmeier (fatigue limit) and (vi) Strohmeier (number of cycles)

21.3.2 Steel Dataset

The experimental data for a German historical steel bridge is obtained from [4]. The number of samples is 36, with 10 of them being intact (runouts). The results of the

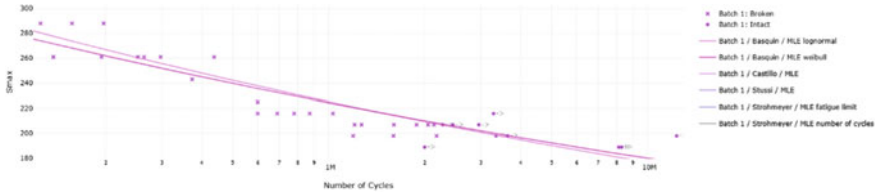


Fig. 21.6 S-N mean curves for steel for Basquin model with log-normal distribution and 2-parameteres Weibull distribution

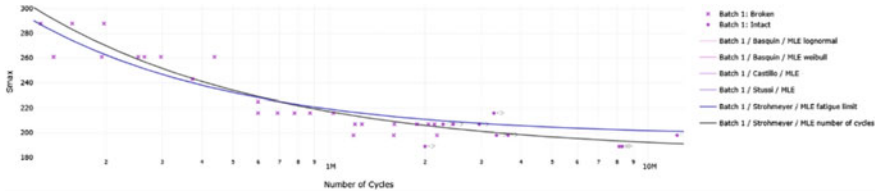


Fig. 21.7 S-N mean curves for steel for Strohmeier model with fatigue limit as random variable and Strohmeier model with number of cycles as random variable

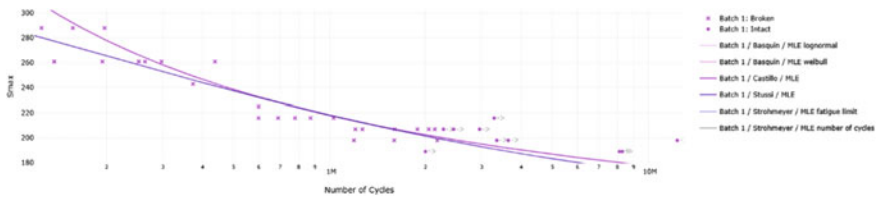


Fig. 21.8 S-N mean curves for steel for Castillo and Fernández-Canteli, and Stüssi model

estimations and comparison for all the models are shown in Figs. 21.5, 21.6, 21.7 and 21.8.

21.4 Conclusion

The results of the parameter estimation for two different material datasets, for composite and steel, and six fatigue models are shown. It can be seen that Strohmeier law with the number of cycles as random variable seems as a better fit than the Basquin law. On the other side, Strohmeier law with the fatigue limit as random variable fails to estimate correct vales for fatigue limit in some cases. It is still to be determined if the quality or quantity of the data is the main cause for that.

Castillo and Fernández-Canteli model shows good fit for both composite and steel datasets. The advantage of Stüssi model is that it provides good fit for both low cycle

and high cycle fatigue regions. The negative side is that the ultimate tensile strength and fatigue limit have to be known in advance.

Our goal is to develop the software code that will apply the most appropriate fatigue law and statistical method based on the dataset, fatigue region, type of the material, and other criteria. For this reason, a criterion should be established to evaluate the quality of the estimations. Other statistical methods, not presented here, are also used in the scope of our work, like Markov Chain Monte Carlo, probability weighted moments and Castillo-Hadi estimators [2], and can provide more efficient solutions in some cases.

Additionally, to enhance the parameter estimation and avoid error bias, results should be validated using goodness of fit statistical test in order to check the normality of residuals [6]. In this way, the choice of the statistical distribution is justified. By using a probabilistic approach, confidence intervals for estimated parameters can be obtained for the proposed models and will be presented in our future work.

References

1. Barbosa JF, Correia JA, Freire Junior RCS, Zhu SP, De Jesus AM (2019) Probabilistic SN fields based on statistical distributions applied to metallic and composite materials: state of the art. *Adv Mech Eng* 11(8)
2. Castillo E, Fernández-Canteli A (2009) A unified statistical methodology for modeling fatigue damage. *Science & Business Media*. Springer
3. Toasa Caiza PD (2019) Consideration of runouts by the evaluation of fatigue experiments. KIT Scientific Publishing
4. Toasa Caiza PD, Ummenhofer T, Correia JA, De Jesus A (2020) Applying the Weibull and Stüssi methods that derive reliable Wöhler curves to historical German bridges. *Pract Periodical on Struct Des Constr* 25(4)
5. Fouchereau R, Celeux G, Pamphile P (2014) Probabilistic modeling of S-N curves. *Int J Fatigue* 68:217–223
6. Harlow DG (2020) Fatigue life estimation with censored data. *Int J Fatigue* 141
7. Sarkani S, Mazzuchi TA, Lewandowski D, Kihl DP (2007) Runout analysis in fatigue investigation. *Eng Fract Mech* 74(18):2971–2980
8. Toasa Caiza PD, Ummenhofer T (2018) A probabilistic Stüssi function for modelling the S-N curves and its application on specimens made of steel S355J2+N. *Int J Fatigue* 117:121–134
9. Gauthier E (2018) Comportement mécano-fiabiliste de structures composites—approche matériaux. ENSAM, Paris

Chapter 22

Evaluating Confidence Interval of Fatigue Damage from One Single Measured Non-stationary Time-History



Julian M. E. Marques  and Denis Benasciutti 

Abstract This paper derives a confidence interval for the expected damage when only one single non-stationary time-history record is available. The proposed confidence interval is inspired on a solution existing in literature, which is restricted to stationary time-history. The proposed procedure divides the non-stationary time-history into stationary segments, and each segment is further partitioned into blocks. This technique allows the confidence interval for expected damage to be constructed. As a case study to check the proposed confidence interval, measured time-histories are obtained directly from a mountain-bike travelling on an off-road track with different speeds, seat and surface conditions over time. All measured time-histories are verified to be non-stationary by qualitative and quantitative approaches, as, for example, the ‘run test’ based on a sequence of damage values. Using the measured time-histories, a sort of ‘calibrator’ sample damage value is computed to estimate the expected damage, and then used to verify the validity of the proposed confidence interval. The obtained results confirm the correctness of the proposed confidence interval of fatigue damage from one single measured non-stationary time-history.

Keywords Confidence interval · Fatigue damage · Non-stationary time-history

22.1 Introduction

Random loadings acting on mechanical components and structures are usually classified as non-stationary. To assess the structural integrity of these structures and components, rainflow counting method and Palmgren-Miner rule are applied to estimate the fatigue damage. In practice, this damage value is normally computed from one single measured time-history, which must be considered as being one sample value out of a

J. M. E. Marques (✉) · D. Benasciutti
Department of Engineering, University of Ferrara, via Saragat 1, 44122 Ferrara, Italy
e-mail: nzvjnm@unife.it

D. Benasciutti
e-mail: denis.benasciutti@unife.it

much larger (infinite) ensemble. The calculated damage values usually change from one measured time-history to the other, as they have an inherent sampling variability.

In a recent work [1], confidence intervals to assess the variability of damage have been derived when only few stationary time-histories or even only one was given. For each case, the confidence interval expression enclosing the (unknown) expected damage was shown to be in good agreement with simulated [1] and measured stationary loadings acting on a Mountain bike [2]. Although these confidence intervals proved to be a useful tool to deal with the variability of damage, they are only applicable to stationary time-histories.

The above confidence interval of damage valid for stationary time-histories is here extended to make it applicable to time-history that is non-stationary. In this situation, the confidence interval for the expected damage is obtained by a technique of dividing the single time-history. The confidence interval is verified by measuring the loads acting on a mountain-bike riding in an off-road track with different speeds, seat and surface conditions. All measured time-histories are quantified as being non-stationary by the run test described in [2], which is based on a sequence-observed damage values. Different measured time-histories are used to estimate the unknown expected damage by a sort of ‘calibrator’ damage, equal to the sample mean of some damage values. The calibrator sample damage is needed to check whether the confidence interval correctly encloses the expected damage. The results then confirm the accuracy of the proposed confidence interval when applied to one single measured non-stationary time-history.

22.2 Expected Damage and Confidence Interval

In the Palmgren-Miner linear rule, the fatigue damage of a given random time-history $z(t)$ of time duration T is the sum of the damage d_i of every counted cycle:

$$D(T) = \sum_{i=1}^{n(T)} d_i = \sum_{i=1}^{n(T)} \frac{s_i^k}{A} \quad (22.1)$$

where s_i is the stress amplitude of the i -th cycle, $n(T)$ is the number of counted cycles and A and k are material constants of the S-N curve $s^k N_f = A$. The damage $D(T)$ strictly depends on the set of stress amplitudes s_i and counted cycles $n(T)$, which is commonly identified by the rainflow method. Due to the randomness of both s and $n(T)$, the damage $D(T)$ may differ if another time-history is considered [1].

The expected damage is the expectation of $D(T)$:

$$E[D(T)] = E \left[\sum_{i=1}^{n(T)} d_i \right] = E[n(T)] \frac{E[s^k]}{A} \quad (22.2)$$

where $E[-]$ is the probabilistic expectation. The expected value in Eq. (22.2) means that the damage is computed over an infinite ensemble of time-histories. However, in a real application, only a finite number of measured time-history is accessible so that $E[D(T)]$ is never known exactly and can only be approximated.

The confidence interval in [1] for expected damage works very well when applied to a single measured time-history, see [2]. However, it is restricted to stationary time-histories. In situations where the time-history is non-stationary, a slightly different procedure is proposed to obtain the confidence interval that includes the expected damage.

This procedure is based on the idea of dividing the non-stationary time-history into N_S disjoint stationary segments. Each segment is further divided into N_B blocks of length T_B . After block subdivision, the damage of each block is computed $D_{B,ij}(T_B)$, $i = 1, 2, \dots, N_S$ and $j = 1, 2, \dots, N_B$ by rainflow method and Palmgren-Miner rule. These damage values and the definition of the confidence interval for independent normal populations with unknown and unequal variances [3] allow the $100(1 - \beta)\%$ confidence interval for the expected damage to be defined:

$$\begin{aligned} \sum_{i=1}^{N_S} \bar{D}_{B,i}(T_B) - t_{\beta/2,v} \sum_{i=1}^{N_S} \sqrt{\frac{\hat{\sigma}_{D_{B,i}}^2}{N_B}} &\leq \sum_{i=1}^{N_S} E[D_{B,i}(T_B)] \\ &\leq \sum_{i=1}^{N_S} \bar{D}_{B,i}(T_B) + t_{\beta/2,v} \sum_{i=1}^{N_S} \sqrt{\hat{\sigma}_{D_{B,i}}^2} \end{aligned} \tag{22.3}$$

where $\bar{D}_B(T)$ is the sample mean and $\hat{\sigma}_{D_B}^2$ is the sample variance of damage of blocks, $t_{\beta/2,v}$ is the quantile of the student's t-distribution with degrees of freedom given by $v = (N_B - 1) \left(\sum_{i=1}^{N_S} \hat{\sigma}_{D_{B,i}}^2 \right)^2 / \sum_{i=1}^{N_S} \left(\hat{\sigma}_{D_{B,i}}^2 \right)^2$. If not integer, the number of degrees of freedom has to be rounded down to the nearest integer [3].

After substituting $\bar{D}_B(T_B) = N_B^{-1} \sum_{i=1}^{N_B} D_{B,i}(T_B)$ into Eq. (22.3) and multiplying this expression by N_B , the confidence interval for expected damage turns out to be

$$\begin{aligned} \sum_{i=1}^{N_S} \sum_{j=1}^{N_B} D_{B,ij}(T_B) - t_{\beta/2,v} \sum_{i=1}^{N_S} \sqrt{N_B \cdot \hat{\sigma}_{D_{B,i}}^2} &\leq \sum_{i=1}^{N_S} N_B E[D_{B,i}(T_B)] \\ &\leq \sum_{i=1}^{N_S} \sum_{j=1}^{N_B} D_{B,ij}(T_B) + t_{\beta/2,v} \sum_{i=1}^{N_S} \sqrt{N_B \cdot \hat{\sigma}_{D_{B,i}}^2} \end{aligned} \tag{22.4}$$

As N_S and N_B are deterministic values, the damage of a given non-stationary time-history and its expected value are $D(T) = \sum_{i=1}^{N_S} \sum_{j=1}^{N_B} D_{B,ij}(T_B)$ and $E[D(T)] = \sum_{i=1}^{N_S} N_B E[D_{B,i}(T_B)]$, respectively. Substituting these terms into Eq. (22.4), the final confidence interval expression for $E[D(T)]$ when considering only one non-stationary time-history is

$$D(T) - t_{\beta/2, \nu} \sum_{i=1}^{N_S} \sqrt{N_B \cdot \hat{\sigma}_{D_B, i}^2} \leq E[D(T)] \leq D(T) + t_{\beta/2, \nu} \sum_{i=1}^{N_S} \sqrt{N_B \cdot \hat{\sigma}_{D_B, i}^2} \quad (22.5)$$

Note that the method requires a minimum number of segments $N_S \geq 2$, of blocks $N_B \geq 2$ and a minimum time length T_B to contain approximately 10^3 [1].

22.3 Measured Time-Histories

This section presents the measured non-stationary time-histories used for calculating the confidence interval and estimating the expected damage. The time-histories were obtained by measuring the loadings action on a mountain-bike on a typically north Italian track. The mountain-bike and its apparatus are detailed in [2].

The mountain-bike travelled on a short off-road track, 500 m in length, located at the Municipal Hippodrome in Ferrara city. This track was almost plane with different surface conditions such as asphalt, gravel and cobblestone, see Fig. 22.1a. A rider of approximately 65-kg mass guided the bicycle in both seated and standing conditions. The speed was varied from 10 to 20 km/h.

A total of 21 measured time-histories were obtained under the same cycling conditions. The first time-history was used to construct the confidence interval, while the other 20 were used for approximating the expected damage and use it to verify whether the proposed confidence interval actually works well.

All measured time-histories were normalized to provide mean $\mu_z = 0$ and variance $\sigma_z^2 = 1$. They also were set with a time duration of $T = 300s$. An example is illustrated in Fig. 22.1b for the first measured time-history $z_1(t)$.

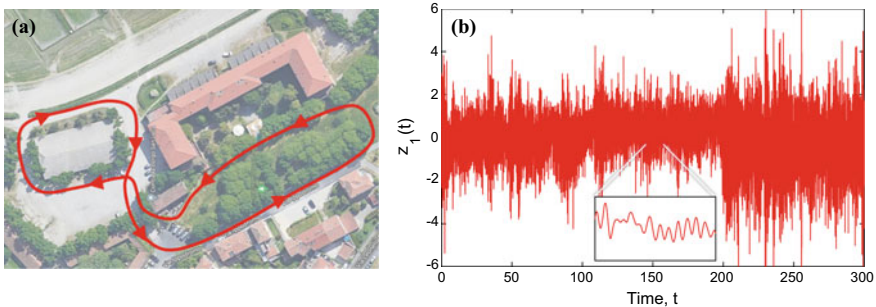


Fig. 22.1 a Off-road track, b overall and zoomed view of the first measured time-history $z_1(t)$

22.3.1 Detecting Non-Stationarity of Time-Histories

Measured time-histories usually have their mean, variance and frequency content that vary over time. For this reason, the non-stationarity of all measured time-histories is verified by two different approaches: comparison of cumulative spectra, run test.

The comparison of the loading (or cumulative) spectrum is used to compare the statistical distribution of rainflow cycles. This qualitative approach is demonstrated in Fig. 22.2a by using five measured non-stationary time-histories.

Figure 22.2a provides a picture of the cycle distribution in each measured time-history. The comparison of loading spectra from different time-histories indicates that the higher the amplitude s is, the worse is the agreement among loading spectra $C(s)$. This suggests that such time-histories are non-stationary. Although all 21 time-histories provide similar results (not shown to avoid clutter) that confirm the non-stationarity, the comparison of loading spectra is just a visual analysis.

To deal with this possible limitation, the run test detailed in [2] is applied, as an example to the first measured time-history, see Fig. 22.2b. This test is a quantitative approach that considers a sequence of damage values (normalized to the median), which are classified as being above or below the sample median. These and all subsequent damage values in this study were computed by rainflow method and Palmgren-Miner rule with $A = 1$ and $k = 3$.

The analysis of the first measured time-history considers a sequence of $N_B = 60$ blocks with length $T_B = 5$ s. The time-history is classified as being non-stationarity since the observed values above and below the median are shown not to follow the same distribution. Such hypothesis is indeed rejected for a 95% level of significance because the number of runs $r = 15$ falls outside the acceptance region limited by the lower $r_{1-\beta/2} = 22$ and upper $r_{\beta/2} = 39$ values, computed as the percentiles of a normal distribution—for more details, see [2, 4].

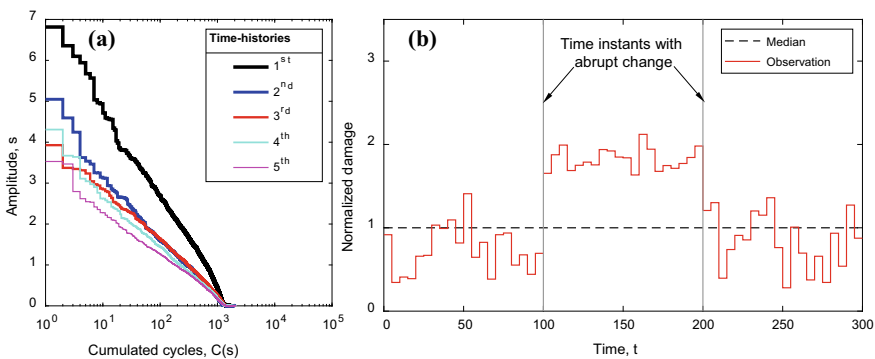


Fig. 22.2 Approaches to detect non-stationarity: **a** comparison of loading spectra and **b** run test based on a sequence of observed damage values

The run test based on a sequence of damage values, shown in Fig. 22.2b for the first time-history, was in fact conducted for all measured time-histories. Although not shown here, the run test quantified all such time-histories as non-stationary.

22.3.2 Confidence Interval and Approximation of the Expected Damage

The confidence interval in Eq. (22.5) is constructed here by considering the first measured non-stationary time-history. It was divided into $N_S = 3$ stationary segments using an algorithm [5] to detect abrupt changes along the observed values of run test method, see Fig. 22.2b. In turn, each stationary segment was divided into $N_B = 4$ blocks containing at least 10^3 counted cycles. The confidence interval was finally obtained with a 95% confidence level after computing sample mean $D_{B,ij}(T_B)$ and variance $\hat{\sigma}_{D_{B,i}}^2$.

To evaluate the correctness of this confidence interval, a reasonable approximation of the expected damage $E[D(T)]$ was required because a large ensemble of measured time-histories was not available. The expected damage $E[D(T)]$ was then estimated by the sample mean of damage values $\bar{D}(T) = N^{-1} \sum_{i=1}^N D_i(T)$, $i = 1, 2, \dots, N$ computed by considering the set of $N = 20$ measured time-histories; $\bar{D}(T)$ is a sort of ‘calibrator’ sample damage used to approximate $E[D(T)]$.

22.4 Results

Table 22.1 lists, on the left, the lower limit $D(T) - t_{\beta/2, \nu} \sum_{i=1}^{N_S} (N_B \cdot \hat{\sigma}_{D_{B,i}}^2)^{1/2}$ and, on the right, the upper limit $D(T) + t_{\beta/2, \nu} \sum_{i=1}^{N_S} (N_B \cdot \hat{\sigma}_{D_{B,i}}^2)^{1/2}$ of the confidence interval; the calibrator $\bar{D}(T)$ is in the centre.

The expected damage $E[D(T)]$, approximated here with the calibrator $\bar{D}(T)$, is within the confidence interval. This attests the correctness of the proposed confidence interval at least when applied to the single non-stationary time-histories of this study.

Note that, to design a structure, the safe region is only when the damage $D(T)$ is greater than $E[D(T)]$. Since $E[D(T)]$ is unknown in practice, it is suggested to take the upper limit of confidence interval as the reference value to be considered in design.

Table 22.1 Lower and upper limits of confidence interval and calibrator $\bar{D}(T)$ sample damage

Lower limit	Calibrator $\bar{D}(T)$	Upper limit
5388	6023	7166

22.5 Conclusion

A confidence interval has been derived to address the statistical variability of the fatigue damage computed from one single non-stationary time-history. A technique in which the time-history is divided into stationary segments, and each segment partitioned into blocks, was developed to build the confidence interval. The proposed confidence interval was verified by the random loadings measured on a mountain-bike travelling on different speeds, seat and surface conditions over time. All measured time-histories were classified as being non-stationary by qualitative and quantitative methods. A quantitative method was the 'run test' based on a sequence of observed damage values, as it can detect simultaneous changes in frequency content, mean and variance in the signal. The expected damage was approximated by a 'calibrator' sample damage computed from the set of damage values from 20 measured time-histories. This calibrator damage, replacing the expected damage, was used to check whether the confidence interval correctly enclose the expected damage. The results then confirm the accuracy of the proposed confidence interval when applied to one single measured time-history.

References

1. Marques JME, Benasciutti D, Tovo R (2020) Variability of the fatigue damage due to the randomness of a stationary vibration loading. *Int J Fatigue* 141:105891
2. Marques JME (2021) Confidence intervals for the expected damage in random loadings: application to measured time-history records from a Mountain-bike. *IOP Conf Ser Mater Sci Eng* 1038:012025
3. Montgomery DC, Runger, G.C.: *Applied statistics and probability for engineers*. 6th edn. John Wiley & Sons, Hoboken, USA (2014)
4. Bendat JS, Piersol AG (1986) *Random data: analysis and measurement procedures*. Wiley-Interscience, New York, USA
5. Killick R, Fearnhead P, Eckley IA (2012) Optimal detection of changepoints with a linear computational cost. *J Am Stat Assoc* 107:500

Chapter 23

Review of the Models for Determining the Moment of the Initiation of the Fatigue Crack in the Frequency Domain for Random Loads with Non-Gaussian Distribution



Michał Böhmi

Abstract Random loading conditions can be rarely defined by a pure gaussian process. Due to this when we are using methods which are based on the concept of pure gaussian distributions of loading we must have a tool to take into account any distortions of the gaussian process. The paper presents a short review of the models for determination of the moment of the initiation of fatigue crack in the frequency domain. The paper discusses the overall problem of fatigue estimation as well as problem arising with the use of different calculation approaches for the frequency domain. The analyzed models have been divided into three main groups, which are the stress, strain and strain energy models. The discussion is centered on the possibility to use these models for non-gaussian random loads. The biggest variation of models is presented for the stress approach. It has been noted that for the strain approach we are missing a non-gaussian correction method. Some of the approaches presented in the literature such as the Bracessi model can be widely used in order to correct the estimated fatigue life in both stress and strain energy approach.

Keywords Fatigue · Crack initiation · Frequency domain · Spectral method

23.1 Introduction

Determining the moment of fatigue crack initiation for random loads is based on the use of fatigue failure accumulation hypotheses. By applying an appropriate model, we obtain a specific number of cycles or directly the time to the fatigue crack initiation. This is extremely important for the planning of the fatigue crack development observation. There are two main groups in the literature for determining the moment of fatigue crack initiation. The first group is based on the counting of the number of cycles and is described in the so-called time domain. The second group is based

M. Böhmi (✉)

Faculty of Mechanical Engineering, Department of Mechanics and Machine Design, Opole University of Technology, ul. Mikołajczyka 5, 45-271, Opole, Poland
e-mail: m.bohm@po.edu.pl

on the use of statistical parameters of the probability distributions of loads and is described in the so-called frequency domain. Both groups have advantages and disadvantages. The greatest advantage of the cycle counting method is its simplicity. On the other hand, the computational speed is the advantage of the methods defined in the frequency domain. For this group, determining the moment of crack initiation is particularly difficult when analyzing statistical distributions with a disturbed gaussian distribution. The idea of applying an appropriate correction of distributions, or the selection of an appropriate method of description of loads by means of stress and strain models or in the form of a recorded strain energy parameter is discussed later in the paper. The presented results are pointing out the existing approaches as well as the lack of such for the strain models.

23.2 Fatigue Crack Initiation Models Defined in the Frequency Domain

The models used to determine the degree of failure in the frequency domain are most often based on the use of the approach based on direct determination of the fatigue failure damage index or failure determined on the basis of the probability density function of the analyzed power spectral density. They are described by the stress distribution, strain or energy parameter. Most often, the damage is used directly to determine the time to fatigue crack initiation. For this purpose, the work of Miles [1] uses, inter alia, the linear Palmgren-Miner hypothesis and the approximation of the amplitudes by the Rayleigh probability distribution. As a result, the relationship on fatigue life per unit of time was obtained:

$$T_{\text{cal}} = \frac{A}{M^+ + (2\xi_0)^{\frac{m}{2}} \Gamma\left(\frac{m+2}{2}\right)}, \quad (23.1)$$

where: $A = \sigma_{af}^m N$ —coefficient calculated from the Wöhler curve, m — is the Wöhler slope coefficient for the analyzed material, M^+ —is the expected number of peaks in a unit of time, ξ_0 —the zero order spectral moment (variance of the stress course), σ_a —stress amplitude, N —number of cycles till failure.

Many approaches take into account the probability density function defined with the use of the spectral moments ξ_i . The most popular one is the Dirlik approach [2]:

$$p(\sigma_a) = \frac{1}{2\sqrt{\xi_0}} \cdot \left[\frac{K_1}{K_4} \cdot e^{-\frac{Z}{K_4}} + \frac{K_2 \cdot Z}{R^2} \cdot e^{-\frac{Z^2}{2R^2}} + K_3 \cdot Z e^{-\frac{Z^2}{2}} \right], \quad (23.2)$$

where: K_1, K_2, K_3, K_4 , and Z are model coefficient.

23.2.1 Stress Models

The stress approach for fatigue lifetime estimation is very well described in the literature. We can find many papers like the Pitosteit and Pneumonts paper [3] or Niesłony and Böhm [4]. Many solutions like i.e. the Benasciutti and Tovo [5–7] are used for direct damage degree calculation and is one of the most popular for the use with the stress information. They proposed inter alia an algorithm for fatigue life estimation till the crack initiation for the case of a non-gaussian distribution. They have proposed a probability density function which in its classical form is presented in Eq. 23.3:

$$p(\sigma_a) = b \frac{\gamma \sigma_a}{\xi_0} \exp\left(\frac{-\sigma_a^2 \gamma}{2}\right) + (1 - b) \frac{\sigma_a}{\gamma^2 \xi_0} \exp\left(\frac{-\sigma_a^2 \gamma^2 \xi_0}{2}\right), \tag{23.3}$$

where b —weight function dependent from the PSD and γ can be calculated with the use of the spectral moments ξ_0, ξ_2 and ξ_4 :

$$\gamma = \frac{\xi_2}{\sqrt{\xi_0 \xi_4}}. \tag{23.4}$$

Braccesi et al. [8] proposed a non-gaussian correction factor λ in order to take into account the non-gaussian effect at the fatigue lifetime estimation stage, that can be used in the fatigue estimation stage as proposed by Niesłony et al. [9]:

$$T_{cal} = \frac{1}{M^+ \int_0^\infty \frac{p(\sigma_a)}{N_0 \left(\frac{\sigma_a}{\sigma_{af}}\right)^m} d\sigma_a} \cdot \frac{1}{\lambda_{ng}}, \tag{23.5}$$

where: σ_{af} —fatigue limit in fully reversed tension-compression, N_0 —number of cycles till failure, λ_{ng} —non-gaussian correction factor defined as:

$$\lambda_{ng} = \exp\left(\frac{m^{\frac{2}{3}}}{\pi} \left(\frac{K - 3}{5} - \frac{S^2}{4}\right)\right), \tag{23.6}$$

where S —skewness, K —kurtosis.

Another important paper in terms of the stress approach has been presented by Palmieri et al. [10], where the authors analyze not only the non-gaussian effect but also take into account the non-stationarity index.

23.2.2 Strain Models

The strain approach has been described by Macha [11] within the frequency domain for multiaxial random loading. In their book Niesłony and Macha [12] presented a simplified approach to fatigue life assessment with the use of the spectral method and strain information:

$$T_{\text{cal}} = \frac{1}{M^+ \int_0^\infty \frac{p(\varepsilon_a)}{\left(\frac{\varepsilon_a E}{\sigma_f}\right)^{\frac{1}{b}}} d\varepsilon_a}, \quad (23.7)$$

where: σ'_f —fatigue strength coefficient.

There are recent papers by Böhm and Niesłony [13] where they explore these concepts with the use of different criteria in order to calculate the fatigue life:

$$T_\varepsilon = \frac{1}{\lambda M^+ \int_0^\infty \frac{p(\varepsilon_a)}{N_f(\varepsilon_a)} d\varepsilon_a}, \quad (23.8)$$

where: the λ coefficient includes the impact of broad frequency spectrum on the fatigue life, M^+ is the expected number of cycles in unit time, $p(\varepsilon_a)$ is the amplitude probability density distribution, and $N_f(\varepsilon_a)$ is a function giving back the cycle number of the fatigue characteristic.

An interesting paper exploring the possibility to use the strain models with the Neuber correction is presented by Rognon et al. [14]. Their approach has been compared with the procedure formulated by Böhm et al. [15] in order to take into account the plastic region of the stress-strain curve for fatigue estimation within the spectral method. Nevertheless till now no correction in terms of non-gaussian effect of the random loading has been presented.

23.2.3 Strain Energy Models

The strain energy approach is using the coupled information from the stress and strain in the form of the energy parameter. We can find many solutions to the topic of the use of advanced models as presented by Kluger and Łagoda [16]. The energy parameter can be used in the frequency domain as presented in the paper by Banvilett et al. [17] and then modified by the Bracessi correction factor with the use of the Energy curve characteristic data such as the slope value:

$$T_{\text{cal}} = \frac{1}{M^+ \int_0^\infty \frac{p(W_a)}{N(W_a)} dW_a} \cdot \frac{1}{\lambda_{W_a}}, \quad (23.9)$$

where: W_a —is the strain energy amplitude, $N(W_a)$ is a function giving back the cycle number of the fatigue characteristic, λ_{W_a} —Bracessi correction factor rescaled for the strain energy fatigue characteristic.

That approach is viable if we are dealing with a time history that can be transformed into a power spectral density. The problem arises if we want to directly use the Power spectral density of the energy parameter as it is non-gaussian under the pure assumptions. A first approach on how to take this effect into account has been presented by Böhm and Łagoda [18] where the probability density function is being modified:

$$T_{cal} = \frac{1}{M^+ \int_0^\infty \frac{p_N(W_a)}{N_0 \left(\frac{W_{af}}{W_a}\right)^{m'}} dW_a}, \quad (23.10)$$

where: W_{af} —strain energy fatigue limit, N_0 —number of cycles till failure, m' —slope of the energy fatigue curve:

A direct damage degree model has been presented by Böhm and Benasciutti [19]. They have presented a solution for the elastic material state, which takes into account the non-gaussian character of the strain energy:

$$E[D_W(T)] = \frac{T v_{0,W}^+}{A_w} (2a\xi_0)^{m'} \Gamma(1 + m'), \quad (23.11)$$

where: a —scale parameter, A_w —fatigue strength coefficient of the S-N curve of $W(t)$, Γ —gamma function, $v_{0,w}^+$ —rate of mean value up-crossings.

The problem with the elastic-plastic state remains still unsolved for the strain energy models and is a topic for future research papers.

23.3 Conclusions and Observations

The non-gaussian effect influencing the loading remains a huge problem for fatigue life estimation methods defined in the frequency domain. The presented review of models does not fully exhaust the topic, but is only an attempt to highlight the most practical solutions, that can be easily implemented within the frequency domain. On the basis of this research one can formulate certain conclusions and observations:

- There are solutions allowing for the correction of the determination of the crack initiation moment due to the Gaussian load disturbance for stress models and with the use of the energy parameter;
- The model proposed by Bracessi et al. has the broadest application range for both stress and strain energy approach;

- The review showed that for strain models there is currently no effective method defined in the frequency domain (work in progress);
- The use of the approach based on the energy parameter allows us to directly analyze also in the field of energy;
- The energy parameter itself has a non-gaussian distribution;
- The study analyzes a wide range of models due to their usefulness in the process of determining the moment of crack initiation due to the possibility of taking into account the phenomenon of gaussian distribution disturbance.

References

1. Miles J (1954) On the structural fatigue under random loading. *J Aeronaut Sci* 21(11):753–762
2. Dirlik T (1985) Application of computers in fatigue analysis, Ph.D. Thesis. University of Warwick, UK
3. Pitoiset X, Preumont A (2000) Spectral methods for multiaxial random fatigue analysis of metallic structures. *Int J Fatigue* 22:541–550
4. Niesłony A, Böhm M (2012) Application of spectral method in fatigue life assessment–determination of crack initiation. *J Theor Appl Mech* 50(3):819–829
5. Benasciutti D, Tovo R (2006) Fatigue life assessment in non-Gaussian random loadings. *Int J Fatigue* 28(7):733–746
6. Benasciutti D, Tovo R (2005) Cycle distribution and fatigue damage assessment in broad-band non-Gaussian random processes. *Probab Eng Mech* 20(2):115–127
7. Benasciutti D, Tovo R (2018) Frequency-based analysis of random fatigue loads: models, hypotheses, reality. *Materialwiss Werkstofftech* 49:345–367
8. Braccesi C, Cianetti F, Lori G, Pioli D (2009) The frequency domain approach in virtual fatigue estimation of non-linear systems: the problem of non-Gaussian states of stress. *Int J Fatigue* 31:766–775
9. Niesłony A, Böhm M, Łagoda T, Cianetti F (2016) The use of spectral methods for fatigue life assessment for non-Gaussian random loads. *Acta Mechanica et Automatica* 10(2):100–103
10. Palmieri M, Česník M, Slavič J, Cianetti F, Boltežar M (2017) Non-Gaussianity and non-stationarity in vibration fatigue. *Int J Fatigue* 97:9–19
11. Macha E (1996) The spectral method of fatigue life calculation under random multiaxial loading, *Physicochemical. Mech Mater* 32:86–96
12. Niesłony A, Macha E (2007) *Spectral method in multiaxial random fatigue*. Springer-Verlag, Berlin Heidelberg
13. Böhm M, Niesłony A (2015) Strain-based multiaxial fatigue life evaluation using spectral method. *Proc Eng* 101:52–60
14. Rognon H, Da Silva Botelho T, Tawfiq I, Galtier A, Bennebach M (2011) Modeling of plasticity in spectral methods for fatigue damage estimation of narrowband random vibrations. In: *Proceedings of the Volume 1: 23rd biennial conference on mechanical vibration and noise, Parts A and B*; ASMEDC: Washington, DC, USA, pp 771–779
15. Böhm M, Kowalski M, Niesłony A (2020) Influence of the elastoplastic strain on fatigue durability determined with the use of the spectral method. *Materials* 13:423
16. Kluger K, Łagoda T (2014) New energy model for fatigue life determination under multiaxial loading with different mean values. *Int J Fatigue* 66:229–245
17. Banvillet A, Łagoda T, Macha E, Niesłony A, Palin-Luc T, Vittori J-F (2004) Fatigue life under non-Gaussian random loading from various models. *Int J Fatigue* 26:349–363
18. Böhm M, Łagoda T (2019) Fatigue life calculation with the use of the energy parameter for the elastic material state in the spectral method. *Lect Notes Mech Eng* 80–87

19. Böhm M, Benasciutti D (2021) A frequency-domain model assessing random loading damage by the strain energy density parameter. *Int J Fatigue* 146(3):1–11

Part IV
Failure Analysis and Recent Advances
on Mixed-Mode Fatigue and Fracture

Chapter 24

On High- and Very High Cycle Fatigue of Metals and Alloys at Axial Loading



E. B. Zavoychinskaya

Abstract There are discussed Mughrabi's diagram and Shanyavskii's bifurcation fatigue curve. Here is shown that the authors represent on one graph the areas of different fatigue curves at different frequencies of uniaxial loading. The well-known mechanisms of micro-fracture initiation are considered. They are ductile and brittle failure mechanisms and they occur at loading with any frequency. The failure stress amplitude is a function of three variables: number of cycles, loading frequency, and temperature. For the nickel alloy EI437B, 9–12% chromium martensitic steel and titanium alloy VT3-1 the fatigue properties of which do not depend on frequency, the areas of brittle micro-, meso- and macro-defect evolution and fatigue curves on defect levels are constructed on the scale-structural fatigue model, they describe the experimental data satisfactorily. The basic characteristics of the model for materials with frequency-dependent fatigue properties are determined as a function of the loading frequency.

Keywords High- and very high fatigue · Frequency · Brittle and viscous fracture · Scale-structural fatigue model

24.1 H. Mughrabi Fatigue Curve [1] and Bifurcation Fatigue Curve [2–4]

A large number of works in recent years are devoted to the problem of safety operation of structures with long service life. For economic reasons, design and operating companies are making efforts to extend the element life. Studies on high- and very high cycle fatigue are carried out in the Institute of Applied Mechanics named after Ishlinsky [5], MAI, MATI named after Tsiolkovsky, VIAM [2–4], IMET named after Baykov [6, 7], IMASH named after Blagonravov [8, 9], SPBPU [10], in the institutes

E. B. Zavoychinskaya (✉)

Department of Theory of Elasticity, Faculty of Mechanics and Mathematics, Moscow State University named after M. V. Lomonosov, Leninskie Gori, GSP-1, Moscow 119991, Russia
e-mail: elen@velesgroup.com

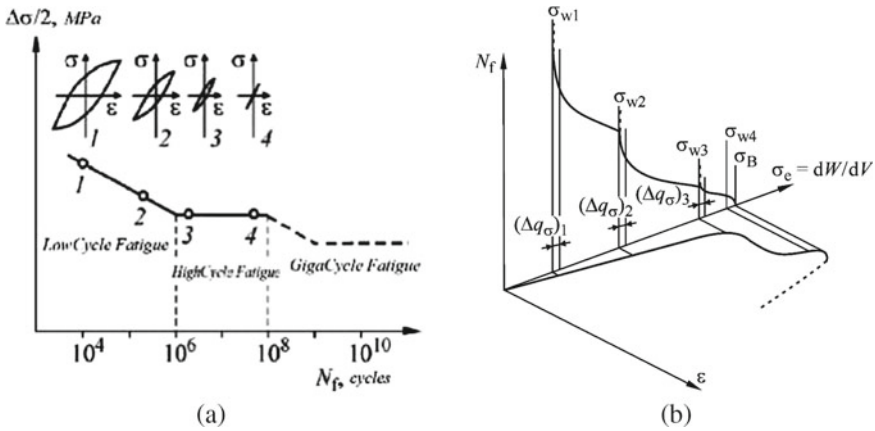


Fig. 24.1 a Mughrabi's chart [1], b Shanyavskii's chart [2–4]

and universities of Germany and Austria [11–13], France and Italy [2, 3, 14, 15], Japan [16, 17], in the institutes of South Korea [18], and other scientific organization.

In the most works the theoretical high- and very high cycle fatigue curve at symmetric uniaxial loading is based on the multistage model of Mughrabi [1] (Fig. 24.1a) with the identification of two mechanisms of fatigue initiation: from microfailure on the sample surface (stable slip bands are observed) and from the geometric concentrators of the structure in the body volume (microfacets are observed inside and at the grain boundaries, in the area of inclusions with the formation of fine-grained structure area “fish eye”) with or not the endurance. This behavior is observed in Cr–Mo steels, bearing steels, titanium alloys. For example, in the VT3-1 two-phase titanium alloy, the micro failure nucleation sites are the phase boundaries, the micro failure occurs by the second mechanism and an optically dark zone near the inclusion is formed. In the area of high cycle fatigue, both mechanisms of micro failure initiation are observed.

In [2–4] the bifurcation fatigue curve (Fig. 24.1b) is considered with the area in which these mechanisms are realized with different probabilities, determined by the energy absorption, it is discussed possible a break of the fatigue curve and several endurance limits. Different branches of fatigue curve are described by different power functions of the failure amplitude from the cycle number. If it is accepted that the fatigue curves have bifurcation regions, possible discontinuities, the presence of several endurance, then there is a problem to describe such fatigue processes (for example on the hypotheses of the scale-structural fatigue theory [19–23]) with transition to the next level to reach the failure state at the previous level. And the problem of determination of basic characteristics for failure probability at each level exists.

24.2 Influence of Frequency on Fatigue Characteristics of Metals and Alloys

The numerous number of experimental works are devoted to the study of high and very high cycle fatigue at various loading frequencies (for example in the works [10, 11, 18, 24–26]). At changing of the modes of high-speed units vibrations can occur in various areas of the sound range (up to 20 kHz), up to the range of ultrasonic frequencies (up to 100 MHz and above). For example, the supporting structures of modern aircraft could be subjected to high-frequency loading due to aerodynamic interaction with the environment and the action of intense acoustic fields generated by jet engines. High-frequency cyclic loads take place in parts of various technological ultrasonic equipment, in hydroacoustic transducers. The Wehler curve in the areas of high- and especially very high cycle fatigue is plotted on the high-frequency test data. For the study of high- and, especially, very high cycle fatigue, as a rule, high-frequency test methods could be applied (as methods of accelerated tests).

For some materials fatigue characteristics are weakly dependent on the loading frequency, for example, for pure metals (aluminum, copper), most nickel alloys, as for alloy EI437B [24, 25] on Fig. 24.2a (the experimental data at a frequency of 10 kHz are marked solid circles, hollow circles correspond to a frequency of 16 Hz). Figure 24.2b is presented a calculation on the model [19–23] for nickel alloy EI437B, fatigue properties not depending on frequency, the I–III areas correspond to

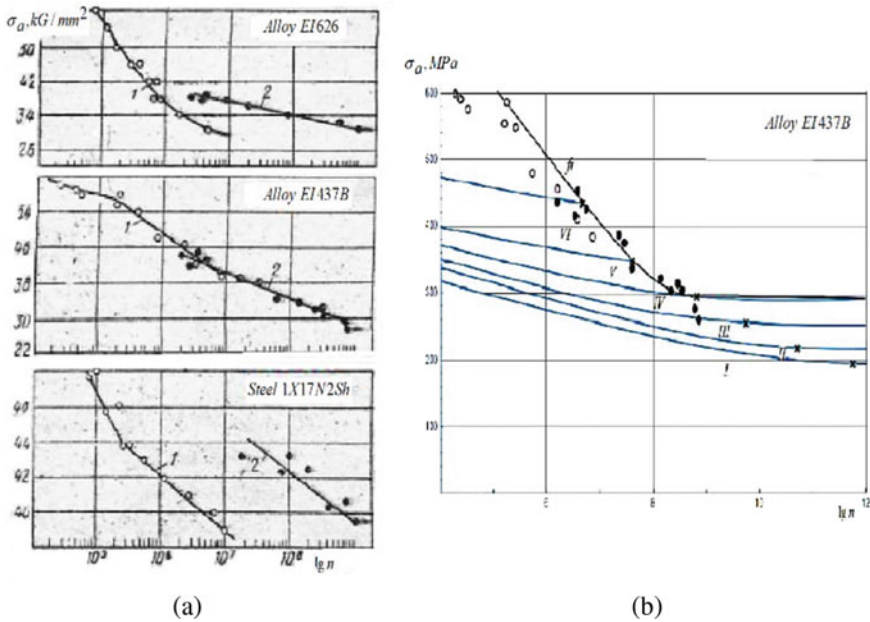


Fig. 24.2 a Experimental data [27], b calculation data for nickel alloy EI437B

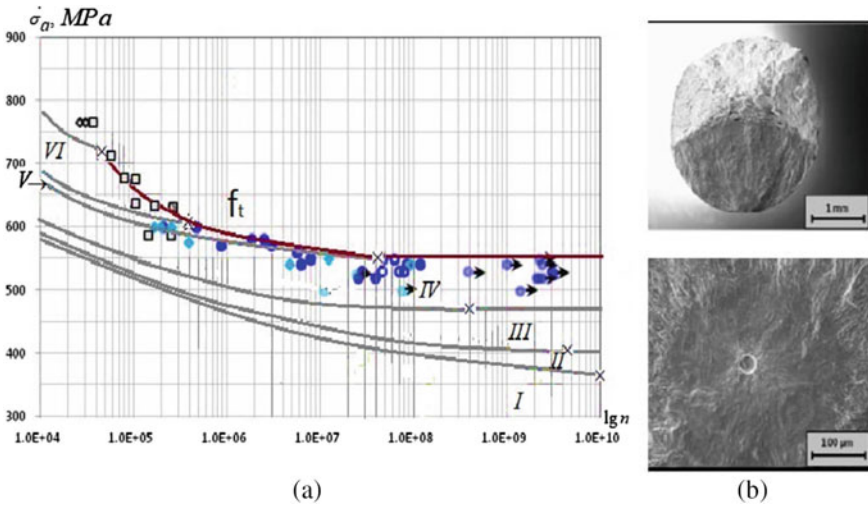


Fig. 24.3 **a** Calculation data for nickel alloy and 9–12% martensitic-chromium steel correspondingly, **b** macro-failure surface with initiation over inclusion, $\sigma_{-1} = 550 \text{ MPa}$, $N_{-1} = 4.66 \cdot 10^7$ cycles [11].

micro level defect nucleation and growing, the IV is the growth of mesodefects (on average, by grain size), the V–VI areas are brittle macro crack growing. Curve fit is the theoretical fatigue curve on the model. It can be seen that the model is satisfactorily described the experimental data at different frequencies. The Wöhler curve of 9–12% martensitic-chromium steel [11] is also independent of frequency. For this steel the experimental [11] and calculation data [21–23] are presents in Fig. 24.3a (solid circles are first mechanism failure, hollow circles are second failure mechanism at frequencies 100 Hz and 20 kHz, black hollow squares are the first mechanism at 25 Hz).

There is observed the same situation for titanium alloy VT3-1 [5, 10, 26]. It was conducted the analysis of fatigue at uniaxial asymmetric loading (at different values of the parameter $\alpha = (\sigma_{\max} + \sigma_{\min}) / (\sigma_{\max} - \sigma_{\min})$) at sound frequencies up to 100 Hz and an ultrasonic frequency of 20 kHz, the basic characteristics of the scale-structural fatigue model were found. The areas of defect growing are obtained. It is shown that the fatigue curves for IV level defects at sound and ultrasonic vibrations practically coincide, the fatigue is practically independent of the frequency. The macro-failure and micro-failure (on the α —phase splitting and the β —phase mesodefekt initiation) are shown in Fig. 24.4.

On the other hand, for example, as for the nickel alloy EI826 and steel 1X17N2Sh on Fig. 24.2a, we can see that the fatigue curves are different for different frequencies. An analysis of exploration on fatigue of steels, nickel, aluminum and titanium alloys at different loading frequencies allows us to conclude that for materials, fatigue properties depending on frequency, different sections on Fig. 24.1 a) describe different failure processes, namely, with subsonic frequency as usually in the region of low

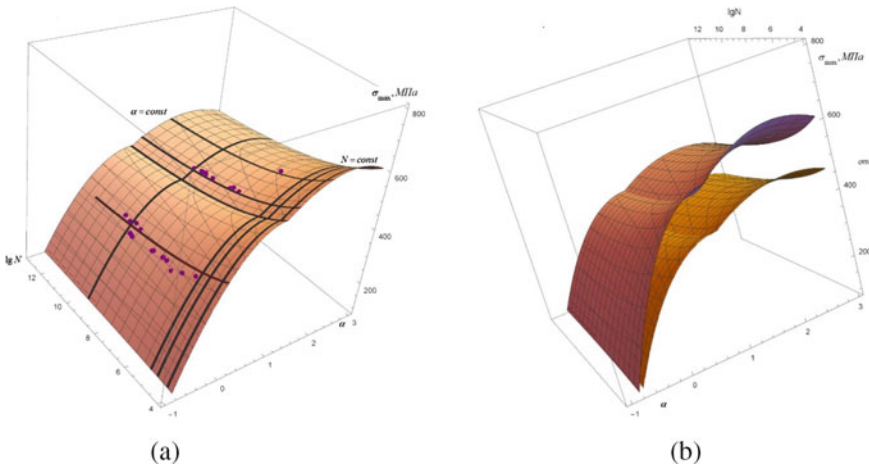


Fig. 24.4 **a** Macro-failure surface of VT3-1 in coordinates $(\sigma_{max}, \lg N)$ and experimental data [2, 3, 5, 10, 26], **b** micro- and macro-failure surface of VT3-1

and high cycle fatigue and with ultrasonic loading frequency at the very high cycle fatigue. This can also explain the break of the fatigue curve mentioned in some works. The diagram of Mughrabi (Fig. 24.1a) and Shanyavskii’s chart (Fig. 24.1b) show two different Wehler curves at different frequencies for a material depending on frequency fatigue characteristics. The right section after point 4 can be continued to the left into the region of low- and high cycle fatigue, while it will be located the Sects. 24.1–24.4, which indicates the material hardening with an increase of SSfrequency, as is observed in most experiments at high cycle fatigue. This is explained by the fact that at subsonic frequencies the material is under a stress of the same sign for a sufficiently long time, and microdefects have time to develop in many microregions, only single microdefects have time to develop at ultrasonic frequencies and a small half-period. The left part 1–4 on Fig. 24.1a can be continued to the right in the area of very high cycle region and it will probably be a different curve than the one plotted on the basis of ultrasonic loading.

So different Wöhler curves as a function of two variables: the number of cycles and the loading frequency, namely, in the area of high cycle fatigue—with one, as a rule, sonic frequency, in the area of gigacycle fatigue—with another, as a rule, ultrasonic frequency, are represented in Fig. 24.1. In this case, both, namely, the first mechanism of viscous fracture, and the second of the brittle failure take place at loading with any frequency, depending on the number of cycles. In the area of endurance of the investigated ductile materials, the viscous mechanism was basic. The temperature is the third independent variable. In using air and water cooling of sample experiments, a dependence on the loading frequency was also observed [11, 24, 25]. In the area of gigacycle fatigue, significant heating of samples (due to irreversible transformations of mechanical energy into thermal energy) leads to

softening of the material with increasing frequency. The basic characteristics of the fatigue model [19–23] should be the functions of loading frequency and temperature.

24.3 On the Mechanisms of Viscous and Brittle Failure

Both described above failure mechanisms take place at loading at any frequency. The first mechanism is the mechanism of viscous failure. In the low cycle region (at $N \in (10^4, 10^6)$ cycles) of plastic materials, inelastic deformation and viscous failure processes are possible, at the nanoscale level there are characterized by the appearance of plastic distortion at the critical curvature of the crystal lattice with the generation and evolution of dislocations by twinning and sliding mechanisms and the cellular substructure formation, which leads to the movement of grain ensembles and the appearance of microshear bands at the microlevel, to the formation of mesoscale slip bands and structural-phase decomposition of the deformable material with the generation and growth of porosity, ending by the initiation of a viscous macrocrack. At the macroscale level, intense sliding of grain ensembles occurs. In this area, the magnitude of inelastic deformations does not exceed elastic strains and inelastic straining inhibits the brittle crack growing.

The second mechanism is the brittle failure mechanism, which is the main in the areas of high- and very high cycle fatigue. A focus of brittle micro-fracture from the structure geometric concentrators is likely both in the volume of the body and on the surface in the case when the surface is ahead of the internal volumes in the accumulation of microdefects. In the area of low cycle fatigue of plastic materials, the process of viscous failure by the first mechanism and the growing of brittle micro- and macro-cracks by the second one take place simultaneously. On the fractographs it is possible to distinguish both a zone of shear fracture, namely, the region of evolution of inelastic straining and viscous cracks with pits, and a zone of brittle fracture by separation. For plastic materials, in many cases, the process of viscous failure is decisive in the macrocrack nucleation.

24.4 Conclusion

Thus, the fatigue analysis in metals and alloys at uniaxial loading, including asymmetric cycles, allows to formulate the following conclusions.

In general, fatigue curves on defect levels are functions of frequency and temperature. So the diagram of H. Mughrabi and Shanyavskii's chart shows two different Wehler curves at different frequencies for a material depending on frequency fatigue characteristics.

Here are presented the areas of micro-, meso- and macro-defect growing and uniform fatigue curves on defect levels and brittle fracture for nickel alloy EI437B, two-phase titanium alloy VT3-1, and 9–12% martensitic-chromium steel, fatigue

properties are independent on the loading frequency, at asymmetric uniaxial loading. The model is satisfactorily described the experimental data at different frequencies.

For materials (for example, nickel alloys, highly alloyed stainless steels, and others), fatigue properties are dependent on the loading frequency, fatigue curves are different for different frequencies.

There are known two mechanisms of fatigue initiation. The first one is from microfailure on the sample surface (stable slip bands are observed). This mechanism is of the viscous failure. And the second one is from the geometric concentrators of the structure in the volume or on the surface of the body with or not the endurance. This is the mechanism of brittle failure.

In the low cycle region of plastic materials, inelastic deformation and viscous failure processes take place. Wherein brittle fracture processes from surface microdefects develop also. In this area the magnitude of inelastic deformations does not exceed elastic strains and inelastic straining inhibits the brittle crack growing.

In the high cycle region, the brittle micro-fracture from the structure geometric concentrators take place in the volume or on the surface of the body.

In the very high cycle region, the brittle micro-fracture from the structure geometric concentrators begins in the volume of the body in many cases.

References

1. Mughrabi H (2002) *Fatigue Fract Eng Mater Struct* 25:755–764
2. Shanyavsky AA, Nikitin AD, Palin-Luc T, Bathias C (2014) *Phys Mesomech* 17(4):59–68 (in Russian)
3. Nikitin A, Bathias C, Palin-Luc T, Shanyavskiy A (2016) Crack path in aeronautical titanium alloy under ultrasonic torsion loading. *Frattura ed Integrità Strutturale* 10(35):213–222
4. Shanyavsky AA, Soldatenkov AP (2019) *Phys Mesomech* 22(1):44–53 (in Russian)
5. Burago N, Nikitin I (2016) *Mathematical modeling and optimization of complex structure*. Springer, Heidelberg, pp 117–130
6. Botvina LR, Bolotnikov AI, Sinev IO (2019) *Phys Mesomech* 22(6):24–36 (in Russian)
7. Terent'ev VF, Korableva SA (2015) *Metal Fatigue*. Nauka (in Russian)
8. Makhutov NA (ed) (2019) *Strength, resource, survivability and safety of machines*. B. H. "Librokom" (in Russian)
9. Makhutov NA, Matvienko Yu-G, Romanov AN (ed) (2018) *Problems of strength, technogenic safety and structural materials science*. Lenand (in Russian)
10. Ngkok N, Kapralov VM, Kolenko GS (2019) *Scientific and technical statements of SPbPU. Nat Eng Sci* 25(2):68–77 (in Russian)
11. Christ HJ (2018) *Fatigue of materials at very high numbers of loading cycles* springer. Springer, Wiesbaden
12. Gunther J, Krewerth D, Lippmann T, Leuders S, Troster T, Weidner A, Biermann H, Niendorf T (2017) *Int J Fatigue* 94(2):236–245
13. Karr U, Sandaiji Y, Tanegashima R, Murakami S, Schonbauer B, Fitzka M, Mayer H (2020) *Int J Fatigue* 34:105525
14. Jeddi D, Palin-Luc T (2018) *Fatigue Fract Eng Mater Struct* 41:969–990
15. Berto F, Campagnolo A (2015) *Frattura ed Integrità Strutturale* 33:229–237
16. Furuya Y, Hirukawa H, Takeuchi E (2019) *Sci Technol Adv Mater* 20(1):643–656
17. Nishimura Y, Yanase K, Tanaka Y, Miyamoto N, Miyakawa S, Endo M (2020) *Int J Damage Mech* 29(1):4–18

18. Sharma A, Min Chul Oh, Byungmin A (2020) Recent advances in very high cycle fatigue behavior of metals and alloys—a review. *Metals* 10:1200
19. Zavoychinskaya E (2021) Understanding complex systems. Springer, Switzerland, pp 71–89
20. Zavoychinskaya EB (2020) *J Phys Conf Ser Inst Phys (United Kingdom)* 1431:012024–012032
21. Zavoychinskaya EB (2020) *Moscow University Mechanics Bulletin Allerton. Press Inc. (United States)* 74(2):36–40 (in Russian)
22. Zavoychinskaya E B 2020 Modern problems of continuum mechanics. In: Proceedings of XX international conference (Rostov-on-Don, June 18-21, 2020) Taganrog, Southern Federal University 2 97–101 (in Russian)
23. Zavoychinskaya EB (2019) Modern problems of mathematics and mechanics. Sadovnichy. Llc MAX Press, pp 694–697
24. Matokhnyuk L, Byalonovich A, Kofto D (2013) *Bulletin of TNTU* 71(3):99–122 (in Russian)
25. Reports of the 2nd and 3rd All-Union Seminars (1980) Strength of materials and structural elements at sound and ultrasonic loading frequencies 1980, 1983 Kiev Naukova Dumka
26. Gabov IG, Kotelnikov AN (2015) *Fundam Res* 9:423–429 (in Russian)
27. Troshchenko VT, Afonin AI, Hamaza LA (1973) *Probl Strength* 6:25–29

Chapter 25

Analysis of Aramid Fabric Damage Mechanisms as a Result of Different Load Speeds



Pawel Zochowski, Dariusz Pyka, Adam Kurzawa, Marcin Bajkowski, Mariusz Magier, Ilmars Blumbergs, Roman Grygoruk, Mirosław Bocian, and Krzysztof Jamroziak

Abstract The study aramid fabrics of Twaron T750 type loaded in quasi-static punching and impact loading tests were tested. The scope of these works was carried out in the form of piercing with a non-deformable steel penetrator with a semi-spherical tip, moving at a constant low speed and on the drop impact test and firing the aramid fabric with a 9×19 mm Parabellum projectile. The areas of damaged yarns were subjected to microscopic analysis using the SEM technique. In this way, efforts were made to show that the speed of piercing is important in terms of the damage to the yarns of the individual fibers of the fabric. The obtained results were used to formulate guidelines for the design of energy-consuming structures.

Keywords Aramid fabric · Fatigue strength · Piercing · SEM analysis · Fiber damage

P. Zochowski

Military Institute of Armament Technology, Wyszyńskiego, 7, 05-220 Zielonka, Poland

D. Pyka · M. Bocian · K. Jamroziak (✉)

Department of Mechanics, Materials Science and Engineering, Faculty of Mechanical Engineering, Wrocław University of Science and Technology, Smoluchowskiego, 25, 50-370 Wrocław, Poland

e-mail: krzysztof.jamroziak@pwr.edu.pl

A. Kurzawa

Department of Lightweight Elements Engineering, Foundry and Automation, Faculty of Mechanical Engineering, Wrocław University of Science and Technology, Smoluchowskiego, 25, 50-370 Wrocław, Poland

M. Bajkowski · M. Magier · R. Grygoruk

Institute of Mechanics and Printing, Faculty of Mechanical and Industrial Engineering, Warsaw University of Technology, Narbutta, 85, 02-524 Warsaw, Poland

I. Blumbergs

Institute of Aeronautics, Riga Technical University, 1 Kalku street, Riga LV-1658, Latvia

25.1 Introduction

High-strength para-aramid fabrics are the basic material in special constructions exposed to impact loads. The basic component of this type of fabric is a fiber with a diameter of several to several micrometers [1, 2]. Due to the specific structure, fabrics made of para-aramid fibers are characterized by a favorable combination of very good mechanical properties and low own weight. Their high efficiency of absorbing and dissipation of impact energy results both from the material properties of the fibers themselves (tensile strength, Young's modulus, relative elongation), but also from the mechanisms and methods of interaction of individual components making up the fabric at all levels of the structure (fibers-yarns-layers-composite laminate) [3, 4]. Bearing in mind the behavior of individual structures of the composite package, an important issue is a detailed analysis of the work of individual yarns at different load speeds in order to determine the important mechanisms that affect their damage. Many papers describing this type of issue [5, 6] refer to the search for optimal solutions in the area of their improvement.

The aim of the study was to investigate the mechanics of destruction (cracking) of the fibers forming the layer of Twaron T750 aramid fabric. This destruction was carried out at different load speeds so that it was possible to observe its influence on the yarn damage process. Knowledge of these processes will be helpful in assessing the ability to absorb impact energy and formulating postulates for the construction of safe structures.

25.2 Materials and Research Methodology

The study analyzed the T750 fabric made of high-tenacity Twaron® para-aramid fibers of The Netherland company Teijin Aramid. The mechanical parameters of the tested fabric are summarized in Table 25.1 and the general view of the fabric in the state before puncture is shown in Fig. 25.1.

As part of the analysis, several tests of material piercing under quasi-static conditions and with a drop hammer as well as firing with a 9×19 mm Parabellum projectile were carried out to check the behavior of the fabric under impact conditions with high deformation rates. The fabrics were fixed in a steel frame with a hole of 100 mm in diameter. Stable fastening of the fabric was carried out linearly around the perimeter

Table 25.1 Selected physical and mechanical properties of the Twaron T750 fabric [1]

Style	Linear density (dtex)	Twaron® type	Weave	Area density (g/cm ²)	Thickness (mm)	Min. breaking strength (N/5 cm × 1000)
T-750	3360	1000	Plain	460	0.65	16.2–17.4

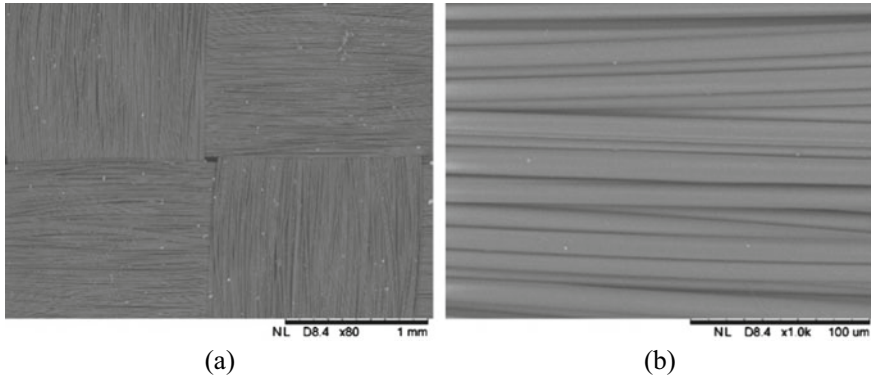
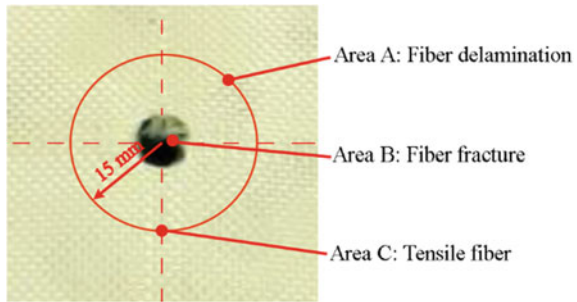


Fig. 25.1 General view of the T750 fabric structure: **a** 80× magnification, **b** 1000× magnification

of the opening. The fabrics were punctured in the axis of the frame opening. The analysis of the fabric structure after the puncture tests was performed on the Hitachi TM-3000 scanning microscope. The microscopic observations were concentrated in the areas determined on the basis of the results of the stress distribution obtained from numerical analyzes.

Microscopic observations were carried out in three reference areas (Fig. 25.2). Area A—the so-called fiber delamination area, area B—puncture area in which the condition of the end sections of the fibers was analyzed, area C—the area where the fibers were drawn. The reference observation points for area A and area C were determined at a distance of 15 mm from the puncture hole axis. In the scope of the observation carried out in the B area, the microscopic characteristics of the end sections of the fibers were taken.

Fig. 25.2 Marking areas selected for microscopic observations



25.3 Results and Discussion

The results of the quasi-static piercing, drop test, and pistol round firing are shown in Fig. 25.3.

According to the Literature [7, 8] as can be seen at low penetration velocity (Fig. 25.3a) the stress wave does not play a significant role in the stress distribution. Energy is absorbed by the sample in the form of deformation, matrix cracking, fiber breakage, and delamination. It has been schematically presented in Fig. 25.3a in relation to the puncturing of the aramid laminate in the drop test (10 layers of T750 fabric) with an impact velocity of 8.8 m/s, where the absorbed energy of app. 92.9 J was recorded.

In the case of a ballistic impact, the energy absorption mechanism is different (overshooting 10 layers of T750). As shown schematically (Fig. 25.3b), the perpendicular impact of the projectile on the target generates compressive and shear stress waves along the direction of the projectile penetrating the composite. Whereas the waves transverse to the penetration direction of the projectile are waves of tensile and shear stresses in the direction of the plane.

The region marked I is under the projectile. Region II is surrounded by the area to which the transverse stress wave runs along with the directions in the plane. As also shown schematically (Fig. 25.3b), the primary yarns run through region I and form a characteristic cross (red color). The secondary yarns are found in region II.

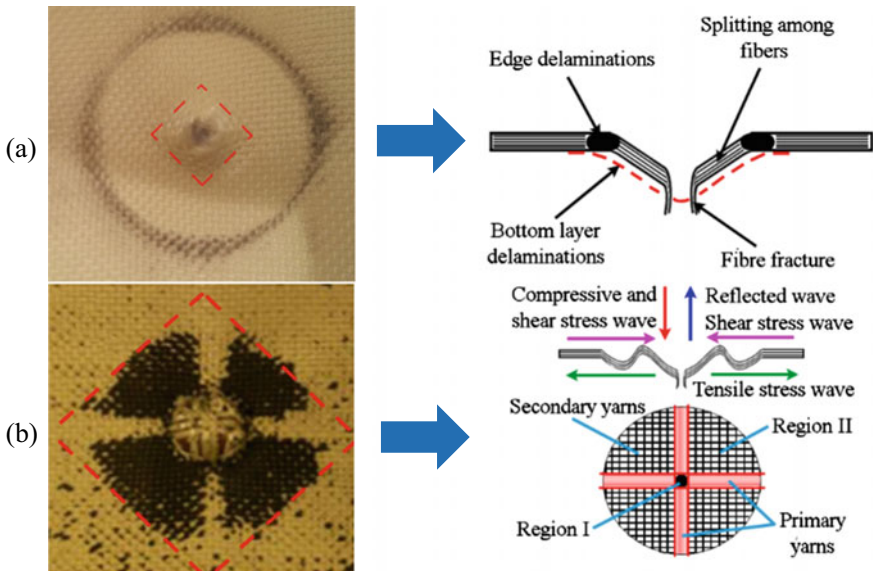


Fig. 25.3 Schematic arrangement of a typical woven-fabric composite target: **a** during drop test, **b** during ballistic impact

Compression of the layers in this region is due to the transverse wave propagating in the directions in the plane. Also in these directions, a tensile stress is generated.

Later on, attention was focused on the analysis of yarns using scanning electron microscopy (SEM). On this basis, the work mechanisms of the warp and weft of the aramid fabric yarn were assessed. For this purpose, two types of failure of the fabric presented in Table 25.2 were analyzed.

In area A (see Fig. 25.2), the so-called in the delamination area, strong deformation of the yarn constituting the weft of fabric is visible. In this area, due to the complex state of stresses caused mainly by tensile and bending forces, yarn damage is observed mainly by pulling single fibers from the weft from the interlacing (Fig. 25.4).

In the drop test, the destruction of the fibers takes place mainly on the surface of the fibers by delamination of the outer surface of the fiber. The impact load of the 9×19 mm projectile increases the number of broken weft fibers with the observed limited surface delamination.

In the area of puncture (area B), the observations confirmed the difference in the failure mechanism between the performed tests. The analysis of the end sections of the fibers participating in the contact with the projectile/penetrator showed that after the drop test, the fibers in this zone were usually sheared, and the observations confirmed their slight delamination (Fig. 25.5a).


During the shooting test, most of the fibers were damaged by tearing, causing the characteristic strong delamination of their tips (Fig. 25.5b).

In the C region, where the fibers are strongly drawn out under high tensile forces, the fibers are delaminated longitudinally, which most often leads to the breaking of the microfiber detached from the outer surfaces in both test cases (Fig. 25.6). This area is characteristic of primary yarns.

25.4 Conclusion

The analysis shows a general conclusion that the mechanism of fiber destruction depends on the piercing velocity. In quasi-static piercing, the fibers are first subjected to compression, tensile, and then, after exceeding the limit strain, they are broken. In an impact load, the fibers are sheared, stretched, and twisted due to the rotational velocity of the projectile. It was shown in microscopic images (Fig. 25.4), in which the fibers after the shooting test show the so-called jagged structure, in contrast to the fibers destroyed in the drop test.

Table 25.2 A general view of the puncture effects of Twaron T750 fabric

Drop test		Shooting test (9 × 19 mm Parabellum)	
Front	Rear	Front	Rear
			

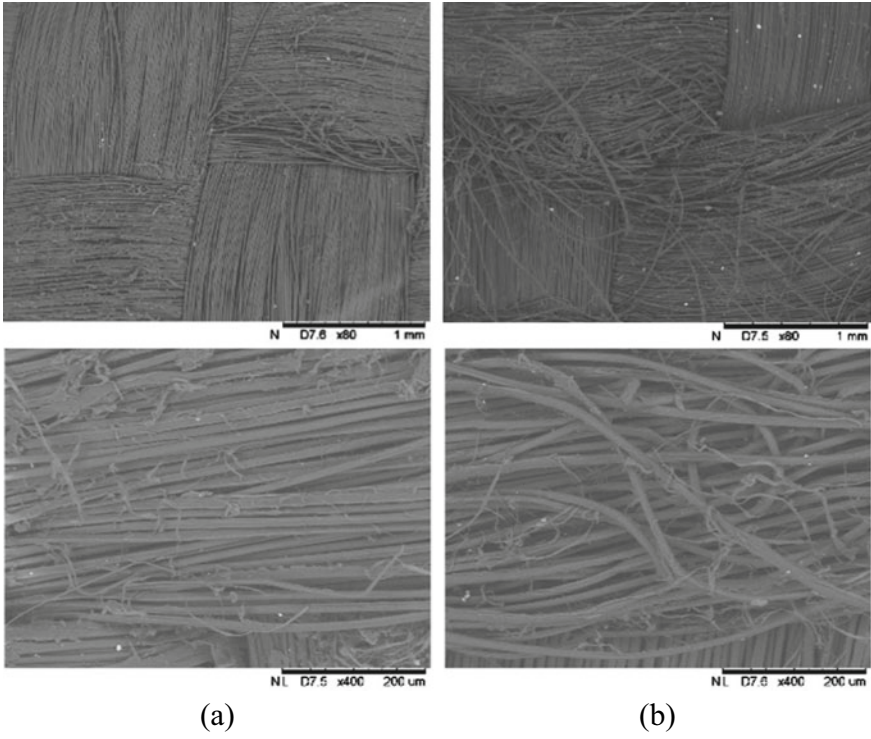


Fig. 25.4 T750 fabric structure after piercing in area A: **a** in the drop test, **b** in shooting test

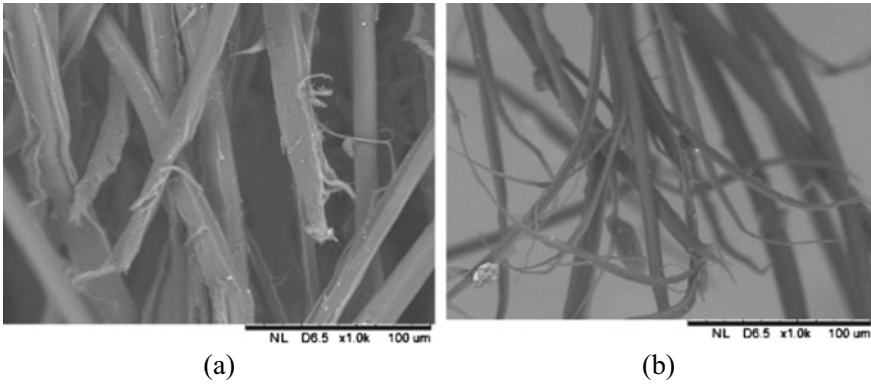


Fig. 25.5 T750 fabric structure after piercing in area B: **a** in the drop test, **b** in shooting test

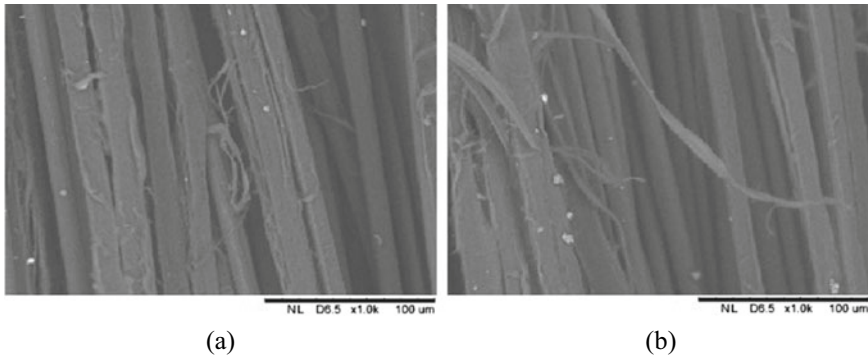


Fig. 25.6 T750 fabric structure after piercing in area C: **a** in the drop test, **b** in shooting test

References

1. Aramid T (2019) Teijin ballistics materials handbook. Teijin Aramid, The Netherlands
2. DuPont (2017) Kevlar® Aramid fiber technical guide. DuPont, US
3. Pach J, Mayer P, Jamroziak K, Polak S, Pyka D (2019) Experimental analysis of puncture resistance of aramid laminates on styrene-butadiene-styrene and epoxy resin matrix for ballistic applications. *Arch Civ Mech Eng* 19(4):1327–1337
4. Mayer P, Pyka D, Jamroziak K, Pach J, Bocian M (2019) Experimental and numerical studies on ballistic laminates on the polyethylene and polypropylene matrix. *J Mech* 35(2):187–197
5. Li TT, Xing M, Gao B, Ren HT, Peng HK, Zhang X, Lin JH, Lou CW (2021) Multiscale synergistic toughened pluronic/PMEA/hydroxyapatite hydrogel laminated aramid soft composites: puncture resistance and self-healing properties. *Compos Part B* 216:108856
6. Pirvu C, Deleanu L (2021) Failure investigation of layered LFT SB1plus package after ballistic tests for level IIA. *Polymers* 13(17):2912
7. Silberschmidt VV (2016) Dynamic deformation, damage and fracture in composite materials and structures. Woodhead Publishing, Cambridge
8. Asemani SS., Liaghat G, Ahmadi H, Anani Y, Khodadadi A, Charandabi SC (2021) The experimental and numerical analysis of the ballistic performance of elastomer matrix Kevlar composites. *Polym Testing* 102:107311

Chapter 26

Experimental Identification of Viscoelastic Properties of Plates Made of Quiet Aluminum



Pasquale Grosso , Alessandro De Felice , and Silvio Sorrentino 

Abstract The present study is aimed at the identification of equivalent viscoelastic models for layered thin-walled structures, obtained from vibration measurement only. Accurate modeling of modal properties is fundamental for describing metal fatigue caused by forced vibration on structural components. A new approach is proposed, based on a definition of an equivalent modal damping ratio applied to the circle-fit technique, to overcome the difficulties related to the identification of modal parameters when adopting non-conventional viscoelastic models. When the structural internal dissipative effects are dominant, this procedure identifies the parameters of an equivalent Young's modulus in the frequency domain. The proposed procedure is applied to the analysis of plates made by Quiet Aluminum, adopting the linear fractional Kelvin-Voigt viscoelastic model and assessing the accuracy of the identified parameters by comparison of numerically simulated with experimentally measured frequency response functions.

Keywords Damping · Viscoelastic models · Fractional derivative models · Modal parameters · Experimental vibration analysis · Quiet aluminum

26.1 Introduction

Accurate evaluation of the damping properties of layered thin-walled structures is a relevant problem for several industrial applications in the field of vibration control and noise reduction [1, 2]. But direct identification from vibration data is generally

P. Grosso · A. De Felice · S. Sorrentino (✉)
Department of Engineering Enzo Ferrari, University of Modena and Reggio Emilia, Via Pietro
Vivarelli 10, 41125 Modena, Italy
e-mail: silvio.sorrentino@unimore.it

P. Grosso
e-mail: pasquale.grosso@unimore.it

A. De Felice
e-mail: alessandro.defelice@unimore.it

a difficult task [3], especially when more refined models than the viscous damping or hysteretic ones are necessary for getting a sufficient accuracy.

The problem of modeling vibrations of layered damped plates has been extensively investigated adopting conventional damping models, but only recently, an approach was developed to identify storage modulus and loss factor with frequency-dependent characteristics [4].

In the present study, a different, indirect approach is proposed, based on the concept of equivalent modal damping ratio (ζ_n). It is well known under which assumptions ζ_n can be defined, by considering a linear viscous dissipative model (integer order Kelvin-Voigt model) or a hysteretic model [5]. However, this theoretical parameter shows a dependency on the related natural frequency that in most cases fails in fitting the experimental data on relatively broad frequency ranges. Better results can be achieved by means of non-integer order differential models [6].

To overcome the difficulty of finding analytical expressions of ζ_n in case of non-conventional dissipative models, a method of general validity is developed, introducing the concept of equivalent modal damping ratio applied to the circle-fit technique [7, 8]. This identification method is based on the assumption that the Nyquist plot of a frequency response function (FRF) for any mode n can be approximated by a circumference, which is still acceptable when considering non-conventional viscoelastic models [9]. An identification algorithm is then proposed, which is valid when the structural internal dissipative effects are dominant with respect to those due to air [10], adopting the fractional Kelvin-Voigt model [6], and applying it to the analysis of a vibrating plate made of Quiet Aluminum (QA) [11]. Among applications, accurate modeling of modal properties would improve the results of vibration-based methods for estimating fatigue in metal or metal-composite structures like QA panels.

26.2 Identification Method

According to the circle-fit technique [8] applied to the integer order Kelvin-Voigt model (in the following simply referred to as Kelvin model), almost circular experimental Nyquist plots of the mobility allow the estimate of the related modal damping ratios ζ_n and natural angular frequencies ω_n , which are given by:

$$\zeta_n = \frac{1}{2\omega_n} \left[\frac{\Omega_{2n}^2 - \Omega_{1n}^2}{\Omega_{2n} \tan(\gamma_{2n}) + \Omega_{1n} \tan(\gamma_{1n})} \right] \quad (26.1)$$

where the symbols refer to Fig. 26.1 a and the natural angular frequency ω_n is identified as the frequency of maximum sweep rate of the circle (say Ω_{0n} ; where the assumption $\omega_n = \Omega_{0n}$ is valid for the Kelvin model, not in general). The result of the identification procedure is a set of experimental modal parameters (ω_n, ζ_n).

However, if the aim of the identification procedure is getting an equivalent Young's modulus in the frequency domain, then the classical dissipative models (Kelvin and also hysteretic) may not be accurate enough. As a consequence, more refined models

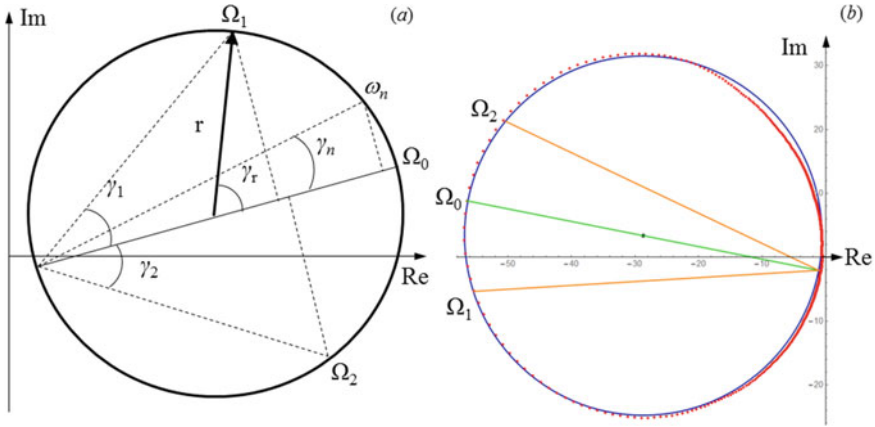


Fig. 26.1 Nyquist plot of mobility, general scheme for mode n (a). Experimental Nyquist plots of mobility, mode at 320 Hz (b)

are often needed. The fractional Kelvin-Voigt model [8] is herein adopted (simply referred to as fractional Kelvin model):

$$\begin{aligned}
 E(\omega) &= E_0 R(\omega) = E_0 [1 + (i\tau\omega)^\alpha], \\
 E(s) &= E_0 R(s) = E_0 [1 + (\tau s)^\alpha],
 \end{aligned}
 \tag{26.2}$$

where α is a non-integer (or fractional) derivative order (values between 0 and 1).

When considering a complex Young's modulus $E(\omega) = E_0 R(\omega)$, the modal mobility can be written as a function of the real and imaginary parts of $R(\omega)$, yielding the following possible definition an equivalent modal viscous damping coefficient:

$$c_n^* = \frac{A_n}{2r} = \frac{k_n \text{Im}[R(\Omega_{0n})]}{\Omega_{0n}}
 \tag{26.3}$$

where k_n is the modal stiffness, A_n is a dimensionless modal coefficient (assumed as real, without loss of generality), r is the radius of the modal Nyquist plot (assumed having circular shape), and Ω_{0n} identifies the maximum sweep rate of the modal circle.

Then, a definition for an equivalent modal viscous damping ratio can be given as

$$\zeta_n^* = \frac{1}{2} \frac{c_n^*}{\sqrt{k_n m_n}} = \frac{1}{2} \omega_n \frac{\text{Im}[R(\Omega_{0n})]}{\Omega_{0n}}
 \tag{26.4}$$

which, compared to Eq. (26.1), yields a direct link between the parameters in the constitutive function R and the experimental data:

$$\text{Im}[E_0 R(\Omega_{0n})] = \frac{\Omega_{0n}}{\lambda_n^2} \left[\frac{\Omega_{2n}^2 - \Omega_{1n}^2}{\Omega_{2n} \tan(\gamma_{2n}) + \Omega_{1n} \tan(\gamma_{1n})} \right] = p_n \quad (26.5)$$

where λ_n is a modal parameter (which can be separately estimated considering a model for the undamped structure). As a possible solution, therefore, an iterative procedure is developed, aimed at identifying the values of the constitutive parameters that minimize an error function between the experimental and the numerically simulated FRFs.

26.3 Experimental Results

The proposed method is applied adopting the fractional Kelvin-Voigt model for identifying the equivalent viscoelastic properties of a QA plate, without any extrapolation beyond the limits of the frequency interval of available data. A uniform square plate was tested with respect to flexural free vibration (height = width = 300 mm; thickness of aluminum layers = 0.987 mm; thickness of intermediate layer = 0.025 mm; total mass = 0.52 kg and equivalent density = 2889 kg/m³). The specimen was restrained to a frame by means of flexible couplings, in order to approximate the free-free boundary conditions. It was excited by means of an instrumented ICP hammer in correspondence of the midpoint, and acceleration responses were evaluated by means of a miniaturized ICP piezoelectric accelerometer placed in the same excitation point, on the opposite face of the plate. An experimental Nyquist plot of modal mobility is displayed in Fig. 26.1b (mode at 320 Hz).

The modal parameters were computed according to the Rayleigh–Ritz method. The equivalent Poisson’s ratios were estimated according to [12], after testing the sensitivity of the natural angular frequencies of the undamped plate. It resulted that the equivalent Poisson’s ratio of QA does not vary significantly with respect to that of aluminum ($\nu = 0.33$, with maximum percentage errors in the natural angular frequencies of less than 0.1%). So, its dependency from frequency was neglected.

The identified equivalent constitutive parameters are reported in Table 26.1, in which $E_{0Al} = 7.1 \times 10^{10}$ [N m⁻²] is the standard value for Young’s modulus of aluminum. A reduction of equivalent static Young’s modulus was expected, and the low values of the fractional exponents mean that the overall dissipative behavior is closer to the hysteretic behavior than to the viscous one.

The experimental estimates of ζ_n are displayed versus the natural frequencies ω_n in Fig. 26.2a. On the experimental data (dots) is superimposed the curve $\zeta_n(\omega_n)$, plotted with the identified equivalent constitutive parameters in the fractional Kelvin model.

Table 26.1 Identified equivalent constitutive parameters in the fractional Kelvin model

$E_0/E_{0Al} = 0.825$	$\alpha = 0.219$	$\tau = 4.829 \times 10^{-8}$ s	$(\rho = 2889 \text{ kg/m}^3, \nu = 0.33)$
-----------------------	------------------	---------------------------------	--

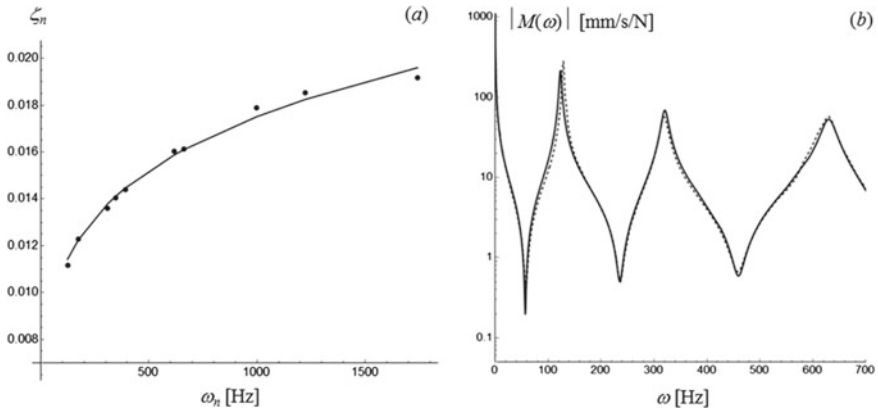


Fig. 26.2 Modal damping ratios ζ_n versus natural frequencies (a): experimental identified data (dots) and fractional Kelvin model interpolation (continuous curve). Mobility modulus versus frequency (b), experimental data (dotted) and fractional Kelvin model numerical simulation (continuous)

The accuracy of the identified parameters in the fractional Kelvin model is assessed by comparison of numerical with experimental FRFs (modulus of mobility), as shown in Fig. 26.2b (where the peaks are related to modes 3, 5 and 11 of the free plate).

The same experimental FRFs were then compared with those obtained adopting an equivalent complex Young's modulus descending from either the Kelvin or the hysteretic models. In this case, the viscoelastic parameters were identified considering a single mode (actually mode 3). Both models are clearly unable to fit the experimental FRFs, as shown in Fig. 26.3a (where 'v' identifies the FRFs computed with the Kelvin model, 'h' those computed with the hysteretic model and 'f' those already displayed in Fig. 26.2b).

Better results were obtained by using whole sets of identified modal parameters, either (ω_n, ζ_n) for viscous damping or (ω_n, η_n) for hysteretic damping. These sets of modal parameters were used for building a viscous damping matrix and a hysteretic damping matrix, respectively. The FRFs thus obtained are displayed in Fig. 26.3b. Also, in this case, the hysteretic damping model gives better results than the viscous damping one. However, notice that the viscous and hysteretic models are not accurate out of the resonances.

26.4 Conclusions

The possibility of applying the circle-fit technique to the identification of non-conventional viscoelastic models from vibration data has been investigated on a plate made of Quiet Aluminum, discussing the limitations due to the adoption of the viscous damping and hysteretic models. A novel procedure has been proposed

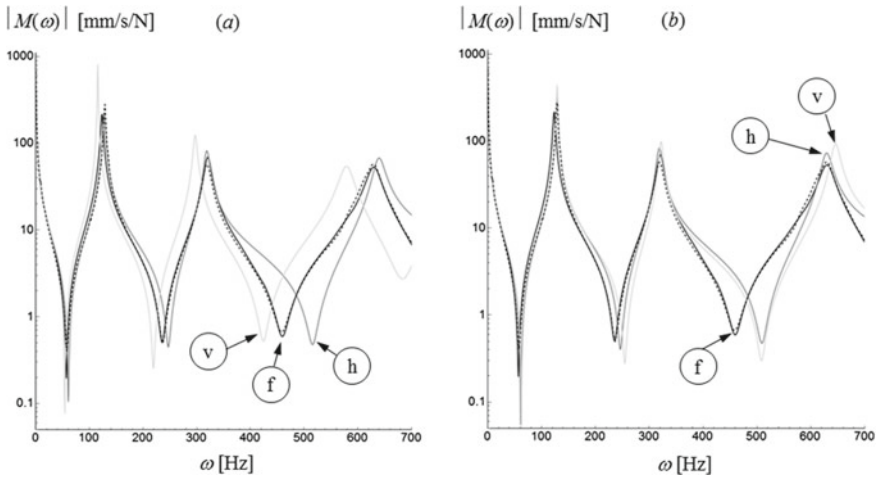


Fig. 26.3 Mobility modulus versus frequency. Experimental (dotted) and numerical simulations. Kelvin and hysteretic models (a) compared with identification based on modal viscous damping and modal hysteretic damping (b)

to overcome the difficulties related to the identification of modal parameters when adopting non-conventional viscoelastic models (in this case the linear fractional Kelvin-Voigt model), based on the concept of equivalent modal damping ratio and aimed at identifying an equivalent Young's modulus when the structural internal dissipative effects are dominant. The proposed identification procedure may also be suitable for application in the finite element method, for studying dissipative effects in thin-walled structures of general shape.

References

1. Oveisi A, Nestorovic T (2016) Mu-synthesis based active robust vibration control of an MRI inlet. *Facta Univ Ser Mech Eng* 14(1):37–53
2. Gabbert U, Duvigneau F, Ringwelski S (2017) Noise control of vehicle drive systems. *Facta Univ Ser Mech Eng* 15(2):183–200
3. Tigh Kuchak AJ, Marinkovic D, Zehn M (2020) Finite element model updating—case study of a rail damper. *Struct Eng Mech* 73(1):27–35
4. Sun W, Wang Z, Yan X, Zhu M (2018) Inverse identification of the frequency-dependent mechanical parameters of viscoelastic materials based on the measured FRFs. *Mech Syst Signal Process* 98(1):816–833
5. Gaul L (1999) The influence of damping on waves and vibrations. *Mech Syst Signal Process* 13:1–30
6. Mainardi F (1997) Fractional calculus: some basic problems in continuum and statistical mechanics. In: *Fractals and fractional calculus in continuum mechanics*. Springer, Wien
7. Kennedy CC, Pancu CDP (1947) Use of vectors in vibration measurement and analysis. *J Aeronaut Sci* 37:603–625

8. Ewins DJ (2000) *Modal testing: theory, practice and application*, 2nd edn. Research Studies Press, Baldock
9. Catania G, Sorrentino S (2009) Experimental evaluation of the damping properties of beams and thin-walled structures made of polymeric materials. In: 27th international proceedings on IMAC, Orlando
10. Wesolowski M, Barkanov E (2016) Air damping influence on dynamic parameters of laminated composite plates. *Measurement* 85:239–248
11. Grosso P, De Felice A, Sorrentino S (2021) A method for the experimental identification of equivalent viscoelastic models from vibration of thin plates. *Mech Syst Signal Process* 153:ID 107527
12. Ege K, Roozen NB, Leclere Q, Rinaldi RG (2018) Assessment of the apparent bending stiffness and damping of multilayered plates; modeling and experiment. *J Sound Vib* 426:129–149

Chapter 27

Influence of Different Surface- and Heat Treatments; Elevated Temperature, Orientation on the Fatigue Properties of Ti6Al4V Processed by L-PBF for Controlled Powder Properties



Benjamin Meier, Fernando Warchomicka, Reinhard Kaindl, Christoph Sommitsch, and Wolfgang Waldhauser

Abstract While static mechanical properties of Laser Powder Bed Fusion (L-PBF) processed titanium alloy Ti6Al4V Grade 5 are sufficient and comparable to classic production processes (DebRoy et al. in *Prog Mater Sci* 92:112–224 [1]; Vrancken et al. in *J Alloys Compd* 541:177–185 [2]) the fatigue properties of L-PBF lack behind (Leuders et al. in *Int J Fatigue* 48:300–307 [3]; Nicoletto in *Int J Fatigue* [4]). However, the reason for this issue are not completely clear and uniquely assignable as combination of (sub surface) porosity, microstructure and surface roughness. This work aims to investigate the influence of several factors on the fatigue properties of controlled, single powder patch of Ti6Al4V. The use of a single patch eliminates the influences of mechanical and chemical powder properties. The investigated factors comprise mechanical and electrochemical polishing (EP) surface treatment, heat treatment (stress relief SR, furnace annealing FA, hot isostatic pressing HIP), print orientation (vertical and horizontal) and load cases ($R = -1$, $R = 0.1$). Additionally, a set of tests is performed at 80 °C. For both load cases HIP and machining show a positive impact with a higher influence of machining. For load case $R = 0.1$ HCF (σ_{aD} , 50%) for HIP and machined is around 400 MPa while the same surface treatment but FA reach 218 MPa and SR/EP samples at just 111 MPa. Elevated environmental temperature and horizontal orientation have a minor positive impact. For $R = -1$ the overall gap narrows to 300 for HIP/machined and 175 MPa for SR/EP respectively.

Keywords Additive manufacturing · L-PBF · Fatigue · Electrochemical polishing · Heat treatment · Surface treatment · Hot isostatic pressing · Powder properties

B. Meier (✉) · R. Kaindl · W. Waldhauser
Joanneum Research Materials, Leobnerstraße 94, 8712 Niklasdorf, Austria
e-mail: benjamin.meier@joanneum.at

F. Warchomicka · C. Sommitsch
IMAT Institute of Material Science, Joining and Forming, Graz University of Technology,
Kopernikusgasse 24/1, 8010 Graz, Austria

27.1 Motivation

Ti6Al4V Grade 5 (Ti64) is a standard titanium alloy with high strength to weight ratio, excellent corrosion resistance and good ductility used in multiple technical applications such as aerospace, medical implants and motorsports. Additive manufacturing processes such as laser powder bed fusion L-PBF offers new design possibilities for this material that is mechanically relatively challenging to process. While static mechanical properties of L-PBF components are found to be superior or on level to their classically processed counterparts [1, 2, 5] the fatigue properties often lack behind. Several effects might be the reason to this. First, the porosity found in the process, secondly, residual stresses, especially in the surface, (anisotropy in) microstructure and finally, surface roughness [3, 4]. However, for most technical application a decent fatigue strength or at least the knowledge of its limit and influence parameters is essential.

Additionally, powder properties and its reuse status are of great influence for L-PBF, especially of reactive materials such as Ti64 [6].

Therefore, within this paper several of these influence factors should be investigated. Surface roughness [7] was addressed by two different surface treatments, machining MA and electrochemical polishing EP, later a technology with the potential to be used on the near net shape structures possible by L-PBF. Both treatments also influence residual stresses and porosity close to the surface, but in various intensity.

Measures against the influence of porosity was further investigated by hot isostatic pressing HIP, which has also an influence on microstructure as does the other applied heat treatment of furnace annealing FA. Finally, just virgin powder from a single patch with measured rheology and chemical composition was used to prevent any influence of changing powder properties.

27.2 Methodology

To determine the chemical composition of the powder, various analytical methods were used: The oxygen and nitrogen content were determined by hot extraction in helium using a LECO TCH 600. (ASTM E 1409-13). Hydrogen concentration was measured using the inert gas fusion thermal conductivity method (JUWE H-Mat 2500 analyser, ASTM E 1447-09), and the argon by mass spectrometry (IPI ESD 100) while aluminum content was investigated by inductively coupled plasma optical emission spectrometry.

PSD as well as sphericity of the powder were measured according to ISO 13322-2 with dynamic image analysis using a CAMSIZER XT. Flow properties were determined by Carney flow meter (ASTM B 213-17).

Build Jobs were performed on an EOS EOSINT M280 L-PBF machine equipped with an 400 W Nd:YAG Laser in Ar 5.0 atmosphere using parameters described in Table 27.1.

Table 27.1 Process parameters

Laser power [W]	Scan speed [mm/s]	Hatching [μm]	Layer thickness [μm]
280	1200	140	30

After removing from the printer all build platforms underwent a stress relieve heat treatment at 650 h for 2 h using an argon flooded oven (Linn High Therm VMK-135). This was essential to achieve working horizontal samples due to the high residual stress in L-PBF of Ti64. Selected mechanical test samples were then FA at 800 °C for 2 h to achieve an $\alpha + \beta$ microstructure using a vacuum oven or underwent HIP in a Quintus QIH213 hot isostatic press. Surface of the gauge length was either electrochemically polished or machined, as were the clamping surfaces. In order to achieve equal minimal diameters for EP and MA two different specimen types were used, since first ablates about 200 μm of material while for machining 1 mm measurement is provided. Final specimen design were cylindrical hourglass samples with a minimal diameter of 5 mm according to ISO and ASTM standards.

For the electrochemical polishing, specimens were first prepared by chemical pickling in acid according to AIRBUS specifications 80-T-35-0106 in order to reduce the increased oxide layer. Polishing took place in a temperature and flow controlled organic $\text{AlCl}_3/\text{ZnCl}_2$ electrolyte. Surface roughness was measured physically with a Mitotoyo SJ-210 portable roughness measurement device.

Fatigue tests were performed in Rumul Testronic 150 (S-Nr. 8205/121) and Rumul Mikrotron 20 (S-Nr. 920/180) test rigs according to ASTM E466 for load cases $R = 1$ and $R = 0.1$ at room temperature RT and vertical specimen in SR, FA, and HIP condition. Surface was either MA or EP. Further FA and EP specimen in horizontal orientation were tested and at an elevated temperature of 80 °C. An overview of the experiments can be found in Table 27.2.

Table 27.2 Overview of fatigue tests performed

Temperature	Orientation	Heat treatment	Surface treatment	Load case R	Stress levels	Specimen per level	Total
RT	Vertical	FA	MA	0.1	6	3	18
RT	Vertical	FA	EP	0.1	6	6	36
RT	Vertical	FA	EP	1	6	6	36
RT	Vertical	HIP	MA	0.1	6	3	18
RT	Vertical	HIP	EP	0.1	6	3	18
RT	Vertical	HIP	EP	1	6	3	18
RT	Vertical	SR	EP	0.1	6	3	18
RT	Vertical	SR	EP	1	6	3	18
RT	Horizontal	FA	EP	0.1	6	6	36
80°	Vertical	FA	EP	0.1	6	3	18

Table 27.3 Chemical composition, PSD, sphericity, bulk density

	Al [wt%]	O [wt%]	N [wt%]	H [ppm]	Ar [ppm]
	6.36	0.14	0.014	38	0.05
Limits Grade 5	5.5–6.5	0.2	0.05	150	
D10 [μm]	D50 [μm]	D90 [μm]	Flow rate [s/50 g]	Sphericity	Bulk density [g/cm^3]
23.9	34.9	47.9	10.5	0.97	2.46

Investigations of microstructure, surface and fracture surfaces was done using SEM (Tescan Mira 3) and light microscopy.

27.3 Results and Discussion

27.3.1 Powder Properties

Table 27.3 gives an overview about the powder properties, chemical composition as well as PDS and sphericity. Values of oxygen, hydrogen and nitrogen are well within limits for Ti64 Grade 5 specifications while PSD and sphericity are well suited for L-PBF.

27.3.2 Surface Roughness

Figure 27.1 shows two final specimens. On the left a MA one with smooth clamping surfaces, on the right side an EP one with afterwards machined M10 threads for clamping.

Surface roughness varied from $R_a = 0.4$, $R_q = 0.5$ and $R_z = 2.6 \mu\text{m}$ for MA and $R_a = 1.1$, $R_q = 1.39$ and $R_z = 4.7 \mu\text{m}$ for EP. Even after EP horizontal samples are rougher ($R_a = 1.6$, $R_q = 1.9$ and $R_z = 10.4 \mu\text{m}$ and show higher deviation (e.g., ± 7.11 instead of ± 0.16 for R_a). (Table 27.4) The facts to explain this are: First,

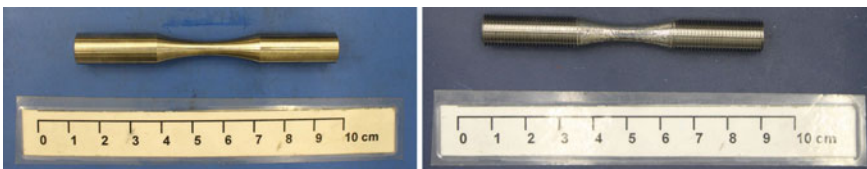


Fig. 27.1 Machined specimen with smooth clamping surfaces (left) and electrochemically polished specimen with machined M10 threads fatigue test performed for $R = -1$ (left) and $R = 0.1$ (right)

Table 27.4 Surface roughness of test specimen, $n = 3$

	Ra		Rq [μm]		Rz [μm]		Ablation	
	[μm]	\pm	[μm]	\pm	[μm]	\pm	g/m^2	[μm]
Vertical MA	0.4	0.09	0.5	0.06	2.6	0.65	–	1000
Vertical EP	1.10	0.16	1.39	0.21	4.77	0.64	573	113
Horizontal EP	1.6	0.7	1.9	0.8	10.4	7.11	575	114

ablation rates should be kept constant and therefore EP parameter were constant. However, if the surface is rougher in the beginning it would call for adapted process parameters to achieve the same surface roughness as on the upskin. Secondly, horizontally build specimen have a higher variation in surface roughness for the as build condition due to the L-PBFs process nature. The orientation of the gauge length surfaces changes from up to downskin, which means it includes the complete roughness spectrum of the L-PBF process from its best (horizontal upskin) to the worst (horizontal downskin with connection to support structure). Hence, the high deviation for the horizontal specimen, especially for Rz. However, it is an improvement from the results obtained by Yang et al. [8].

27.3.3 Heat Treatment—Microstructure

Figure 27.2 shows the microstructure after heat treatments. Left, after SR, an initial transformation from martensitic α' microstructure to stable $\alpha + \beta$ phase took place at just 650° , with remaining nests of α' phase. Grains are elongated in build direction as shown by Royer et al. [9]. FA (middle) and HIP (right) lead to a full $\alpha + \beta$ structure, with a slight effect on the morphology of the α laths. HIP structure is finer, probably due to higher cooling rates in the process.

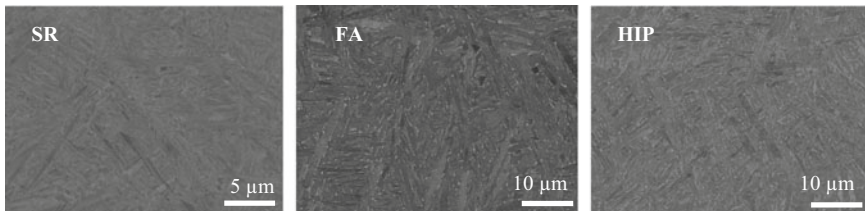


Fig. 27.2 Microstructure after heat treatment for stress relieved SR, furnace annealed FA and hipped HIP

27.3.4 Fatigue Performance

Figure 27.3 gives an overview of the results from all performed tests for $R = -1$ (left) and $R = 0.1$ (right).

Machined samples reach a $\sigma_{aD, 50\%}$ of 218 MPa for furnace annealing and a value of 360 MPa for HIP samples for $R = 0.1$. However, the number of tests and runner troughs were not sufficient to make a statistic meaningful statement (Fig. 27.4), but indicate a positive effect of HIP treatment. Additionally, a smaller spread is indicated. These positive effects of HIP are also described by Leuders et al. [3] and Khalid Rafi et al. [5], however, later reaches higher fatigue strength.

EP specimen cannot reach the values achieved by their machined counterparts, with a $\sigma_{aD, 50\%}$ of 111 MPa and 146 MPa for FA and HIP, respectively (Fig. 27.4).

31

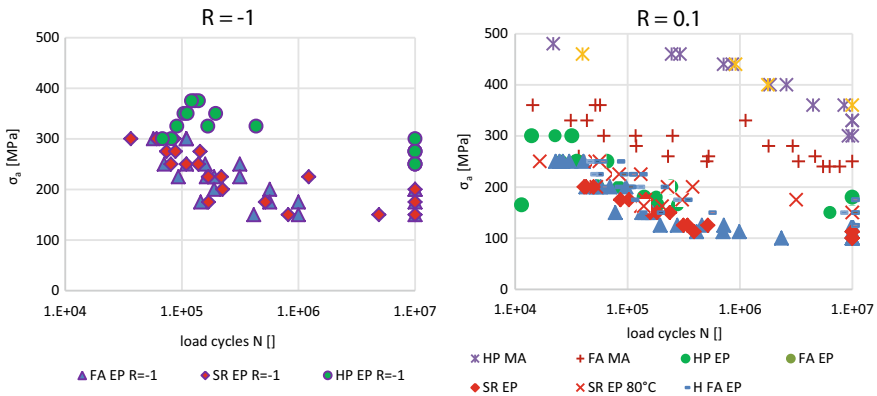


Fig. 27.3 Fatigue test performed for $R = -1$ (left) and $R = 0.1$ (right)

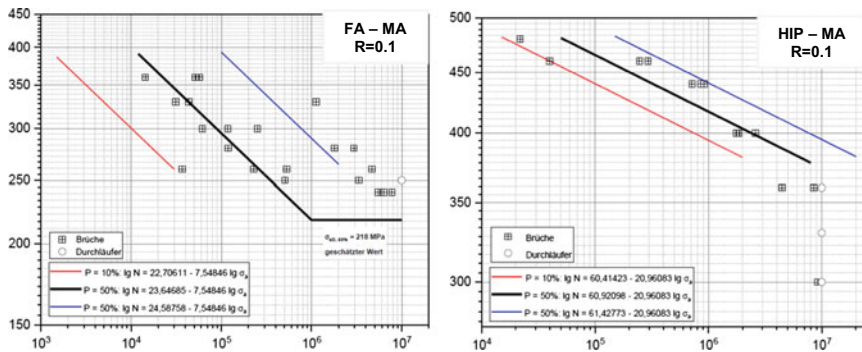


Fig. 27.4 HCF for machined specimen: FA (left) and HIP (right)

For vertical orientation no difference between FA and SR can be found, with $\sigma_{aD, 50\%}$ of 114 for SR. It might be due to the fact that even after SR the microstructure was partly transformed to $\alpha + \beta$ with just nests of remaining martensitic α' case.

Concerning anisotropy, HCF of horizontal FA EP samples are higher of their vertical counterparts with a $\sigma_{aD, 50\%}$ of 160 MPa, however the spread is a little larger with a $\sigma_{aD, 90\%}$ of 194 and $\sigma_{aD, 10\%}$ of 126 MPa (Fig. 27.5 left). Nicoletto [4] also found this anisotropy, however, it cannot be explained by the surface roughness since it is inferior in this case. Possibly, rather anisotropy in microstructure or porosity distribution lead to the behavior. During experiments at 80 °C no further impact in fatigue life is observed, as illustrated in Fig. 27.6, left.

Load case $R = -1$ shows a similar effect (Fig. 27.7). For all tested conditions, SR EP, FA EP and HIP EP the $\sigma_{aD, 50\%}$ is higher at 148, 175 and 300 MPa, respectively compared to the values obtained by $R = 0.1$. Further investigations will be needed to determine the difference between both R-conditions.

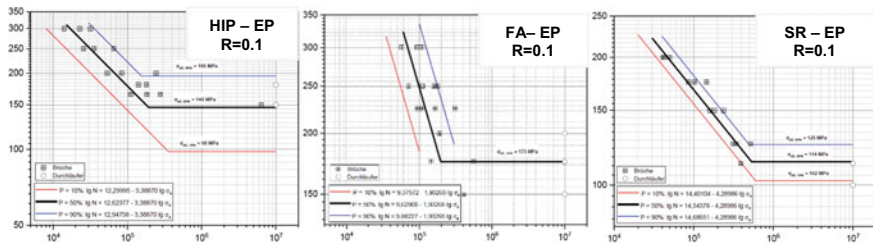


Fig. 27.5 HCF results for $R = 0.1$ and EP specimen with various heat treatment: (left) HIP, (middle) FA and (right) SR

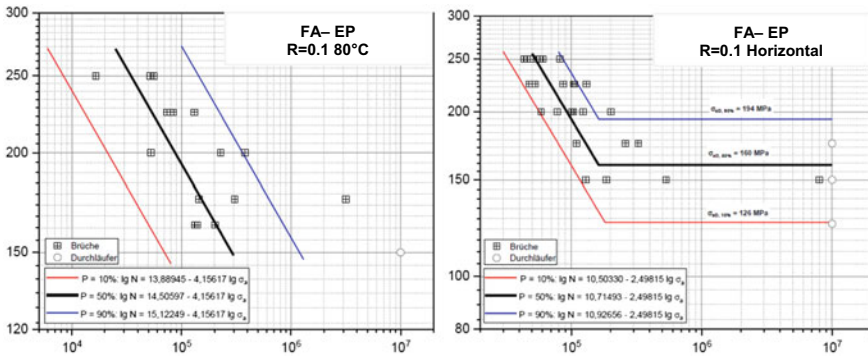


Fig. 27.6 HCF results for elevated temperature of 80 °C (left) and horizontal (right) EP specimen for $R = 0.1$

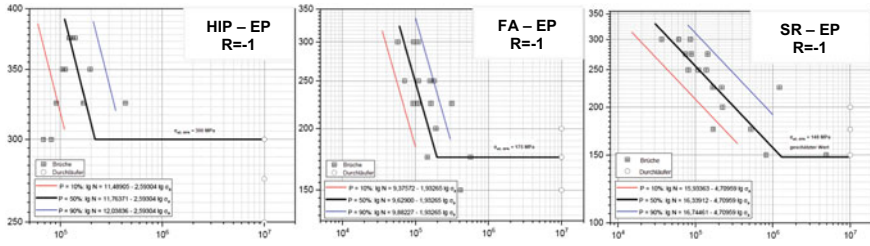


Fig. 27.7 HCF results for $R = -1$ and EP specimen with various heat treatment: (left) HIP, (middle) FA and (right) SR

27.4 Conclusion and Discussion

In theory, fatigue strength should be increased by a reduction in surface roughness due to the reduction in stress concentration found in roughness spikes. Though electrochemical polishing shows promising results in the reduction of surface roughness, the fatigue behavior does not reach that of machined specimen.

Besides the still rougher surface two effects might contribute to this. First, by removing just around $200 \mu\text{m}$ instead of 1 mm in machining, the zone of sub surface porosity found in L-PBF samples is probably fully removed by MA but just partially by EP. This can also lead to open pores on the surface, not measurable with the used equipment for surface roughness measurement but forming weak spots. Secondly, distribution of residual stresses in the surface is different in the two processes and also depends on the amount of material removed and highly influences fatigue behavior.

Considering heat treatments, HIP delivered the best results for EP and MA surface treatments, with higher $\sigma_{aD, 50\%}$ and smaller spread than FA samples. An overall reduction in pores reduces spots of stress concentration. HIP always delivers the best results, but way inferior for EP compared to the results from MA specimen. For EP samples no difference for FA and SR can be found for $R = 0.1$ but a minor improvement for $R = 1$.

Concisely, this indicates a higher influence of the type of surface treatment and amount of removed material, than the form of heat treatment. Overall, the fatigue performance obtained is below than the classical processed Ti64, as found in standard data sheets [10].

References

1. DebRoy T, Wei HL, Zuback JS, Mukherejee T, Elmer JW, Milewski JO, Beese AM, Wilson-Heid A, De A, Zhang W (2018) Additive manufacturing of metallic components—process, structure and properties. Prog Mater Sci 92:112–224
2. Vrancken B, Thijs I, Kruth J-P, Van Humbeeck J (2012) Heat treatment of Ti6Al4V produced by selective laser melting: microstructure and mechanical properties. J Alloys Compd 541:177–185

3. Leuders S, Thöne M, Riemer A, Niendorf T, Tröster T, Ricahrd HA, Maier HJ (2013) On the mechanical behavior of titanium alloy Ti6Al4V manufactured by selective laser melting: fatigue and crack growth performance. *Int J Fatigue* 48:300–307
4. Nicoletto G (2016) Anisotropic HCF behavior of Ti6Al4V obtained by powder bed laser fusion. *International Journal of Fatigue* 94:255–262
5. Khalid Rafi H, Starr TL, Stucker BE (2013) A comparison of the tensile, fatigue, and fracture behavior of Ti–6Al–4V and 15-5 PH stainless steel parts made by selective laser melting. *Int J Adv Manuf Technol* 69:1299–1309
6. Meier B, Skalon M, Warchomicka F, Belei C, Görtler M, Kaindl R, Sommitsch C (2019) Effect of the reuse of powder on material properties of Ti6Al4V processed by SLM. In: *Esaform conference proceedings*
7. Król M, Tański T (2016) Surface quality research for selective laser melting of Ti 6Al 4V alloy. *Arch Metall Mater* 61:1291–1296
8. Yang L, Gu H, Lassell A (2014) Surface treatment of Ti6Al4V parts made by powder bed fusion additive manufacturing processes using electropolishing; *Solid Freeform Fabrication Symposium*, 268–277
9. Royer F, Bienvenu Y, Gaslain F (2015) EBSD observation of grains microstructures produced by selective laser melting. In: *Conference proceedings Euro PM2015*
10. MMPDS-6 (2001)

Chapter 28

Fatigue Crack Growth Resistance of Heat-Resistant Steel 15H11MF After Operation in Blades of a Steam Turbine



Halyna Krechkovska , Myroslava Hredil , and Oleksandra Student 

Abstract The causes of damage of blades after their operation in steam turbine rotors are considered. Premature failures of the blades after the short operation time (approx. 10^4 h) are caused by fatigue crack initiation from technological stress concentrators, namely, large slag inclusions, grooves formed as a result of intensive corrosion and erosion wear, and a significant number of large pores in the surface-hardened layers. It is supposed that such short operation time of prematurely fractured blades is not enough for a noticeable degradation of their microstructure. In contrast, the structure of steel that has operated in the rotor blades for about 3×10^5 h changed noticeably. The fracture of such blades usually occurs in the phase transition zone, where hydrogen absorption by metal from the steam–water mixture is possible. Hydrogen could facilitate diffusion redistribution of alloying elements with precipitation and coagulation of carbides along the grain boundaries. The most sensitive to the structural degradation of the steel of the blades are the threshold values of the stress intensity factor range ΔK_{th} and $\Delta K_{th,eff}$. These parameters unambiguously decrease with increasing the blade operation time. Fractographic examination of specimens after fatigue testing made it possible to visualize intergranular fracture fragments caused by in-service damaging in the bulk of the operated blades. The part of intergranular fracture elements at the unit fracture surface of the specimens correlates with the change in the $\Delta K_{th,eff}$ due to the steel operational degradation.

Keywords Steam turbine · Rotor · Blades · Fatigue crack growth resistance · Fracture mechanism

H. Krechkovska (✉) · M. Hredil · O. Student
Karpenko Physico-Mechanical Institute, National Academy of Sciences of Ukraine, Lviv, Ukraine

H. Krechkovska
Lviv Polytechnic National University, Lviv, Ukraine

28.1 Introduction

Steam turbine (ST) rotor blades are considered to be critical components; their fracture can cause significant damage to the turbine with a high cost for their elimination, threatens personnel and the environment. The most common causes of blade damaging during their long-term operation are crack initiation and propagation due to significant vibrations and cyclic loads, the presence of stress concentrators, and favorable conditions for fretting and corrosion fatigue [1–3], cavitation and erosion wear [4, 5] etc. The long-term (approx. 3×10^5 h) impact of operational factors leads to the redistribution of carbon and alloying elements along the grain boundaries and packets of high-temperature tempered martensite, where carbides form and pores occur around them with their further coalescence and the formation of microcracks [6]. Cracks weaken blades' cross-section, change their own vibration frequency and the conditions of their resonance. The reasons for premature (up to 10^4 h of operation) failures of rotors due to fracture of blades are associated with technological influences, and not with structural changes.

To evaluate the current state of long-term operated steels, it is important to substantiate the choice of mechanical characteristics that are sensitive to their degradation. Hardness, strength and plasticity are usually used for these purposes, which are available to operators, but are slightly sensitive to degradation [7]. At the same time, impact toughness, fracture toughness and fatigue crack growth resistance are highly sensitive to steel degradation, as shown by the example of low-alloy heat-resistant steels of steam pipelines of thermal power plants [8].

The aim of the research is to analyze the causes of premature fracture of ST blades; to rank the mechanical characteristics of high-alloyed heat-resistant steel according to their sensitivity to operational degradation and to substantiate the choice of the most sensitive ones; to identify fractographic signs of steel degradation on fracture surfaces of laboratory specimens made of operated blades; to find out a correlation dependence of the change in the mechanical and fractographic indicators of heat-resistant steel degradation on its operation time in ST rotor.

28.2 Materials and Methods

The blades after various operation times (from 338 h up to $\sim 3 \times 10^5$ h) in the high pressure (HPR) and the low pressure (LPR) rotors have been analyzed. Operational parameters of the tested components are shown in the Table 28.1.

The steel 20H13 ([7] in Table 28.1) was used to substantiate the choice of a mechanical indicator sensitive to degradation due to its high-temperature operation in LPR blades. Its properties were compared with the corresponding values for the initial state ($\sigma_{UTS} = 798$ MPa, $\sigma_{YS} = 582$ MPa, elongation = 20%, RA = 55%). The degradation of steel caused by the combined effect of a set of operational factors was assessed by the coefficient $\lambda = [(C_\tau - C_0)/C_0]$, which characterizes

Table 28.1 Operational parameters of ST rotors

Rotor type	Operation time τ , h	Shutdowns, N	T , °C	Steel	Designation
HPR	338	14	535	15H11MF	[1]
	31519	693			[2]
	266962	3405			[3]
	302000	3852			[4]
LPR	7400	8	40–70	15H11MF	[5]
	3929	44		X12CrNiMoV12-3	[6]
LPR	0	–	40–70	20H13	
	approx. 320000				[7]

the relative changes in steel's mechanical characteristics C_τ comparing to the corresponding characteristics in the initial state C_0 . To assess the current state of the operated metal, the following characteristics were used: strength (σ_{UTS} and σ_{YS}), plasticity (Elongation and RA), impact toughness KCU, fracture toughness by J-integral (ASTM-E1820), fatigue crack growth resistance (the threshold values of SIF ΔK_{th} and $\Delta K_{th,eff}$ determined by cantilever bending with the frequency of 10 Hz and R-ratio of 0.05). In addition, the structural state of the steels operated in blades of various ST rotors, as well as the fractographic peculiarities of the tested specimens were evaluated using SEM EVO-40XVP.

28.3 Results and Discussion

28.3.1 Analysis of the Fracture Cases of Rotor Blades in Steam Turbines

The fracture of ST rotor blades were analyzed depending on their operation time. Premature failure of HPR blades ([1], see Table 28.1) and LPR blades ([5, 6] in Table 28.1), which chemical composition and mechanical properties satisfied the requirements of regulations ($\sigma_{UTS} = 666$ MPa; $\sigma_{YS} = 490$ – 657 MPa; RA = 50%, Elongation = 18%, KCU = 0.7 MJ/m²) was caused by different factors. Fractographic examination of blades after 338 h of operation revealed large (over 5 mm long) slag inclusions formed along the fusion line of shanks (Fig. 28.1a). Their localization in the fillet zone of the blade root created additional stress concentration and facilitated crack initiation from these inclusions with the formation of fatigue striations (Fig. 28.1b). In LPR blades fractured after 7.4×10^3 h of operation, the origins of fracture were groove-like corrosion and erosion damages which served as stress concentrators for fatigue cracks initiation. Structural inhomogeneity and acute-angled morphology of carbides after surface electro spark treatment contributed to the rapid crack propagation over the entire section of the blades (Fig. 28.1c). For LPR blades after ~4

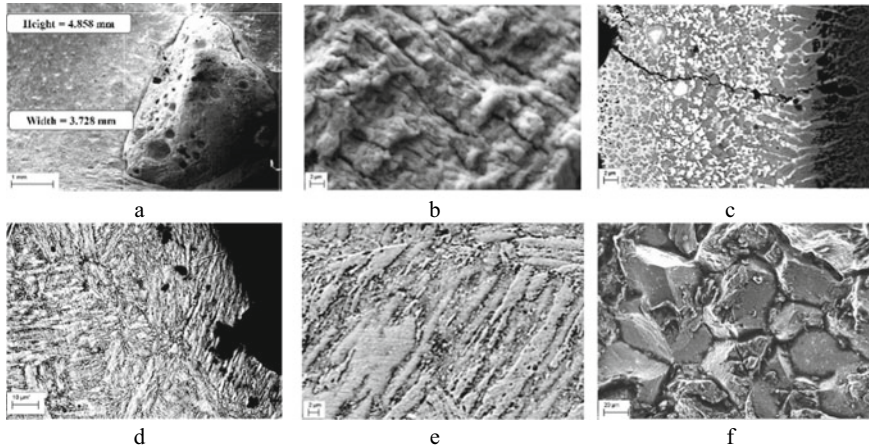


Fig. 28.1 **a** Subsurface slag inclusions along the fusion line of paired blade shanks of HPR, **b** fatigue striations in the steel blades [1], **c** microcrack in the surface layer after electro spark treatment [5], **d** typical operational defects in the surface-hardened layer of the steel [6], **e** typical structure of the operated steel [3], and **f** typical crack initiation mechanism near the leading edge of the blade. See designations in Table 28.1

$\times 10^3$ h of operation, the key factor was a low resistance to corrosion and erosion wear of their leading edges due to the uneven strengthening of their surface layer by laser surface hardening. Fatigue cracks in this layer originated from grooves of corrosion-erosion wear, and propagated because of overloads (Fig. 28.1d). The operation time of prematurely damaged blades was insufficient for structural and phase transformations in the metal. Thus, their fracture was concerned with technological factors.

For the metal operated in blades up to $\sim 3 \times 10^5$ h, the degradation of the steel structure should be taken into account, which led to the precipitation and coagulation of carbides (up to $1.5 \mu\text{m}$) along the grain boundaries and packets of high-temperature tempered martensite (Fig. 28.3e). It was suggested that such changes in steels at the sub- and microstructural levels under the influence of high-gradient temperature force operating conditions of the blades followed by the decohesion of carbides from the adjacent matrix, the formation of pores along their interfaces with further coalescence and growth of much larger defects in the form of intergranular cracks (Fig. 28.3f). This leads to a decrease in mechanical properties of steels; in particular, such intergranular defects weaken the pre-fracture zone at the fatigue crack tip and thus accelerate fracture of the operated steel.

28.3.2 Substantiation of the Choice of the Mechanical Indicator Sensitive to the Steel Operational Degradation

Comparing the mechanical properties of the steel 20H13 in the initial state and after its operation in LPR blades of ST, these have been ranked according to their sensitivity to high-temperature operational degradation using the parameter λ (Fig. 28.2).

Standard tensile characteristics included in the industrial regulatory documents are insufficiently sensitive to degradation. Elongation (as the most sensitive among these characteristics) decreased by almost 40% which is consistent with an increase in σ_{YS} (by 27%). Regarding the fatigue crack growth resistance, the most sensitive to degradation was the parameter $\Delta K_{th\,eff}$ (a decrease by almost 60%) whereas the change in ΔK_{th} did not exceed 10%. Such a significant difference between these characteristics indicates an essential impact of the crack closure effect in the operated

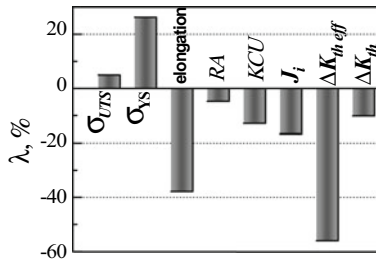


Fig. 28.2 Ranking the mechanical properties of the steel 20H13 operated for $\sim 3.2 \times 10^5$ h in LPR blades by the indicator λ as a quantitative parameter of the steel sensitivity to degradation

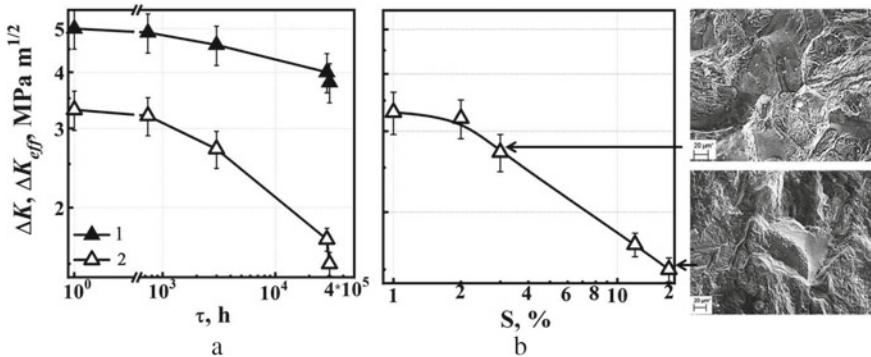


Fig. 28.3 a Dependences of the nominal ΔK_{th} (1) and effective $\Delta K_{th\,eff}$ (2) threshold values of SIF for the steel 15H11MF on the operation time τ , and b dependence of $\Delta K_{th\,eff}$ on the part of intergranular fracture elements per unit area S in the near-threshold zone of the fracture surfaces of specimens after fatigue testing

steel. Usually this effect is associated with residual plasticity, high roughness of the conjugated fracture surfaces, autocatalytic build-up of the oxide films. Anyway, premature contact of the crack edges near its tip necessarily occurs during a certain positive part of the loading cycle. As a result, the effective SIF level ΔK_{eff} at the crack tip becomes much less than its ΔK level. In the case of crack growth at a near-threshold rate and, as a rule, with a transgranular fatigue relief, areas of an intergranular relief against its background, which are caused by degradation (not revealed for the steel in the initial state), led to premature contact of the crack faces [6]. As a consequence, the effective fatigue threshold $\Delta K_{\text{th eff}}$ is the most sensitive to degradation of 20H13 steel. Thus, its advantage has been proved for assessing the degradation of high-chromium heat-resistant steels after their long-term high-temperature operation.

28.3.3 Evaluation of the Technical State of Heat-Resistant Steel After Various Operation Times in Steam Turbine Rotor Blades

The nominal and effective threshold values of SIF (ΔK_{th} , $\Delta K_{\text{th eff}}$) were determined experimentally for 15H11MF steel in the initial state and after various operation times. Both mentioned characteristics of the steel decreased with time of operation τ in steam turbines (Fig. 28.3a). As in the case of the steel 20H13, a more intense decrease in $\Delta K_{\text{th eff}}$ in comparison with ΔK_{th} indicates an impact of the crack closure effect due to the steel operational degradation.

This was manifested fractographically by an increase in the fracture surface roughness due to the occurrence of volumetric intergranular fragments on it just in the near-threshold region of crack growth, protruding above the generally lower transgranular fatigue relief. In this case, the part of the area of intergranular fragments S on the fracture surfaces increases and clearly correlates with a decrease in the $\Delta K_{\text{th eff}}$ level (Fig. 28.3b). The obtained dependence substantiates the parameter S as a quantitative fractographic indicator of high-temperature degradation of high-alloyed blade steel. These intergranular fragments are the result of either the evolution of already formed intergranular defects or the cohesion weakening between adjacent grains due to pore formation around the carbide particles or non-metallic inclusions along their boundaries. In any case, defects have been formed during the steel operation in the blades; the fatigue crack grew along the path of the minimum fracture resistance and only contributed to their visualization.

28.4 Conclusions

Premature failures of the blades (operated up to 10^4 h) are caused by fatigue crack initiation from technological stress concentrators; no considerable structure transformations were noticed. In contrast, the metal of long-term operated (approx. 3×10^5 h) blades is essentially degraded. Here, cracks initiated and propagated from the grooves of corrosion and erosion wear by the intergranular mechanism. Intergranular crack propagation in these steels is caused by the formation and coalescence of micropores along the boundaries of formed carbides. The most sensitive to the steel operational degradation are the threshold fatigue crack growth characteristics which pronouncedly decrease with the operation time. The part of intergranular fracture elements at the unit area on the fracture surfaces of the specimens after the fatigue testing strongly correlates with the threshold values of SIF for the corresponding steels.

References

1. Kubiak SJ, Urquiza BG, García CJ, Sierra EF (2007) Failure analysis of steam turbine last stage blade tenon and shroud. *Eng Fail Anal* 14:1476–1487
2. Ebara R (2010) Corrosion fatigue crack initiation behavior of stainless steels. *Procedia Eng* 2:1297–1306
3. Ziegler D, Puccinelli M, Bergallo B, Picasso A (2013) Investigation of turbine blade failure in a thermal power plant. *Case Stud Eng Fail Anal* 1(3):192–199
4. Markovic S (2006) Cavitation wear of the blades of Francis turbine. *Tribol Ind* 289(3–4):17–22
5. Lee B-E, Riu K-L, Shin S-H, Kwon S-B (2003) Development of a water droplet erosion model for large steam turbine blades. *KSME Int J* 17(1):114–121
6. Nykyforchyn HM, Student OZ, Krechkovs'ka HV, Markov AD (2010) Evaluation of the influence of shutdowns of a technological process on changes in the in-service state of the metal of main steam pipelines of thermal power plants. *Mater Sci* 46(2):177–189
7. Lesiuk G, Correia JAFO, Krechkovska HV, Pekalski G, de Jesus AMP, Student O (2021) Degradation theory of long term operated materials and structures. In: *Structural integrity series*, vol 15. Springer, Heidelberg, 170 p
8. Student OZ, Krechkovs'ka HV, Svirská LM, Kindratskui BI, Shyrokov VV (2021) Ranking of mechanical characteristics of HPP pipeline steels by their sensitivity to operational degradation. *Physicochem Mech Mater* 57(3):110–117

Chapter 29

Operational Degradation of Fatigue Strength of Structural Steels: Role of Corrosive-Hydrogenating Environments



Hryhoriy Nykyforchyn and Olha Zvirko

Abstract Operational degradation of steels under the combined action of cyclic loading and aggressive hydrogenating environments is a crucial problem for structural integrity. Two approaches for assessing the operational degradation of structural steels under cyclic loading are considered. The former one implies the clarification of the impact of long-term operational conditions, including corrosive environment action, on fatigue strength characteristics sensitive to in-service degradation and determined by testing both smooth and fatigue pre-cracked specimens. The latter consists in the evaluation of the effect of operational cyclic loading on the physical and mechanical characteristics of steels which are sensitive to degradation but don't attribute to fatigue strength. From the mechanical properties, these are the characteristics of brittle fracture resistance, namely, impact strength and fracture toughness, as well as the characteristics of plasticity. The important role of the texture of rolled steels in their operational degradation under cyclic loading, which causes micro-delamination between elongated texture fibres and non-metallic inclusions, is analysed.

Keywords Steel · Mechanical properties · Degradation · Fatigue strength · Fatigue crack growth · Hydrogen delamination

29.1 Introduction

Long-term operation of structural steels in various fields of industry, as a rule, leads to a significant degradation of the initial mechanical properties, mainly, the characteristics of brittle fracture resistance [1–5]. The main reason for their decrease is the intensive evolution of nano- and micro-damage in the bulk of metal [6–8]. Plasticity characteristics are less sensitive to in-service changes in the metal, furthermore, elongation seems to be unsuitable for assessing the metal state, since it additionally includes the disclosure of multiple micro-damages [9]. Therefore, impact

H. Nykyforchyn (✉) · O. Zvirko
Karpenko Physico-Mechanical Institute, National Academy of Sciences of Ukraine, 5 Naukova St., Lviv 79060, Ukraine

strength and fracture toughness are most commonly used to assess the operational degradation of steels, which is mainly associated with development of dissipated micro-damages in in-bulk metal. Steel hydrogenation during its long-term operation intensifies damaging at nano- and microscale, and this enhances the deterioration of brittle fracture resistance [10].

Materials subjected to cyclic loading in a course of long-term operation are inherent to plasticity exhaustion, which is also characterized by a decrease in resistance to brittle fracture and the development of dissipated damages [4, 11–13]. Therefore, the problem of operational degradation of steels under long-term cyclic loading is especially important for structural integrity.

A significant part of the steel structures is operated under the combined action of cyclic loading and aggressive hydrogenating environments. These environments are, first of all, corrosive solutions in which electrochemical interaction with metal leads to hydrogen evolution. Penetrating into metal, hydrogen jointly with applied stresses intensifies the dissipated micro-damaging [3, 8, 14]. Thus, the problem of steel degradation under the combined action of cyclic loading and hydrogenating environment on structural integrity is of great importance.

Two approaches for assessing the operational degradation of structural steels under cyclic loading are considered in this paper. The first one consists in the clarification of the impact of conditions of long-term operation, including corrosive environment action, on fatigue strength characteristics, which are sensitive to in-service degradation and are determined by testing both smooth and fatigue pre-cracked specimens. Another approach consists in the determination of the effect of operational cyclic loading on the physical and mechanical characteristics of steels, which are sensitive to degradation, but do not associate with fatigue strength estimation.

29.2 Effect of Operational Degradation on Fatigue Characteristics of Steels

It is known that long-term operation of structural steels under cyclic loading leads to a decrease in fatigue properties, in particular, fatigue limit [15, 16]. Obviously, such operational degradation is associated with intensive development of micro-damages in a metal, since, in general, strain hardening of steels by preliminary plastic deformation increases fatigue resistance of cyclically strengthened materials [17], which corresponds to a common relationship between strength (yield strength and ultimate strength) and fatigue strength.

Figure 29.1 illustrates the changes in strength and plasticity characteristics, and also fatigue limit σ_{-1} for the 20Kh13 stainless steel from the low-pressure rotor blade of the steam turbine of thermal power plant after its operation for approximately 3×10^5 h [18] on the basis of the parameter $\lambda = (P_{op} - P_0)/P_0$, where P_0 and P_{op} are characteristics of steel in the initial and operated states, respectively. It is clear that the steel has strengthened due to operation, especially noticeable by yield strength

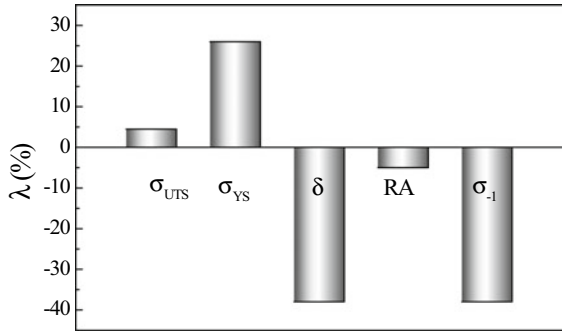


Fig. 29.1 Relative changes in ultimate strength σ_{UTS} , yield strength σ_Y , elongation δ , reduction of area RA and fatigue limit σ_{-1} of the steel 20H13 after its operation for approx. 3×10^5 h in blades of a steam turbine

σ_{YS} . However, fatigue limit of the operated steel has dropped by almost half in comparison with unoperated one. Thus, in this case, there is no common correlation between strength and fatigue strength. This could be explained by the intensive development of micro-damages in the metal during its operation.

The effect of long-term operation of steels on the regularities in fatigue crack growth is more unambiguous, because both strength hardening and damage accumulation reduce the resistance to fatigue fracture at the crack propagation stage, as well as brittle fracture resistance in general. However, the effect of operation on crack growth da/dN in the near-threshold region and in the mid-amplitude section of the fatigue crack growth curve $da/dN - \Delta K$, where ΔK is the stress intensity factor range at the crack tip, should be considered separately. In the first case, the crack closure influences the fatigue threshold ΔK_{th} , especially for the operated steel, where it is much more pronounced due to increasing fracture surface roughness [19]. Thus, the nominal fatigue threshold could even rise for the operated steel whereas the effective value $\Delta K_{th\,eff}$ (determined taking into account the crack closure effect) decreases. Therefore, it is important to use ΔK_{eff} , as the mechanical driving force of fatigue crack growth, for the assessment of the steel operational degradation.

The medium-amplitude part of the fatigue crack growth curve obeying the Paris law is usually either insensitive or only weakly sensitive to steel operational degradation, which corresponds to a common trend of the low sensitivity of fatigue crack growth to metal's state [19]. However, fatigue crack growth in this range can be significantly accelerated under testing in aqueous environments for the operated steel, which is caused by its increased sensitivity to stress corrosion cracking, most likely by the hydrogen-assisted mechanism.

It is demonstrated in Fig. 29.2 by fatigue testing of the 17G1S pipeline steel at high load ratio $R = 0.9$, simulating operational loading of natural gas transit pipelines, that fatigue crack growth is significantly accelerated in NS4 near-neutral pH soil solution only in the operated metal of welded joint [20]. At the same time, it can be seen that fatigue crack growth in air is almost insensitive to the metal state.

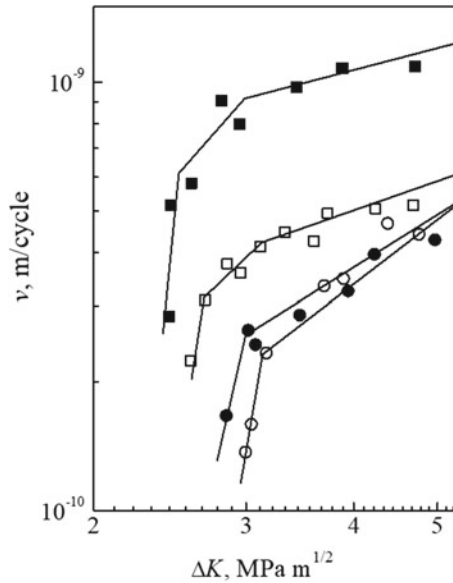


Fig. 29.2 Fatigue crack growth rate in weld metal for unoperated (○, □) and operated (●, ■) 17G1S steel in air (○, ●) and NS4 (□, ■) solution at $R = 0.9$

29.3 Effect of Operational Cyclic Loading on Physical and Mechanical Properties of Steels

Among mechanical properties, the characteristics of brittle fracture resistance, namely, impact strength and fracture toughness, and also plasticity characteristics are used most often to assess the operational degradation of steels [3–5, 11, 18]. Fracture toughness, characterizing resistance of material to crack propagation locally, is considered as parameter with higher sensitivity to operational degradation of materials than impact strength as integrated characteristic [10]. However, impact strength is practically always regulated by normative documents. A striking example of a decrease in brittle fracture resistance due to operational cyclic loading is catastrophic drop in impact toughness of steels of port loading and unloading equipment subjected to intense cyclic loads [11–13]; it was suggested considering impact toughness KCV as the main indicator in the assessment of the steel operational degradation of such structures.

A significant part of metal structures is made of rolled steel. On this evidence, the important role of the texture of rolled steels in their operational degradation under cyclic loading should be emphasized. Analysing results on the operational decrease in impact toughness of the steel using specimens cut along and across the rolling direction [11, 13], it can be concluded that transversal specimens regarding the rolling direction are more sensitive than longitudinal ones for the assessment of steel degradation by impact toughness. It can be explained by the fact that operation causes

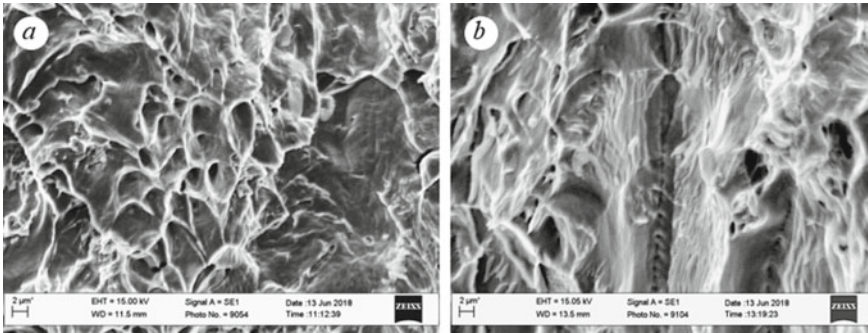


Fig. 29.3 Fracture surfaces of transversal impact specimens for the rolled mild steel in the initial state (a) and after operation (b)

micro-delamination between elongated fibres of texture and non-metallic inclusions, as demonstrated in Fig. 29.3: operationally degraded steel of a portal crane exhibited intensive micro-delaminations in the rolling direction, which are clearly visible on the fracture surface of the transversal specimen.

Thus, considering impact toughness as the important mechanical parameter for the assessment of the current technical state of rolled steels operated under cyclic loading, preference should be given to testing specimens cut in the transverse direction to the rolling direction.

29.4 Concluding Remarks

Operational degradation of structural steels under the combined action of cyclic loading and hydrogenating environment is suggested to be considered in two approaches: the effect of operational degradation on fatigue characteristics, and the influence of operational cyclic loading on the physical and mechanical properties. In both cases, dissipated micro-damages in in-bulk of a metal play a destructive role. This is the reason for the atypical phenomenon of operational decrease in fatigue strength with increasing strength. The fatigue threshold ΔK_{th} in air for the operated steel can be even higher than that for the initial state due to the crack closure effect whereas the effective threshold $\Delta K_{th\,eff}$ (taking into account the crack closure) clearly decreases. The effect of operation on crack propagation rate is insignificant at the middle region of the fatigue crack growth curve in air; however, it is evident in corrosive environments due to the increased susceptibility of the operated steel to stress corrosion cracking. The operational decrease in impact toughness as a brittle fracture resistance parameter can be considered as the key indicator of steel degradation, including under cyclic loading. For the rolled steels, the specimens cut in the transverse direction are preferable for impact testing due to the orientation of micro-delaminations in the rolling direction.

References

1. Yasniy P, Maruschak P, Lapusta Y, Hlado V, Baran D (2008) Thermal fatigue material degradation of caster rolls' surface layers. *Mech Adv Mater Struct* 15(6–7):499–507
2. Lesiuk G, Szata M (2014) Fatigue properties and fatigue crack growth in puddled steel with consideration of microstructural degradation processes after 100-years operating time. *Procedia Eng* 74:64–67
3. Nykyforchyn H, Zvirko O, Dzioba I, Krechkovska H, Hredil M, Tsyulnyk O, Student O, Lipiec S, Pala R (2021) Assessment of operational degradation of pipeline steels. *Materials* 14:3247
4. Kharchenko EV, Polishchuk LK, Zvirko OI (2014) Estimation of the in-service degradation of steel shapes for the boom of a clamp-forming machine. *Mater Sci* 49(4):501–507
5. Krechkovska HV, Tsyulnyk OT, Student OZ (2019) In-service degradation of mechanical characteristics of pipe steels in gas mains. *Strength Mater* 51(3):406–417
6. Nechaev YuS (2008) Metallic materials for the hydrogen energy industry and main gas pipelines: complex physical problems of aging, embrittlement, and failure. *Usp Fiz Nauk* 51(7):681–697
7. Maruschak P, Panin S, Danyliuk I, Poberezhnyi L, Pyrig T, Bishchak R, Vlasov I (2015) Structural and mechanical defects of materials of offshore and onshore main gas pipelines after long-term operation. *Open Eng* 5:365–372
8. Hredil MI (2011) Role of disseminated damages in operational degradation of steels of the main gas conduits. *Metallofizika i Noveishie Tekhnologii* 33(spec. iss.):419–426
9. Nykyforchyn HM, Student OZ, Markov AD (2007) Abnormal manifestation of the high-temperature degradation of the weld metal of a low alloy steel welded joint. *Mater Sci* 43(1):77–84
10. Nykyforchyn H, Tsyulnyk O, Zvirko O, Hredil M (2020) Role of hydrogen in operational degradation of pipeline steel. *Procedia Struct Integrity* 28:896–902
11. Nemchuk OO, Nesterov OA (2020) In-service brittle fracture resistance degradation of steel in a ship-to-shore portal crane. *Strength Mater* 52(2):275–280
12. Semenov PO, Pustovyi VM (2020) Complex diagnostics of the state of operated elements of a grab reloader. *Mater Sci* 56:181–187
13. Nemchuk OO, Krechkovska HV (2019) Fractographic substantiation of the loss of resistance to brittle fracture of steel after operation in the marine gantry crane elements. *Metallofiz Noveishie Tekhnol* 41:825–836
14. Dmytrakh IM, Syrotyuk AM, Leshchak RL (2018) Specific features of the deformation and fracture of low-alloy steels in hydrogen-containing media: influence of hydrogen concentration in the metal. *Mater Sci* 54(3):295–308
15. Sosnovskii LA, Vorob'ev VV (2000) The influence of long operation on fatigue strength of pipe steel. *Strength Mater* 32:523–529
16. Polishchuk LK, Kharchenko HV, Zvirko OI (2015) Corrosion-fatigue crack-growth resistance of steel of the boom of a clamp-forming machine. *Mater Sci* 51(2):229–234
17. Kang M, Aono Y, Noguchi H (2007) Effect of prestrain on and prediction of fatigue limit in carbon steel. *Int J Fatigue* 29:1855–1862
18. Nykyforchyn HM, Tkachuk YuM, Student OZ (2012) In-service degradation of 20Kh13 steel for blades of steam turbines of thermal power plants. *Mater Sci* 47(4):447–456
19. Nazarchuk ZT, Nykyforchyn HM (2018) Structural and corrosion fracture mechanics as components of the physicochemical mechanics of materials. *Mater Sci* 54(1):7–21
20. Voloshyn VA (2020) Cyclic corrosion crack resistance of an exploited welded joint of 17G1S pipe steel. *Mater Sci* 56(1):119–124

Chapter 30

Global Statistical Analysis of Old Iron and Steel Properties Based on Old and Recent Literature Review



Stéphane Sire 

Abstract This study deals with the statistical analysis of the chemical and mechanical properties of irons and steels produced from the 1840s. The mechanical characteristics (in this study only the results of tests under static loading are considered) of the irons tested in the nineteenth century seem different from the results of recent analyses. In addition, the statistical analysis of the chemical characteristics of irons and steels enables a better knowledge of these metals. A first exploratory global analysis of these properties makes it possible the identification of groups of individuals particularly through the phosphorus and manganese contents.

Keywords Iron and steel · Properties · Statistical analysis · Review

30.1 Introduction

Irons and steels have been used in the construction of structures for over two centuries. Wrought irons have been progressively replaced by steels in constructions, leading to an evolution of the regulations regarding the minimum mechanical characteristics required for these metals [1]. From the end of the 1820s, characterization tests were carried out, particularly in France, on iron wires. Progressively, the development of these tests followed the strongly increasing evolution of the iron and steel production. From the 1870s onwards, the organization of testing and industrial research laboratories expanded, particularly in the United States, Germany, England and France.

From the 1860s, chemical analysis was introduced into the practices of metallurgists when the new Bessemer and Martin processes were established. Thus, the early literature offers a large amount of data from mechanical and chemical laboratory tests. The materials nowadays tested are irons and steels of structures that are the subject of studies either within a context of heritage preservation/valorization or

S. Sire (✉)

UMR CNRS 6027 IRDL, University of Brest, 29200 Brest, France

e-mail: stephane.sire@univ-brest.fr

within a context of preventive maintenance for repair/restoration operations. These publications from the laboratories also inform us about all these different properties.

This non-exhaustive and regularly updated statistical study includes data from experimental campaigns carried out on wrought irons and steels produced since the 1840s from structures erected in many countries. The database indeed includes data mainly from France, Germany, USA, Poland, UK, Portugal, Italy, Sweden, Austria and Brazil.

First, a statistical analysis of mechanical properties is proposed for irons. Then, recent literature data from analysis of materials taken from structures such as frames or bridges (irons and steels) will be presented, see for instance [2, 3] and [4].

30.2 Mechanical Properties of Wrought Irons (Static Loadings)

The old literature is very large and provides, in particular, the results of numerous tests carried out on very diverse irons; see [5] for instance. These results show in particular the important scatter of the mechanical characteristics of the various irons of the second half of the nineteenth century.

The following Fig. 30.1 (top) shows for example the distribution (density) of the yield stress of the irons in the database under the label “old literature” (964 specimens). Figure 30.1 (bottom) comparatively shows the distribution of the yield

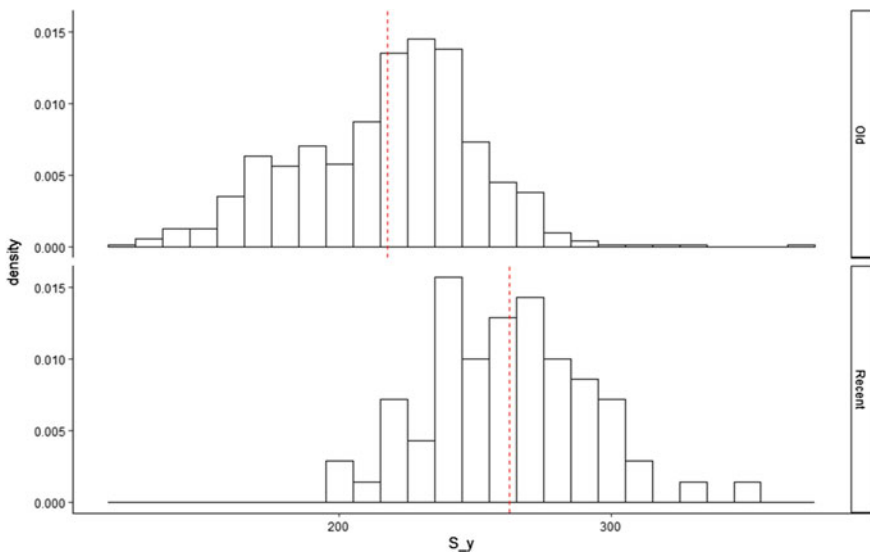


Fig. 30.1 Yield stress (MPa) density from the studied database (irons only); top: from “old” literature, bottom: from “recent” literature

Table 30.1 Cross-sections characteristics (mm^2) of tested irons specimens from the “old” and the “recent” literature

	Mean (mm^2)	Median (mm^2)	IQR (mm^2)
“Old” literature	970.4	804.4	972.0
“Recent” literature	87.2	47.9	79.8

stress of irons labeled “recent literature” (86 specimens). Even if the number of data is different, these two distributions show a gap in the mean value of the yield stress (dashed red line): 217.7 MPa for the “old literature” irons and 262.6 MPa for the “recent literature” irons.

These mean values are, nevertheless, in accordance with the analysis proposed by [6]. In addition to the uncertainty of the results of the tests carried out on old machines, the analysis of the dimensions of the specimens can be taken into account to explain the observed difference. Indeed, as shown in Table 30.1, the cross-sections of the specimens tested in the nineteenth century are much larger than those of the specimens currently tested. This table presents the mean, the median and the interquartile range (IQR) for iron specimens described in both old and recent literature. IQR represents the difference between the 75th percentile and the 25th percentile.

Different distributions are also observed for the steels in the studied database (“old” literature vs. “recent” literature).

30.3 Chemical Composition Analysis of Irons and Steels

Given the differences observed and the presumably increased reliability of the results of recent characterizations, the chemical compositions of the irons and steels studied recently (post 1970) are presented in this section. The studied database includes 177 metals divided into 91 different steels and 86 different irons. It also includes metals from structures erected from the 1840s. Figures 30.2 and 30.3 show the significant differences in composition between these two groups of metals (only C, P, S, Mn and Si are presented in this study).

Among the significant results, the phosphorus content is higher for irons than for steels; on the other hand, the manganese content is higher in the case of steels. These known differences can be explained by the composition of the ores and the manufacturing processes used (puddling processes for irons, mainly Martin and Bessemer processes for the studied steels). The carbon content is also very low for wrought irons and can reach higher values in structural steels.

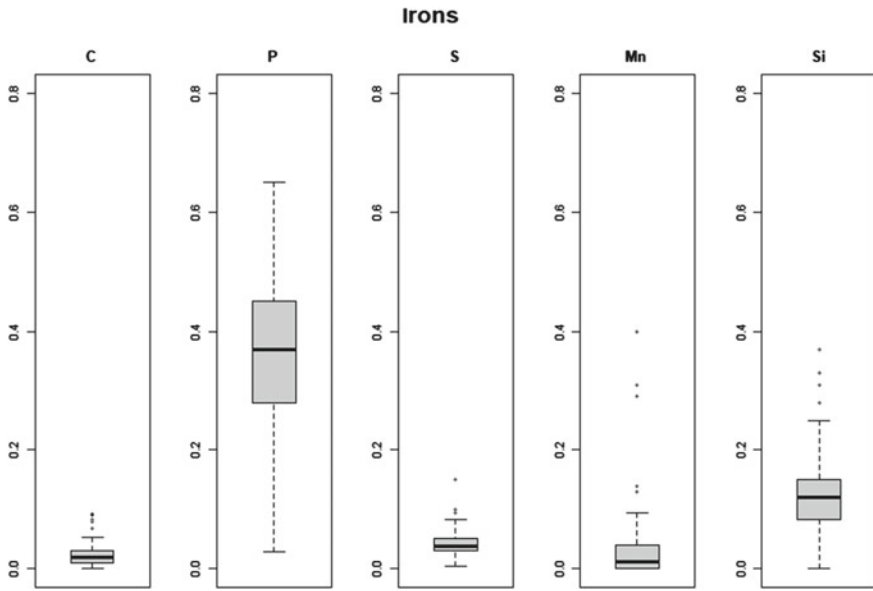


Fig. 30.2 Chemical composition of wrought irons (86 specimens) from nineteenth-century structures

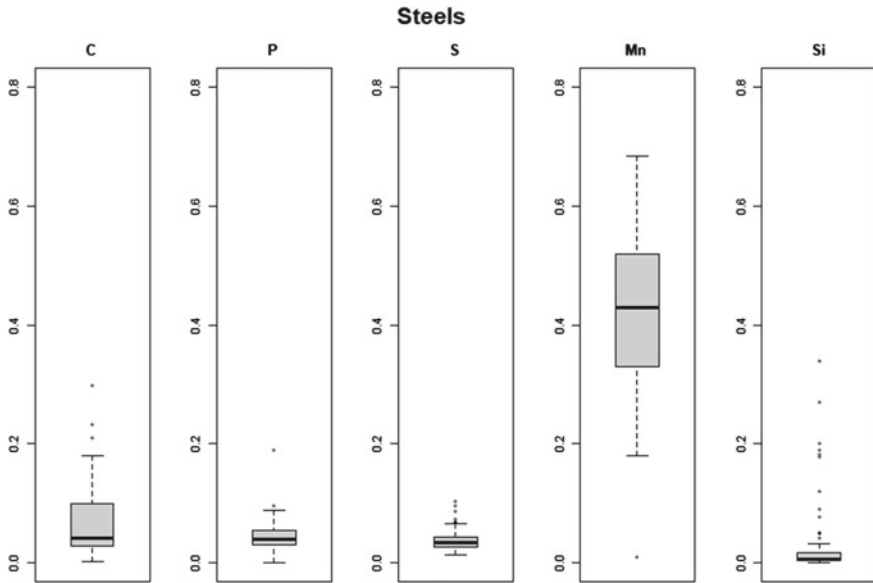


Fig. 30.3 Chemical composition of steels (91 specimens) from nineteenth-century structures

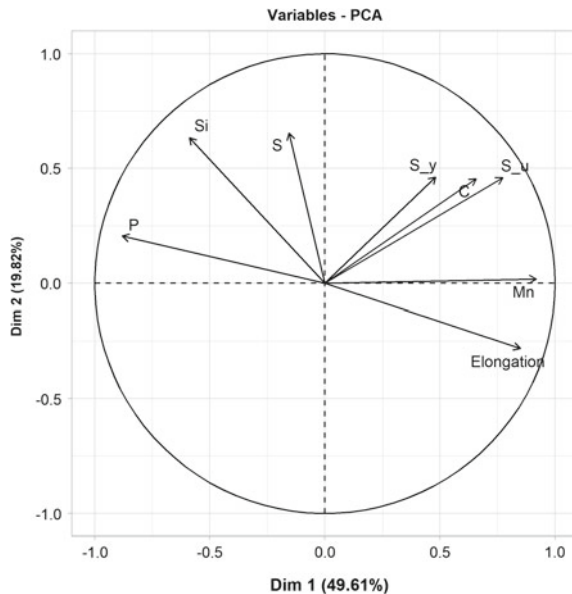
30.4 Principal Component Analysis (PCA) and Irons and Steels Chemical and Mechanical Characteristics

The objective of this multivariate descriptive statistics analysis is to determine the correlations between the different characteristics of the database including features from the mechanical and chemical characterizations. This geometrical and statistical approach performed with R [7] enables, with the graph of variables, to determine the features that present positive correlations (they can be grouped), negative correlations (will be plotted on the opposing quadrants of this plot) and totally uncorrelated features which are orthogonal to each other.

To carry out this analysis, it is necessary to have for each studied specimen, a maximum of both mechanical and chemical characteristics. The database includes 177 specimens (steels and wrought irons) taken from structures built between from the 1840s. PCA reduces the number of variables in a database while preserving as much information as possible. With the studied database, PCA reduces the number of variables in a database while preserving as much information as possible; 90% of cumulative percentage of variance can be covered with only 4 dimensions (i.e., principal components). These dimensions are constructed as linear combinations or mixtures of the initial variables. As an example, the next Figs. 30.4 and 30.5 present graphs with the two first calculated dimensions.

As shown in these figures, the two first dimensions cover 69% of cumulative percentage variance. As presented in Fig. 30.4, when an arrow is longer, the amount from the total variance is larger; we can conclude that there is a negative correlation between the Elongation (at failure) and the phosphorus content P. This result confirms

Fig. 30.4 PCA—graph of variables with the two first principal components



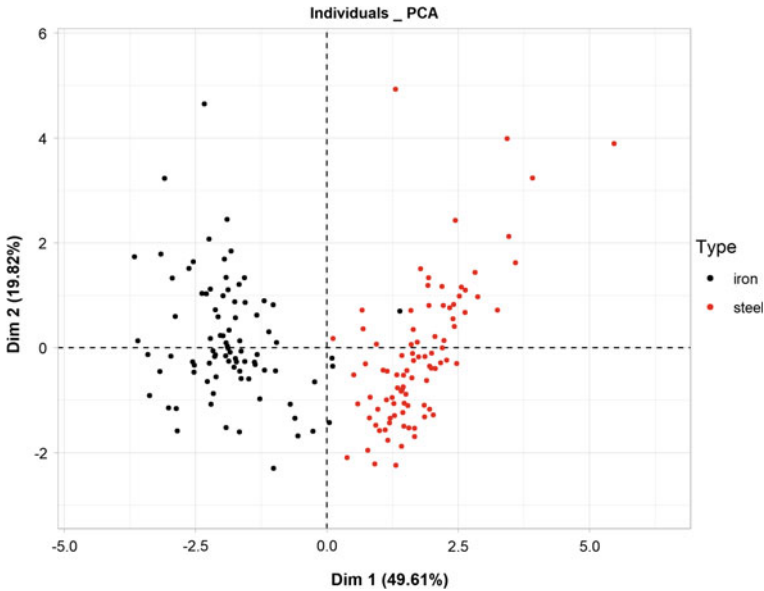


Fig. 30.5 PCA—graph of individuals with the two first principal components

that high phosphorus content corresponds to a brittle metal and high manganese content suggests a ductile material. Figure 30.5 (diagram of individuals) shows then that the irons in the studied database are more brittle than the steels (each dot corresponds to a specimen of the database).

30.5 Conclusions

The statistical analysis proposed in this study underlines the significance of the cross-section of the tested specimens in order not to incorrectly estimate the mechanical characteristics. This is particularly important for metals with non-metallic inclusions, like wrought irons.

Multivariate descriptive statistics, such as PCA, carried out on global dataset including (among others) chemical and mechanical characteristics seem to be an interesting tool to study old metals and give valuable information for the assessment of old metallic structures.

References

1. Sire S, Ragueneau M (2019) Fatigue design of metallic railway bridges in France at the end of the nineteenth century. *Proc Inst Civ Eng Forensic Eng* 172(4):167–174
2. Lesiuk G, Rymcza B, Rabięga J, Correia JAF, De Jesus AMP, Calcada R (2019) Influence of loading direction on the static and fatigue fracture properties of the long term operated metallic materials. *Eng Fail Anal* 96:409–425
3. Kowal M, Szala M (2020) Diagnosis of the microstructural and mechanical properties of over century-old steel railway bridge components. *Eng Fail Anal* 110:104447
4. Holowaty J, Wichtowski B (2015) Properties of steel in railway bridge constructed in 1887. *Roads Bridges* 14:271–283
5. Kirkaldy WG (1891) *Strength and properties of materials with description of the system of testing*. Samson Low, London
6. O’Sullivan M, Swailes T (2009) A study of historical test data for better informed assessment of wrought iron structures. *Int J Archit Herit* 3(4):260–275
7. R Core Team (2021) *R: a language and environment for statistical computing*. R Foundation for Statistical Computing, Vienna, Austria. <https://www.R-project.org>

Chapter 31

Forming Stress-Induced Initial Damage in Case Hardening Steel 16MnCrS5 Under Cyclic Axial Loading in LCF Regime



Kerstin Moehring and Frank Walther

Abstract Present materials used for industrial applications are significantly influenced by manufacturing technologies used during production of industrial goods and applied strains or stresses. For the latter are pre-deformations resulting, these induce changes in the material like hardening, residual stresses, changes in microstructure. In dependence on the level of pre-deformation initial damage is also induced in the microstructure. This study investigates the influence for the direction of pre-deformation on the fatigue performance in the load regime of low cycle fatigue (LCF). In order to quantify the influence of pre-deformation, destructive and non-destructive analyses by means of fatigue tests, hardness measurements, residual stress analyses, quantification of the pore partition and scanning electron analyses of the volume and the surface of the specimen were performed. The results obtained indicate a damage tolerance of the microstructure and the overcompensating effect of the orientation of manganese sulfides precepted. It is concluded that further investigations are necessary in order to quantify the influence of forming induced damage on the fatigue loading capability.

Keywords Forming stress induced initial damage · Low cycle fatigue regime · Low alloyed case hardening steel 16MnCrS5

31.1 Introduction

The properties and especially mechanical properties of industrially used components are influenced by the pre-deformation induced by the specific manufacturing technology. Whereby machining determines pre-dominantly the surface and the surface layer of the material volume up to several microns of the component, forming affects the entire material volume. Depending on the heights and direction of the stress state during forming, microstructural changes are induced. The thereby determined

K. Moehring (✉) · F. Walther
Department of Materials Test Engineering (WPT), TU Dortmund University, Baroper Str. 303,
44227 Dortmund, Germany
e-mail: kerstin.moehring@tu-dortmund.de

changes in hardness due to strain hardening, the induced residual stresses due to inhomogeneities of elastic and elastic properties of the material matrix, the different phases as well as non-metallic inclusions and the general changes of microstructure with regard to grain orientation and size changes have been investigated sufficiently. Nevertheless, recent studies conducted by Hirt et al. [1, 2] emphasize the need to take into consideration forming induced damage additionally.

Forming induced damage is thereby characterized as pores induced on non-metallic inclusions or different microstructural stress risers under applied forming loads [3]. This local material discontinuities in the range of around 5 μm can emerge up to significant and material or component failure relevant length scales depending on the height of stress either during the different stages of forming or during utilization under service conditions [4, 5]. One major field of utilization of components on basis of the investigated case hardening steel 16MnCrS5 (AISI 5117, 1.7319) in industrial application is the field of mechanical and plant engineering. Characteristic components are frequently subjected to cyclic torsional (e.g. shafts) or cyclic axial loads (e.g. combined gearwheels and shafts in drive technologies). For these loads the question arises, how forming induced damage influences the fatigue performance, since it was not sufficiently addressed so far [5]. To answer this question, investigations were conducted with regard to axial loads to obtain a basic understanding of the proceeding mechanisms, the microstructural interdependencies and the effect of forming induced, so-called, initial damage on the fatigue performance. Therefore, a microstructural characterization of the material as well as fatigue experiments were performed.

31.2 Materials and Methods

Within this study the low alloyed case hardening steel 16MnCrS5 (AISI 5117, 1.7139) was used as the base material for a down streamed forming process. The base material was provided by the material supplier Georgsmarienhütte as rolled and drawn round material with a ferrite-pearlite microstructure. The chemical composition of the material is shown in Table 31.1. No additional heat treatment has been conducted.

The base material was further deformed by cold forward rod extrusion up to an extrusion rate of 0.5. Afterwards, the pre-deformation was applied under axial and torsional load paths up to a degree of deformation of 5% using the axial-torsional fatigue testing system (Fig. 31.2), in order to investigate the effect of the load direction.

Table 31.1 Chemical composition of the low alloyed case hardening steel 16MnCrS5, in wt%

Material	C	Si	Mn	S	Cr
16MnCrS5	0.14–0.19	≤0.4	1.0–1.3	≤0.02–0.04	0.8–1.1

The geometry of the specimen used during this study as well as the extraction position of the specimen out of the workpiece after forward rod extrusion are documented in Fig. 31.1.

Fig. 31.1 **a** Workpiece produced by forward rod extrusion with extraction position of the specimen and **b** specimen geometry

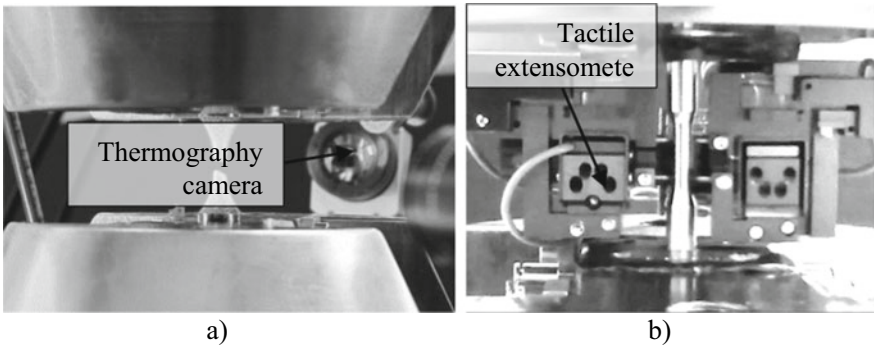
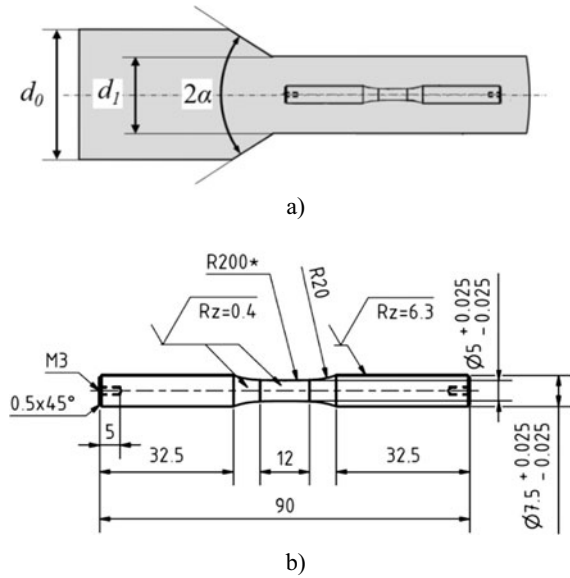


Fig. 31.2 **a** Experimental setup for strain-controlled tension/compression constant amplitude tests and **b** tactile extensometer for strain control

31.3 Experimental Setup and Procedure

The cyclic tests were performed using the servo-hydraulic axial–torsional testing system (Walter+Bai, LFV-T250 T2500 HH) with the nominal axial respectively torsional loads of $F_n = 50$ kN and $M_t = 100$ Nm nominal axial and torsional loads.

For fatigue characterization total strain-controlled tests were performed at a strain ratio of $R = -1$. The strain was hold constant at a total strain amplitude of $\varepsilon_{a,t} = 0.1$ mm and was measured over a gauge length of 10 mm. The temperature during testing was $T = 25$ °C. The temperature change due to plastic deformation and dissipation during forming was detected by means of thermography (Fig. 31.2).

31.4 Results

The Vickers hardness (HV0.01) as well as the tangential and axial residual stress detected by X-Ray diffractometer Bruker D8 discover for $2\theta = 114.7$ were proved to be comparable for the material states investigated. The microstructure was found to be comparable banded ferrite-pearlite with comparable spacing between the ferrite and pearlite bands. Nevertheless, the position of the manganese sulfides present in the low alloyed steel varied (Fig. 31.3). The degree of pre-forming induced damage in terms of pore fraction was by 7.64% higher for the material state pre-deformed under tensile loads.

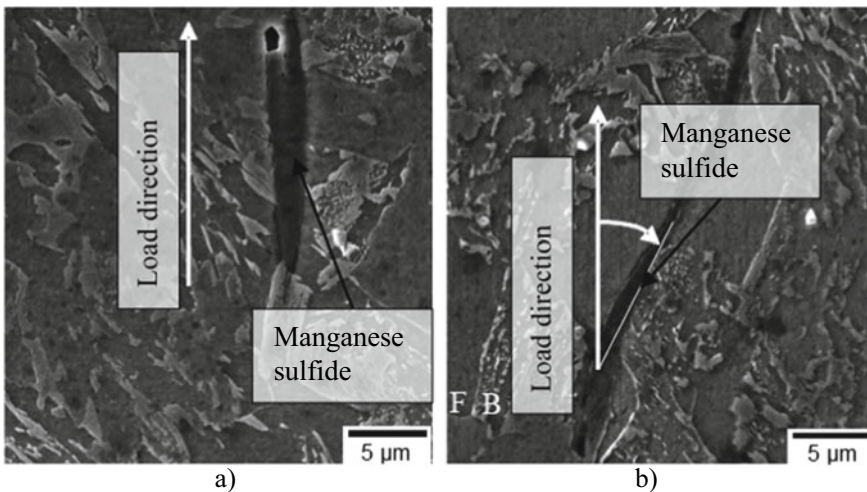


Fig. 31.3 Orientation of the manganese sulfide after **a** tensile and **b** torsional pre-deformation with regard to the loading axis

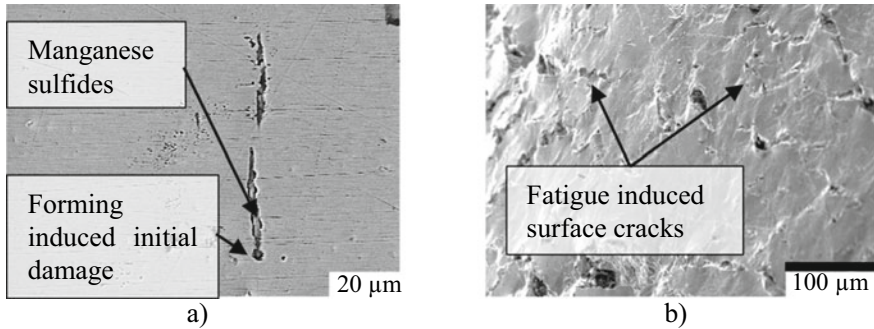


Fig. 31.4 Surface morphology: **a** before and **b** after fatigue testing

The fatigue performance of the material state pre-deformed with torsional loads performed worse than the material state pre-deformed with tensile loads. The difference between the material state was 24,272 cycles to failure compared to 23,104 cycles to failure and thereby 7%. In the meantime, manganese sulfides after fatigue testing in the volume and on the surface show an increased tendency of cracking in cases, when the loading was not perpendicular to the specimen axis or the axis of the extruded manganese sulfides documented in Fig. 31.3b.

SE-observations of the surface of the specimen indicate the influence of forming induced initial damage (Fig. 31.4a). The initial damage induced inside of the work piece (Fig. 31.1b) was located also on the surface of the specimen due to the extraction of the specimen out of the work piece. Thus, the fatigue testing with the—for the load regime of LCF characteristic—failure location at the surface can be considered as appropriate for the evaluation of the influence of initial damage. The surface of the specimen after fatigue testing shows multiple cracks, whereby no clear influence of and evidence for the influence of the initial damage was detected.

Results of a fractographic analysis are documented in Fig. 31.5. The fracture surface (Fig. 31.5a) shows multiple crack initiation sides typical for LCF fracture. The fracture surfaces indicate a high degree of plastic deformation. Caused by the high strain amplitudes that were causing a Low Cycle Fatigue Failure, a dimple like fracture morphology was present (Fig. 31.5b). This morphology, typical for high strain rates predominantly of quasi-static, but also for LCF load conditions with high strain rates, represent ductile fracture. At the same time, also areas were present that indicate fatigue fracture (Fig. 31.5d). The fracture surface indicates the simultaneous fracture of both, ferrite and pearlite phase partitions, as can be seen in Fig. 31.5c. The effect of forming induced initial damage was not detectable by conventional fractographic analyses.

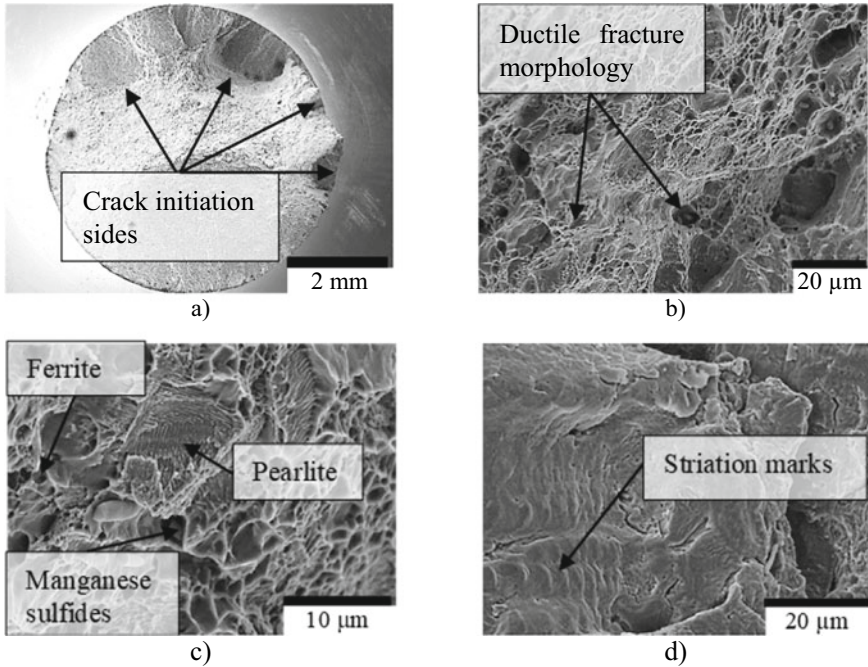


Fig. 31.5 Fracture surface of case hardening steel 16MnCrS5 after tension/compression fatigue testing at LCF regime: **a** complete fracture surface, **b** ductile fracture morphology, **c** ferrite and pearlite fracture partitions and **d** striation marks

31.5 Conclusions

It was shown, that the orientation of the manganese sulfides in the 16MnCrS5 steel determines the fatigue performance to a high extent and overcompensates the effect of initial damage. In order to quantify and systematically analyze the effect of forming induced damage and the interdependencies between forming induced initial damage and microstructure, further investigations are necessary. This includes the digitalization of the results shown above for quantification and comparison. Furthermore, intermittent tests are necessary in order to investigate the damage tolerance of the microstructure induced during deformation and the impact on damage evolution.

Acknowledgements The authors gratefully acknowledge the funding by the German Research Foundation (Deutsche Forschungsgemeinschaft, DFG) for the sub-project C01 (project no. 278868966) within the TRR 188 “Damage-Controlled Forming Processes”. We also thank the DFG and the Ministry of Culture and Science of North Rhine-Westphalia for their financial support within the Major Research Instrumentation Program for the X-ray diffractometer (INST 212/399-1 FUGG).

References

1. Hirt G, Tekkaya AE, Clausmeyer T, Lohmar J (2020) Potential and status of damage controlled forming processes. *Prod Eng* 14(1):1–4
2. Gerin B, Pessard E, Morel F, Verdu C, Mary A (2016) Beneficial effect of prestrain due to cold extrusion on the multiaxial fatigue strength of a 27MnCr5 steel. *Int J Fatigue* 92:345–359
3. Zapara M, Augenstein E, Helm D (2014) Prediction of damage in cold bulk forming processes. *Proc Appl Math Mech* 14:1037–1040
4. Schwab W, Lange K (1985) Effect of process parameters in metal forming on fatigue behavior. *Ann CIRP* 34:215–219
5. Murakami Y, Endo M (1994) Effect of defects, inclusions and inhomogeneities on fatigue strength. *Int J Fatigue* 16:163–182

Chapter 32

Stress Ratio Effect on Fatigue Crack Growth Rate Based on Magnetic Flux Leakage Parameters



Azli Arifin, Shahrum Abdullah, Ahmad Kamal Ariffin, Nordin Jamaludin, and Salvinder Singh Karam Singh

Abstract This study on fatigue failure based on the magnetic flux gradient, $dH(y)/dx$, mostly focuses on the identification of high stress zones, crack propagation monitoring and the characterisation of $dH(y)/dx$ intensity in the crack areas. The main objective of this study was to determine the relationship between fatigue crack growth parameters, $dH(y)/dx$, and stress ratio, R . Fatigue crack growth tests with constant amplitude tensile load were performed on a steel material, SAE 1045, in the form of single-edged crack, according to ASTM E647 standard. Five $R = (0, 0.1, 0.2, 0.3$ and $0.4)$ were used to study the characteristics of magnetic flux gradients. Magnetic sensors were used to detect the magnitude of the magnetic flux induced during the experiment while a crack opening device was used to measure the stress intensity factor range, ΔK , and the fatigue crack growth rate, da/dN , for all range of R . The normal components of magnetic flux signals, $H(y)$, were recorded for every crack increment of 1 mm. An equation for da/dN and the maximum magnetic flux gradient, K_{max} , was established, based on the Paris equation. Using the Huang and Moan method, the R parameter was added to the newly developed $da/dN-K_{max}$ equation. In conclusion, $dH(y)/dx$ signals can be used to develop a model of crack growth behaviour and potentially an alternative method for predicting material fatigue life.

Keywords Metal magnetic memory · Magnetic flux gradient · Fatigue crack growth

32.1 Introduction

The metal magnetic memory (MMM) technique can effectively evaluate stress concentration and the presence of defects in ferromagnetic materials that may initiate fatigue cracking. Under applied stress and geomagnetic field, self-magnetic leakage signals at the stress concentration zone will change due to the irreversible movement

A. Arifin (✉) · S. Abdullah · A. K. Ariffin · N. Jamaludin · S. S. K. Singh
Universiti Kebangsaan Malaysia, 43600 Bangi, Selangor, Malaysia
e-mail: azli@ukm.edu.my

Fig. 32.1 Schematic diagram of the 3 mm-thick specimen and MMM scanning line



and reorientation of the magnetic domains [1]. This method can be used for detecting the development of fatigue failure [2, 3].

The Paris equation, which relates the fatigue crack growth rate with a range of stress intensity factors, is widely used in analysing fatigue crack growth, including the components experiencing different stress ratios [4]. Zhan et al. [5] proposed a new model that combines stress ratios to predict crack propagation. Huang et al. [6] found that the maximum magnetic signal gradient could measure the degree of stress concentration and this showed a uniform increase with the stress intensity factor.

In this paper, the normal components, $H_p(y)$, of MMM signals were measured on SAE1045 steel single notch specimens during fatigue testing at a constant amplitude loading with different stress ratios, R . A quantitative relationship between the fatigue crack growth rate and magnetic flux gradient was established for different stress ratios, based on the Paris equation and the Huang and Moan model [7].

32.2 Methodology

32.2.1 Specimens

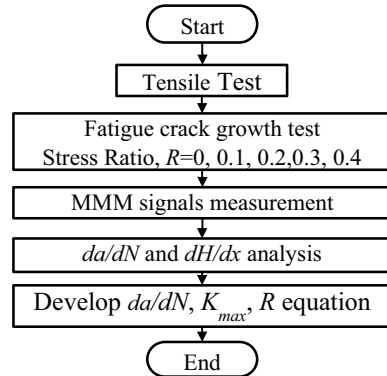
The material used in this study was a ferromagnetic material SAE 1045 medium-carbon steel, which is widely used in engineering structural components. Its composition and mechanical properties can be referred to in [8]. In order to accelerate the initiation of a fatigue crack, single-edged notched specimens were fabricated according to the ASTM E647 standard, as shown in Fig. 32.1. The surface of the specimen was polished prior to testing. Scanning line, $L_x = 100$ mm, which was a parallel line on the surface of the specimen, was used to measure the magnetic signals during the test.

32.2.2 Materials and Method

A constant amplitude loading fatigue test was performed using a 100 kN Servo-Hydraulic Machine under constant amplitude loading. Each specimen was positioned vertically between grip holders. The details of the experimental loading for different stress ratios are presented in Table 32.1.

Table 32.1 Loading parameters of fatigue test at 10 Hz

Stress ratio, R	0	0.1	0.2	0.3	0.4
Maximum load, kN	4	4.44	5.00	5.71	6.67
Minimum load, kN	0	0.44	1.00	1.71	2.67

Fig. 32.2 Flow diagram of experimental work

A crack opening displacement (COD) device was used to measure the fatigue crack growth parameter. Meanwhile, the range of the stress intensity factor ΔK , crack propagation rate and loading cycles were recorded using a software system. During the cycle test, for every 1 mm crack length propagation, the fatigue test was paused for 30 s and the magnetic signals of the specimen were measured along the scanning line using an MMM scanning device, TSCM-2FM. The lift-off value between the sensors and the specimen surface was 1 mm. Figure 32.2 shows the process flow of this work.

32.3 Results and Discussion

32.3.1 MMM Signals

During the fatigue tests, the crack initiated and continued to expand along a direction perpendicular to the scanning line. The final failure of the specimens occurred after 80,356, 72,465, 65,901, 60,936 and 51,725 cycles for $R = 0, 0.1, 0.2, 0.3$ and 0.4 , respectively. The distributions of the normal components of MMM signals during the experiment under different stress ratios were recorded and the gradient, dH/dx , was plotted. Figure 32.3 shows the characteristics of magnetic parameters with different stress ratios. It can be seen that the dH/dx at Lx between 45 and 55 mm are higher than the other positions. The variation of the normal component, $H_p(y)$, and the gradient dH/dx indicate the stress concentration region of the tested positions [8].

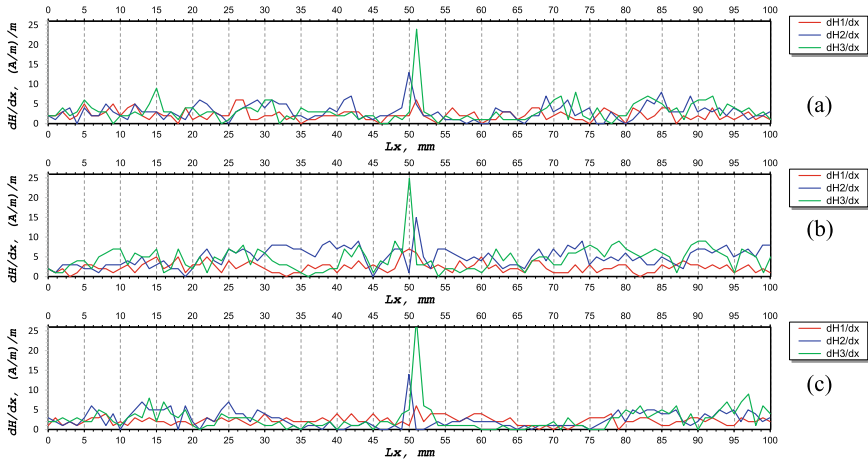


Fig. 32.3 Results for $R = 0$ at the crack length of 5 mm ($dH1/dx$), 10 mm ($dH2/dx$) and 15 mm ($dH3/dx$) for **a** $R = 0$, **b** $R = 0.2$ and **c** $R = 0.4$

The dH/dx signal patterns for all R were almost identical. During the fatigue tests, the magnetic properties of the specimens would be affected due to microstructural changes, primarily the dislocation process [9, 10]. At the early and middle stages of crack propagation, dH/dx increased slowly with the increasing crack length, however, at the late stage of crack propagation, dH/dx increased rapidly with the increasing crack length due to spontaneous generation of abnormal magnetic signals [11].

32.3.2 Fatigue Crack Growth Rate

The Paris model is used to describe the fatigue crack growth rate and is represented by the equation:

$$\frac{da}{dN} = C(\Delta K)^m \tag{32.1}$$

where ΔK is the stress intensity range, and C and m are the Paris model coefficients, which are material and stress ratio dependent. Huang and Moan [7] proposed a fatigue crack growth rate model by considering the effect of stress ratio as:

$$\frac{da}{dN} = C_h(M\Delta K)^{m_h} \tag{32.2}$$

$$M = (1 - R)^{-\beta}, \quad 0 \leq R < 0.5 \tag{32.3}$$

where C_h and m_h are coefficients corresponding to $R = 0$, M is the correction factor and β is the additional material constant.

The maximum normal magnetic gradient, K_{max} , is considered to establish the relationship with da/dN . The graph of the crack growth rate versus K_{max} for different stress ratios is presented in a logarithmic scale in Fig. 32.4 with the best-fitted lines to the data. Applying the same method as in Eq. (32.1) obtains the coefficient, a new proposed equation based on Eq. (32.2) is given as follows:

$$\frac{da}{dN} = C_m (K_{max})^{m_m}, \quad 0 \leq R \leq 0.4 \tag{32.4}$$

where C_m and m_m are coefficients based on MMM signals. The values of these coefficient for different stress ratios are presented in Table 32.2.

Figure 32.5 shows the variations of C_m according to the stress ratios, indicating that C_m increases as R increases. The graph can be fitted using a linear line through the data with $R^2 = 0.97$, yielding the following equations:

$$C_m = 4.182 \times 10^{-8} (R + 2.457) \tag{32.5}$$

$$\frac{da}{dN} = (4.18R + 2.457) \times 10^{-8} (K_{max})^{m_m}, \quad 0 \leq R \leq 0.4 \tag{32.6}$$

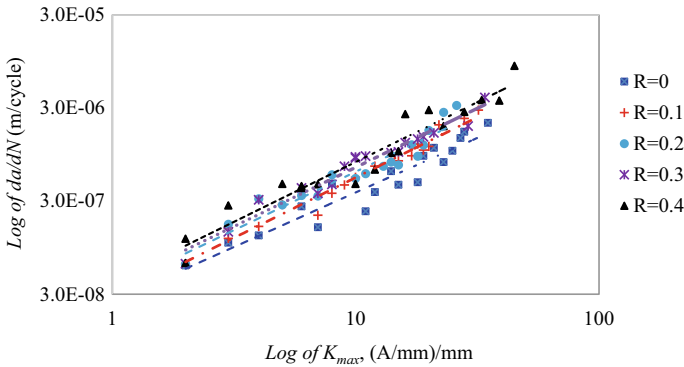


Fig. 32.4 Relationship of da/dN versus K_{max} plotted in log scale for $R = 0, 0.1, 0.2, 0.3$ and 0.4

Table 32.2 Magnetic gradient equation parameter based on the Paris equation

Stress ratio, R	0	0.1	0.2	0.3	0.4
m_m	1.301	1.296	1.279	1.268	1.256
$C_m, \times 10^{-8}$	2.498	2.717	3.444	3.723	4.086
R^2	0.90	0.96	0.85	0.91	0.85

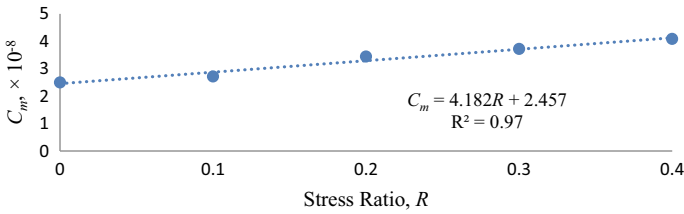


Fig. 32.5 Variation of C_m and R

Equation (32.5) shows that the MMM coefficient, C_m is dependent on the variation in the stress ratio and can be defined by a linear equation. Similar findings were also obtained by Mehrzadi and Taheri in their study of the Paris equation and variations of the stress ratio, R [12].

32.4 Conclusion

The fatigue crack growth behaviour of SAE 1045 was studied and characterised by magnetic flux signals using the MMM method. As fatigue cycles, crack length and stress ratios increased, the magnetic flux gradient increased due to structural changes to the sample. The variation trend of the maximum magnetic flux gradient, K_{\max} , had a good relationship with the fatigue crack growth rate, da/dN . The correlation between da/dN , K_{\max} and R was established based on the Paris and the Huang and Moan model for $R = 0, 0.1, 0.2, 0.3$ and 0.4 , with a correlation of determination, R^2 , between 0.85 and 0.96 . Thus, the equation provided a new approach and an alternative method for predicting fatigue crack growth for different stress ratios using the MMM method.

Acknowledgements The authors would like to express their gratitude to Universiti Kebangsaan Malaysia and Ministry of Education Malaysia through the fund of GUP-2018-148 and FRGS/1/2018/TK03/UKM/02/1 for supporting this research project.

References


1. Wang H, Dong L, Wang H, Ma G, Xu B, Zhao Y (2021) Effect of tensile stress on metal magnetic memory signals during on-line measurement in ferromagnetic steel. *NDT E Int* 117:102378
2. Chongchong L, Lihong D, Haidou W, Guolu L, Binshi X (2016) Metal magnetic memory technique used to predict the fatigue crack propagation behavior of 0.45% C steel. *J Magn Mater* 405:150–157
3. Zhao X, Su S, Wang W, Zhang X (2020) Metal magnetic memory inspection of Q345B steel beam in four point bending fatigue test. *J Magn Mater* 514:167155

4. Ding Z, Gao Z, Wang X, Jiang Y (2015) Modeling of fatigue crack growth in a pressure vessel steel Q345R. *Eng Fract Mech* 135:245–258
5. Zhan W, Lu N, Zhang C (2014) A new approximate model for the R-ratio effect on fatigue crack growth rate. *Eng Fract Mech* 119:85–96
6. Huang H, Jiang S, Wang Y, Zhang L, Liu Z (2014) Characterization of spontaneous magnetic signals induced by cyclic tensile stress in crack propagation stage. *J Magn Magn Mater* 365:70–75
7. Huang X, Moan T (2007) Improved modeling of the effect of R-ratio on crack growth rate. *Int J Fatigue* 29:591–602
8. Anuar NH, Abdullah S, Singh SSK, Arifin A (2021) Characterisation of steel components fatigue life phenomenon based on magnetic flux leakage parameters. *Exp Tech* 45:133–142
9. Ni C, Hua L, Wang X, Wang Z, Qin X, Fang Z (2016) Coupling method of magnetic memory and eddy current nondestructive testing for retired crankshafts. *J Mech Sci Technol* 30(7):3097–3104
10. Wang H, Dong L, Dong S, Xu B (2014) Fatigue damage evaluation by metal magnetic memory testing. *J Cent South Univ* 21(1):65–70
11. Hu Z, Fan J, Wu S, Dai H, Liu S (2018) Characteristics of metal magnetic memory testing of 35CrMo steel during fatigue loading. *Metals* 8(2):119
12. Mehrzadi M, Taheri F (2012) The influence of negative and positive stress ratios on crack growth rate in AM60B magnesium alloy. *Mater Sci Eng A* 545:68–77

Chapter 33

Influence of Heat Treatment Temperature on Fatigue Toughness in Medium-Carbon High-Strength Steels



G. Wheatley, R. Branco, José A. F. O. Correia , R. F. Martins, W. Macek, Z. Marciniak, and M. Szala

Abstract Current research has demonstrated that the tempering temperature affects the martensitic transformation of medium-carbon high-strength steels. This temperature plays an important role in the final microstructure, percentage ratios of martensite to ferrite phases and, consequently, in the mechanical properties and the fatigue response. So far, the relationship between the martensitic tempering temperature and the cyclic deformation properties is not clearly understood. Moreover, the effect of the martensitic tempering temperature on fatigue toughness has not been studied yet. Therefore, this paper aims to study, in a systematic manner, the fatigue toughness of medium-carbon high-strength steels heat treated at different temperatures under fully reversed strain-controlled conditions.

G. Wheatley

College of Science and Engineering, James Cook University, Bebegu Yumba Campus Building
15-124, Townsville, QLD 4811, Australia

R. Branco (✉)

Department of Mechanical Engineering, CEMMPRE, University of Coimbra, Coimbra, Portugal
e-mail: ricardo.branco@dem.uc.pt

J. A. F. O. Correia

Faculty of Engineering, INEGI and CONSTRUCT, University of Porto, Porto, Portugal

R. F. Martins

Department of Mechanical and Industrial Engineering, Nova School of Science and Technology,
UNIDEMI, Campus de Caparica, 2829-516 Caparica, Portugal

W. Macek

Faculty of Mechanical and Ocean Engineering, Gdańsk University of Technology, 11/12 Gabriela
Narutowicza, 80-233 Gdańsk, Poland

Z. Marciniak

Faculty of Mechanical Engineering, Opole University of Technology, Mikolajczyka 5, 45-271
Opole, Poland

M. Szala

Department of Materials Engineering, Faculty of Mechanical Engineering, Lublin University of
Technology, 36D Nadbystrzycka Street, 20-618 Lublin, Poland

Keywords High-strength steels · Cyclic plastic behaviour · Heat treatments · Tempering · Fatigue toughness

33.1 Introduction

Modern railway industry, driven by economic and environmental factors, faces an urgent need to improve efficiency, safety, and reliability. In particular, higher train speeds and heavier traffic loads lead to larger wheel/rail contact forces, which can result in rolling contact fatigue failure. In order to avoid this major concern, new generations of rail materials are being developed, aiming at enhancing the mechanical properties, prolong service life, and reduced cost. Despite the development of new materials, medium-carbon high-strength steels remain outstanding materials in this challenging scenario, mainly due to their superior features, namely the strength-to-weight ratio, toughness, ductility, among others. The development of new materials for applications subjected to cyclic loading requires not only the deep understanding of mechanical behaviour but also reliable fatigue design approaches. Despite the long debate over the last decades on the identification of a universal fatigue damage parameter, no consensus has been found. In general, fatigue models are expressed in terms of stress-based, strain-based, or energy-based relationships [1]. Energy-based relationships are quite versatile and have been successfully applied, either for uniaxial or for multiaxial loading [2–4].

Although not new in the literature, the concept of cumulative strain energy density has been less studied, and its capabilities and limitations are not completely clear, particularly when we are dealing with new engineering materials, such as the new medium-carbon high-strength steels, which can be produced for different heat treatment temperature programmes. In the literature, a power relationship between the cumulative strain energy density and the number of cycles to failure is reported in the low-cycle fatigue regime, either at room temperature or at elevated temperature, for different materials, such as ferritic steels, structural steels, rail steels, austenitic stainless steels, high-strength steels, and bainitic steels, among others. As recently demonstrated in the paper by Martins et al. [5], this well-defined relationship opens the possibility to develop new energy-based approaches to estimate the fatigue lifetime.

This paper aims at studying the effect of tempering temperature on cumulative strain energy density, also known as fatigue toughness, for medium-carbon high-strength steels. At a first stage, we perform a series of low-cycle fatigue tests, under strain-controlled conditions, for different strain amplitudes and heat treatment temperatures. After that, the fatigue toughness for each condition is computed using the stress–strain response collected in the experiments. Finally, the values determined for each tested condition are compared.

Table 33.1 Nominal chemical composition (wt%) of the tested steel

C	Mn	Si	Cr	Mo	Fe
0.18	2.9	1.7	0.8	0.26	Rem.

33.2 Experimental Procedure

In this research, a medium-carbon high-strength steel subjected is studied in the low-cycle fatigue regime for different strain amplitudes and heat treatment temperatures. The nominal chemical composition, in weight percentage, of the tested steel, the 18Mn3Si2CrMo steel, is summarised in Table 33.1. The steel was austenitised at 900 °C, then tempered for 1 h for four different temperatures (i.e. 190 °C, 230 °C, 275 °C, and 315 °C), and finally cooled, in air, to room temperature.

Specimens were machined in accordance with the ASTM E606 standard with a 10 mm long and a 5 mm diameter gauge section. Gauge sections were polished to a scratch-free condition using carbide papers and diamond-based paste. Low-cycle fatigue tests were performed in a conventional servo-hydraulic machine, at strain control mode, under fully reversed conditions, using sinusoidal waves and a constant strain rate, i.e. $d\varepsilon/dt = 6 \times 10^{-3}$. The studied strain amplitudes (ε_a) were 0.50%, 0.65%, 0.80%, and 1.00%. Tests started in compression and stopped when the specimens separated into two parts.

33.3 Results and Discussion

33.3.1 Low-Cycle Fatigue Tests

Examples of the typical stress–strain response observed for different heat treatment temperatures for the same strain amplitude ($\varepsilon_a = 1.0\%$) are presented in Fig. 33.1. As can be seen in the figure, the cyclic plastic response affected the heat treatment temperature from the first cycle to the second cycle, and then showed a strain-softening behaviour until the total failure. We can clearly see that after the mid-life cycle, this strain-softening behaviour is more and more evident, leading to distorted hysteresis loops with a very limited portion of the linear elastic tensile part. This means that the strain energy density changes considerably during the tests.

The effect of the heat treatment temperature on cyclic plastic behaviour can be better analysed via the analysis of stress amplitude during the tests. Figure 33.2 plots the stress amplitude against the number of cycles for four different strain amplitudes (1.0%, 0.80%, 0.65%, and 0.5%) and two different heat treatment temperatures (190 and 315 °C). It is clear from the figure that the material does not exhibit a fully saturated state for all the plotted cases. In several situations, particularly at higher strain amplitudes, the stress amplitude changes continuously with the number of

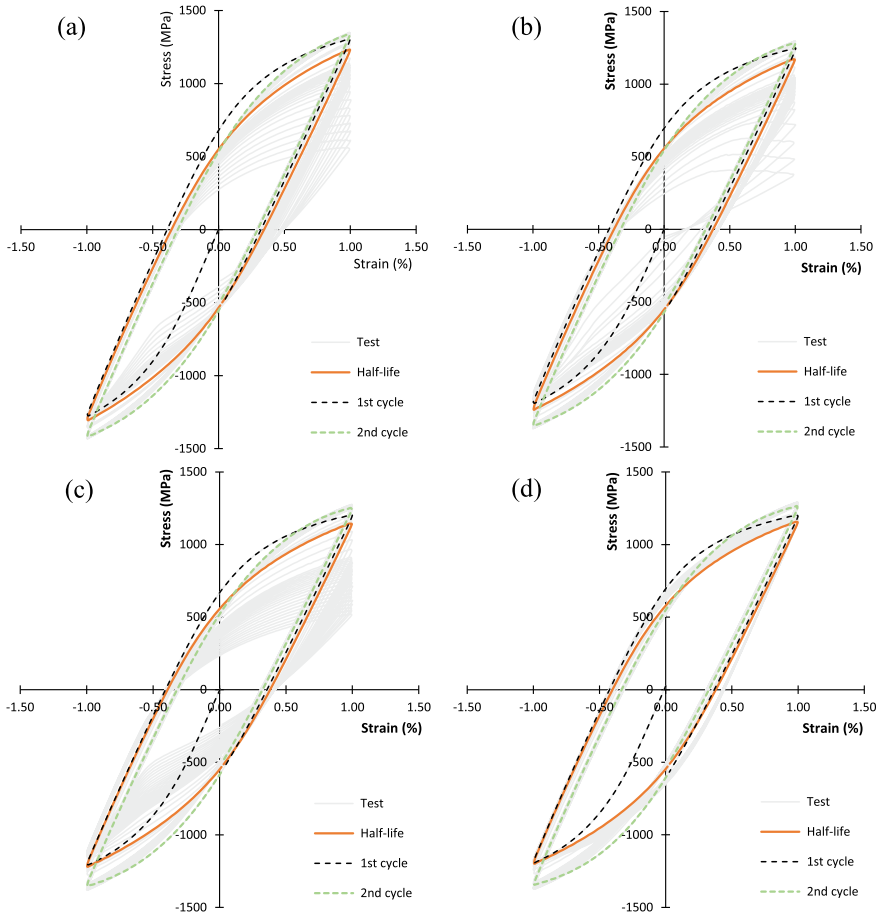


Fig. 33.1 Cyclic stress–strain response of the tested material for a strain amplitude of 1.0% and a heat treatment temperature of: **a** 190 °C, **b** 230 °C, **c** 235 °C, and **d** 315 °C

cycles, without reaching a stable value; in other cases, although the stable value is reached, it occurs in a relatively short period of the test. On the contrary, at lower strain amplitudes, the stabilised response is clearer, and the stress amplitude tends to be constant for a long period of the test. A close look at the figure also shows that the effect of heat treatment process is more pronounced at lower quench temperatures.

The relationship between the plastic strain energy density (ΔW_p) at the mid-life cycle and the number of cycles to failure for the different heat treatment temperatures is exhibited in Fig. 33.3. In this study, the plastic strain energy density, i.e. the area of the hysteresis stress–strain loop was computed numerically using about 200 data points collected in the tests for each cycle. As can be seen, the fitted curves do not follow a unique curve, which suggests that ΔW_p is affected by the heat treatment temperature. Regarding the total strain energy density, defined here as the sum of

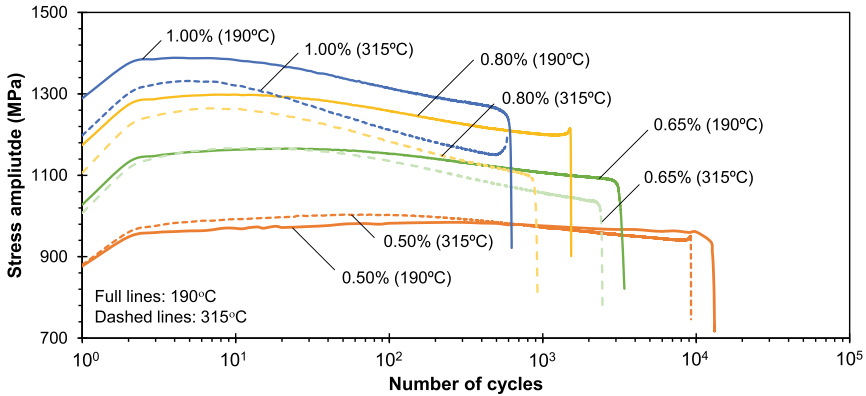


Fig. 33.2 Stress amplitude versus number of cycles for different strain amplitudes (0.50%, 0.65%, 0.80%, and 1.00%) and two different heat treatment temperatures (190 and 315 °C)

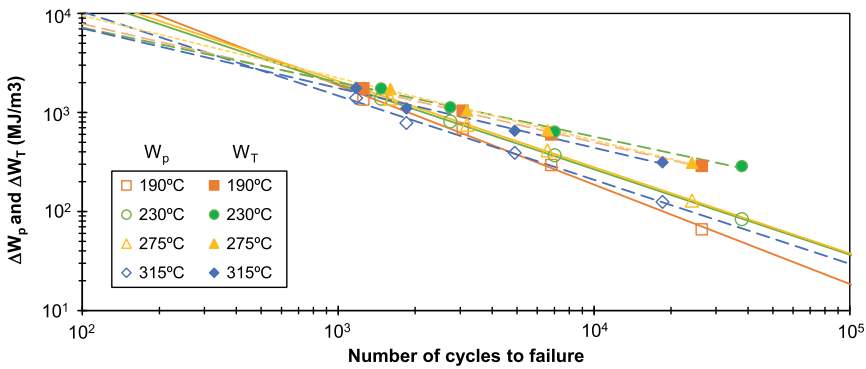


Fig. 33.3 Total strain energy density (ΔW_T) versus number of cycles to failure and plastic strain energy density (ΔW_P) versus number of cycles to failure for different heat treatment temperatures

both the plastic and the tensile positive components, the conclusions are similar. Figure 33.3 plots the total strain energy density (ΔW_T) at the mid-life cycle against the number of cycles to failure for the different heat treatment temperatures. In a similar manner to the plastic strain energy density, the fitted functions are also affected by the heat treatment temperature, leading to different energy-life responses, which are not an attractive solution in terms of fatigue design, since it requires an individual experimental programme for each temperature, in order to define the material fatigue properties.

If we analyse the energy response in terms of cumulated values, i.e. cumulated plastic strain energy density (W_P) and cumulated total strain energy density (W_T), the conclusions are different. Here, the cumulated values were computed numerically, using a cycle-by-cycle integration basis. The typical trends found in this study are exhibited in Fig. 33.4. As can be seen in the figure, unlike the previous case, the

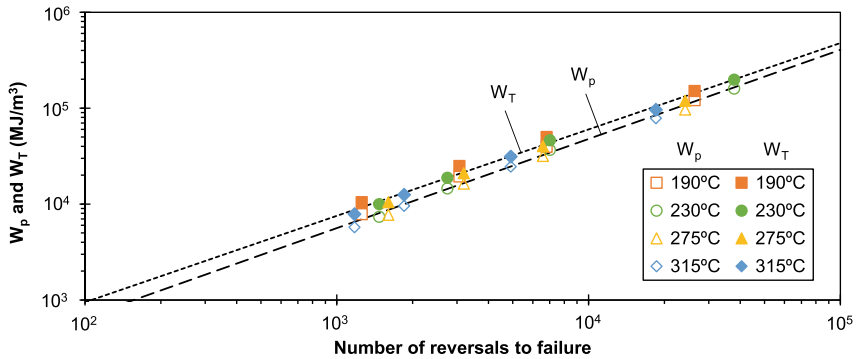


Fig. 33.4 Cumulated strain energy density versus number of cycles to failure for different strain amplitudes and heat treatment at temperatures. W_T represents the cumulated total strain energy density, and W_P represents the cumulated plastic strain energy density

relationships between the cumulated plastic strain energy and fatigue life, and the cumulated total strain energy density and the fatigue life, can be defined using single functions (see dashed lines). In fact, the data points are collapsed in the same trends, irrespective of the heat treatment temperature. This approach deeply simplifies the design approach, since a single function can be used, which reduces costs and time associated with the characterisation of material fatigue properties.

33.4 Conclusions

This study aimed at analysing the effect of heat treatment temperature on cumulated strain energy density, also known as fatigue toughness, in medium-carbon high-strength steels tested in the low-cycle fatigue regime. The experimental programme comprised four different tempering temperatures (190 °C, 230 °C, 275 °C, and 315 °C) and four strain amplitudes (0.50%, 0.65%, 0.80%, and 1.0%). The following conclusions can be drawn:

- the tested steel, irrespective of the tempering temperature, exhibited an initial strain-hardening behaviour, in the first two cycles, and then showed a strain-softening behaviour until the total failure;
- the cyclic stress–strain response was clearly affected by the heat treatment temperature. In most cases, a fully saturated stage was not achieved, leading to significant changes in the hysteresis loop shapes throughout the entire test;
- the energy-life relationships, defined in terms plastic or total components using the mid-life cycle, were strongly affected by the heat treatment temperature. Individual energy-life functions were required to fit the data;

- the energy-life relationships (plastic and total components), defined in terms of cumulated values, were not affected by the heat treatment temperature. A single function could fit the results, which is an interesting outcome.

Acknowledgements This research is sponsored by FEDER funds through the programme COMPETE—Programa Operacional Factores de Competitividade—and by national funds through FCT—Fundação para a Ciência e a Tecnologia—under Project UIDB/00285/2020.

References

1. Branco R, Costa JD, Borrego LP, Berto F, Razavi S, Macek W (2021) Comparison of different one-parameter damage laws and local stress-strain approaches in multiaxial fatigue life assessment of notched components. *Int J Fatigue* 151:106405
2. Liao D, Zhu SP (2019) Energy field intensity approach for notch fatigue analysis. *Int J Fatigue* 127:190–202
3. Lesiuk G, Szata M, Rozumek D, Marciniak Z, Correia JAFO, Jesus AMP (2018) Energy response of S355 and 41Cr4 steel during fatigue crack growth process. *J Strain Anal Eng Des* 53:663–675
4. Nejad R, Berto F (2021) Fatigue fracture and fatigue life assessment of railway wheel using non-linear model for fatigue crack growth. *Int J Fatigue* 153:106516
5. Martins RF, Branco R, Long XL (2020) Fatigue life assessment in bainitic steels based on the cumulative strain energy density. *Appl Sci* 10:7774

Chapter 34

Effect of Specimen Thickness on Fatigue Crack Growth Resistance in Paris Region in AISI 304 STEEL



Stanislav Seitl , Pavel Pokorný , Jan Klusák , Szymon Duda , and Grzegorz Lesiuk 

Abstract Stainless steels are widely used engineering materials providing excellent properties. They have applications in many industries (chemical, energy, food production and civil engineering). The presented study aims to evaluate the effect of specimen thickness on fatigue crack growth behavior in stainless steels AISI 304L. Two grades of stainless steel with different chemical composition were employed: DIN 1.4307 and DIN 1.4306. ΔK -decreasing/increasing FCG tests were carried out on a standard compact tension specimens with 5, 10, 15 and 20 mm in thickness and compared to results gained on compact tension specimens of 6 mm in thickness.

Keywords Fatigue crack growth resistance · Stainless steel · AISI 304 · Thickness effect · Paris' law

34.1 Introduction

Stainless steels are widely used engineering materials providing excellent combination of corrosion resistance and advanced fracture mechanical properties. Stainless steels have applications in many industries, such as chemical and energy industries, food production and nowadays in civil engineering [1]. Significant technological advances in the use of stainless steel in civil engineering construction/structures are described, for example, in [2, 3] and [10].

It is known that many failure problems of civil engineering structures are caused by fatigue of used materials, see [4, 5]. Therefore, the improvement of fatigue crack growth resistance of civil engineering structural materials as well as development of safety design and fabrication processes is strongly required for safety of construction.

S. Seitl (✉) · P. Pokorný · J. Klusák

Institute of Physics of Materials, Czech Academy of Science, Žitkova 22, 616 00 Brno, Czech Republic
e-mail: seitl@ipm.cz

S. Duda · G. Lesiuk

Department of Mechanics, Materials and Biomedical Engineering, Faculty of Mechanical Engineering, Wrocław University of Science and Technology, Smoluchowskiego 25 St., 50-370 Wrocław, Poland

Fatigue crack growth life is an important part in total life of components with initiation concentrators like notches or welded joints, which are unavoidable in most of civil engineering structures and their elements.

The presented study aims to evaluate the effect of specimen thickness [6] on fatigue crack growth behavior [7] in two kinds of stainless steel with different chemical composition: DIN 1.4307 and DIN 1.4306. ΔK -decreasing/increasing fatigue crack growth tests were carried out on standard compact tension (CT) specimens with 5, 10, 15 and 20 mm in thickness and compared to results gained on CT specimen of 6 mm thickness which were taken from literature [8, 9].

34.2 Materials, Mechanical Properties and Fatigue Specimens

The material AISI 304L steels were delivered in the form of hot-rolled sheets with the thickness of 20 mm. The chemical compositions and basic mechanical properties of AISI 304L steels are mentioned in Tables 34.1 and 34.2, respectively. The used specimens were manufactured from a plate of material regarding the direction of rolling, see Fig. 34.1.

Table 34.1 Chemical compositions of the steel grades AISI 304L (in wt% provided by supplier)

AISI 304L	C	Cr	Ni	Mn	S	P	Si	Fe
1.4307	0.023	18.12	8.180	1.790	0.0030	0.0400	0.170	Bal
1.4306	0.009	18.27	10.033	1.851	0.0002	0.0379	0.301	Bal

Table 34.2 Basic mechanical properties of both grades DIN 1.4307 and DIN 1.4306

AISI 304L	0.2% offset yield strength [MPa]	Ultimate tensile strength [MPa]	Elongation at fracture [%]
1.4307	266.6 ± 1.8	665 ± 4.2	76.5 ± 0.5
1.4306	240 ± 2.8	578 ± 6.2	79.9 ± 0.7

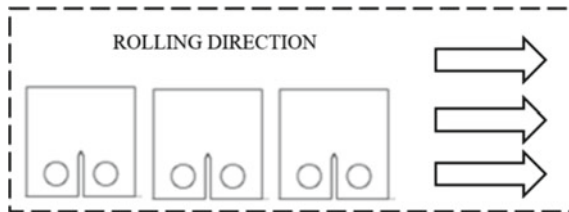


Fig. 34.1 Orientation of specimens with respect to the rolling direction, notches for fatigue crack initiation are perpendicular to the rolling direction

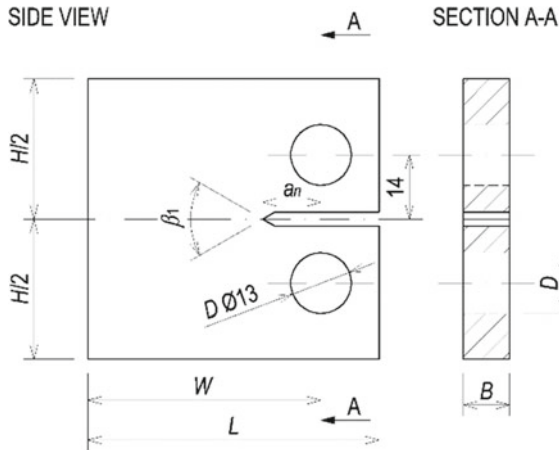


Fig. 34.2 Geometry of compact tension specimens: $W = 50$ mm, $H = 50$ mm, $B \in \{5, 10, 15, 20\}$ mm

The geometry of the CT specimens is shown in Fig. 34.2. Specimens' thickness applied for measurement was selected 5, 10 and 15. The last specimen thickness was selected 20 mm, but due to preparation from plate with nominal thickness 20 mm the real specimen thickness was approximately less -0.2 mm depending of brushing layers.

34.3 Fatigue Crack Growth Rate Measurement

The da/dN versus ΔK curves were determined according to the standard ASTM E647 using the CT specimens with the parameter $W = 50$ mm and the varied thickness $B = 5, 10, 15$ and 20 mm, the recommended thickness according ASTM E647 is in interval:

$$\frac{W}{20} \leq B \leq \frac{W}{4}, \tag{34.1}$$

where W is the distance between the load pin center and the backface of CT specimen, see Fig. 34.2. The stress intensity factor range, ΔK , for CT specimen was calculated from the following expression ASTM E647:

$$\Delta K = \frac{\Delta P}{B\sqrt{W}} \frac{(2 + \alpha)}{(1 - \alpha)^{3/2}} (0.886 + 4.64\alpha - 13.32\alpha^2 + 14.72\alpha^3 + 5.6\alpha^4) \tag{34.2}$$

where P is a load and $\alpha = a/W$ (ratio of a crack length including notch and parameter W).

The FCG rate for the applied loading is defined by the crack length increment for given number of loading cycles. Paris' law, [7], expressed by Eq. (34.3)

$$\frac{da}{dN} = C(\Delta K)^m, \quad (34.3)$$

is often used for the description of the crack growth. C and m are material constants, da/dN is the fatigue crack growth rate (da —crack length increment, dN —corresponding number of cycles) and ΔK is the stress intensity factor range. The number of load cycles to failure (N_f) can be calculated by integrating the crack propagation between an initial crack length (a_i) and critical crack length (a_c), Eq. (34.4)

$$N_f = \int_{a_i}^{a_c} \frac{da}{C(\Delta K)^m}. \quad (34.4)$$

The compact tension fatigue tests were conducted at various load levels with a load ratio of $R = 0.1$. Measurement of the fatigue crack growth rate was carried out using the resonant testing machine Amsler 20 HFP 5100. The loading frequency varied in the range from 50 to 95 Hz, depending on the specimen stiffness (given by specimen thickness and crack length). The experiments were done in a laboratory with controlled temperature and humidity. The temperature was set to 23 °C and the absolute humidity was kept at 10 g/m³ (the corresponding relative humidity is 50%).

34.4 Results

Fatigue crack growth rate were measured using the CT specimens made from two kinds of the 304L steels. Due to civil engineering application on structure, the specimens were fabricated with a notch perpendicular to the rolling texture.

34.4.1 AISI 304L—DIN 1.4307

The average grain size for DIN 1.4307 was measured to be $32 \mu\text{m} \pm 11 \mu\text{m}$ excluding twin interfaces, detail information could be found in paper [8, 9]. In Fig. 34.3, Paris law constants C and m , from experimental measurement performed on CT specimens with 5, 10 and 15 mm of thickness and CT specimen with thickness 6 mm literature [8] performed on AISI 304L (DIN 1.4307) are compared.

Note that experimental constants C and m are not easily related with any physical properties of materials. The Paris' law is a curve fit of the central region (Paris' region) of results of a fatigue crack growth experiment. The interval of m is usually for metallic materials from 2 up 8 [4, 5].

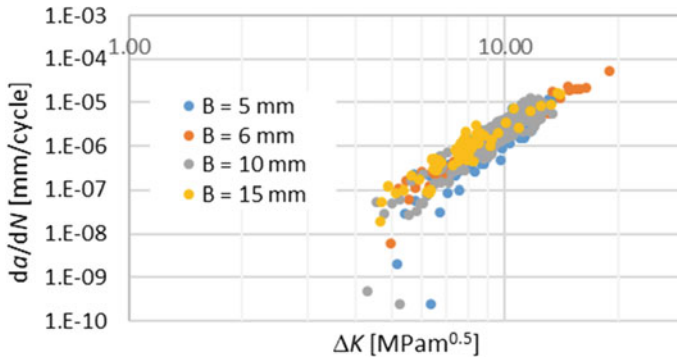


Fig. 34.3 Measured crack growth rates da/dN at the load ratio $R = 0.1$ for the thicknesses 5, 10 and 15 mm and comparison with data for $B = 6$ mm from [8] for DIN 1.4307

Table 34.3 Comparison of material DIN 1.4307 constants C and m , from experimental measurement and literature [8] for various thickness

AISI 304L	Source	B [mm]	C [m/cycle MPam ^{0.5}]	m [-]	R^2
1.4307		5	9×10^{-12}	5.38	0.71
		10	2×10^{-11}	4.98	0.65
		15	4×10^{-11}	4.86	0.81
	[8]	6	1×10^{-11}	5.35	0.96
Ni 8.09	[12]	10	8.16×10^{-13}	3.61	–

In [11], the results for the AISI 304 with similar chemical composition: C 0.06 mass%, Si 0.42 mass%, Mn 0.84 mass%, P 0.030 mass %, S 0.002 mass%, **Ni 8.09** mass%, Cr 18.16 mass%, and the remainder composed of Fe, was mentioned. The fatigue properties are mentioned in Table 34.3 and a strong influence of specimen thickness B on the fatigue crack growth was observed for the DIN 1.4307.

We can see slight increase of DIN 1.4307 fatigue crack growth rate with increasing thickness of the specimens. Despite of some scatter observed in da/dN data, the results for all four thicknesses can be represented by a single curve for the two-parameter crack growth rate relation as applied for AISI 304 L.

34.4.2 AISI 304L—DIN 1.4306

For DIN 1.4306 grade of AISI 304 L steel the experimental data shows that the similar fatigue behavior is observed for $B = 5$ mm, 10 mm and 20 mm. However, the influence of thickness on da/dN is less pronounced, and becomes virtually absent for da/dN close to 1×10^{-5} mm/cycle and still $\Delta K = 12$ MPam^{0.5} (Fig. 34.4 and Table 34.4).

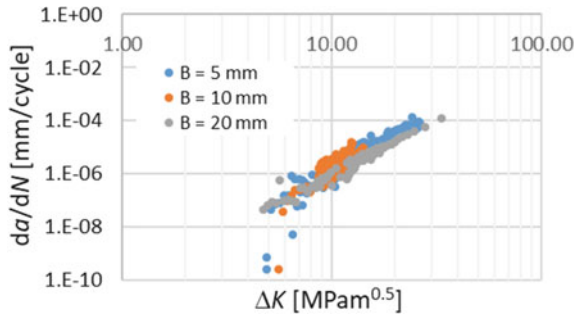


Fig. 34.4 Measured crack growth rates da/dN at the load ratio $R = 0.1$ for the four specimens thickness 5, 10, 15 and 20 mm for DIN 1.4306

Table 34.4 Comparison of material DIN 1.4306 constants C and m , from experimental measurement for various thickness

AISI 304L	B [mm]	C [mm/cycle MPam ^{0.5}]	m [-]	R^2
1.4306	5	3×10^{-11}	4.67	0.89
	10	3×10^{-11}	4.70	0.48
	20	3×10^{-11}	4.47	0.93

According to the results obtained, the Paris’ law materials constant for various thicknesses could be recommended for practical applications in civil engineering structural analysis under fatigue load regime, where properties are utilized as input parameters, see [11–13].

34.5 Conclusion

Growth of long fatigue cracks was experimentally investigated in two grades of stainless steel AISI 304 L. The results were compared with literature data. However, the paper presents preliminary results, and more detail microstructural and fractographic analysis will be performed. The following conclusions can be drawn:

- A slight influence of specimen thickness B on the fatigue crack growth was observed for the DIN 1.4307 grades of AISI 304 L steel.
- For DIN 1.4306 grades of AISI 304 L steel the experimental data shows similar fatigue behavior for $B = 5$ mm, 10 mm and 20 mm. However, the influence of thickness on da/dN is less pronounced than in case of DIN 1.4307, and becomes virtually absent for da/dN close to 1×10^{-5} mm/cycle and still $\Delta K = 12$ MPam^{0.5}.

Acknowledgements The research was supported by the project No. 20-00761S.

References

1. Gardner L (2005) The use of stainless steel in structures. *Prog Struct Mat Eng* 7(2):45–55
2. Baddoo NR (2008) Stainless steel in construction: a review of research, applications, challenges and opportunities. *J Constr Steel Res* 64(11):1199–1206
3. Gedge G (2008) Structural uses of stainless steel—buildings and civil engineering. *J Constr Steel Res* 64(11):1194–1198
4. Suresh S (1998) *Fatigue of materials*, 2nd edn. Cambridge University Press, Cambridge
5. Schijve J (2003) Fatigue of structures and materials in the 20th century and the state of the art. *Int J Fatigue* 25:679–702
6. Korda AA, Mutoh Y, Miyashita Y, Sadasue T (2006) Effects of pearlite morphology and specimen thickness on fatigue crack growth resistance in ferritic–pearlitic steels. *Mater Sci Eng A* 428(1–2):262–269
7. Paris PC, Erdogan F (1963) A critical analysis of crack propagation laws. *J Basic Eng* 85:528–533
8. Jambor M, Vojtek T, Pokorný P, Šmíd M (2021) Effect of solution annealing on fatigue crack propagation in the AISI 304L TRIP steel. *Materials* 14:1331
9. Šmíd M, Kuběna I, Jambor M, Fintová S (2021) Effect of solution annealing on low cycle fatigue of 304L stainless steel. *Mater Sci Eng A* 824:141807
10. Nagaishi N, Yoshikawa M, Okazaki S, Yamabe J, Yoshida F, Matsunaga H (2019) Evaluation of fatigue life and fatigue limit of circumferentially-notched type 304 stainless steel in air and hydrogen gas based on crack-growth property and cyclic stress-strain response. *Eng Fract Mech* 215:164–177
11. Kala Z (2017) Identification of stochastic interactions in nonlinear models of structural mechanics. In: *AIP conference proceedings*, vol 1863, p 480004
12. Kala Z, Omishore A (2016) Fuzzy stochastic approaches for analysing the serviceability limit state of load bearing systems. *Int J Math Comput Simul* 10:294–301
13. Krejsa M, Koubová L, Flodr J, Protivinsky J, Nguyen QT (2017) Probabilistic prediction of fatigue damage based on linear fracture mechanics. *Frattura ed Integrità Strutturale* 11(39):143–159

Chapter 35

Fracture Mechanics Assessment of Notches Subjected to Very High-Cycle Fatigue Loading



Kamila Kozakova and Jan Klusak

Abstract The aim of this article is to introduce method for evaluation of the lifetimes of smooth and notched specimens in the area of highcycle and gigacycle fatigue of materials. The theory of critical distances is used for evaluation and recalculation of the fatigue life curves. The effect of the notch is quantified using the line method, which uses the length parameter l . This critical parameter l can be used for predictions of fatigue lifetimes of notched components.

Keywords Wöhler curve · High-frequency loading · Gigacycle fatigue · Notches · Theory of critical distances · Line method · Ultrasonic fatigue tests

35.1 Introduction

In process of designing cyclically loaded components, designers usually rely on fatigue data measured on smooth specimens. However, there are stress concentrators in real components. There are several ways how data from notched specimens can be related to the data from smooth samples. At the same time, there are several ways how fatigue life curves of smooth specimens can be converted to estimate lifetime of a notched component. In this work, methods of finite fracture mechanics are applied to find the relationship between $S-N$ data measured on notched and smooth specimens. The article describes the application of the theory of critical distances in the field of high-cycle and gigacycle fatigue.

K. Kozakova (✉) · J. Klusak
Institute of Physics of Materials, Czech Academy of Sciences, Zizkova 513/22, 616 00 Brno,
Czech Republic
e-mail: kozakova@ipm.cz

J. Klusak
e-mail: klusak@ipm.cz

35.1.1 Gigacycle Fatigue

August Wöhler was one of the first researchers, who dealt with the fatigue of materials. He assumed the existence of a fatigue limit of metals. The fatigue limit can be described as the highest stress that does not lead to fracture at 10^7 cycles [3]. Nowadays, new technologies require studying possible fracture behavior beyond 10^7 cycles [9]. By means of ultrasonic fatigue testing machines, fatigue testing beyond 10^7 cycles can be realized in real-time, and it was shown that fracture can occur in the gigacycle fatigue region [1, 5]. In the gigacycle fatigue regime, cracks often initiate in subsurface on inclusions, “supergrains” and pores. These cracks lead to fish-eye propagation around the defects [2].

35.1.2 Theory of Critical Distances

Stress concentrations like notches often lead to a crack initiation and consequent failure. Fracture mechanics describes the behavior of components with cracks. Notches can be seen as cracks in some way. Thus generalizations of fracture mechanics led to the birth of the finite fracture mechanics (FFM) and the theory of critical distances (TCD), which is derived from linear elastic fracture mechanics. TCD uses a length parameter, the critical distance l . The theory of critical distances uses the distribution of opening stress of notched components for lifetime prediction. The best-known approaches of TCD are the point method and the line method. These methods were formulated in a similar form by Neuber and Peterson, but now they have been refreshed and improved with the availability of finite element analysis. The point method states that failure will occur when the elastic stress at a certain distance from the notch reaches some critical value. The line method is very similar but uses the average stress over this distance [4, 7, 8] (Fig. 35.1).

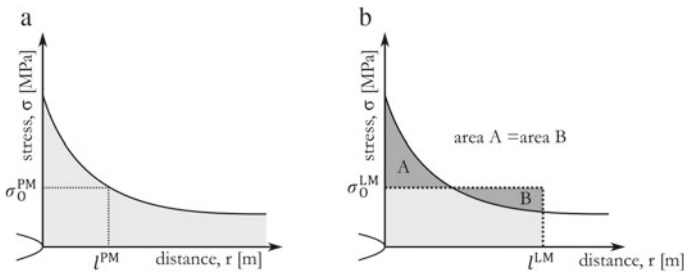


Fig. 35.1 a Critical distance—point method, b critical distance—line method

35.2 Process of Evaluation

The work deals with the evaluation of lifetime of smooth and notched specimens in the field of high-cycle and gigacycle fatigue of materials. The theory of critical distances, particularly the line method is used here to find the critical length parameter l . To apply the theory, the model distribution of axial stress in the narrowest part of the notched specimen is analyzed numerically. Commonly, $S-N$ data of smooth and notched specimens are presented by means of nominal stresses. Where the nominal stress is the average stress across the entire cross-section in the narrowest part. Based on the axial stress distribution, the $S-N$ curves for smooth and notched specimens are evaluated and the critical distance l is determined in the following way. The experimental data for smooth and notched specimens are approximated by the $S-N$ curves. The critical distance, measured from the notch tip, is determined so that the average stress over the critical distance in the notched specimen is the same as the nominal stress of smooth specimen at the same number of cycles to fracture.

35.2.1 Application—Aluminum Alloy Specimens

The aluminum alloy specimens were designed for ultrasonic fatigue tests (UFT). For UFT, the intrinsic frequencies of the longitudinal vibrations of the specimens shall be close to 20 kHz. Figure 35.2a shows the specimens dimensions, where the total lengths and intrinsic frequencies are listed in Table 35.1.

Using numerical calculations, the axial stresses σ_y in the narrowest cross-section were determined (see Fig. 35.3a) for the model notched specimen. Experimental $S-N$ data were approximated by $S-N$ curves (Fig. 35.3b). Then the critical distance follows from Formula (35.1), where $\sigma_{a,nom}^{notched}(N_f)$, and $\sigma_{a,nom}^{smooth}(N_f)$ are the values on the $S-N$ curves for an arbitrary, but the same number of cycles (N_f), $\sigma_{y,LM}(l)$ is the average stress over the distance l , and $\sigma_{y,LM,nom}$ is the average stress over entire cross-section of the model notched specimen from Fig. 35.3a and it is equal to 93 MPa.

$$\sigma_{y, LM}(l) = \frac{\sigma_{a,nom}^{smooth}(N_f)}{\sigma_{a,nom}^{smooth}(N_f)} \cdot \sigma_{y, LM, nom} \quad (35.1)$$

The result of Eq. (35.1) is the average stress over a critical distance l . Finally, in the stress distribution, we look for the critical distance l that satisfies Eq. (35.1). This calculation is performed for the entire range of values N_f .

The dependence of the critical distance on the number of cycles to fracture is shown in Fig. 35.3c. This dependence can be described by Eq. (35.2).

$$l = 0.8992 \cdot N_f^{-0.04939} \quad (35.2)$$

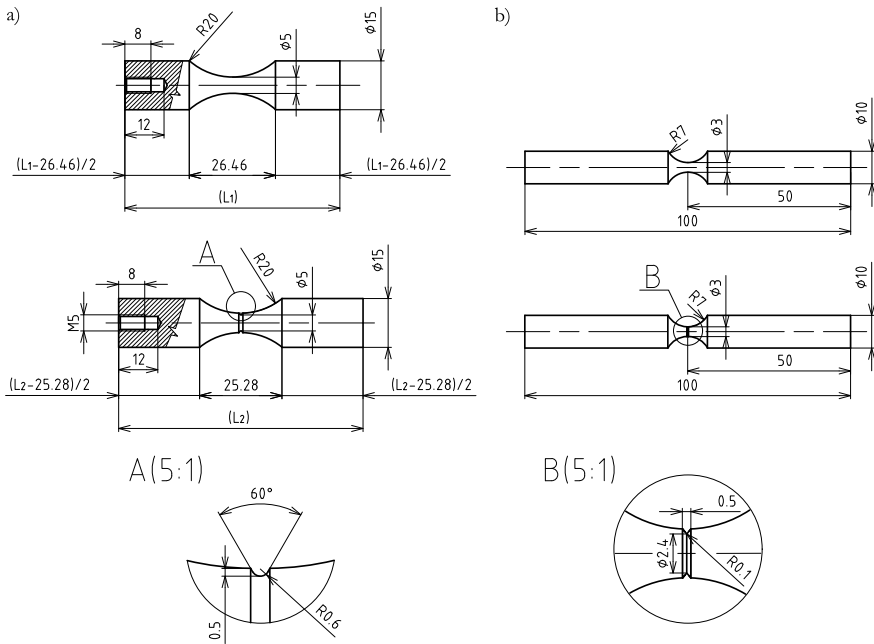


Fig. 35.2 Parameters of specimens: **a** aluminum alloy, **b** structural steel

Table 35.1 The total lengths and intrinsic frequencies of specimens

Smooth specimens	$L_1 = 66 \text{ mm}$	$f_1 = 20,012 \text{ Hz}$
Notched Specimens	$L_2 = 75 \text{ mm}$	$f_2 = 20,042 \text{ Hz}$

When knowing the critical distance, we can make a prediction of lifetime of a notched component via an estimation of the $S-N$ curve of specimens with given notch radius. We assume that the critical distance is a material parameter, and we use an inverse approach based on Eq. (35.1). The estimation for the given notch radius is based on knowledge of $S-N$ curve of smooth specimens and knowledge of the model stress distribution for the given notch. We determine the notch stress concentration factor $K_{t,LM}(l)$ based on the line method from the model stress distribution:

$$K_{t,LM}(l) = \frac{\sigma_{y,LM}(l)}{\sigma_{y,LM,nom}} \tag{35.3}$$

Then we can calculate the points of the estimated $S-N$ curve of notched specimens from the $S-N$ curve measured at smooth specimens:

$$\sigma_{a,nom}^{notched}(N_f) = \frac{\sigma_{a,nom}^{smooth}(N_f)}{K_{t,LM}(l)} \tag{35.4}$$

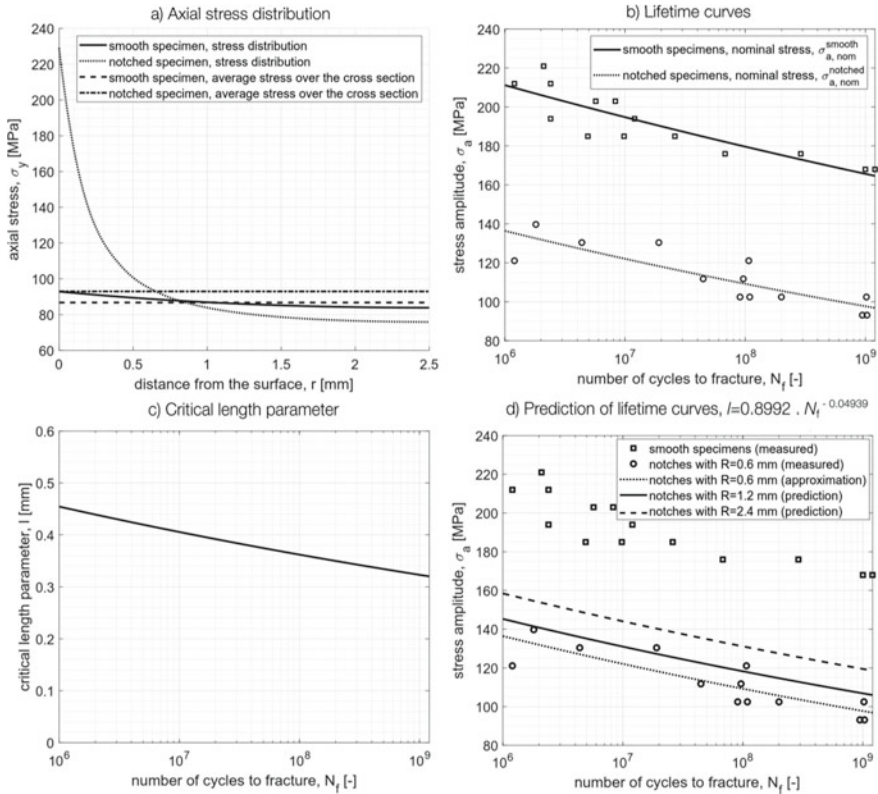


Fig. 35.3 Results on aluminum alloy

Figure 35.3d shows the predictions of $S-N$ curves for notched specimens with the notch radii of 0.6, 1.2, and 2.4 mm.

35.2.2 Application—Steel Specimens

Similar calculations using Eq. (35.1) were performed for steel specimens shown in Fig. 35.2b, where the notch radius was 0.1 mm. Experimental data were taken from [6]. Based on the model distribution of axial stress, the value of the critical distance was determined as 0.08 mm. This value was ascertained for $N_f = 2 \times 10^6$ and, although it slightly depends on N_f , it was considered as a constant for entire range of N_f . Then we can use the model axial stress distributions of various notches, and we can apply the inverse approach given by Eqs. (35.3) and (35.4) on $S-N$ curve of the smooth specimens to get the predictions of lifetime curves of notched specimens.

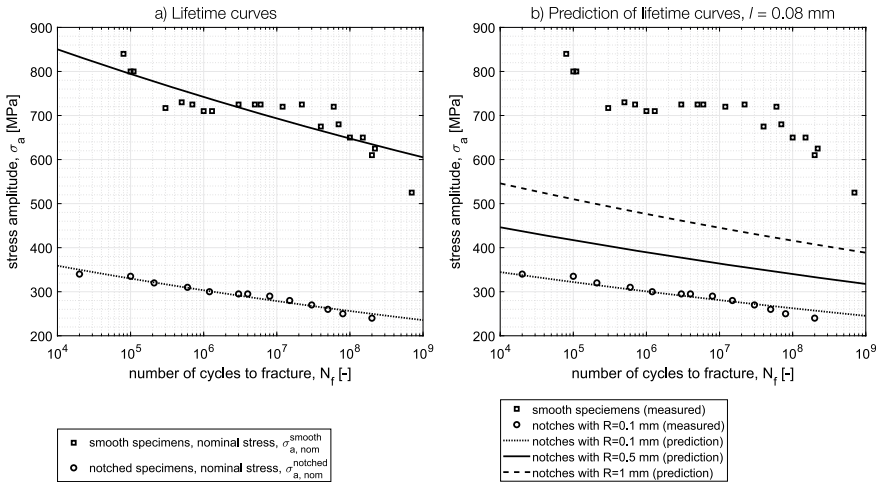


Fig. 35.4 Results on structural steel

The estimations of $S-N$ curves for notches with radii of 0.1, 0.5, and 1 mm are shown in Fig. 35.4b.

35.3 Conclusion

In the study, the theory of critical distances was applied to estimate the lifetime curves of notched specimens in the field of high-cycle and gigacycle fatigue. The average critical distance was 0.38 mm for specimens of aluminum alloy with a notch (radius 0.6 mm). In the case of structural steel specimens with a sharper notch (radius 0.1 mm), the average value of critical distance was 0.08 mm. Both in the case of aluminum alloy and structural steel, the critical distance slightly decreases with the increasing number of cycles. This corresponds to the fact that with increasing N_f the loading level decreases and at the same time crack initiation can be caused by structural defects, voids, and inhomogeneities of smaller size. The average critical distance can be used for predictions of lifetime of notched components with various notch radii. Experimental verification of these predictions will be object of our further study.

Acknowledgements The research was supported by the Czech Science Foundation through the project No. 20-00761S.






References

1. Bathias C (1999) There is no infinite fatigue life in metallic materials. *Fatigue Fract Eng Mater Struct* 22(7):559–565
2. Huang Z, Wagner D, Bathias C, Paris PC (2010) Subsurface crack initiation and propagation mechanisms in gigacycle fatigue. *Acta Mater* 58(18):6046–6054
3. Marines I, Bin X, Bathias C (2003) An understanding of very high cycle fatigue of metals. *Int J Fatigue* 25(9):1101–1107
4. Mei J, Xing S, Vasu A, Chung J, Desai R, Dong P (2020) The fatigue limit prediction of notched components—a critical review and modified stress gradient based approach. *Int J Fatigue* 135:105531
5. Mughrabi H, Antolovich SD (2016) A tribute to Claude Bathias—highlights of his pioneering work in gigacycle fatigue. *Int J Fatigue* 93:217–223
6. Qian G, Hong Y, Zhou C (2010) Investigation of high cycle and very-high-cycle fatigue behaviors for a structural steel with smooth and notched specimens. *Eng Fail Anal* 17(7):1517–1525
7. Taylor D (2008) The theory of critical distances. *Eng Fract Mech* 75(7):1696–1705
8. Taylor D (2017) The theory of critical distances: a link to micromechanisms. *Theoret Appl Fract Mech* 90:228–233
9. Wagner D, Cavalieri F, Bathias C, Ranc N (2012) Ultrasonic fatigue tests at high temperature on an austenitic steel. *Propul Power Res* 1(1):29–35

Chapter 36

Fatigue Failure of 51CrV4 Steel Under Rotating Bending and Tensile



V. M. G. Gomes , Abílio M. P. De Jesus , M. Figueiredo ,
José A. F. O. Correia , and R. Calcada 

Abstract Railway has proved to be a sustainable transportation alternative. This potential has caused a huge investment in the sector in recent years. However, in the freight sector, leaf spring suspensions have been suffering failures due to fatigue, causing derailments and serious losses. This work intends to provide resources to predict future structural failures due to fatigue, focusing on an analysis of fatigue in terms of the effect of loading type and applied load amplitude. It also evaluates the failure modes that occur on rotating bending and tensile fatigue testing. For this reason, a classical SN approach and SEM have been used to analyze the total fatigue life and fracture surfaces, respectively. According to the analyzed results, there is a great sensitivity to micro-notches and crack initiation on the free surface and from non-metallic inclusions.

Keywords Railway · Rolling stock · Spring steel · Fatigue failure · Non-metallic inclusions · Roughness

36.1 Introduction

Over the years the freight rail sector has shown a great impact on the world economy. This type of transport has been demonstrating to have a big potential to prevent climate change. Nowadays, Portugal has been seeking to invest in this sector, acquiring new trains, modernizing the services provided, and improving the maintenance practices in infrastructures and rolling stock [1].

Regarding the freight wagon running gear, this is standardized by the International Union of Railways (UIC), having different configurations of bogies [2]. The link

V. M. G. Gomes (✉) · A. M. P. De Jesus · M. Figueiredo · J. A. F. O. Correia · R. Calcada
Faculty of Engineering, University of Porto, 4200-465 Porto, Portugal
e-mail: vgomes@inegi.up.pt

V. M. G. Gomes · A. M. P. De Jesus · J. A. F. O. Correia
INEGI, University of Porto, FEUP Campus, 4200-465 Porto, Portugal

R. Calcada
Centre of Competence in Railways (CSF), 4200-465 Porto, Portugal

suspension bogie with parabolic leaf springs is one of the possible configurations for UIC freight wagons. Although this mechanism originated in the 1900s, it is still widely used in several freight wagons, its leaf springs are failing by fatigue and hence originating derailments and economic losses [3].

These occurrences has proved the existence of a lack of knowledge about “health” of leaf springs, though the longevity of the link suspension bogie in the railway sector [2]. In order to prevent fatigue issues on leaf springs, a deep investigation into its fatigue resistance needs to be undertaken. This paper intends to provide information about the total-life of spring steels used in parabolic leaf springs for freight wagons based on an SN curve approach. Also, it presented the probability of different fatigue failure modes observed from scanning electron microscopy, (SEM).

36.2 Material and Methods

The spring steel is a high-strength alloyed steel standardized as DIN 51CrV4. The chemical composition was measured according to the optical emission spectroscopy and compared with the standardized values as shown in Table 36.1.

From the optical microscopy performed, the spring steel shows a lath tempered martensitic structure [4]. No difference in the microstructure has been verified in longitudinal, transversal, and planar planes. However, some samples can show decarburization in the vicinity of the surface. This phenomenon is verified with a dimension of about 5 μm . Figure 36.1 left and—right show the structure in the core and the vicinity of the surface, respectively.

In terms of mechanical strength, the spring steel presents a very high yield and ultimate strengths, $\sigma_{0.2}$ and σ_{uts} with low ductility, ϵ_f . Furthermore, charpyV tests showed low impact toughness. Table 36.2 shows the mechanical properties obtained from standard tests in summary [5–7].

The fatigue strength of spring steel is evaluated according to the SN curve for total-life. Specimen with cylindrical geometry were manufactured for rotating bending ($R = -1$) and tensile ($R = 0$) fatigue tests according to standards [9] [10]. Both geometries are illustrated in Fig. 36.2. The diameter D of specimen A is 5 mm, whereas specimen B has a diameter equal to 4 and 6 mm. Both geometries have a reduction radius, R ensuring there is no stress concentration effect. Specimens B have a length L greater than 10 mm.

Table 36.1 Chemical composition of spring steel and comparison with standard values (% weight)

	C	Si	Mn	P	S	Cr	V
Measured	0.462	0.347	0.914	0.0113	0.0126	0.970	0.131
Values	± 0.001	± 0.003	± 0.003	± 0.0009	± 0.0007	± 0.002	± 0.001
DIN 51CrV4	0.47–0.55	≤ 0.40	0.70–1.10	≤ 0.025	≤ 0.025	0.90–1.20	≤ 0.10 –0.25

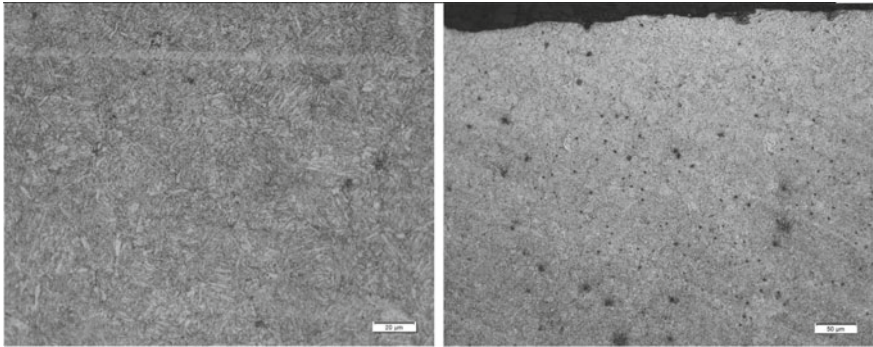


Fig. 36.1 51CrV4 Microstructure left in the core; right in the surface

Table 36.2 Mechanical properties: monotonic, hardness, and impact

	E (GPa)	$\sigma_{0.2}$ (MPa)	σ_{uts} (MPa)	ε_f (%)	RA_f (%)	HV	Charpy-V (J)
Measured	202.1	1258.6	1414.0	7.97	48.07	424.3	10.9
Values	± 5.2	± 51.0	± 63.6	± 0.608	± 30	± 7.07	± 1.45
DIN 51CrV4	200	1200	1350–1650	6	30	–	8

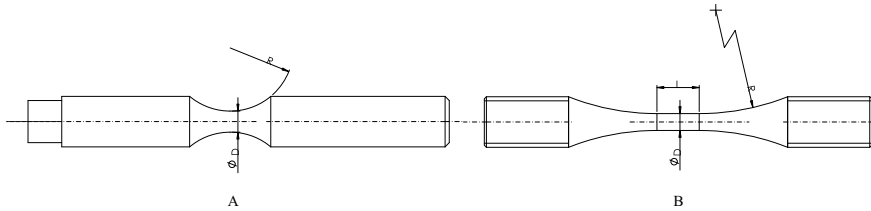


Fig. 36.2 The geometry of specimens used for fatigue tests: **a** Rotating bending ($R = -1$), **b** tensile ($R = 0.1$)

Fatigue test outcomes for total-life approach are usually described in terms of SN curves. SN curves are usually described such that the stress amplitude, σ_a is a function of the number of cycles to failure, N_f as written:

$$\sigma_a = C N_f^n, \tag{36.1}$$

Fatigue Failure of 51CrV4 Steel under Rotating Bending and Tensile.

where C and n are respectively the coefficient and exponent of the curve, and they are given by:

$$C = (10^{\beta_0/\beta_1}), n = (\beta_1)^{-1}, \tag{36.2}$$

The estimation of the average SN curve can be given by linear regression model, such that [8]:

$$\mathbf{Y} = \beta_0 + \beta_1 \mathbf{x}, \quad (36.3)$$

where y_i is the value of the dependent variable, and x_i , the value of independent variable. The elements of vector \mathbf{x} and \mathbf{Y} are transformed quantities by logarithmic, such that $\sigma_{a,i}$ and $N_{f,i}$ are respectively $x_i = \log \sigma_{a,i}$ e $y_i = \log N_{f,i}$. The fitting parameters, β_0 e β_1 are computed as:

$$\hat{\beta}_0 = \bar{Y} - \hat{\beta}_1 \bar{x}, \hat{\beta}_1 = \frac{n \sum_{i=1}^n y_i x_i - (\sum_{i=1}^n y_i)(\sum_{i=1}^n x_i)}{n \sum_{i=1}^n x_i^2 - (\sum_{i=1}^n x_i)^2} \quad (36.4)$$

with \bar{Y} and \bar{x} denoting the sample expected values for dependent and independent random variables. Note that the linear regression model does not consider run-outs obtained in fatigue tests.

36.3 Results and Discussion

As aforementioned, the analysis of fatigue results is based on the classical SN model for specimens A and B. As the results are documented, a discussion is carried out referring to the fracture surfaces analyzed according to SEM technology.

Figure 36.3 includes red and blue regression curves for rotating bending, RB curve, and tensile, T curve, respectively. Curve T presents a larger dispersion in fatigue life than the RB curve. This is easily explained after measuring the surface roughness. According to roughness results, RB specimens have $0.6394 \pm 0.1200 \mu\text{m}$ whereas T specimens have $0.7120 \pm 0.3596 \mu\text{m}$. The highest surface roughnesses are $0.9203 \mu\text{m}$ e $1.7833 \mu\text{m}$ for RB and T specimens, respectively. That is, the spring steel is highly sensitive to the surface state (Fig. 36.4).

Fatigue Failure of 51CrV4 Steel under Rotating Bending and Tensile (36.5)

Analyzing the regression parameters, β_0 and β_1 , one verifies that with the mean stress increases and loading changes from bending to tensile, the slope tends to be slightly superior. A summary of results is presented in Table 36.3.

Now, analyzing the failure modes, we verified that under rotating bending, all failures have initiated at the free surface (numbers 1 and 2). On the other hand, under tensile conditions, failure has initiated at free surface (number 3) or at non-metallic inclusions (for two samples, marked with numbers 4 and 5) for $1\text{E}+06$ cycles. Rotating bending strength appears to have clearly a fatigue limit of 600 MPa for values greater than $1\text{E}+07$ cycles. In tensile conditions, run-outs can occur for stress values

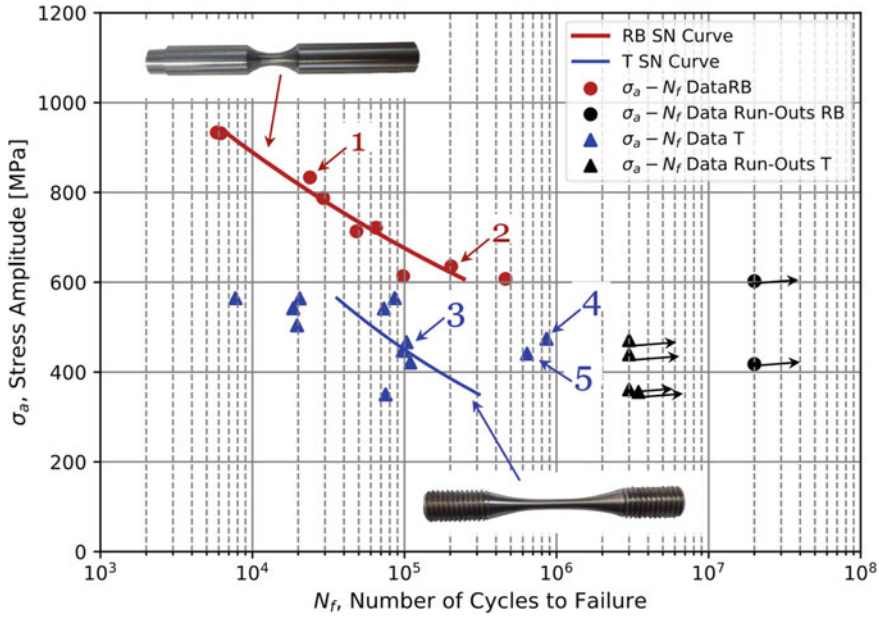


Fig. 36.3 SN curve for rotating bending and tensile loading conditions obtained from a regression linear model. Numeration of some failure modes verified

equal to them in which crack initiation at non-metallic inclusion occurred. However, if the quality of the surface is bad, failure can occur early.

36.4 Conclusions

Throughout this research work the specimens tested in rotating bending and tensile conditions exhibit high dispersion in results due to surface roughness. Roughness surface analysis suggests this dispersion is strongly influenced by the surface quality and then the quenched and tempered spring steel 51CrV4 is highly sensitive to micro-notches. Fracture analysis suggests that crack initiation takes place preferably at free surface. However, for materials with internal inclusions with size greater than their critical value, the initiation begins around them leading to failures.

Posterior researches will consist of the quantification of the sensitivity of material for notches, and the determination of critical sizes of the evaluated inclusions. Moreover, an analysis of the mean stress effect in the fatigue resistance will be also reported.

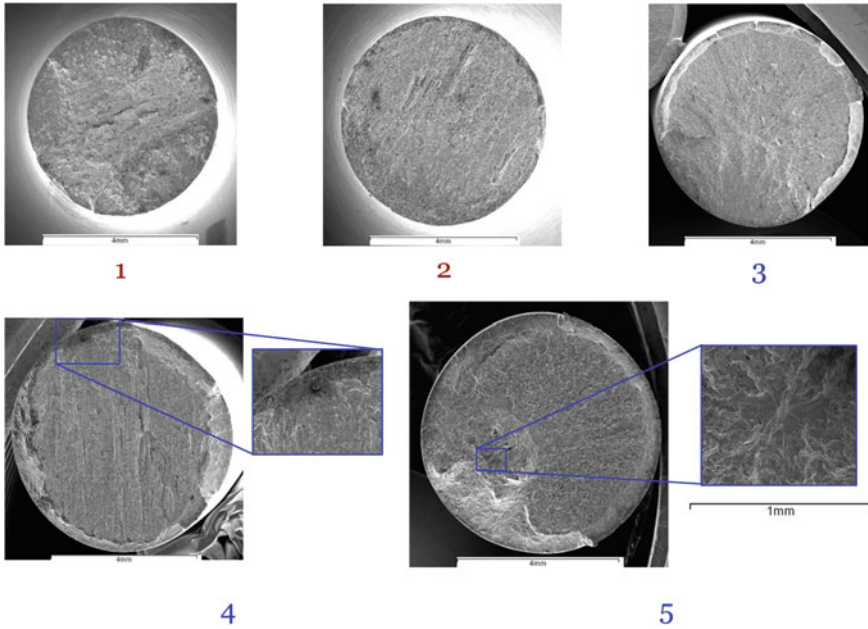


Fig. 36.4. Illustration of failure modes verified from rotating and tensile fatigue tests. Number 1 and 2—Rotating bending condition—Crack initiation at free surface; Number 3—Tensile condition—Crack initiation at free surface; Number 4 and 5—Tensile Condition—Crack initiation at non-metallic inclusion

Table 36.3 Summary of SN Curve parameters

Load condition	R_σ	β_0	β_1	Coefficient C	Exponent n	σ_{uts}	Ra (μm)
Rotating bending	-1	28.74	-8.39	2666.18	-0.12	1412.0 ± 61.1	0.6394 ± 0.1200
Tensile	0.1	16.96	-4.51	5783.92	-0.22	1429.7 ± 56.8	0.7120 ± 0.3596

Acknowledgements The authors thank to its industrial partner, MEDWAY (Maintenance and Repair), and the Doctoral Programme iRail- Innovation in Railway Systems and Technologies funding by the Portuguese Foundation for Science and Technology, IP (FCT) through the PhD grant (PD/BD/143141/2019).

References

1. TE Neg'ocios. <https://www.transportesenegocios.pt/transportesconcentrammetade-do-pni-2030>. Last accessed 31 Oct 2020
2. UIC, U. of Railways, Wagons—suspension gear—standardization, (2007)

3. Kumbhalkar MA, Bhope DV, Vanalkar AV, Chaoji PP (2018) Failure analysis of primary suspension spring of rail road vehicle. *J Fail Anal Preven* 18:1447–1460. <https://doi.org/10.1007/s11668-018-0542-1>
4. Kumar VA, Karthikeyan MK, Gupta RK, Ramkumar P, Prakash MU (2015) Heat treatment studies on 50CrV4 spring steel. *J Fail Anal Preven* 830831:139–142. <https://doi.org/10.4028/www.scientific.net/MSF.830-831.139>
5. European Committee for Standardization (CEN) (2009) Metallic materials—tensile testing—part 1: method of test at room temperature. EN ISO 6892-1
6. ASTM International, Standard Test Methods for Vickers Hardness and Knoop Hardness of Metallic Materials. ASTM E92-17 (2017)
7. European Committee for Standardization (CEN) (1983) Steel—Charpy impact test (Vnotch). EN ISO 6892-1
8. ASTM International (2014) Standard practice for statistical analysis of linear or linearized stress-life (S-N) and strain-life (ϵ -N) Fatigue Data. Annual book of ASTM standards, vol 3, no(1), pp 1–7
9. International Standard (2010) Metallic materials—rotating bar bending fatigue testing. ISO 1143
10. ASTM International (2015) Standard practice for conducting force controlled constant amplitude axial fatigue tests of metallic materials. ASTM International. <https://doi.org/10.1520/E0466-15>

Chapter 37

The Role of the Surface in Crack Initiation in Sharp and Bi-material Notches



Jan Klusák  and Dalibor Kopp

Abstract The study deals with description of stress distribution and conditions of crack initiation in sharp and bi-material notches. Particularly, it uses 3D numerical models of the notches and focuses on stress conditions along the notches fronts, especially near the free surface. The study describes how free surface influences the stress conditions along the notches fronts and whether crack initiates in a central or in a surface layer of the model. It can be shown that some geometries of the notches lead to crack initiation in the central layer, some of them lead to crack initiation in the surface layer, and some notches exhibit stress distribution leading to almost the same probability of crack initiation along whole notch front. The criterion of average tangential stress is used to distinguish the place of failure initiation.

Keywords Crack initiation · Stability of notches · The influence of surface · Generalized fracture mechanics

37.1 Introduction

37.1.1 Background

Sharp and bi-material notches occur in engineering components. Sharp notches are induced by requirements on a shape of components and structures. Bi-material notches are often related to components for electrical equipment (wire-insulator connection), or in civil engineering (steel-concrete junction). Such notches lead to stress concentrations, to an initiation of a crack, and consequently to a failure of whole component or structure.

In the following, stress state is studied in the vicinity of the notch tip. The stress is monitored along the notch front in order to describe the influence of free surface. Based on the detailed description of stress distribution, crack initiation conditions

J. Klusák (✉) · D. Kopp
Institute of Physics of Materials, Czech Academy of Science, Žitkova 513/22, 616 00 Brno,
Czech Republic
e-mail: klusak@ipm.cz

can be estimated. Particularly, by means of precise 3D models, we have studied whether a crack initiates in the middle of the specimen or near the free surface. Thus, the role of the free surface in the process of crack initiation can be assessed and described. Figure 37.1 shows geometry of sharp and bi-material notch. In the case of homogeneous notch, materials 1 and 2 are considered to be equal.

37.1.2 Crack Initiation Criterion

According to the approaches of generalized fracture mechanics of notches, conditions of crack initiation are associated with reaching a critical value of a controlling quantity [1]. We have used an average value of tangential stress $\overline{\sigma_{\theta\theta}}(\theta)$ evaluated ahead of the notch front:

$$\overline{\sigma_{\theta\theta}}(\theta) = \frac{1}{d} \int_0^d \sigma_{\theta\theta}(r, \theta) dr, \quad (37.1)$$

Assumed crack initiation direction corresponds to the direction θ of the maximum of average tangential stress. The level of the critical applied loading stress depends on the critical opening stress determined from a fracture characteristic of the material where the crack initiation is expected [2]. In the case of bi-material notch, there are the materials 1, 2, and the interface 0 between the materials. The critical value of the average tangential stress is:

$$\overline{\sigma_{\theta\theta c,m}} = \frac{2K_{c,m}}{\sqrt{2\pi d}}, \quad (37.2)$$

where $K_{c,m}$ is the fracture characteristic of the material m (where $m = 1, 2, 0$) and it is represented by the fracture toughness K_{Ic} for brittle fracture or by the threshold value K_{Ith} for fatigue crack initiation during cyclic loading, and d represents the averaging distance.

The absolute value of average tangential stress, induced around and along the notch front, directly depends on the level of the applied loading stress σ_{appl} and is numerically calculated in dependence on the polar coordinate θ . The direction, where the average value of tangential stress is maximal, corresponds to the direction of potential crack initiation. This direction is denoted $\theta_{0,m}^{\text{notch}}$. The average tangential stress in this direction is $\overline{\sigma_{\theta\theta}}(\sigma_{\text{appl}}, \theta_{0,m}^{\text{notch}})$. Finally, the critical value of applied stress is determined as:

$$\sigma_{\text{appl,c,m}} = \overline{\sigma_{\theta\theta c,m}} \frac{\sigma_{\text{appl}}}{\overline{\sigma_{\theta\theta}}(\sigma_{\text{appl}}, \theta_{0,m}^{\text{notch}})}. \quad (37.3)$$

The crack initiation criterion can be formulated in the following form:

$$\sigma_{\text{appl}} > \sigma_{\text{appl},c,m}$$

A crack is initiated in the notch if the applied loading is greater than its critical value. The crack initiation is a local phenomenon. It is initiated in the place of the highest opening stress. We have studied distribution of tangential opening stress along the notches fronts. It can be shown, that the distribution of the tangential stress is influenced by the free surface. The tangential stress can increase or decrease toward the free surface. The critical applied stress depends on the average tangential stress; see the Eq. (37.3). Thus, the critical applied stress, at which a crack is initiated in particular location, can be calculated as a function of z coordinate (along the notch front). Then the crack initiation occurs in the place of the lowest critical applied stress $\sigma_{\text{appl},c,m}(z)$.

37.2 Comparison of Sharp and Bi-material Notches

37.2.1 Numerical Calculation of the Stress Distribution

The distribution of tangential stress around and along the notch front is calculated in finite element system ANSYS with highly refined mesh near the notch front and the surface (the smallest element size is about $1 \mu\text{m}$). Only half of the specimen has been modeled with the use of symmetry layer, see Fig. 37.1.

We have analyzed opening stress distributions around and along homogeneous and bi-material notches. Typical stress distributions (average tangential stress) in the

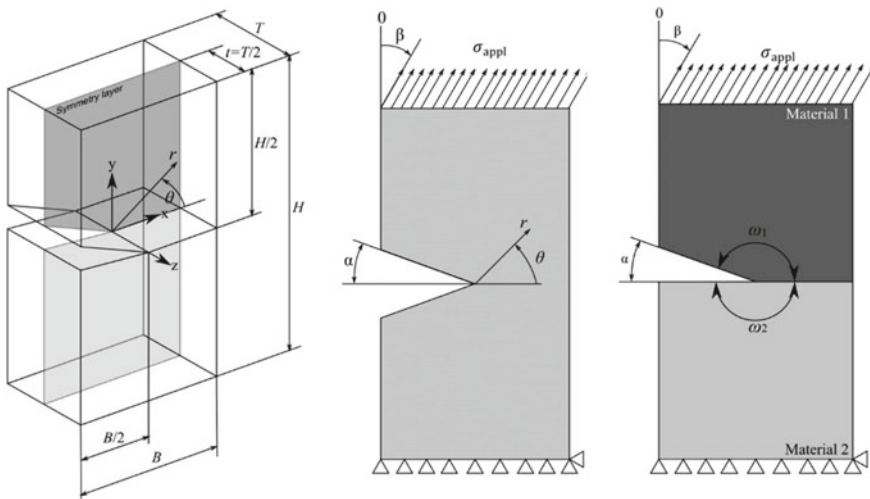


Fig. 37.1 3D model of the specimen (left) with sharp (in the middle) or bi-material (right) notch

vicinity of sharp and bi-material notches are shown in Fig. 37.3. Note that the case of bi-material notch is represented here by the ratio of Young’s moduli $E_1/E_2 = 0.1$ and the thickness of the specimen is $T = 2$ mm, so the coordinate $z = 1$ mm corresponds to the free surface.

It is apparent that the surface influence is different in the cases of homogeneous and bi-material notches. While in the case of a homogeneous material, the surface usually acts as a retarder to initiate the crack, in the case of bi-material notch it may work the other way around. Particular situation depends on the Young’s moduli ratio and on the notch opening angle. The steep peak of tangential stress near the surface (as shown in Fig. 37.3 (right)) is observed for bi-material notches with significant mismatch of elastic moduli E_1 and E_2 and with large notch opening angles (Fig. 37.2).

Then the distribution of critical applied stress is calculated from the average tangential stress based on Eq. (37.3). Typical distributions of critical applied stresses are shown in Fig. 37.4 for homogeneous (left) and bi-material (right) notches. It is apparent that the local increase of tangential stress leads to local decrease of the

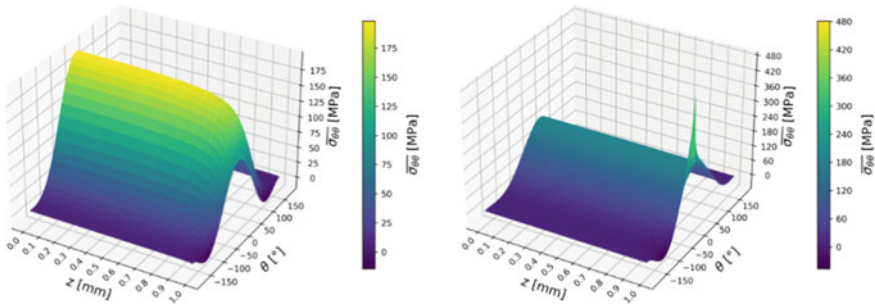


Fig. 37.2 The distribution of average tangential stress around a notch front with opening angle $\alpha = 5^\circ$, $T = 2$ mm in homogeneous material (left), and a bi-material notch front (right)

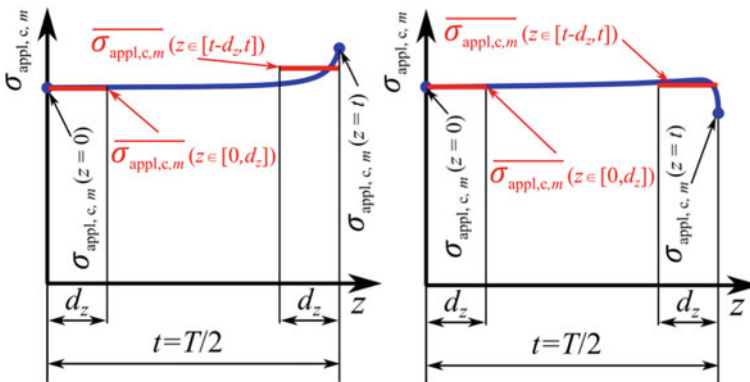


Fig. 37.3 Analysis of critical applied stress along the notch front in homogeneous material (left), and a bi-material configuration (right)

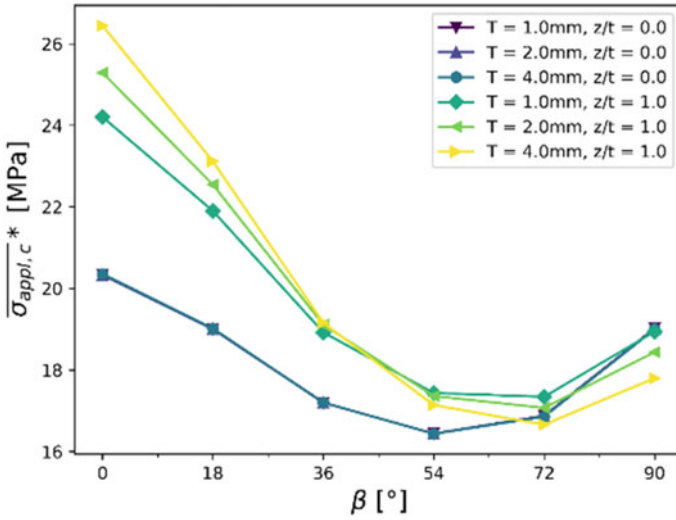


Fig. 37.4 Average critical applied stress for homogeneous notch with $\alpha = 5^\circ$, $z/t = 0$ and $z/t = 1$, and $T = 1, 2$ and 4 mm

critical applied stress and vice versa. Further, we can see, that the peak of average tangential stress near the surface of bi-material notch is meaningfully localized and it leads to the sudden drop of the critical applied stress. The lowest values of $\sigma_{\text{appl},c}$ in $z = t$ would indicate a crack initiation at the surface layer. Nevertheless, the size of the drop area is really small (typically less than $10 \mu\text{m}$), which may not be enough to initiate the crack. Based on this, we evaluate an average value of critical applied stress $\overline{\sigma_{\text{appl},c}}(z)$, in the direction of the coordinate z . The averaging distance in z -direction is d_z and it is chosen as $d_z = 0.1 \text{ mm}$. The choice of the distance d_z is subjected to similar requirements as the averaging distance d . It corresponds to the assumed crack initiation increment (therefore, it depends on crack initiation mechanism), it can be related to a size of a microstructural element (grain size), etc. The distance can also be estimated via the approaches known from literature [3–5].

The values of average critical applied stresses in the middle (37.4) and at the surface (37.5) of the model can be expressed in the following form:

$$\overline{\sigma_{\text{appl},c,m}}(z \in [0, d_z]) \doteq \sigma_{\text{appl},c,m}(z = 0) = \overline{\sigma_{\text{appl},c,m}}(z/t = 0) \tag{37.4}$$

$$\overline{\sigma_{\text{appl},c,m}}(z \in [t - d_z, t]) = \frac{1}{d_z} \int_{t-d_z}^t \sigma_{\text{appl},c,m} dz = \overline{\sigma_{\text{appl},c,m}}(z/t = 1) \tag{37.5}$$

in the middle of the sample, the average value can be considered the same as the current value in the sample (37.4). For simplicity, we can denote the values in (37.4)

as $\overline{\sigma_{\text{appl},c,m}}(z/t = 0)$ and in (5) as $\overline{\sigma_{\text{appl},c,m}}(z/t = 1)$. The values of $\overline{\sigma_{\text{appl},c,m}}(z)$ ascertained for the middle and for the surface layer of the sample are compared, where the lower one indicates the crack initiation place. Note that in the case of bi-material notch, the values of $\overline{\sigma_{\text{appl},c,m}}$ must be evaluated in all materials regions ($m = 1, 2, 0$) and the critical applied stress corresponds to the least of them:

$$\sigma_{\text{appl},c} = \min\{\overline{\sigma_{\text{appl},c,m}}(z)\} \quad (37.6)$$

The average value of critical applied stress allows to assess whether a crack initiates in the middle or in the surface layer of the specimen. By the choice of the averaging distance, we can include the mechanism of failure (brittle fracture or fatigue crack initiation) into evaluation. The average value of critical applied stress eliminates the influences of local peaks of stresses that occur in very small areas and are not able to lead to crack initiation and propagation. These circumstances can be captured by the choice of the averaging distance. Smaller distance d_z is more sensitive to local peaks of stress, while greater d_z reduces the influence of local stress changes and allows to adjust the theoretical model to real behavior of materials. By means of the approach described above, the average critical applied stress was locally analyzed. Most of the cases of sharp and bi-material notches lead to crack initiation in the middle of specimens or the stress distribution along notch front provides almost equal probability of crack initiation along whole notch front. This means that the free surface acts as a retarder for crack initiation. It corresponds to the behavior of a crack in homogeneous material, where the free surface causes curvature of the crack front [6]. In the case of sharp notches, only the inclined loading with the direction β of about 90° can lead to crack initiation in the surface. See Fig. 37.4 where the curves of the average critical applied stress for $z/t = 1$ are above the curves for $z/t = 0$ for almost whole range of β . Only for $\beta = 72$ and 90° the curves for $z/t = 1$ fall below the curves valid for $z/t = 0$. Similarly, in the case of bi-material notches, surface crack initiation is observed for significant mismatch of elastic moduli ($E_1/E_2 = 0.2, 0.1$ or less) and for larger opening angles α . In the case of bi-material notches, the surface crack initiation is caused by the drop of the critical applied stress under the surface, see Fig. 37.5.

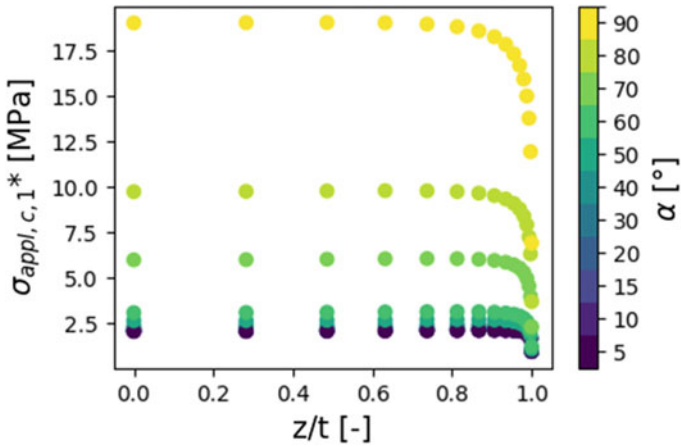


Fig. 37.5 Critical applied stress for bi-material notch with $E_1/E_2 = 0.1$ and α from 5 to 90°

Acknowledgements The research was supported by the Czech Science Foundation through the project No. 20-00761S.

References

1. Klusák J, Krepl O, Profant T (2019) An easy and engineering stability criterion of general singular stress concentrators. *Theor Appl Fract Mech* 104:102341
2. Knésl Z (1991) A criterion of V-notch stability. *Int J Fract* 48(4):R79–R83
3. Leguillon D (2002) Strength or toughness? A criterion for crack onset at a notch. *Eur J Mech A/Solids* 21(1):61–72
4. Cornetti P, Pugno N, Sapora A, Taylor D (2006) Finite fracture mechanics: a coupled stress and energy failure criterion. *Eng Fract Mech* 73(14):1736–1752
5. Taylor D (2017) The theory of critical distances: A link to micromechanisms. *Theoret Appl Fract Mech* 90:228–233
6. Hutář P, Náhlík L, Knésl Z (2010) The effect of a free surface on fatigue crack behaviour. *Int J Fatigue* 32(8):1265–1269

Chapter 38

Experimental Study on Failure Mechanisms of Novel Visco-Hyperelastic Material Target Under Ballistic Impact Conditions



Pawel Zochowski, Marcin Cegla, Marcin Bajkowski, Roman Grygoruk, Mariusz Magier, Krzysztof Szczurowski, Jędrzej Maczak, Mirosław Bocian, Roman Gieleta, and Krzysztof Jamroziak

Abstract The main aim of the study was to define the static and dynamic properties of novel visco-hyperelastic material and its behavior under 7.62×25 mm Full Metal Jacket (FMJ) projectile impact condition. Mechanical tests were performed in both quasi-static and dynamic conditions. Uniaxial quasi-static compression tests were performed at different temperatures in order to characterize the influence of thermal effects on the plastic flow of the material. The Split Hopkinson Pressure Bar (SPHB) apparatus was used to assess strain rate sensitivity of the novel material. Residual velocity of projectiles (after perforation of the target) was recorded during the test allowing to evaluate energy absorption and dissipation capability of the visco-hyperelastic layer. The material is intended to be used in different ballistic applications such as projectile catching systems and anti-ricochet layers covering walls of shooting ranges, ballistic tunnels.

Keywords Ballistic impact · Numerical simulation · Failure

P. Zochowski · M. Cegla

Military Institute of Armament Technology, Wyszyńskiego 7, 05-220 Zielonka, Poland

M. Bajkowski · R. Grygoruk · M. Magier

Institute of Mechanics and Printing, Faculty of Mechanical and Industrial Engineering, Warsaw University of Technology, Narbutta 85, 02-524 Warsaw, Poland

K. Szczurowski · J. Maczak

Institute of Vehicles, Faculty of Automotive and Construction Machinery Engineering, Warsaw University of Technology, Narbutta 84, 02-524 Warsaw, Poland

M. Bocian · K. Jamroziak (✉)

Department of Mechanics, Materials Science and Engineering, Faculty of Mechanical Engineering, Wrocław University of Science and Technology, Smoluchowskiego 25, 50-370 Wrocław, Poland

e-mail: krzysztof.jamroziak@pwr.edu.pl

R. Gieleta

Faculty of Mechanical Engineering, Military University of Technology, Kaliskiego 2 St., 00-908 Warsaw, Poland

38.1 Introduction

Hyperelastic rubber-like materials have been widely used in various engineering applications. Specific features of those materials makes them very effective when used as damping layers or shock absorbers [1–4]. Efficiency of hyperelastic tissue simulants was confirmed in numerous studies of ballistic impact phenomenon [5–7]. When hyperelastic materials are included in the study they become even more complicated due to high elastic recovery of rubbers and temporary character of their deformations. Rubbers and gels can significantly deform under mechanical load and return to their nearly original shape when the load is removed. The rubber-like materials show a highly non-linear stress-strain-deformation relationship in the deformation range above 5%. Even with the use of sophisticated measuring techniques the amount of information that can be collected during ballistic tests on rubber-like materials is often significantly limited due to the nature of the phenomenon and properties of materials. Firstly, the mechanical experiments characterizing the response of the material to the applied loads in a wide range of strain rates were carried out.

38.2 Material Characterization Tests

38.2.1 *Quasi-Static Compression Tests*

The novel material is a elastomer based on modified silicones. The material density is about 900 kg/m^3 . First of all, compressive response of the target material (conditioned at 293 K) at quasi-static strain rates was examined. Cylindrical samples of 20 mm in height and 19.5 mm in diameter were tested. Tests were registered with a camera in order to record the values of specimens diameter that was changing together with the movement of jaws due to the barreling effect caused by friction at specimen/jaws interfaces. The tests of the mechanical properties of the projectile and target materials were carried out on a Zwick Z100 universal testing machine with a hydraulic drive. The compression process was shown in Fig. 38.1.

The results of quasi-static compression tests of the target material were shown in Fig. 38.2. The actual stresses and strains determined in this way were affected with some errors (omission of the value of correction methods, e.g. by the Bridgmann correction coefficient). However, the influence of these errors on the behavior of numerical models of materials was checked during the validation process.

38.2.2 *Dynamic Compression of Hyperelastic Target Material*

The samples from the visco-hyperelastic material were cut with a waterjet cutting machine and then milled to the required thickness. Samples for SHPB tests were made

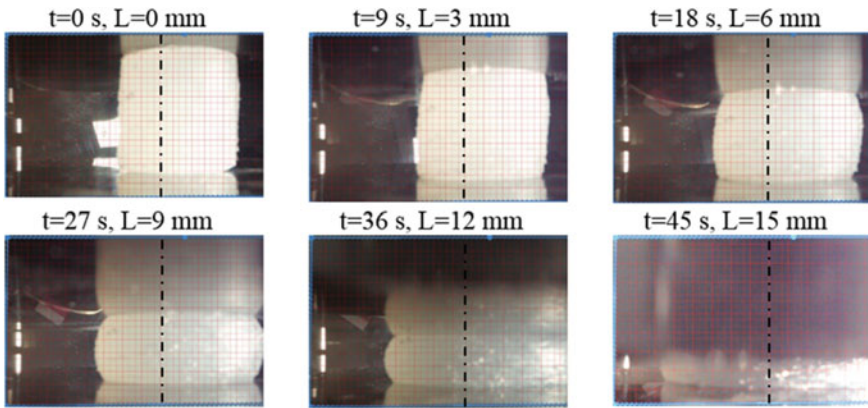


Fig. 38.1 The chosen result of the compression process

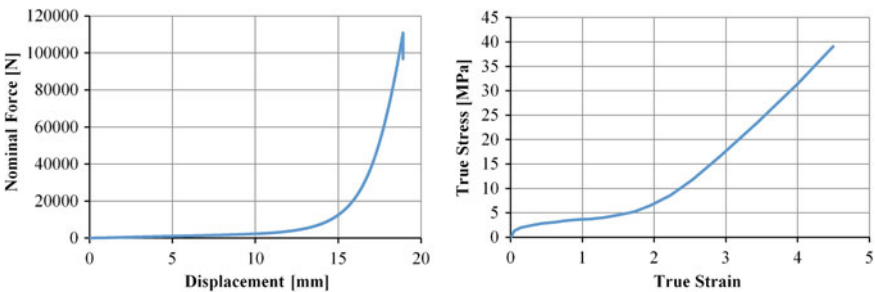


Fig. 38.2 The graphs of the nominal force versus displacement (left) and true stress versus true strain (right)

in the form of disks with the diameter $D = 23$ mm and two different thicknesses $L = 3$ and 1.5 mm. This allowed different strain rates to be obtained.

Experimental compression tests at high strain rates were performed on the conventional SHPB apparatus (see Fig. 38.3).

The apparatus consists of a gas gun, incident and transmission bars (both 2000 mm long) made of V720 maraging steel, an energy absorber, a data acquisition system and a control system. The striker is launched using compressed gas (argon) and impacts the incident bar. The details of this technique are included in [8, 9]. Waves in the incident and transmission bars are sensed by strain gauges (EA-06-060LZ-120, Vishay, USA) which are placed in the middle of the bars. In order to measure pressure bar signals, strain gauges connected in a half bridge configuration are used. The signals from the strain gauges (the Wheatstone bridges) are conditioned with a transient amplifier LTT 500 (LTT Labortechnik Tasler GmbH, Germany) and recorded with a computer and high-speed A/D computer board NI USB-6366 (National Instruments, USA). In the described apparatus, the amplifier and the A/D computer board with

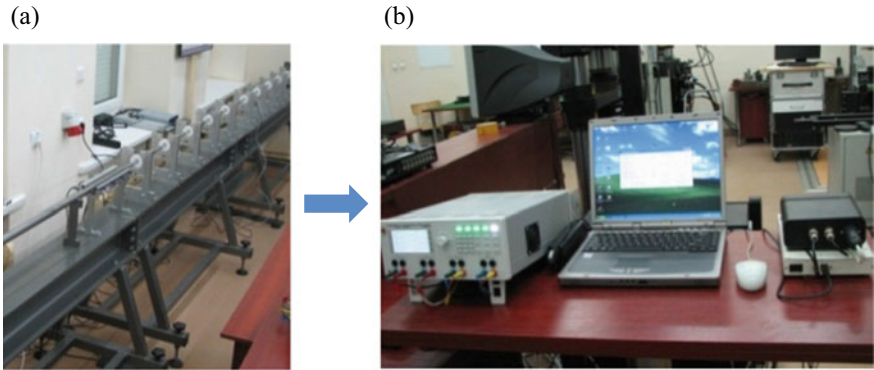


Fig. 38.3 Stand for testing materials at high strain rates: **a** Hopkinson bar system, **b** computer control system

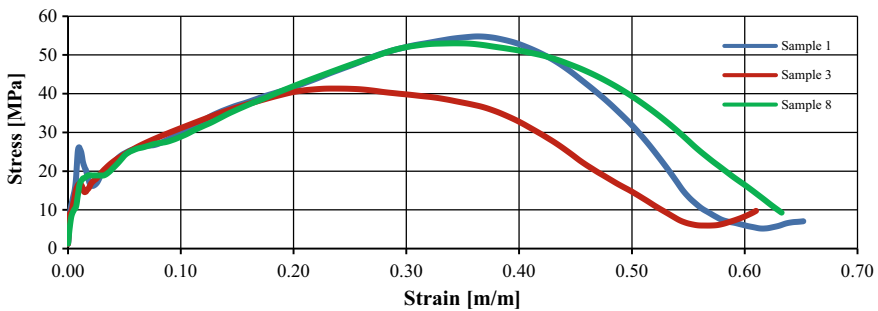


Fig. 38.4 Results of the compression test under high strain rate conditions

1 MHz frequency response are used what allows for accurately recording the transient signals from the strain gauges of the SHPB apparatus. During experimental investigations striker velocities were about 14.0 m/s. Pulse shaping technique was used to shape the profile of the incident pulse. Disks made of rubber with $D = 8$ mm and $L = 2$ mm were used as pulse shapers. An exemplary graph obtained in the compression test under high strain rate conditions for chosen samples was shown in Fig. 38.4.

38.3 Ballistic Impact Experiments

The behavior of the hyperelastic target material under high strain rate conditions including failure was analyzed during the ballistic impact tests. The scheme of the test stand was shown in Fig. 38.5. Several variants of hyperelastic target with various thickness were tested. The projectile was fired from a ballistic barrel placed in a holder

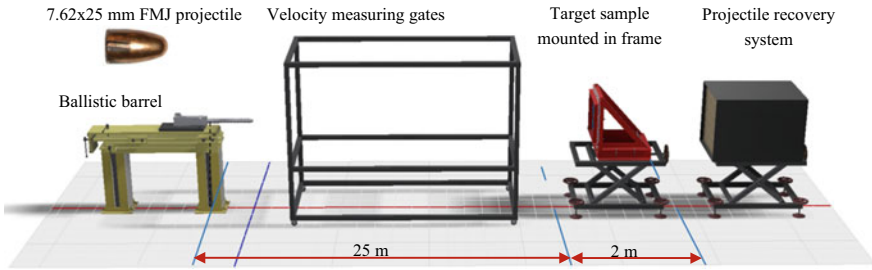


Fig. 38.5 The scheme of the ballistic impact test

on a metal platform fixed to the ground. During the ballistic impact tests, the distance between the ballistic barrel and the sample was $L = 25$ m. The axis of the barrel was perpendicular to the surface of the sample in a vertical and horizontal plane. The sample was mounted in the holder and its edges were fixed by the clamp of the frame (internal dimensions of 200×200 mm) tightened with screws. A projectile recovery system was set up at a distance of 2 m behind the sample surface in order to catch the projectiles after perforating the samples. The velocity of the projectile in front of the target was measured by measuring gates. Doppler radar was used to measure residual velocity of projectile after perforation of the target. The results of the ballistic experiments of the 7.62×25 mm FMJ projectile impact into plastic targets were shown in Table 38.1 and Fig. 38.6. Three shots were performed for each of target

Table 38.1 Results of ballistic impact experiments

Target thickness, (mm)	0	10	20	30	80	140	180	220
Residual velocity of projectile, (m/s)*	450	441.5	432.8	426.4	373.2	124.3	45.6	0

* average value from 3 trials

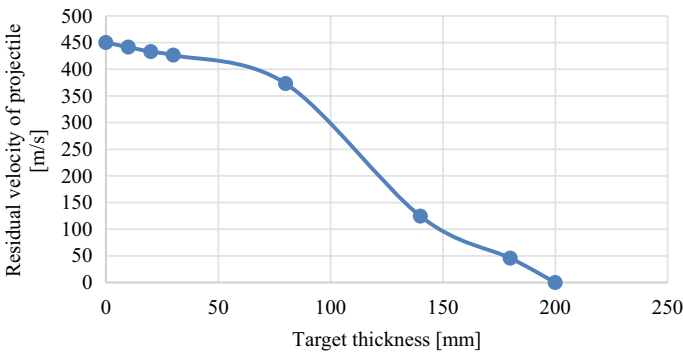
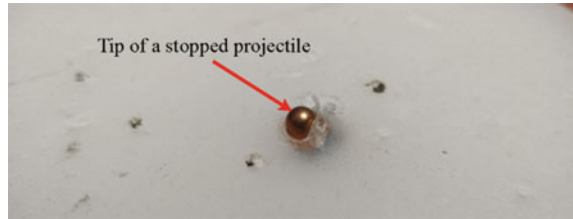


Fig. 38.6 The graph of the residual velocity versus target thickness

Fig. 38.7 The example of the 220 mm target deformation after projectile's stopping



variant. The dimensions of the deformed projectiles and their residual velocities after in case of perforation of the target were measured after impact (Fig. 38.6).

Deformations of the targets after the projectile impact were shown in Fig. 38.7.

38.4 Conclusions

Various types of experimental tests were carried out in order to determine the response of the novel visco-hyperelastic target to specific loads as well as to define the initial parameters to the numerical model. The plastic behavior at high strain rates was examined, as well as the mechanisms of the material failure depending on the thickness of the layer was analyzed. Residual velocity of projectiles (after perforation of the target) was recorded during the test allowing to evaluate energy absorption and dissipation capability of the plastic layer. On the basis of the data collected during experimental tests the numerical models of 7.62×25 mm FMJ projectile and the novel visco-hyperelastic target will be defined. The models will be used in numerical simulations reproduced the experiments performed in the future.

References

1. Yang H, Yao X, Zheng Z, Gong L, Yuan L, Yuan Y, Liu Y (2018) Highly sensitive and stretchable graphene-silicone rubber composites for strain sensing. *Compos Sci Technol* 167:371–378
2. Pouriaeyali H, Guo Y, Shim V (2011) A visco-hyperelastic constitutive description of elastomer behaviour at high strain rates. *Procedia Eng* 10:2274–2279
3. Tubaldi E, Mitoulis S, Ahmadi H (2018) Comparison of different models for high damping rubber bearings in seismically isolated bridges. *Soil Dyn Earthq Eng* 104:329–345
4. Yang H, Yao X-F, Wang S, Ke Y-C, Huang S-H, Liu Y-H (2018) Analysis and inversion of contact stress for the finite thickness Neo-Hookean layer. *J Appl Mech* 85(10):101008
5. Mabbott A, Carr DJ, Champion S, Malbon C, Tichler C (2013) Comparison of 10% Gelatine, 20% Gelatine and Perma-Gel™ for Ballistic Testing. In: *Proceedings of international symposium on ballistics*, pp 648–654. Lancaster, Freiberg
6. Kalcioğlu ZI, Qu M, Strawhecker KE, Shazly T, Edelman E, VanLandingham MR, Smith JF, Van Vliet KJ (2011) Dynamic impact indentation of hydrated biological tissues and tissue surrogate gels. *Phil Mag* 91(7):1339–1355

7. Bracq A, Haugou G, Delille R, Lauro F, Roth S, Mauzac O (2017) Experimental study of the strain rate dependence of a synthetic gel for ballistic blunt trauma assessment. *J Mech Behav Biomed Mater* 72:138–147
8. Chen W, Song B (2011) Split Hopkinson (Kolsky) Bar. Design, testing and applications, Springer
9. Sharpe WN (2008) Springer handbook of experimental solid mechanics. Springer.
10. Banaszkiwicz M (2016) Analysis of rotating components based on a characteristic strain model of creep. *J Eng Mater Technol Trans ASME* 138(3):031004-1–11
11. Banaszkiwicz M (2019) Creep life assessment method for online monitoring of steam turbine rotors. *Mater High Temp* 36(4):154–367
12. Zeiler G, Bauer R, Putschoegl A (2010) Experiences in manufacturing of forgings for power generation application. *La Metallurgia Italiana* 6:33–40
13. IEC 60045-1 (2020) Steam turbines—part 1: Specifications. International Electrotechnical Commission, 2nd edn

Part V
Structural Integrity and Fatigue
Assessment of Additive Manufactured
Metals and Biomaterials

Chapter 39

Fatigue Behavior of As-Built L-PBF Inconel 718 and Surface Roughness-Based Modeling



Gianni Nicoletto and Federico Uriati

Abstract Metal parts obtained by the layer-wise selective melting of a powder bed are characterized by surfaces that are considerably rougher than conventionally machined parts. Original fatigue data of L-PBF Inconel 718 obtained with specimens after individual surface roughness characterization demonstrates the considerable scatter and fatigue debit with respect to machined surfaces. Since in many engineering applications surface machining and polishing is not a viable solution, fatigue-critical applications of L-PBF Inconel 718 require an understanding of the link between surface quality and fatigue. A fatigue model accounting for the roughness-related stress concentration at as-built surface micronotches is presented and discussed.

Keywords Additive manufacturing · Inconel 718 · High cycle fatigue · Roughness · Fatigue model

39.1 Introduction

The powder bed fusion (L-PBF), one of the most promising metal additive manufacturing technologies, has reached a remarkably high level of development, and it is widely used in the production of metal parts of high geometrical complexity, [1]. Inconel 718 powder is one of the metal alloys that are successfully processed by L-PBF. However, L-PBF Inconel 718 parts show inferior fatigue strength compared to conventionally manufactured counterparts when tested with surfaces in the as-built condition [2]. Since in many engineering applications surface machining and polishing is not a viable solution, the use of L-PBF technology for producing fatigue-critical applications of Inconel 718 will be possible when a thorough understanding and control of the fatigue behavior of AM parts as a function of surface quality [3].

G. Nicoletto (✉) · F. Uriati
Department of Engineering and Architecture, University of Parma, Parma, Italy
e-mail: gianni.nicoletto@unipr.it

F. Uriati
e-mail: federico.uriati@unipr.it

Rough surfaces of L-PBF metals are affected by several phenomena including stair-stepping, balling, and attachment of partially bonded powder particles. Those undesired outcomes are directly related with many technological factors, such as powder quality, process parameters, layer thickness, and surface orientation with respect to growth direction. [4].

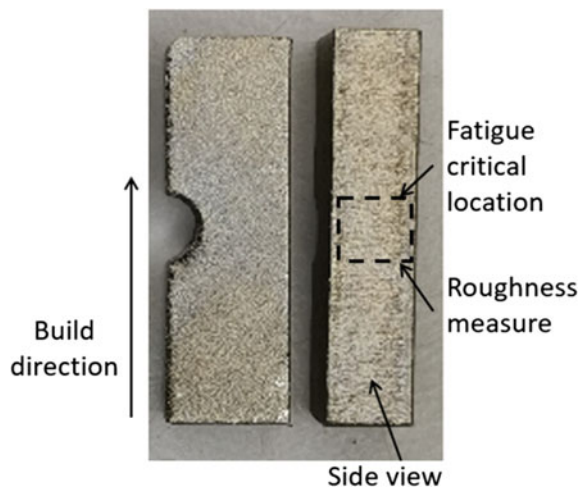
From the fatigue perspective, the as-built surface morphology will show notch-like features that serve as stress concentration sites where fatigue crack nucleation is favored even at relatively low stresses [2, 3]. This investigation presents original scattered fatigue data of L-PBF Inconel 718 specimens, each one characterized in terms of surface roughness.

The link between rough surfaces and fatigue performance has been sought using different modeling approaches, namely (i) finite element-based modeling of surface profiles stress calculations [5] and (ii) theoretical notch-based models [3]. Following the second approach, here, a fatigue model that accounts for the roughness-related stress concentration at as-built surface micronotches implements the theoretical solution for a half plane with sinusoidal profile in tension and a local plasticity correction.

39.2 Material and Experimental Details

A significant set of fatigue specimens of L-PBF Inconel 718 was produced on an SLM 500 system (SLM Solutions GmbH, Germany) working at a layer thickness $\lambda = 60 \mu\text{m}$. The specimen geometry, shown in Fig. 39.1, is miniaturized (22 mm long), prismatic and with minimum cross-section of $5 \times 5 \text{ mm}^2$, [6]. The long axis was oriented vertically with respect to the build plate.

Fig. 39.1 Fatigue specimen geometry and as-build reference surface



After removal from build plate, specimens were heat treated according to solution treatment plus an aging step. The solution consisted of heating up to a temperature of 954 °C and a soaking time of 1 h, while the aging treatment was divided into two steps, a first one at a temperature of 718 °C and a second at 621 °C, each of these steps lasting 8 h. The heat treatment optimized mechanical strength and drastically reduced residual stresses [2]. The reference static mechanical properties were the following: ultimate tensile strength $R_m = 1400$ MPa, yield stress $R_s = 1200$ MPa, and elongation to rupture $A\% = 17\%$ [3].

Before fatigue testing, the flat surface of each individual specimen (see, Fig. 39.1) was characterized in terms of ISO 4287 roughness parameters R_a ; R_q ; R_z ; R_t using a surface roughness tester SA6220 (SAMA Tools, Italy) with a 5 μm —radius probe tip.

Specimens were then fatigue tested under cyclic plane bending using a dedicated electromechanical testing machine working at a frequency of 25 Hz [6]. Testing was interrupted when crack initiation at the flat surface reduced the applied stress of 5% with respect to initial value or 2 10^6 cycles were reached without appreciable change in applied stress.

39.3 As-Built Fatigue Behavior of L-PBF Inconel 718

The plot of Fig. 39.2 shows data (σ_{max} vs. number of cycles to fatigue crack initiation) obtained in the experimental campaign. The S/N trend is characterized by significant scatter linked to surface roughness by symbol size as shown in the plot. Measured roughness of the individual specimens varied in the range $5 \mu\text{m} < R_z < 50 \mu\text{m}$. Qualitatively, high roughness values decrease observed fatigue lives for a given stress level.

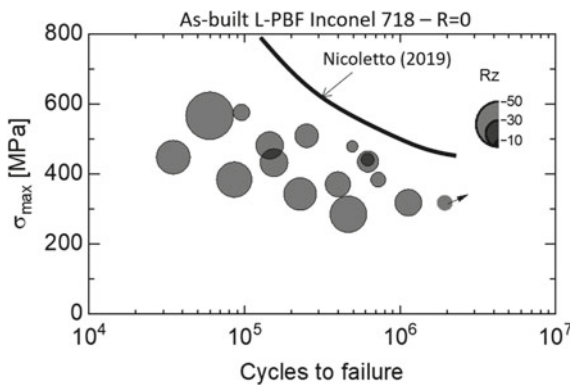


Fig. 39.2 Fatigue data of as-built IN718 (symbol size proportional to specimen roughness R_z)

The present data in Fig. 39.2 are compared with the previously published data of an Inconel 718 fabricated with an SLM280HL system (SLM Solutions GmbH, Germany) working at 50 μm layer thickness, [6]. The scatter in surface roughness was limited for that specimen set, that is, $R_z = 11.5 \pm 1.5 \mu\text{m}$. The present data reveal a considerably lower fatigue performance possibly because the present set of specimens was produced by a brand-new metal additive system operating at sub-optimal working conditions.

39.4 Roughness-Based Fatigue Modeling

A roughness-based fatigue model was developed to address the observed scatter of Fig. 39.2 and try and link it to individual surface roughness which varies significantly from specimen to specimen. The modeling considered two ingredients: (1) the analytical stress concentration factor K_t solution for a semi-infinite plane with a sinusoidal profile in remote tension, schematically represented in Fig. 39.3, [7]; (2) the elastic-plastic Neuber's correction approach for localized plasticity at a notch root [8].

The model originates from two considerations: (i) an as-built vertical surface is rough and formed by a regular series of valleys and peaks where the valleys act like periodic notches; (ii) periodic notches are characterized by a lower stress concentration when compared to the single notch case because of a shielding effect, [8]. The half plane with a sinusoidal profile in tension schematically shown in Fig. 39.3a is assumed representative for the study of the stress distribution in a material delimited by a rough surface due to layer-by-layer fabrication.

The magnified longitudinal profile of an as-built vertical specimen of Fig. 39.3b shows a periodicity with a valley spacing of approx. 120 μm (i.e., twice the layer thickness, $\lambda = 60 \mu\text{m}$). Therefore, the sinusoidal pitch $d = 120 \mu\text{m}$ is assumed. The other characteristic geometrical parameter is the total height l of the sinusoidal profile of Fig. 39.3a; here it is assumed equal to the roughness parameter R_z of each individual specimen as shown in Fig. 39.2.

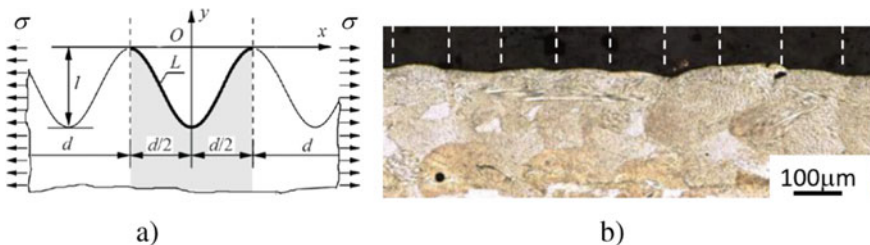


Fig. 39.3 a Half plane with sinusoidal profile under tension b theoretical profile for as-built L-PBF Inconel 718 (broken lines are 120 μm apart)

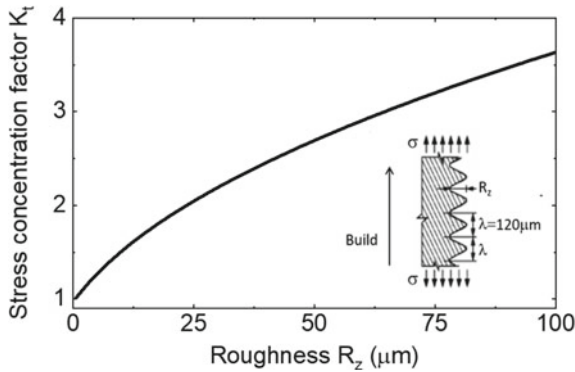


Fig. 39.4 Stress concentration factor for a half plane with a sinusoidal profile in tension

The solution to the boundary-value problem for an elastic half plane with a sinusoidal edge in tension of Fig. 39.3a was obtained solving a singular integral equation with Hilbert kernel by the mechanical quadrature method [7]. The following analytic dependence of the stress concentration factor coefficient K_t from the numerical results was determined

$$K_t = 1 + [1 + 1.5 \tanh(0.3 \ln \gamma + 0.7)]\gamma \tag{39.1}$$

where the parameter $\gamma = 2/d = 2R_z/2\lambda$. Figure 39.4 shows the dependence of K_t for R_z in the 0 to 100 μm range μm and for a prescribed sinusoidal pitch d of 120 μm . K_t ranges from 1 to 3.6. The theoretical local stress concentration of a rough surface notch is thus determined for each specimen of Fig. 39.2.

However, at high max nominal stresses and in the presence of high roughness, local plasticity at the notch roots is expected. Therefore, the cyclic stress–strain curve $(\sigma_a, \varepsilon_a)$ of L-PBF Inconel 718 obtained by push–pull testing of polished specimens, [9], is used along with the stress concentration factor K_t and the nominal stress σ_{\max} to determine the max effective stress σ_{eff} of each specimen according to the well-known Neuber’s rule [8],

$$\sigma_{\text{eff}}\varepsilon = (K_t\sigma_{\max})^2/E \tag{39.2}$$

The nominal max stress σ_{\max} versus N_f plot of Fig. 39.2 is therefore transformed into effective max stress $\sigma_{\max,\text{eff}}$ versus N_f plot of Fig. 39.5 after application of the roughness-based fatigue model outlined above. The model successfully collapses the scattered data of Fig. 39.2 in a narrower band. The plot also shows that the modified scatter band accounting for the surface roughness matches the reference fatigue data for L-PBF Inconel 718 obtained using standard specimens with low-stress-ground surfaces by [10].

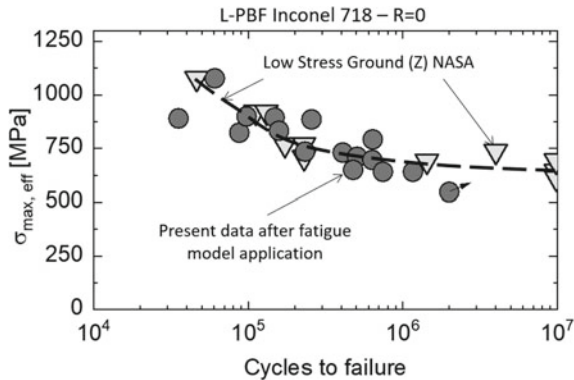


Fig. 39.5 Fatigue data of as-built IN718 after application of roughness-based model proposed here

The roughness-based fatigue model proposed apparently accounts for the as-built surface effect and therefore can be used to predict the fatigue debit with respect to the reference fatigue performance once the local R_z parameter and the layer-dependent periodicity λ are determined.

39.5 Conclusions

The aim of this study was the presentation of (i) original fatigue data of as-built L-PBF Inconel 718 specimens and (ii) a fatigue model that accounts for the roughness-dependent performance. This study led to the following conclusions:

- The roughness of as-built surfaces strongly affects the fatigue performance of L-PBF metals.
- The present experiments showed that specimens were produced with the new L-PBF system operating at sub-optimal level. Reference fatigue data of identical specimens produced with an optimized system were significantly better.
- A fatigue model was proposed to account for the roughness-related stress concentration at as-built surface micronotches. It implemented the theoretical solution for a half plane with sinusoidal profile in tension and the Neuber's rule for notch plasticity correction.
- The fatigue model converted the original scattered fatigue data into a smooth surface performance which showed a good matching with reference fatigue data for L-PBF Inconel 718 with low-stress-ground surfaces.

References

1. Sanchez S, Smith P, Zhengkai X, Gaspart DG (2021) Powder Bed Fusion of nickel-based superalloys: a review *Int J of Mach Tools Manufact* 165:1
2. Hosseini E, Popovich VA (2019) A review of mechanical properties of additively manufactured Inconel 718. *Addit Manufact* 30:100877
3. Chan KS, Peralta-Duran A (2019) A methodology for predicting surface crack nucleation in additively manufactured metallic components. *Metall Mater Trans A* 4378 50a
4. VDI-Guideline 3405 Part 3 (2015) Additive manufacturing processes. In: *Rapid manufacturing—design rules for part production using laser sintering and laser beam melting*
5. Vayssette NB, Saintier N, Brugger C, El Maya M, Pessard E (2019) Numerical modelling of surface roughness effect on the fatigue behavior of Ti-6Al-4V obtained by additive manufacturing. *Int J Fatigue* 123:180–195
6. Nicoletto G (2019) Smooth and notch fatigue behavior of selectively laser melted Inconel 718 with as-built surfaces *Int J Fatigue* 128:105211
7. Savrouk MP, Kazberouk A (2017) *Stress concentration at notches*. Springer International Publishing
8. Dowling NE (2008) *Mechanical behavior of materials*. Prentice Hall
9. Scurria M, Möller B, Wagener, Bein T, Chapter 15 characterization of the cyclic material behavior of AlSi10Mg and Inconel® 718 produced by SLM. In: Correia JAFO et al (eds) *Mechanical fatigue of metals*, pp 115–121
10. Morgan K, Wells D (2016) Overview of fatigue and damage tolerance performance of SLM Alloy 718. In: *National space and missile materials symposium*, NASA Doc. 20160007853

Chapter 40

Fatigue Behavior of the Titanium-Tantalum Alloy Obtained by Additive Manufacturing



Teresa Morgado , Catarina Valente, Josu Leunda ,
Alexandre Velhinho , and Rui Silva 

Abstract Tantalum is used in titanium alloy. However, there is still little knowledge about the mechanical properties of Ti-Ta alloys. And about their fatigue behavior, no documented information is known. The potential applications of Ti-Ta alloys are medical, naval, aerospace. Data related to the Ti-Ta alloys obtained by additive manufacturing is innovative and crucial for developing new Ti-Ta mechanical components. This work studies the additive manufacturing parameters to manufacture the Ti-Ta alloy with a weight percentage of 10% of tantalum and 90% of titanium, each element with 99,9% purity. Vicker's hardness, tensile and fatigue tests were performed. The true and engineering tensile properties were obtained. The plastic deformation was characterized. Fatigue behavior study was realized. And the fracture surface morphology was analyzed.

Keywords Ti-Ta alloy · Additive manufacturing · Fatigue behavior

T. Morgado (✉)

ISEL—Escola Superior de Engenharia de Lisboa, Rua Conselheiro Emídio Navarro 1, 1959-007
Lisboa, Portugal

e-mail: t.morgado@dem.isel.ipl.pt; t.morgado@fct.unl.pt

UNIDEMI/FCT NOVA—Research and Development Unit for Mechanical and Industrial
Engineering/Faculty of Science and Technology, NOVA University of Lisbon, Campus da
FCT/UNL, 2829-516 Caparica, Portugal

CINAV—Navy Research Center, Alfeite, 2810-001 Almada, Portugal

C. Valente

DEMI/ FCT NOVA—Department of Mechanical and Industrial Engineering/Faculty of Science
and Technology, NOVA University of Lisbon, Campus da FCT/UNL, 2829-516 Caparica, Portugal

J. Leunda

IK4-TEKNIKER, Advanced Manufacturing Technologies Unit, Polo Tecnológico de Eibar, Calle
Iñaki Goenaga 5, 20600 Eibar (Gipuzkoa), Spain

A. Velhinho · R. Silva

CENIMAT/I3N—Materials Research Centre/Institute for Nanostructures, Nanomodelling and
Nanofabrication, NOVA University of Lisbon, Campus da Caparica, Lisbon, Portugal

40.1 Introduction

Among the properties of pure titanium and pure tantalum [1], the main ones are excellent biocompatibility, corrosion resistance, besides a high strength and a low elastic modulus. In the '40 s of the twentieth century, pure tantalum was introduced in surgical implants, such as screws to fix bones or plates. Still in the twentieth century, during the '50 s, titanium appeared as a material used in surgical implants and medical instruments. However, despite its advantages when used individually, metallurgical studies proved that joining the two materials can improve the mechanical properties in relation to the properties of each one of the materials in the pure state [2–5].

According to Zhou et al. [6] work, it was possible to conclude that the dynamic modulus of elasticity reduces, almost linearly, with the increase of the percentage of tantalum until it reaches a minimum value (69 GPa) at 30% tantalum. After this minimum, the modulus increases as the percentage of tantalum also continues to increase until Young's modulus reaches 88 GPa for the Ti-50%Ta alloy. Then, the modulus of elasticity decreases again, getting a new minimum of 67 GPa, at 70% tantalum.

Considering more recent studies performed in the last decade, in an experimental Faria et al. [7] study, a comparison of the mechanical properties and biocompatibility of Ti-5Zr, Ti-5Ta and Ti-5Ta-5Zr alloys (in wt.%) with those of commercially pure titanium was performed. The results showed that the Ti-5Ta alloy presents the lowest Young's modulus and tensile strength (UTS) among the three alloys.

In a study by Kesteven et al. [8], the corrosion degradation behavior of Ti-Ta alloys with compositions Ti10Ta, Ti20Ta and Ti30Ta were investigated. Ti20Ta showed minor degradation. Furthermore, all Ti-Ta alloys presented a degradation rate lower than that of pure commercial titanium, which indicated the advantage of using tantalum.

Liu et al. [9] manufactured Ti-Ta alloys in five distinct compositions in at.% (Ti-20Ta, Ti-25Ta, Ti-30Ta, Ti-35Ta and Ti-50Ta) by sintering, after compacting into a cylindrical shape of each mixture of titanium and tantalum powders. The porosity of the alloys increases with the tantalum content, mainly due to the increased difficulty in sintering. At the level of mechanical properties, it could also be concluded that these sintered alloys presented a low Young's modulus and high tensile strength (UTS). These properties almost doubled to the same alloys produced by vacuum casting followed by pouring (ingot metallurgy). It was also concluded that the presence of tantalum in the alloys contributes to the increase of the tensile strength (UTS) and reduces Young's modulus. Furthermore, with the presence of porosities due to the low diffusion of tantalum, Young's modulus is further reduced.

Regarding Ti-Ta alloys manufactured by LASER cladding, Morgado et al. [1] developed an experimental study to evaluate the wear behavior of these alloys, specifically of Ti-30%Ta and Ti-52%Ta (wt.%) alloys. The results obtained were similar for both compositions.

In 2017, Yin et al. [10] studied the Ti-28%Ta (at.%—atomic percentage) alloy manufactured by casting. A sample was extracted to be reduced to powder PREP—Plasma Rotating Electrode Process. Through this process, powders with spherical geometry in the 30–260 μm range were obtained. It was verified significant increase in hardness, between the 226 μm particles with a hardness of 148.8 ± 6.7 HV and those of 198.8 μm with 164.3 ± 7.1 HV. Below 126 μm , small reductions in particle size already result again in significant increases in hardness.

The objective of the present work is to study the fatigue behavior of the Ti10Ta alloy manufactured by additive manufacturing.

40.2 Material and Experimental Procedure

40.2.1 Specimens Manufacturing

A 2.2 kW diode-pumped Nd: YAG LASER was used for additive manufacturing (Fig. 40.1). The LASER head was fixed into a six-axis robot arm. The powder mixture was carried to the LASER head employing a powder feeder with two powder hoppers (Fig. 40.1), using argon as a carrier gas [11]. Two plates of titanium grade 2 with dimensions of $15 \times 160 \times 160$ mm were used as the substrate. Titanium and tantalum

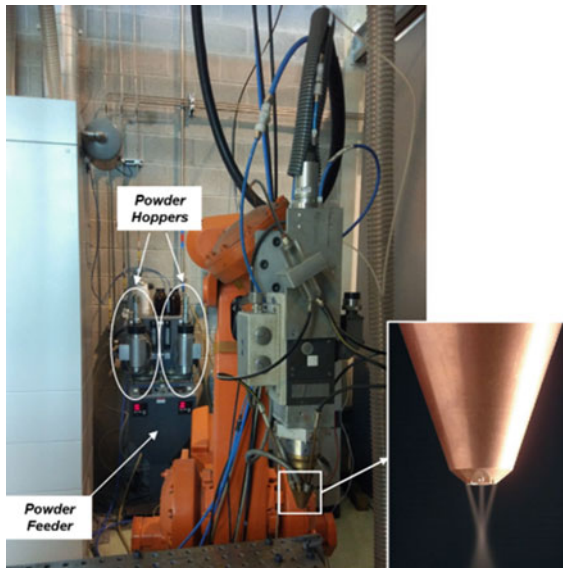


Fig. 40.1 Equipment used to manufacture the specimens of Ti10Ta alloy: LASER, six-axis robot arm, three orifices coaxial nozzle, powder feeder with two powder hoppers

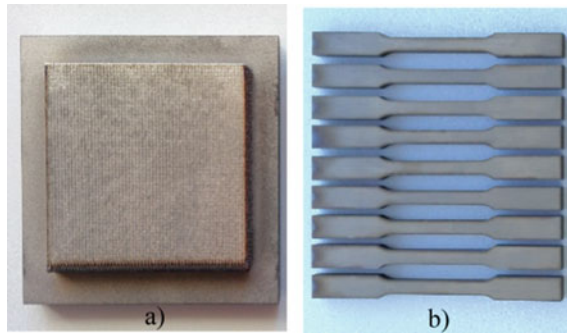


Fig. 40.2 Ti10Ta block manufactured by additive manufacturing, **a** $10 \times 120 \times 120$ mm block **b** Nine test specimens obtained after cutting process (wire-EDM, with a brass wire)

powders were mixed in a weight percentage of 90% to 10%, respectively. These powders have a range of $45\text{--}90\ \mu\text{m}$ and a purity of 99.9%.

During the manufacturing tests, cross-sections samples were extracted to analyse the manufacturing quality. The cut surfaces were processed by SiC-based grinding and diamond suspension-based polishing down to $R_a < 0.01\ \mu\text{m}$. The metallurgical characterization of the samples was based on optical microscopy inspection to study the alloy quality. No cracks were observed, and the adherence to the substrate was also solid, with enough dilution. Porosity issues were detected. The final process parameters, with minimal porosity, were selected for producing the Ti10Ta alloy: 0.7 kW of LASER power; 15 mm/s of scanning speed, 3.95 g/min of powder feed rate, 20 l/min of shielding gas flow.

Two blocks of Ti10Ta were produced, with dimensions of roughly $120 \times 120 \times 10$ mm, by depositing 50-layer with 120 overlapped tracks in each layer (Fig. 40.2). From these blocks, 18 specimens and three samples of Ti10Ta were extracted to develop the experimental study of this work. The tensile and fatigue specimens were extracted with geometry normalized following ASTM E8/E8M [12]. Figure 40.3 is presented the geometry dimensions of the specimens.

40.2.2 Vickers Hardness Tests

ASTME3-11 standard [13] was followed to prepare the samples. In addition, Vickers microhardness tests were performed on the three Ti10Ta samples following ASTM E384-17 [14]. The specimens were cylindrical with 20 mm of diameter and 4 mm of height. A spacing of 0.5 mm was used between each indentation, thus ensuring a minimum distance of 2.5 times greater than the Vickers diagonal, using a test load of 500 g.f and with a duration of 10 s in each test. Ten indentations were made in each specimen. Software Minitab was used to verify if the results obtained followed a normal distribution, as required in the ASTM standard [14]. Probability plots were

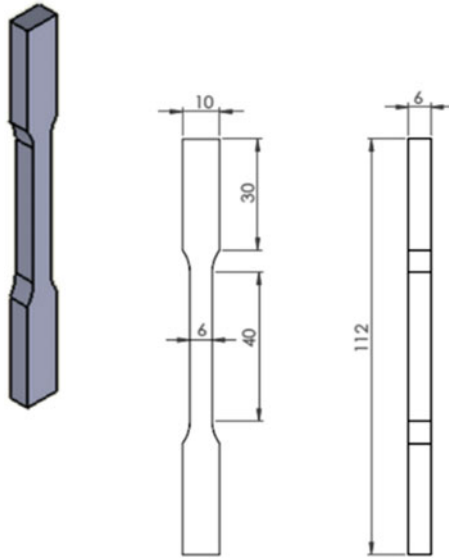


Fig. 40.3 Geometry dimensions of the specimens according to ASTM E8/E8M-16ae1

made using the Anderson-Darling test, in which the p-value must be equal or higher than the confidence value $\alpha = 0.05$. The Ti10Ta alloy hardness obtained was $255.2^{+4.4}_{-3.7}$ HV0.5.

40.2.3 Tensile and Fatigue Tests

Uniaxial tensile tests were performed at room temperature, with a 3 mm/min stroke rate, as prescribed by ASTM E8/E8M [12]. The fatigue tests were carried out using the universal servo-hydraulic equipment (see Fig. 40.4). Its system has a maximum load capacity of up to 100 kN. A sinusoidal wave was used in executing the tests, with a constant amplitude and stress ratio of $R = 0.05$. It was also applied a frequency $f = 10$ Hz during each test. It was considered a room temperature of 25 °C.

40.3 Results and Discussion

Table 40.1 presents the mechanical properties of the alloy Ti10Ta. The lower value of Young's modulus is a consequence of the tantalum presence [15, 16]. The average values of the strain after fracture and the cross-section area reduction are, respectively, 16.8% and 22.8%. Fragile materials have a strain after fracture smaller than 5% [17]

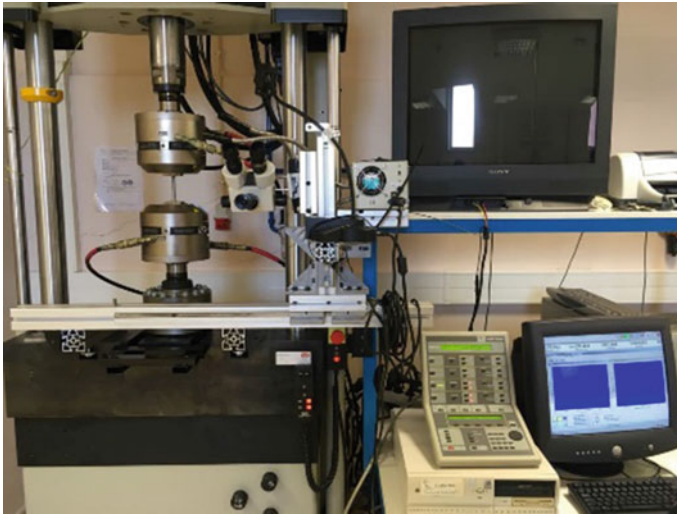


Fig. 40.4 Setup of mechanical tests (servo-hydraulic equipment, the controller, and the computer)

Table 40.1 Tensile properties of Ti10Ta alloy

Mechanical properties	Engineering values	True values
Young's modulus (GPa)	8.35	9.77
Yield strength (MPa)	642	692
Yield strain	0.0771	0.0743
Tensile strength (MPa)	735	855
Uniform tensile strain	0.164	0.152

therefore, Ti10Ta alloy exhibits a ductile behavior. Also, the tensile curves obtained already indicated ductile behavior [18].

The uniform plastic deformation region was also determined. The hardening, $n \cong 0.272$, and resistance $K \cong 1453.83$ MPa were determined. Equation (40.1) describes the additive manufacturing Ti10Ta alloy's behavior under a uniform plastic deformation regime

$$\bar{\sigma} = 1453.83\bar{\epsilon}^{0.272} \tag{40.1}$$

The S-N curve was determined from the fatigue tests performed, and the S-N curve determined (Eq. 40.1), where (N) is the number of cycles and (σ_{\max}) is the maximum applied stress.

$$\sigma_{\max} N^{0.181} = 3369 \tag{40.2}$$

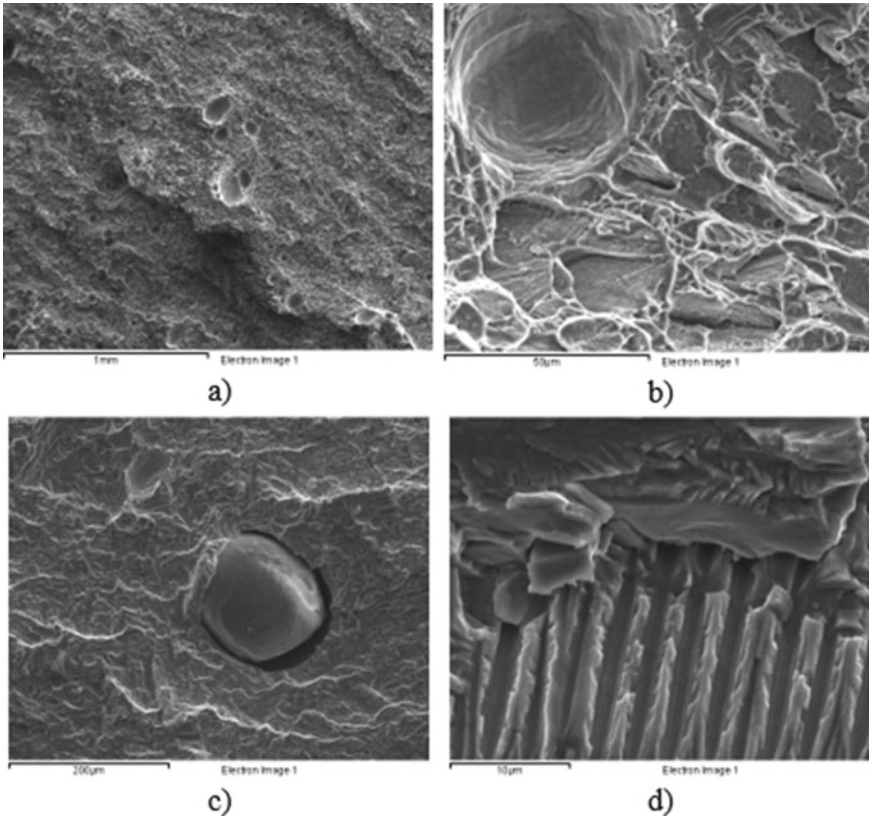


Fig. 40.5 SEM image of a fracture surface of a Ti10Ta specimen obtained by additive manufacturing

Figure 40.5 presents an image selection of the fracture surface of the fatigue specimens observed by Scanning Electron Microscope (SEM). From the analysis of the images, the rupture mode by coalescence of cavities is identified (Fig. 40.5a, b). Grain boundaries (Fig. 40.5c), porosities or other types of heterogeneities are some points where microcavities' nucleation develops more. In addition, it is possible to check the various deep secondary cracks between the grains (Fig. 40.5b, c), called an intergranular fracture. The cleavage of transgranular facets is visible in the images of Fig. 40.5d. The morphological features observed on the various fracture surfaces are typical of fatigue fractures [19, 20].

40.4 Conclusions

A new alloy of Titanium and Tantalum (Ti10Ta) was manufactured by additive manufacturing technology with success. The only intrinsic manufacturing defects identified were porous.

The mechanical proprieties of the material and the hardness were determined. It was possible to conclude that the material presents a ductile behavior. The uniform plastic deformation region was also determined.

The S-N curve was obtained. Through SEM images, the intergranular and transgranular fracture was identified. It was also concluded that the rupture mode is the coalescence of cavities.

Acknowledgements The authors would like to thank the Portuguese Foundation for Science and Technology (FCT), under grants Strategic Project FCT.IP—UIDB/00667/2020, for the financial support. Moreover, to thank the Faculty of Science and Technology—Universidade NOVA de Lisboa for the work carried out in the framework of the research centers, UNIDEMI/NOVA—Research & Development Unit for Mechanical and Industrial Engineering and CENIMAT/i3N—Materials Research Center.

References

1. Morgado TLM, Navas H, Brites R (2016) Wear study of Innovative Ti-Ta alloys. *Procedia Struct Integr* 2:1266–1276
2. Leyens C, Peters M (eds) (2003) Titanium and titanium alloys: fundamentals and applications. WILEY-VCH, Germany
3. Froes FH (ed) (2015) Titanium physical metallurgy processing and applications. ASM International, USA
4. Zhou YL, Niinomi M, Akahori T, Nakai M, Fukui H (2007) Comparison of various properties between titanium-tantalum alloy and pure titanium for biomedical applications. *Mater Trans* 48(3):380–384
5. Moiseyev VN (2006) Titanium alloys: Russian aircraft and aerospace applications. CRC Press, USA
6. Zhou YL, Niinomi M, Akahori T (2004) Effects of Ta content on Young's modulus and tensile properties of binary Ti-Ta alloys for biomedical applications. *Mater Sci Eng A* 371(1–2):283–290
7. Faria ACL, Rodrigues RCS, Rosa AL, Ribeiro RF (2014) Experimental titanium alloys for dental applications. *J Prosthet Dent* 112(6):1448–1460
8. Kesteven J, Kannan MB, Walter R, Khakbaz H, Choe HC (2015) Low elastic modulus Ti-Ta alloys for load-bearing permanent implants: Enhancing the biodegradation resistance by electrochemical surface engineering. *Mater Sci Eng C* 46:226–231
9. Liu Y, Li K, Wu H, Song M, Wang W, Li N, Tang H (2015) Synthesis of Ti-Ta alloys with dual structure by incomplete diffusion between elemental powders. *J Mech Behav Biomed Mater* 51:302–312
10. Yin JO, Chen G, Zhao SY, Ge Y, Li ZF, Yang PJ, Han WZ, Wang J, Tang HP, Cao P (2017) Microstructural characterisation and properties of Ti-28Ta at.% powders produced by plasma rotating electrode process. *J Alloys Compd* 713:222–228

11. Valente C, Morgado T, Sharma N (2019) LASER cladding—a post processing technique for coating, repair and re-manufacturing. *Materials Forming, Machining and Tribology*, chapter 10. Springer
12. ASTM E8/E8M-16a (2016) Standard test methods for tension testing of metallic materials. ASTM International, West Conshohocken, PA. https://doi.org/10.1520/E0008_0008M-16A
13. ASTM E3–11 (2017). Standard practice for preparation of metallographic specimens. ASTM International, West Conshohocken, PA. <https://doi.org/10.1520/E0003-11R17>
14. ASTM E384–17 (2017) Standard test method for micro indentation hardness of materials. ASTM International, West Conshohocken, PA. <https://doi.org/10.1520/E0384-17>
15. Song Y, Xo DS, Yang R, Li D, Wu WT, Guo ZX (1999) Theoretical study of the effects of alloying elements on the strength and modulus of β -type bio-titanium alloys. *Mater Sci Eng A* 260(1–2):269–274
16. Kunčická L, Kocich R, Lowe TC (2017) Advances in metals and alloys for joint replacement. *Prog Mater Sci* 88:232–280
17. Costa MYP (2009) Fatigue of aeronautic titanium, cladding with PVD. (in Portuguese by Brasil) Doctor Thesis, Faculdade de Engenharia de Guaratinguetá, Universidade Estadual Paulista, Brasil
18. Narayan RJ (ed) (2012) *ASM Handbook*, vol 23. ASM International, USA
19. Hertzberg RW (1989) *Deformation and fracture mechanics of engineering material*, 3rd edn. Wiley, Canada
20. *ASM Handbook* (1990) Fatigue and fracture, vol. 19, 2nd edn. ASM International

Chapter 41

Some Observation Concerning Fatigue Response of Additively Manufactured Specimens from Ti-6Al-4V



Martin Nesládek , Martin Matušů , Jan Papuga , Matěj Mžourek ,
and Michaela Roudnická 

Abstract The aim of this work is to analyze the impact of production parameters and different production additive manufacturing methods on the porosity, roughness, quality of the final product, and its fatigue performance. Unmachined samples were tested, with and without heat treatment. Although differing porosities of the samples were detected across various test series, the surface defects were observed to be much more significant in deciding the final fatigue performance. Cracks initiated from the surface of the specimens.

Keywords Additive manufacturing · Porosity · Fatigue life

41.1 Introduction

The demand for titanium alloys is rising, as these are used in critical structures, such as aircraft, engine, and biomedical applications thanks to their low weight, high toughness, biocompatibility, and corrosion resistance. As titanium is an expensive material, additive manufacturing (AM) is a suitable method for its production because of its envisaged minimum material waste. AM of metals can be divided into powder bed fusion (PBF) and directed energy deposition (DED). Selective laser melting (SLM) and electron beam melting (EBM), which both belong to PBF technologies, are the most successful AM technologies for metals. For PBF, however, it has been shown that AM specimens in as-built form made from Ti-6Al-4V suffer from lower

M. Nesládek (✉) · M. Matušů · J. Papuga · M. Mžourek
Faculty of Mechanical Engineering, Czech Technical University in Prague, Technická 4, 166 07
Prague 6, Czechia
e-mail: martin.nesladek@fs.cvut.cz

M. Nesládek · M. Matušů · M. Mžourek
Department of Instrumentation and Control Engineering, FME CTU in Prague, Center of
Advanced Aerospace Technology, Technická 4, 166 07 Prague 6, Czechia

M. Roudnická
Department of Metals and Corrosion Engineering, University of Chemistry and Technology,
Technická 5, 166 28 Prague 6, Czechia

fatigue performance compared to wrought or cast Ti-6Al-4V despite similarly high static strength [1, 2].

This paper is based on comparing unmachined samples of Ti-6Al-4V alloy produced by different AM methods with different production parameters. The comparison is focused on their fatigue performance, while different types of defects and features such as porosity, residual stresses, or surface roughness are discussed.

41.2 Fatigue Experiments

The material used in this study was Ti-6Al-4V titanium alloy. Fatigue specimens of 7.98 mm diameter and 30 mm in length in the active cross-section were tested on Amsler 100 kN resonator. Grips of the specimens had machined M16 × 1 threads, and the transition radius between the active part and the heads was 32 mm. Load-controlled testing was imposed on the specimens in the fully reversed push-pull mode. A part of results of this campaign has already been published in [3].

While all specimens were of equal design, the way they were manufactured differed, see Table 41.1. In each configuration, 14 specimens at least were tested to obtain an S-N curve. Production parameters are in Table 41.2 except for the parameters for the SLM process at MIRDC research center (T series), which did not provide them. Due to varying production parameters, the residual stresses detected at the surface of the specimens differ, see Table 41.1. As MIRDC applied shot peening procedure to T series, compressive residual stresses were introduced on the specimen surface.

Table 41.1 Description of five experimental series along with values of surface residual stresses

Series	Method, producer, treatment	Residual stresses [MPa]	
		Axial	Transversal
A	SLM, ProSpon	182 ± 12	172 ± 6
C	SLM, ProSpon, heat treatment	46 ± 13	29 ± 5
A2018	SLM, ProSpon	277 ± 32	129 ± 16
N	EBM, MIRDC	-6 ± 27	-7 ± 11
T	SLM, MIRDC, mech. surf. treatment	-218 ± 45	-541 ± 40

Table 41.2 Printing parameters as provided by the producers

Series	Laser power (W)	Laser speed (mm/s)	Layer thickness (mm)	Vector spacing (mm)	Energy density (J/mm ³)	Average powder size (mm)	Sieve mesh (mm)
A, C	200	800	0.030	0.112	74.4	0.03	0.100
A2018	200	1088	0.030	0.0525	116.8	0.03	0.063
N	900	4530	0.050	0.200			

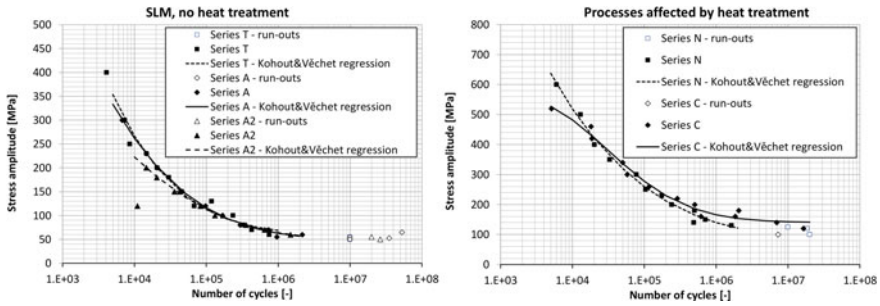


Fig. 41.1 S-N curves for all described specimen types

Results of the fatigue experiments are shown in Fig. 41.1. Five S–N curves were obtained by fitting the Kohout–Věchet function [4], which includes the characteristic transition to the fatigue limit domain. The curves are divided into two graphs based on the heat treatment applied. Series A, A2018, and T were not affected by any subsequent heat treatment. Although the production parameters, final porosity, residual stresses, and surface quality, differ substantially (as will be discussed in the next section), the resulting S–N curves are similar.

The heat treatment improves the response of the additively manufactured material. While the heat treatment of series C was performed subsequently after manufacturing (820 °C/90 min, vacuum), the EBM process (series N) is performed at 740 °C (thanks to inherent preheating by electron beam); thus, no heat treatment is needed.

Fractographic analysis (examples in Fig. 41.2) reveals the cracks initiation on the surface of samples. Additionally, surface structure and porosity were analyzed in the longitudinal direction, see Fig. 41.3. According to our observations, the influence of pores on the formation of fatigue cracks is smaller than the influence of surface roughness. It can be observed in Figs. 41.2 and 41.3 that the propagation of the crack is initiated from the surface.

In specimens loaded in high-cycle fatigue (HCF), a singular spot was found (Fig. 41.2a, b) where the crack initiated in both cases (A5, T10). In low-cycle fatigue (LCF), the crack initiated from one spot on the T2 sample surface (Fig. 41.2d), on the contrary to A10 (Fig. 41.2 c) where multiple spots can be seen.

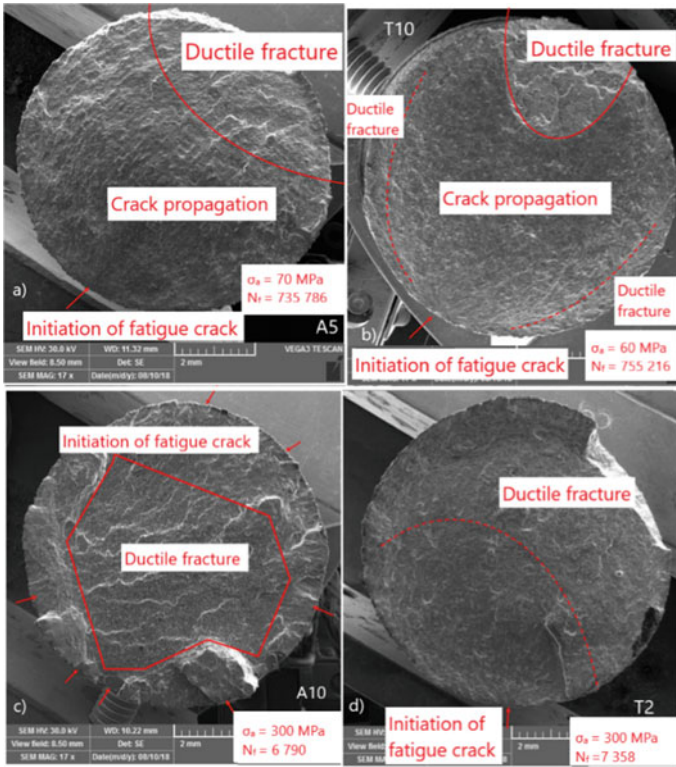


Fig. 41.2 Fractography of specimen **a** A5, **b** T10, **c** A10 with multiple fatigue crack initiation sites, and **d** T2 with single crack initiation site

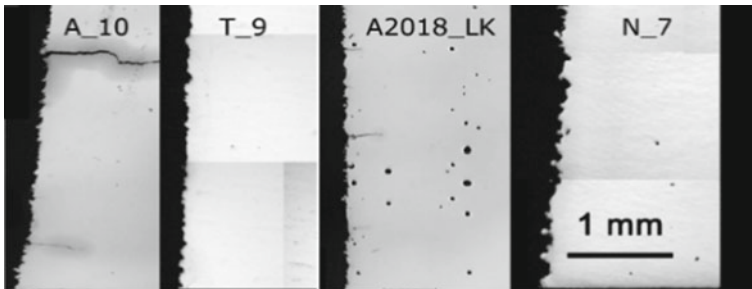


Fig. 41.3 Longitudinal cuts of samples for analyses of the surface quality and porosity

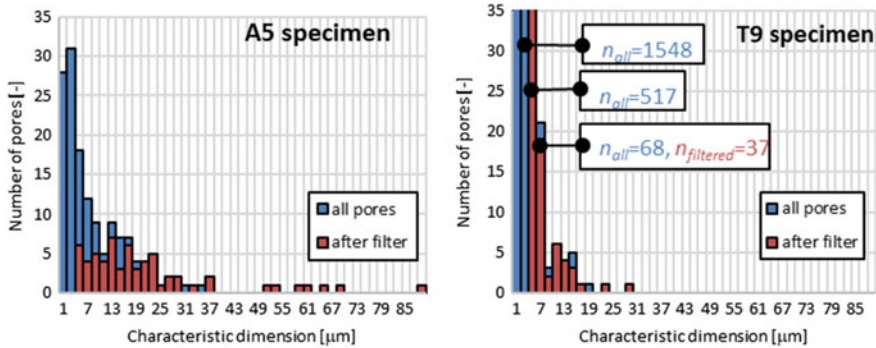


Fig. 41.4 Graph of porosity distribution in A and T series with and without filtration

41.3 Analysis of Some of the Features Affecting Fatigue

41.3.1 Porosity

Porosity is affected by various production aspects of 3D printing. Lack of fusion (LOF), manifested as an improper fusion between tracks or layers of deposited material (irregularly shaped pores), results from insufficient energy input. Conversely, excessive energy can cause gas to stay entrapped in the structure (round pores) [5].

While the more distinct pores in the A2018 series are clearly visible in Fig. 41.3, the difference in porosity between series A and T is compared in Fig. 41.4. The roundness of the pores was analyzed because rounder pores are expected to be less dangerous to trigger the crack initiation, while the less round can be considered as a sharp notch. A filter was applied to enforce the roundness of pores less than 0.85, while their characteristic dimension (CD—square root of area) was set as $CD > 4 \mu\text{m}$. In T9 sample, a high number of pores $< 4 \mu\text{m}$ were present, while no pores had $CD > 30 \mu\text{m}$. On the other hand, A5 sample from A series had a smaller number of pores with $CD < 4 \mu\text{m}$ but relatively high number of big pores with CD of up to 88 μm .

Despite the observed differences, A, A2018, and T series behaved similarly under fatigue (Fig. 41.1). Porosity is, thus, not the fatigue-controlling factor here.

41.3.2 Residual Stresses

Thanks to high processing temperature, the EBM printing method does not create considerable residual stresses (see Table 41.1) [2, 6]. During the SLM method, on the other hand, the molten part is rapidly cooled, which causes substantial residual stresses on the surface of the specimen [2]. These were successfully released by the heat treatment applied on C samples, which also modifies the original martensitic structure to a stable lamellar microstructure of $\alpha + \beta$ phases. Heat treatment (either

inherent or applied additionally), thus, diminishes the negative effect of stresses on fatigue (see the shift of S-N curves in Fig. 41.1 to higher amplitude values).

Differences among A, A2018, and T series occur due to different processing. The residual stresses induced in A2018 are higher than in A series, which can be caused by increased laser speed and so increased cooling rate. The high compressive residual stresses in T series are then related to the performed mechanical surface treatment.

Although the shot peening of series T had a considerable effect on residual stresses, its effect on fatigue life is limited (Fig. 41.1). On the other hand, the shape of the remaining cross-section at the final break of T10 specimen (Fig. 41.2b) supports the expectation that the residual stresses were able to hinder the crack growth in the subsurface layer. Though, this positive effect was also surpassed by another fatigue-controlling mechanism.

41.3.3 Surface Roughness

Surface roughness seems to be the main fatigue-controlling mechanism in the studied samples. The surface roughness of unmachined samples is related to the principle of PBF, particle size of input powders as well as printing parameters. The measurement presented in Table 41.3 is, thus, focused on the differences between A and A2018 series provided both by Prosson using the same powder but different printing parameters (Table 41.2).

On most of the surface of A2018 specimens, the measured surface roughness was about two times lower than on A specimens. However, a pattern presented in the photograph in Table 41.3 was detected on several locations across each A2018 series specimen, showing roughness values presented in Table 41.3. These locations then decided about the fatigue behavior despite better surface quality of the remaining specimen surface. The characteristic distance of this grid of 0.3 mm equals 10 times the layer thickness, which relates to the applied “island” scanning strategy and higher beam speed.

41.4 Conclusion

Results show that shot peening of SLM-fabricated Ti-6Al-4V with high compressive residual stresses does not ensure by itself better fatigue performance than the as-built specimens provide. Moreover, the observed differences in porosity among the individual SLM series lead to the conclusion that the fatigue performance is ultimately affected by the surface quality. On the other hand, the heat treatment had a superior effect on specimens, because they then yielded properties similar to the EBM output.

Table 41.3 Surface roughness of A and A2018 series and the photograph of the relates

	A series		A2018 series	
	Mean	St.dev	Mean	St.dev
R_a (μm)	11.4	2.7	10.8	5.2
R_q (μm)	13.8	3.0	13.1	5.8
R_z (μm)	58.8	10.5	56.3	17.8



Acknowledgements The support from ESIF, EU Operational Programme Research, Development and Education, from the Center of Advanced Aerospace Technology (CZ.02.1.01/0.0/0.0/16_019/0000826), Faculty of Mechanical Engineering, Czech Technical University in Prague, and from the Grant Agency of the Czech Technical University in Prague (SGS20/158/OHK2/3T/12) is gratefully acknowledged.

References

1. Zhang H, Dong D, Su S, Chen A (2019) Experimental study of effect of post processing on fracture toughness and fatigue crack growth performance of selective laser melting Ti-6Al-4V. *Chin J Aeronaut* 32(10):2383–2393
2. Chastand V, Quaegebeur P, Maia W, Charkaluk E (2018) Comparative study of fatigue properties of Ti-6Al-4V specimens built by electron beam melting (EBM) and selective laser melting (SLM). *Mater Charact* 143(-):76–81
3. Fousová M, Vojtěch D, Doubrava K, Daniel M, Lin C-F (2018) Influence of inherent surface and internal defects on mechanical properties of additively manufactured Ti6Al4V alloy: comparison between selective laser melting and electron beam melting. *Materials* 11(4):537
4. Kohout J, Věchet S (2001) A new function for fatigue curves characterization and its multiple merits. *Int J Fatigue* 23(2):175–183
5. Sanaei N, Fatemi A (2021) Defects in additive manufactured metals and their effect on fatigue performance: a state-of-the-art review. *Prog Mater Sci* 117
6. Weiwei H, Wenpeng J, Haiyan L, Huiping T, Xinting K, Yu H (2011) Research on preheating of titanium alloy powder in electron beam melting technology. *Rare Metal Mater Eng* 40(12):2072–2075

Chapter 42

Cyclic Plasticity and Low-Cycle Fatigue of an AISI 316L Stainless Steel Tested at Room Temperature



Denis Benasciutti , Marco Pelegatti , Alex Lanzutti , Enrico Salvati , Jelena Srnc Novak , and Francesco De Bona 

Abstract This paper presents experimental results aimed at characterizing and modeling the elastoplastic cyclic response and low-cycle fatigue behavior of an AISI 316L stainless steel, subjected to strain-controlled tests at room temperature. Experimental data are used to calibrate kinematic and isotropic plasticity models, as well as the Manson–Coffin equation, which is compared to design strain-life curves at 5% failure probability estimated by four statistical methods (deterministic, “equivalent prediction interval,” univariate tolerance interval, and Owen’s tolerance interval for regression).

Keywords AISI 316L · Low-cycle fatigue · Cyclic plasticity · Design curves

42.1 Introduction

AISI 316L austenitic stainless steel is used in those engineering applications, at room or high temperature, that require a combination of toughness, ductility, and resistance to corrosion. When subjected to cyclic loading, this type of steel exhibits a cyclic plasticity response with three main consecutive stages: hardening, softening, and secondary hardening/softening [1, 2]. Besides cyclic plasticity, fatigue strength is also significant when employing this steel for cyclic loadings in service. Put together, all these features explain the interest of this study in investigating the cyclic behavior and low-cycle fatigue strength of an AISI 316L steel.

Experimental results under strain-controlled tests at room temperature are used for estimating parameters of kinematic and isotropic plasticity models. Several issues

D. Benasciutti (✉) · M. Pelegatti
University of Ferrara, via Saragat 1, 44122 Ferrara, Italy
e-mail: denis.benasciutti@unife.it

A. Lanzutti · E. Salvati · F. De Bona
Polytechnic Department of Engineering and Architecture, University of Udine, via delle Scienze
208, 33100 Udine, Italy

J. S. Novak
Faculty of Engineering, University of Rijeka, Vukovarska 58, 51000 Rijeka, Croatia

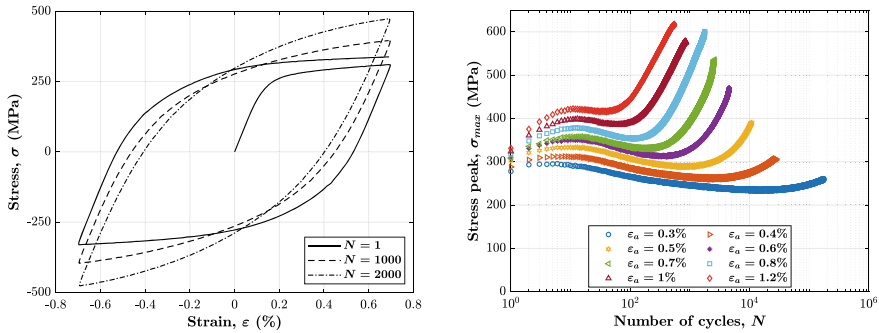


Fig. 42.1 (left) Example of experimental stress–strain cycles (for $\epsilon_a = 0.7\%$) at 1, 1000 and 2000 cycles; (right) trends of maximum stress per cycle at different strain amplitudes [1]

observed in model calibration, due to the sequence of hardening and softening response characterizing the behavior of this material, are discussed. Experimental results are also used for estimating the Manson–Coffin curves, not only for a 50% failure probability, but also for lower probabilities identifying the allowable strain amplitudes. A more comprehensive description of the present study is given in [1].

42.2 Experiments

Low-cycle fatigue tests were carried out at room temperature on cylindrical specimens with uniform gauge section (25 mm length, 10 mm diameter). Fully reversed strain-controlled cycles were applied at constant strain rate 0.004 s^{-1} . Different strain amplitudes were considered in the range from 0.3 to 1.2%, totaling n. 8 experimental tests. Tests were interrupted short of complete specimen separation, when the strain exceeded the safety limit of the testing machine. Figure 42.1(left) shows three experimental cycles at strain amplitude 0.7%.

Figure 42.1(right) highlights that the material never reaches a well-defined stabilized state during cycling. Instead, it followed a sequence of strain hardening and/or softening phases depending on the applied strain amplitude. This behavior, observed also in other studies (e.g., [3]), is attributed in [2] to a mechanism based on densification and rearrangement of dislocations.

42.3 Calibration of Plasticity Models (Kinematic and Isotropic)

In the calibration procedure, elastic modulus and yield stress were determined first. The elastic modulus was estimated from the initial tensile branch of each test and also

from the tensile/compressive branches of the “stabilized” cycle. Since the estimated values did not show any noticeable difference, they were averaged out to obtain a single value of $E = 191626\text{MPa}$, used in the following analysis.

The second parameter to be estimated is the yield stress, as it establishes the onset of plastic deformation. As the material does not exhibit a discontinuous yielding, the initial $(\sigma_{y,0})$ and stabilized $(\sigma_{y,s})$ yield stresses were determined conventionally by introducing an offset in plastic strain. As also suggested in [3], a plastic strain offset of 0.0025% and 0.01% was considered for the initial tensile and for tensile/compressive branches of the “stabilized” cycle, respectively. After estimating the yield stress from each test, an average value $\sigma_{y,0} = 169\text{MPa}$ was finally determined.

The next step was to calibrate kinematic model parameters by considering—for the reasons explained in [1]—the cycles at the end of the softening stage and with only strain amplitudes from 0.3 to 0.7%. Figure 42.2(left) compares the experimental points (markers) with the fitting curve (dashed line) corresponding to the rightmost equation in the following kinematic model (with $M = 2$) (for more details see [1]):

$$X = \sum_i X_i, dX_i = \frac{2}{3}C_i d\epsilon_{pl} - \gamma_i X_i dp \rightarrow \sigma_a = \sigma_{y,s} + \sum_{i=1}^M \frac{C_i}{\gamma_i} \tanh(\gamma_i \epsilon_{pl,a})$$

An additional parameter refinement was performed to further improve the fitting (see continuous line Fig. 42.2(left)); the obtained kinematic parameters are listed in the last column in Table 42.1.

Consistently with the choice adopted for the kinematic model, also isotropic model parameters were determined from the experimental response up to the end of the softening stage (i.e., the local minimum of the cyclic response curve in Fig. 42.1(right)). Since the material response shows a sequence of hardening and softening stages, it was decided to use a two-term isotropic hardening model to improve the fitting [1]:

$$\sigma_{\max} - \sigma_{\max}^{\text{kin}} \cong R = R_{\infty,1}(1 - e^{-b_1 p}) + R_{\infty,2}(1 - e^{-b_2 p})$$

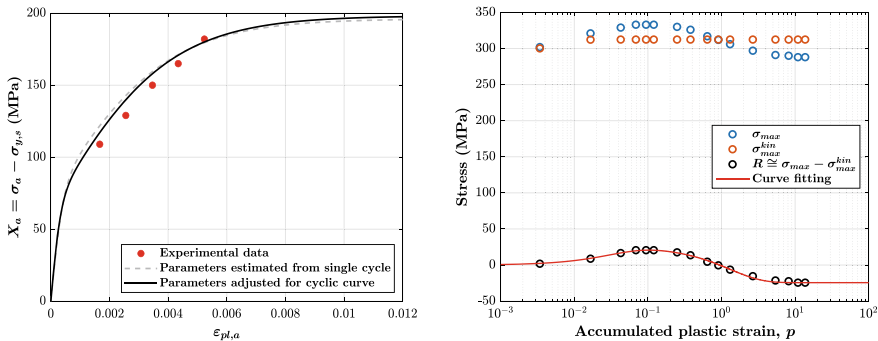


Fig. 42.2 Fitting to experimental data of kinematic model (left) and isotropic model (right) [1]

Table 42.1 Estimated parameters for kinematic and isotropic plasticity models

Strain amplitude, ε_a (%)	$R_{\infty,1}$ (MPa)	$R_{\infty,2}$ (MPa)	b_1	b_2	Kinematic model
0.3	13.7	-58.9	90.00	0.8841	$C_1 = 189,500$ MPa $\gamma_1 = 2950$ $C_2 = 33,500$ MPa $\gamma_2 = 350$
0.4	14.8	-51.8	46.26	0.7596	
0.5	25.8	-49.8	29.18	0.7792	
0.6	41.0	-48.0	16.19	0.9851	
0.7	48.6	-42	11.37	1.280	

in which σ_{max} is the experimental stress peak, σ_{max}^{kin} is the stress peak after considering only the kinematic model, and p is the accumulated plastic strain evaluated experimentally. R_i is the saturated stress and b_i the speed of stabilization of R_i —they are the fitting parameters to be determined. Since the experimental hardening or softening behavior depends upon the strain amplitude, R_i differs for each test. Curve fitting also requires that $R_{\infty,1} + R_{\infty,2} = \sigma_{max,s} - \sigma_{max,s}^{kin}$, where subscript s indicates that the stress peak is referred to the cycle at the end of the softening stage. Figure 42.2(right) shows the fitting procedure applied to a single test.

Table 42.1 lists the isotropic model parameters estimated from experimental tests at each strain amplitude. A polynomial interpolation was used in [1] to determine the parameters at other strain amplitude values that are within the range used in tests.

An algorithm was developed to simulate the uniaxial stress–strain cyclic response. Figure 42.3(left) compares experiments vs. simulation with kinematic and isotropic model, for cycles 1 and 1000 at strain amplitude 0.5%. Figure 42.3(right) shows the evolution of the peak stress in each cycle, during each test at different strain amplitudes.

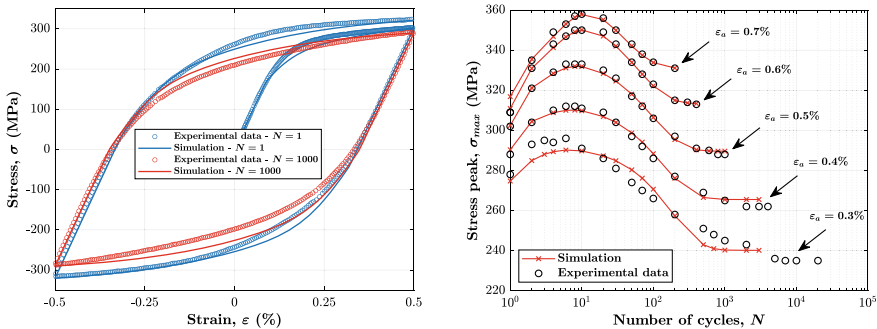


Fig. 42.3 Comparison between simulation and experiment: (left) stress–strain cycles for test with 0.5% strain amplitude; (right) cyclic stress response [1]

42.4 Strain-Life Curves (Regression Lines and Design Lines)

The experimental results are also used for estimating the Manson–Coffin equation:

$$\epsilon_a = \epsilon_{a,el} + \epsilon_{a,pl} = \frac{\sigma'_f}{E} (2N_f)^{b'} + \epsilon'_f (2N_f)^{c'}$$

where $\epsilon_{a,el}$ and $\epsilon_{a,pl}$ are the amplitudes of elastic and plastic strains, respectively, σ'_f = fatigue strength coefficient, b' = fatigue strength exponent, ϵ'_f = fatigue ductility coefficient, c' = fatigue ductility exponent, $2N_f$ = reversals to failure.

Equation parameters follow from a regression analysis of experimental data, performed separately for elastic and plastic strain contributions. In regression model, $y = A + Bx + \delta$, symbols, $x = \log(\epsilon_{a,*})$ and $y = \log(2N_f)$ (where $\epsilon_{a,*} = \epsilon_{a,el}$ or $\epsilon_{a,*} = \epsilon_{a,pl}$ for elastic and plastic strain amplitude); δ is a normal random variable with zero mean and standard deviation s , introduced to account for the scatter of $2N_f$.

Since in each test the AISI 316L steel does not fully stabilize, it is not obvious to establish at which number of reversals is the “stabilized” cycle in which elastic and plastic strain amplitudes must be computed. Conventionally, the data in Fig. 42.4 refer to half the number of reversals to failure. The Manson–Coffin parameters estimated from experimental data are listed in the first row of Table 42.2.

It has to be noted that a regression strain-life line describes a “median” behavior referred to a failure probability $P_f = 50\%$, a value not enough conservative for a safe design. A lower probability is obtained by shifting the “median” line to the left to define a design strain-life line [4]:

$$\hat{Y}_d = \hat{Y} - K(\alpha, \beta, n, x, x) \cdot \hat{s}$$

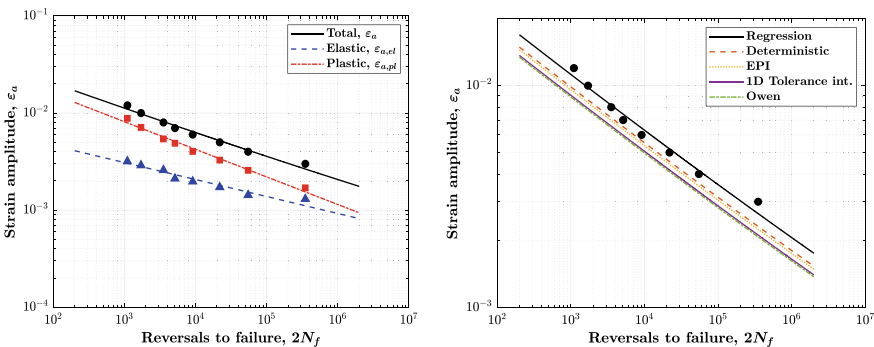


Fig. 42.4 Estimated strain-life lines: (left) regression analysis (50% failure probability); (right) design curves at lower failure probability [1]

Table 42.2 Parameters of “median” and design strain-life curve; $\varepsilon_{a,d}$ refers to $2N_f = 2 \times 10^5$

Method	K	$\left(\frac{\hat{\sigma}'_f}{E}\right)_d$	\hat{b}'_d	$\left(\hat{\varepsilon}'_f\right)_d$	\hat{c}'_d	$\varepsilon_{a,d}$
Regression ($\alpha = 50\%$)	–	0.01034	–0.1748	0.05799	–0.2842	0.003031
Deterministic ($\alpha = 5\%$)	1.645	0.00890	–0.1748	0.05138	–0.2842	0.002654
EPI ($\alpha = 5\%, n = 8$)	2.0187	0.00860	–0.1748	0.04999	–0.2842	0.002575
1D tol.interv ($\alpha = 5\%, \beta = 90\%, n = 8$)	2.755	0.00804	–0.1748	0.04735	–0.2842	0.002427
1D tol.interv Owen ($\alpha = 5\%, \beta = 90\%, n = 8$)	2.9864	0.00787	–0.1748	0.04655	–0.2842	0.002382

where $\hat{Y} = \hat{A} + \hat{B}x$ is the regression line ($P_f = 50\%$) that links the (log-) reversals to failure $\hat{y} = \log(2\hat{N}_f)$ to the (log-)strain amplitude $x = \log(\varepsilon_{a,*})$. The previous expression must be applied separately to elastic and plastic parts. Coefficient $K(\alpha, \beta, n, x, x)$ is a function of failure probability α , confidence β , number of test samples n , and strain amplitudes x used in tests, while \hat{s} is the standard deviation estimated from test results.

The specific expression of $K(-)$ depends on the statistical model used, e.g., deterministic, “equivalent prediction interval—EPI,” univariate tolerance interval, Owen’s tolerance interval for regression [1, 4]. Figure 42.4(right) compares the regression lines with the design lines obtained by various statistical methods.

Being shifted to the left, the design lines are obviously more conservative than the regression line. The degree of conservatism can be appreciated by comparing, for example, the strain amplitudes at a given number of reversals $2N_f = 2 \times 10^5$ estimated by different models; see Table 42.2. A reduction of the design strain amplitude up to 20% is observed, although this ratio is not constant over the whole strain-life curve.

42.5 Conclusions

This work dealt with the experimental characterization of cyclic response and low-cycle fatigue strength of an AISI 316L stainless steel at room temperature. Experimental data were used to calibrate the kinematic and isotropic model parameters. A critical issue was to identify an equivalent stabilized state necessary for model calibration, since the material did not fully stabilize during each cyclic test, but rather showed a sequence of softening and/or hardening phases. The experimental data were also used to estimate the “mean” Manson–Coffin curve for 50% failure probability, and the design curves at lower probability by using four statistical methods. Compared to the “mean” curve line, the design curves are more conservative, showing a reduction of the allowable strain amplitude of about 20% at 2×10^5 reversals to failure.

Acknowledgements This work was funded by the “Fondo per l’Incentivazione alla Ricerca (FIR 2019)” (Prot. No. 117147) promoted by the University of Ferrara.

References

1. Pelegatti M, Lanzutti L, Salvati E, Srnec Novak J, De Bona F, Benasciutti D (2021) Cyclic plasticity and low cycle fatigue of an AISI 316L stainless steel: Experimental evaluation of material parameters for durability design. *Materials* 14(13):3588
2. Pham MS, Holdsworth SR, Janssens KGF, Mazza E (2013) Cyclic deformation response of AISI 316L at room temperature: Mechanical behaviour, microstructural evolution, physically-based evolutionary constitutive modelling. *Int J Plasticity* 47:143–164
3. Zhou J, Sun Z, Kanouté P, Reirant D (2018) Experimental analysis and constitutive modelling of cyclic behaviour of 316L steels including hardening/softening and strain range memory effect in LCF regime. *Int J Plasticity* 107:54–78
4. Shen CL, Wirsching PH, Cashman GT (1996) Design curve to characterize fatigue strength. *J Eng Mater Technol Trans ASME* 118(4), 535–541

Chapter 43

Contribution to the Study of the Fatigue of Riveted Joints, Influence of the Material and of the Stress Ratio



Stéphane Sire , Paul Dario Toasa Caiza , Bernard Espion ,
and Muriel Ragueneau

Abstract This paper deals with the study of the fatigue behavior of riveted joints. In particular, the description of the fatigue curves stress range vs. number of cycles to failure (Wöhler curves) requires a certain number of failure points to be relevant. We propose the analysis of the relevance of three models for the description of fatigue curves from the LCF regime to the VHCF regime. The models of Basquin, Weibull (Castillo and Fernandez-Canteli), and Stüssi are studied for the case of a single-rivet assembly, made of steel and wrought iron, for two stress ratios ($R = 0$ and $R = 0.6$). We show that the Weibull and Stüssi models are similar to the linear Basquin model in a range from about 10^5 cycles to 10^7 cycles. The Stüssi model based on the fatigue limit obtained with the Weibull model and the tensile limit of the assembly seems to offer a better description of the Wöhler curves. Nevertheless, the model requires additional failure points in the LCF and VHCF domains to improve the description.

Keywords Fatigue · Wöhler curves · Stüssi · Basquin

43.1 Introduction

The French railway network includes more than 2000 old metal bridges. They are made of wrought iron for most of those built during the second half of the nineteenth century or steel for the majority of those built in the twentieth century. Thus, many of them have a life span of more than one hundred years. During their lifetime, the

S. Sire (✉)
UMR CNRS 6027 IRDL, University of Brest, 29200 Brest, France
e-mail: stephane.sire@univ-brest.fr

P. D. T. Caiza
Research Center for Steel, Timber & Masonry, Karlsruhe Institute of Technology (KIT),
Karlsruhe, Germany

B. Espion
Université Libre de Bruxelles (ULB), BATIR Lab, Brussels, Belgium

M. Ragueneau
National Society of French Railways, La Plaine, Saint-Denis, France

traffic has strongly increased in weight, frequency and speed. Since the construction details of these bridges are riveted connections (the subject of this study), studying the durability of these connections is a major challenge to ensure the best possible maintenance [1]. Indeed, riveted connections undergo various pathologies over time, such as deconsolidation or propagation of fatigue cracks, mainly at the stringer to cross-beam connection [2]. The issue of maintenance is the most important one for obvious reasons of safety and also of heritage preservation.

The fatigue life of riveted joints has been the subject of numerous studies. Thus, Taras and Greiner propose a review of studies carried out and define the detail category $\Delta\sigma_c = 71$ Mpa at 2 million cycles to failure, as being conservative for all the work carried out [3]. However, few data are available in the relevant field of civil engineering structures in the railway domain (beyond 10 million cycles to failure). Moreover, this same study proposes to take into account the mean stress (stress ratio R) via a formula depending on the material (wrought iron or steel) and depending on the manufacturing period of the material. But, as it is specified in this paper, “the R-dependency is not fully backed for riveted assemblies” and “only a small number of fatigue tests were performed with the specific intent of determining the relationship between stress ratio and fatigue strength.” This study presents a contribution to the study of riveted assemblies by taking into account the stress ratio dependency.

43.2 Specimens and Models

43.2.1 Riveted Specimens Design and Fabrication

For this study, two materials have been studied; a modern S235 grade steel and a wrought iron from a 1864 dismantled bridge; for more details about the bridge, see [1]. Specimens have been manufactured taking into account dimensions of riveted connections described in historical technical documentations. Plates are 8 mm thick for the S235 steel and 7.2 mm thick for the wrought iron. The S235 grade steel was chosen because it has mechanical characteristics similar to those of wrought irons and steels used in the construction of old metal bridges. The riveting procedure carried out by the repairing of metal bridges (RMP) team of the SNCF includes different steps:

- drilling then reaming the holes,
- cutting the rivet to the appropriate length,
- heating of the rivet up to 1000 °C,
- insertion of the rivet,
- pressing on the rivet and forming of the second rivet head,
- cooling down of the connection.

Dimensions of the riveted specimens are described in Fig. 43.1.

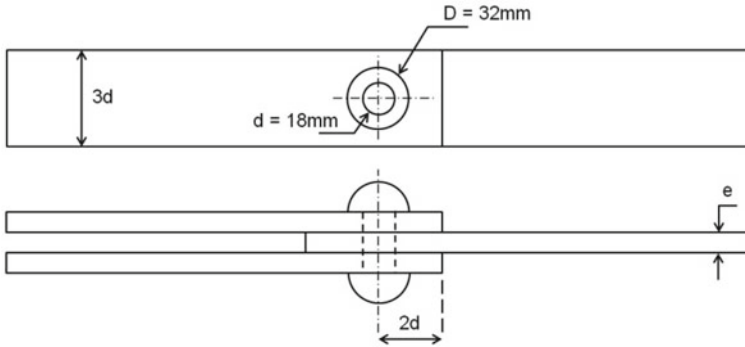


Fig. 43.1 Geometry of the riveted specimens

More than thirty single riveted specimens were manufactured for this experimental campaign.

43.2.2 Models Used for the Description of Wöhler Curves

Three models have been studied in this work. The linear Basquin model (in a logarithmic diagram), see [4], given by Eq. (43.1). The Weibull model proposed by Castillo and Fernandez-Canteli [5–7], which describes the probability of failure, see Eq. (43.2). And finally, the Stüssi model [8] given by Eq. (43.3).

$$\text{Log } N = A - B \text{Log } \Delta\sigma; \Delta\sigma \geq \Delta\sigma_\infty \tag{43.1}$$

$$p = 1 - \exp\left(-\left(\frac{(\text{Log}(N) - B) \cdot (\text{Log}(\Delta\sigma) - C) - \lambda}{\delta}\right)^\beta\right) \tag{43.2}$$

$$\Delta\sigma = \frac{R_m(1 - R) + \alpha N^\beta \Delta\sigma_\infty}{1 + \alpha N^\beta}, |R| \leq 1 \tag{43.3}$$

The Stüssi model considers the fatigue limit $\Delta\sigma_\infty$ estimated by the Weibull model and it also requires, by definition, to know the ultimate tensile stress R_m of the joint. α and β are geometrical parameters.

43.3 Results at $R = 0$

The tests at $R = 0$ for the steel and iron specimens are presented in Fig. 43.2 (the green dots correspond to the failure points for iron specimens and the red dots to steel). In

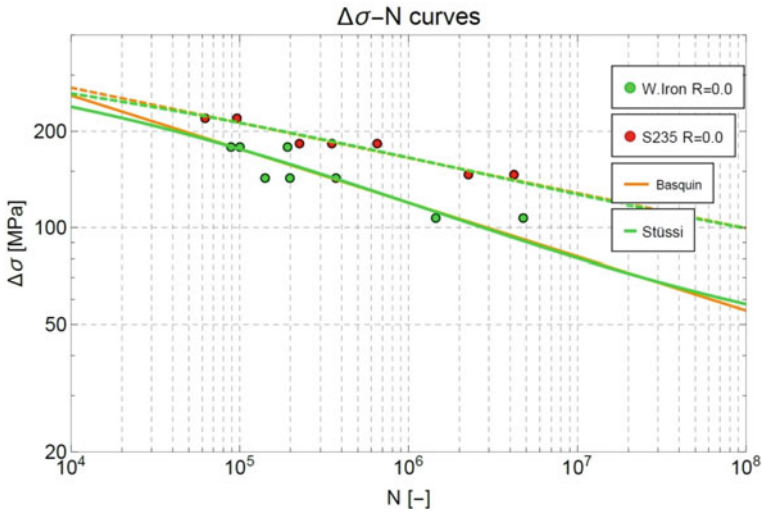


Fig. 43.2 Linear and Stüssi model Wöhler curves of riveted specimens made of wrought iron (green dots) and steel (red dots)

the presented range of number of cycles to failure, the behaviors are almost identical with the Stüssi model and the linear Basquin model; in order not to unnecessarily complicate the diagram, the curve of the Weibull model is not represented but has an identical shape. These curves thus underline the relevance of the linear model between 10⁵ and 10⁷ cycles. The slopes of these two lines are different, which shows that the fatigue performance of the wrought iron in the study is worse than that of the modern S235 steel.

As the fatigue curves are assumed to be asymptotic (by definition of the proposed Weibull model), the fatigue limit analysis shows a significant difference between the fatigue limit for steel specimens (54 MPa) and iron specimens (35.9 MPa), see Fig. 43.3. These curves also show the need for more failure points in the VHCF regime in order to increase the accuracy of the estimation of the fatigue limits. This is all the more important considering the railway context for which the fatigue data of assemblies are missing in the VHCF domain. On the other hand, in the LCF domain, the application of the linear model is also inappropriate and the application of the Stüssi model shows the consideration of ultimate tensile stresses. Similarly, the need for more weak points in the LCF regime is underlined by the shape of these curves.

43.4 Steel Specimens, R-dependency

The first results of the study of the influence of the mean stress on the fatigue life of riveted joints have been presented in [9].

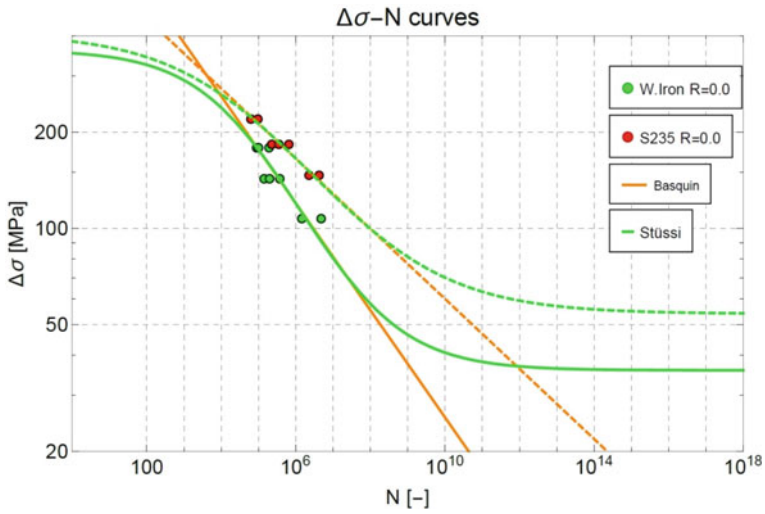


Fig. 43.3 Global view of the Wöhler curves, from LCF regime to VHCF regime for riveted specimens made of wrought iron (green dots) and steel (red dots)

The following Fig. 43.4 shows, for steel specimens, the results of test campaigns conducted for $R = 0$ and $R = 0.6$. Given the similarity between the Basquin and Stüssi models in the proposed range of number of cycles to failure (from 10^5 to 10^7), only the Stüssi and Weibull models are proposed. The slopes of these curves

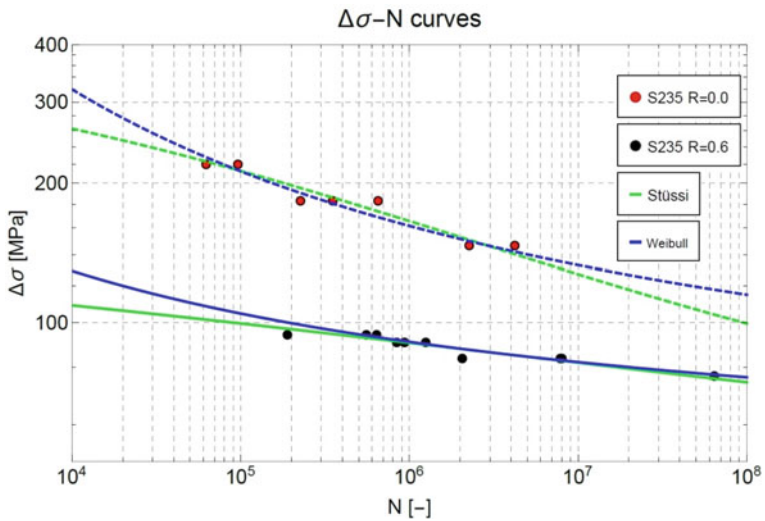


Fig. 43.4 Wöhler curves of steel riveted specimens for two different stress ratios $R = 0$ and $R = 0.6$

are significantly different for the two studied stress ratios. Thus, at $R = 0.6$, the line gets closer to the horizontal which underlines a more important scatter of the results (i.e., at imposed stress range, the number of cycles to failure can vary a lot). Another important result is that by definition the Weibull model is based on two asymptotes, one of which is vertical (parameter B in Eq. (43.2)), which describes the transition from the plastic to the elastic regime (or crack initiation period to the crack growth period). Thus, the Weibull model does not allow to estimate the fatigue strength in the LCF regime.

In these two cases, as pointed out previously, having more failure points in the different domains presented by a fatigue curve will improve its modeling.

43.5 Conclusions

A contribution to the study of the fatigue behavior of riveted assemblies has been proposed. The influence of the material (steel and a wrought iron) and the influence of the mean stress ($R = 0$ and $R = 0.6$) are investigated. The description of the fatigue curves from the experimental data is proposed using three models.

The advantage of using a linear model has been underlined for a range of number of cycles to failure between 10^5 and 10^7 cycles. In the field of civil engineering railway structures, more failure points should be considered to improve the evaluation of its experimental results. In particular, an improved evaluation will allow to refine the estimation of the fatigue limit which is a parameter used in the definition of the Stüssi model.

References

1. Gallegos Mayorga L, Sire S, Ragueneau M, Plu B (2017) Understanding the behaviour of wrought-iron riveted assemblies: manufacture and testing in France. In: Proceedings of the institution of civil engineers—engineering history & heritage, vol 170(2), pp 67–79
2. Sire S, Ragueneau M (2019) Fatigue design of metallic railway bridges in France at the end of the nineteenth century. In: Proceedings of the institution of civil engineers—forensic engineering, vol 172(4), pp 167–174
3. Taras A, Greiner R (2010) Development and application of a fatigue class catalogue for riveted bridge components. *Struct Eng Int* 20(1):91–103
4. Basquin OH (1910) The exponential law of endurance tests. *Am Soc Test Mater Proc* 10:625–630
5. Castillo E, Fernández-Canteli A (2009) A unified statistical methodology for modeling fatigue damage. Springer
6. Toasa Caiza PD, Ummenhofer T (2011) General probability weighted moments for the three-parameter Weibull distribution and their application in S-N curves modelling. *Int J Fatigue* 33(12):1533–1538
7. Fonseca Barbosa J, Correia JAFO, Freire Júnior RCS, Zhu S-P, De Jesus AMP (2019) Probabilistic S-N fields based on statistical distributions applied to metallic and composite materials: state of the art. *Adv Mech Eng* 11(8):1–22

8. Toasa Caiza PD, Ummenhofer T (2018) A probabilistic Stüssi function for modelling the S-N curves and its application on specimens made of steel S355J2+N. *Int J Fatigue* 117:121–134
9. Sire S, Toasa Caiza PD, Espion E, Ragueneau M (2020) Contribution to the study of the influence of the stress ratio on the high cycle fatigue behaviour of riveted joints. *Fatigue Fract Eng Mater Struct* 43(12):3027–3036